



**HAL**  
open science

# Photorefractive and electro-optic properties of metal ion doped lithium niobate crystals

Anush Danielyan

► **To cite this version:**

Anush Danielyan. Photorefractive and electro-optic properties of metal ion doped lithium niobate crystals. Optics / Photonics. Université de Lorraine; Armenian state pedagogical university after Khachatur Abovyan, 2019. English. NNT : 2019LORR0256 . tel-02557319

**HAL Id: tel-02557319**

**<https://hal.univ-lorraine.fr/tel-02557319>**

Submitted on 28 Apr 2020

**HAL** is a multi-disciplinary open access archive for the deposit and dissemination of scientific research documents, whether they are published or not. The documents may come from teaching and research institutions in France or abroad, or from public or private research centers.

L'archive ouverte pluridisciplinaire **HAL**, est destinée au dépôt et à la diffusion de documents scientifiques de niveau recherche, publiés ou non, émanant des établissements d'enseignement et de recherche français ou étrangers, des laboratoires publics ou privés.



## AVERTISSEMENT

Ce document est le fruit d'un long travail approuvé par le jury de soutenance et mis à disposition de l'ensemble de la communauté universitaire élargie.

Il est soumis à la propriété intellectuelle de l'auteur. Ceci implique une obligation de citation et de référencement lors de l'utilisation de ce document.

D'autre part, toute contrefaçon, plagiat, reproduction illicite encourt une poursuite pénale.

Contact : [ddoc-theses-contact@univ-lorraine.fr](mailto:ddoc-theses-contact@univ-lorraine.fr)

## LIENS

Code de la Propriété Intellectuelle. articles L 122. 4

Code de la Propriété Intellectuelle. articles L 335.2- L 335.10

[http://www.cfcopies.com/V2/leg/leg\\_droi.php](http://www.cfcopies.com/V2/leg/leg_droi.php)

<http://www.culture.gouv.fr/culture/infos-pratiques/droits/protection.htm>

**Laboratoire Matériaux  
Optiques, Photonique**

**Thèse de Doctorat de L'Université de Lorraine**  
*Ecole Doctorale C2MP: Chimie - Mécanique - Matériaux- Physique*

**Spécialité : Physique**

Présentée et soutenue publiquement par:

**ANUSH DANIELYAN**

le 25 septembre 2019

à l'Armenian State Pedagogical University after Khachatur Abovyan,  
Yerevan Armenie

**Propriétés photoréfractives et  
électro-optiques des cristaux de niobate de  
lithium dopés aux ions métalliques**

devant le jury composé de :

Yannick MUGNIER	Laboratoire Système et Matériaux pour la Mécatronique, SYMME, Université Savoie Mont Blanc, Annecy, France	Rapporteur
Kamo AHARONYAN	National Polytechnic University of Armenia, Department of Applied Mathematics and Physics, Yerevan, Armenia	Rapporteur
Ninel KOKANYAN	Laboratoire Matériaux Optiques Photonique et Systèmes, LMOPS, CentraleSupélec, Université de Paris-Saclay, Metz, France	Examineur
Narine BABAJANYAN	Armenian State Pedagogical University after Khachatur Abovyan, Department of Physics and its Teaching Methods, Yerevan, Armenia	Examineur
Edvard KOKANYAN	Armenian State Pedagogical University after Khachatur Abovyan, Department of Physics and its Teaching Methods, Institute for Physical Research, National Academy of Sciences; Armenia	Directeur
Michel AILLERIE	Laboratoire Matériaux Optiques, Photonique et Systèmes, LMOPS, Université de Lorraine & CentraleSupélec, Paris-Saclay, Metz, France	Directeur
Sergey KOSTRITSKII	R&D Department, RPC Optolink, Zelenograd, Moscow, Russia	Invité



## **Acknowledgement**

*Firstly, I would like to express my sincere gratitude to my scientific supervisors Profs. Edvard Kokanyan and Michel Aillerie for the continuous support of my PhD study and related research, for their motivation, inspiration. Thanks to them in the frame of the collaboration between Institute of Physical Research of National Academy of Sciences of the Republic of Armenia and Universite of Lorraine I have realized part of my PhD research at the Laboratoire Matériaux Optiques Photonique et Systèmes of the Université Lorraine et CentraleSupélec (Metz, France). Their guidance helped me in all the time of research and writing of this thesis. I could not have imagined having a better advisors and mentors for my PhD study This PhD investigation is the result of the productive international collaboration. I would like also to be grateful to:*

*Prof. Marco Bazzan for providing me an opportunity to join his group and to access to the research facilities in the Physics and Astronomy Department of the University of Padova (Italy). Dr. Laura Vitadello from the same university for the joint research of the photorefractive properties and the concentrations of iron ions for the iron doped lithium niobate crystals.*

*Prof. Sergey Kostriskii from R&D Department, RPC Optolink (Zelenograd, Moscow, Russia) for the valuable discussion and not just.*

*Assistant Prof. Ninel Kokanyan from Laboratoire Matériaux Optiques Photonique et Systèmes of the Université Lorraine et CentraleSupélec (Metz, France) for the long discussions related to the Raman spectroscopy and not just.*

*Another special thanks to all employee of Laboratoire Matériaux Optiques Photonique et Systèmes of the Université Lorraine et CentraleSupélec (Metz, France) for the technical support.*

*Without the support of all this persons it would not be possible to conduct this PhD research.*



# Contents

<i>Introduction</i> .....	1
Introduction-general information about lithium niobate .....	3
<i>References-Introduction</i> .....	11
Chapter 1.....	15
Samples for research .....	15
§ 1.1. <i>Growth of crystals</i> .....	16
§ 1.2. <i>Preparation of samples</i> .....	18
§ 1.3. <i>Conclusion-Chapter 1</i> .....	20
Chapter 2.....	23
Structure and composition of doped LN crystals .....	23
§ 2.1 <i>X-ray diffraction. Lattice parameters of crystals</i> .....	24
<i>Literature Review</i> .....	24
<i>Theory</i> .....	25
§2.1.1. <i>Experimental Technique</i> .....	29
§ 2.1.2. <i>Results and discussion</i> .....	31
§ 2.2 <i>Raman spectroscopy</i> .....	38
<i>Literature review</i> .....	38
<i>Theory</i> .....	40
§ 2.2.1. <i>Experimental Technique</i> .....	44
§ 2.2.2. <i>Results and Discussion</i> .....	46
§ 2.3. <i>Optical absorption</i> .....	52
<i>Theory</i> .....	52
§ 2.3.1. <i>Experimental Technique</i> .....	52
§ 2.3.2. <i>Results and Discussion</i> .....	55
§ 2.4. <i>Conclusion-Chapter 2</i> .....	58
<i>References-Chapter 2</i> .....	60
Chapter 3.....	65
Electro-optical Properties.....	65
<i>Electro-Optic Effect</i> .....	66
<i>Electro-Optic Effect in Lithium Niobate (LN) Crystals</i> .....	71
<i>Dielectric properties of lithium niobate</i> .....	73
<i>Relationship between linear electro-optic coefficients and dielectric permittivity</i> .....	78
<i>Literature Review of the investigation of electro-optic (EO) effect in LN crystals</i> .....	80
§ 3.1. <i>Used experimental techniques</i> .....	87

§ 3.1.1. <i>Experimental technique for EO measurements.</i>	87
§ 3.1.1.1. <i>One-Beam Senarmont-Type Ellipsometric Technique</i>	87
<i>The compensation of the natural retardation.</i>	89
§ 3.1.1.1.1. <i>The frequency-doubling electro-optic modulation measurement method (FDEOM method)</i>	92
§ 3.1.1.1.2. <i>The modulation depth measurement method (MDM)</i>	94
§ 3.1.1.2. <i>Interferometric measurements</i>	96
§ 3.1.1.3. <i>Time Response method (TRM)</i>	99
§ 3.1.1.4. <i>The opto-geometric configurations required for EO measurements</i>	101
§ 3.1.2 <i>Experimental technique for dielectric measurements.</i>	102
§ 3.2. <i>EO and dielectric coefficients of LN crystals doped with non-photorefractive ions.</i>	103
§ 3.2.1. <i>Zr doped crystals</i>	103
§ 3.2.1.1. <i>Details of Experiments</i>	103
<i>Electro-Optic measurements</i>	103
<i>Dielectric measurements</i>	106
§ 3.2.2 <i>In doped crystals</i>	107
§ 3.2.2.1 <i>Details of Experiments</i>	107
<i>Electro-Optic measurements</i>	107
<i>Dielectric measurements.</i>	108
§ 3.3. <i>EO and dielectric coefficients of LN crystals doped with transition metal (Fe) ions.</i>	109
§ 3.3.1. <i>Details of Experiments</i>	109
<i>Electro-Optic Measurements</i>	109
<i>Dielectric Measurements</i>	110
§ 3.4. <i>Results and Discussion</i>	110
§ 3.4.1. <i>LN crystals doped with non-photorefractive ions.</i>	110
§ 3.4.1.1. <i>Zr doped crystals</i>	110
§ 3.4.1.2. <i>In doped crystals</i>	115
§ 3.4.2. <i>LN crystals doped with transition metal (Fe) ions</i>	119
§ 3.5. <i>Conclusion-Chapter 3</i>	127
<i>References-Chapter 3</i>	130
Chapter 4	139
Photorefractive properties of Lithium niobate crystals	139
§ 4.1. <i>Photorefractive effect</i>	140
§ 4.2. <i>Photogalvanic effect</i>	146
§ 4.3. <i>Photoconductivity</i>	148

§ 4.4. <i>Space charge field</i> .....	155
§ 4.5. <i>The used experimental technique</i> .....	156
§ 4.5.1. <i>Digital holographic technique</i> .....	157
§ 4.5.2. <i>The phase shift modeling</i> .....	162
§ 4.6. <i>Data Analysis</i> .....	168
§ 4.6.1. <i>Experimental results</i> .....	168
§ 4.7. <i>Simulation</i> .....	175
§ 4.7.1. <i>Marcus-Holstein polaron hopping model</i> .....	175
§ 4.7.2. <i>Monte Carlo simulation</i> .....	177
§ 4.8. <i>Yields</i> .....	179
§ 4.9. <i>Discussion</i> .....	185
§ 4.10. <i>Conclusion-Chapter 4</i> .....	187
<i>References-Chapter 4</i> .....	189
Conclusion .....	199
Résumé.....	202
Summary .....	204



## ***Introduction***

### ***Brief justification of the modernity of the thesis***

Lithium niobate (LN) is attractive material more than 50 years for the frequency mixers and doublers, integrated optical devices, electro-optical modulators, holographic data recording and storage thanks to the acousto-optical, non-linear optical, piezo-electrical, electro-optical and photorefractive properties. However, the overall understanding of certain phenomena that is photorefractive effect occurring in the crystal is still under heavy discussion. The mentioned phenomenon plays a key role: on one side it substantially restricted the main part of the wavelength conversion applications as when illuminated by visible light or near infrared, there are semi-permanent changes in the refractive index of the crystal, causing a distortion of the beam, greatly reducing the efficiency of the device, on the other hand it need to improve for holographic applications. From this point of view LN:Fe crystals offer the fascinating possibilities due to the sensitivity to the photorefractivity and the possibility to obtain the crystals with high optical qualities.

### ***Purpose of the thesis***

The dissertation is devoted to the investigation of the photorefractive, structural, electro-optical (EO) and dielectrical properties depending on the intrinsic and extrinsic (introduced by incorporation of non photorefractive ( $Zr^{4+}$ ,  $In^{3+}$ ) and photorefractive ( $Fe^{2+/3+}$ ) ions) defects in LN crystals resulting to the purposeful control the photorefractive properties taking into account the features of the applications of LN crystals.

### ***Objectives***

The aim of the thesis is a development of a vision on advanced photorefractive and electro-optic properties in LN crystals doped with the transition metal ( $Fe^{2+/3+}$ ) and non-photorefractive ( $Zr^{4+}$ ,  $In^{3+}$ ) ions on the base of a full investigation of structural, compositional, electro-optical, photorefractive properties of the mentioned crystals, to work out the parameters for a strong control of photorefractive properties of this material and optimal conditions for the growth of high quality crystals with controlled physical properties and to grow these crystals as well.

The thesis consists of introduction and four chapters:

Introduction includes the general information about lithium niobate (LN).

The first chapter is dedicated to the description of growth process of the crystals (§ 1.1) and the preparation of samples (§ 1.2).

The second chapter is devoted to the structural and composition investigations of the understudy samples LN:Fe1-1÷LN:Fe1-3 (the results are given in Table 1). In § 2.1 it is discussed the theory, literary review, experimental details and the results of the X-Ray diffraction analysis used to obtain lattice parameters  $a$  and  $c$ .

§ 2.2 is dedicated to the theory, literary review, details of experiments and the experimental results of Raman backscattering spectroscopy utilized to determine  $Li_2O$  content in the crystal as well as to study the frequency shift of A1(TO) phonons as a function of crystal composition and the introduction of iron ions in LN:Fe1-1÷LN:Fe1-3 samples.

In § 2.3 the discussed optical absorption measurements has been realized to investigate the concentrations of ions  $Fe^{2+}$  and  $Fe^{3+}$  in the understudy LN:Fe1-1÷LN:Fe1-3 samples.

Chapter 3 is dedicated to the theory, literary review and the experimental methods and techniques of electro-optic (EO) and dielectric investigations (§3.1) realized for LN samples doped with non photorefractive (§3.2.1 and §3.2.2) and transition metal ions (§3.3).

Chapter 4 is dedicated to the investigation of the photorefractive effect in LN:Fe1-1÷LN:Fe1-3 and LN:Fe2-1÷LN:Fe2-3 samples. We described and analyzed the theoretical observations of the photorefractive and photogalvanic effects, photoconductivity and the influence of the space charge field on these properties.

# **Introduction-general information about lithium niobate**

## Introduction-general information about lithium niobate.

The synthetic Lithium niobate (LN) crystals first obtained in 1949 by Matthias and Remeika [1], a colorless, chemically stable and insoluble in water, having high melting points, belong to the  $ABO_3$  -type ferroelectrics with oxygen octahedron and exhibits spontaneous electric polarization (Ferroelectricity). At room temperature LN electro-optic crystals belong to the rhombohedral (trigonal) space group  $R_{3C}$  with  $3m$  point group ( $C6v$  in Schonflies notation) [2] as it demonstrates three-fold rotation symmetry about its  $c$  axis. The unit cell of the crystallographic rhombohedral structure consists of ten atoms (Figure 1) where parallel planes of oxygen atoms are approximately hexagonal (Figure 2). The latter is related to the metal atoms filling the oxygen octahedron, along the ferroelectric axis (trigonal), by the following arrangement:  $Nb \square LiNb \square LiNb \square LiNb \dots$  where  $\square$  demonstrates a vacant site. Li and Nb ions are shifted from the center of oxygen octahedron in the direction of the crystallographic  $c$  axis of the hexagonal lattice.

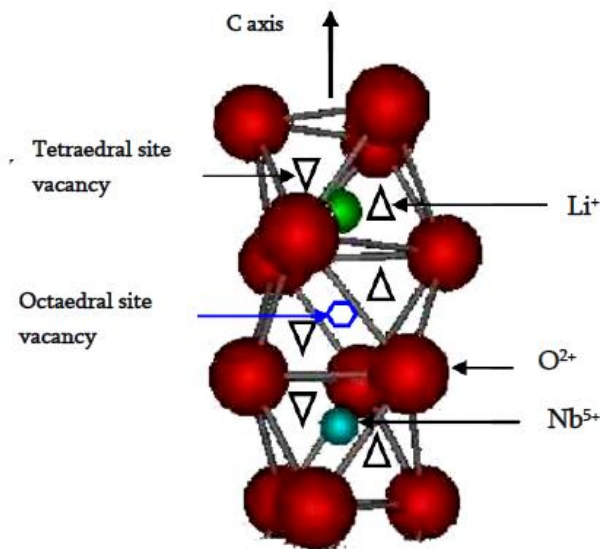


Figure 1: The primitive rhombohedral cell of LN crystals.

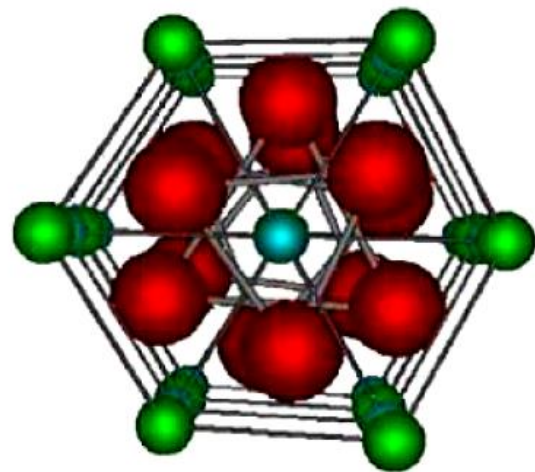


Figure 2: Atomic arrangement of the LN structure along the  $c$  axis.

This space group is stable in the wide temperature range from room temperature up to the Curie temperature above  $1100^{\circ}C$ . At the temperature below Curie temperature  $T < T_C$ , the

oxygen octahedron is one-third filled by lithium atoms, one-third by niobium atoms and one-third by vacancies. [3]. In the paraelectric phase above Curie temperature  $T > T_c$ , where LN crystal belongs to the  $R\bar{3}c$  space group and  $\bar{3}m$  point group,  $Li^+$  cations lie in an oxygen layer  $c/4$  away from the Nb atoms, whereas  $Nb^{5+}$  ions are centered between oxygen layers [4]. As the temperature decreased from the Curie temperature, Nb and Li atoms occupy their new positions caused of dominant elastic forces resulting to the charge separation. Following to this phenomena LN crystal exhibits the spontaneous polarization.

There are three choices of axes so-called rhombohedral, hexagonal, orthohexagonal. Among them the orthohexagonal setting is preferred as all axes are mutually orthogonal. The conventional cell of LN crystal (Figure 3) includes hexagonal axes  $a, b, c$  and the axes of Cartesian crystal coordinate system  $x, y, z$ .

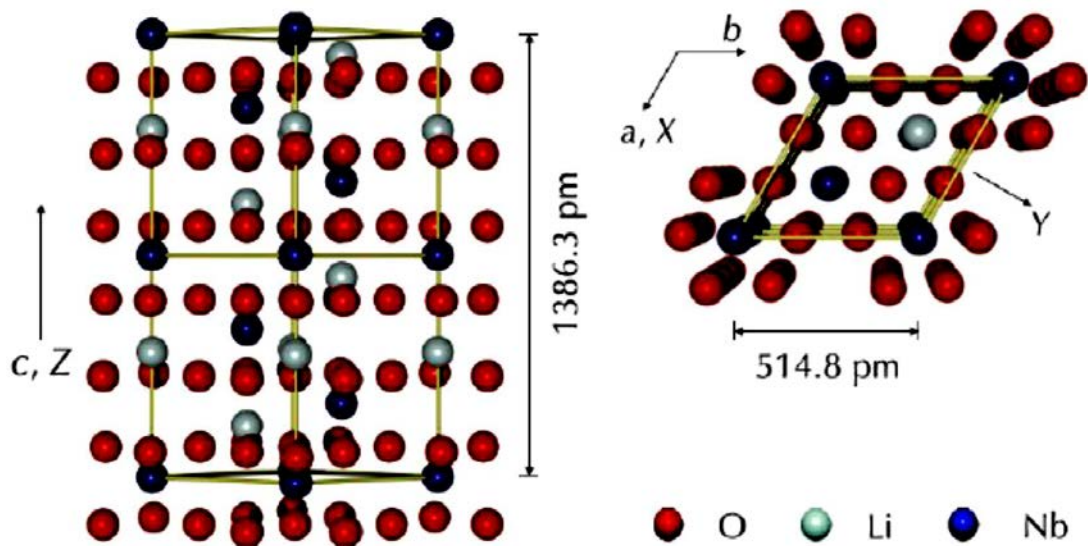


Figure 3: The structure of LN by using hexagonal axes.

The unit cell about crystallographic  $c$  axis exhibits the three fold rotation symmetry [5]. The  $c$  axis is parallel to the polar  $z$  axis, whereas  $x$  axis is parallel to one of the three equivalent crystallographic axes spaced by  $120^\circ$  angle perpendicular to the  $z$  axis and  $y - z$  plane. Thus the  $y$  axis is along of symmetry and is perpendicular to the  $x$  and  $z$  axes [6].

Lattice parameters observed by Hsu et al. [7] are given in Table 1.

Table 1: Lattice  $a$  and  $c$  parameters and positions of atoms in the unit cell of LN crystal [7].

Lattice parameters			
$a = b = 5.148(3)\text{\AA}$	$c = 13.863(3)\text{\AA}$		$v = 318.2(4)\text{\AA}^3$
Positions of atoms in the lattice (Nb is taken as the origin)			
Nb	0	0	-0.02210(2)
O	0.0475(5)	0.34301(5)	0.0625(5)
Li	0	0	0.2086(4)

LN cleaves along  $\{01\bar{1}2\}$  planes and there are three cleavage planes  $\{01\bar{1}2\}$ ,  $\{\bar{1}012\}$  and  $\{1\bar{1}02\}$  as LN crystal indicates three-fold rotation symmetry [8].

The comparison of LN crystal grown from congruent melt containing Li deficiency and stoichiometric crystal can be given by the following schematic phase diagram (Figure 4) [9].

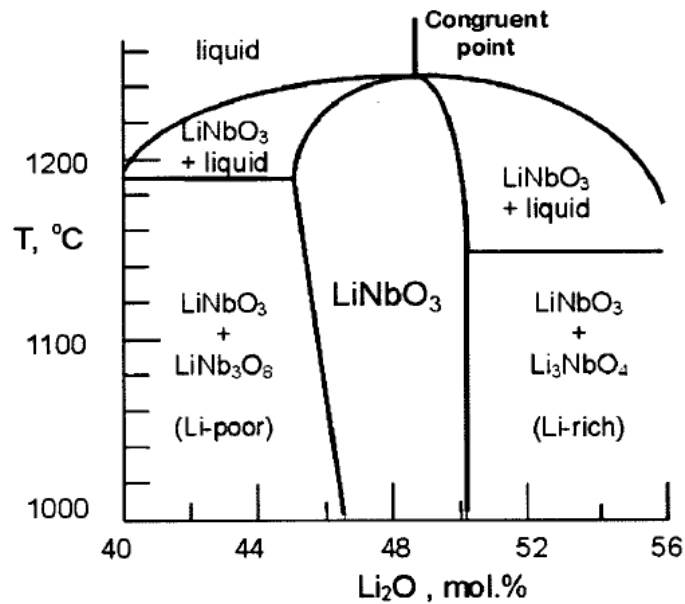
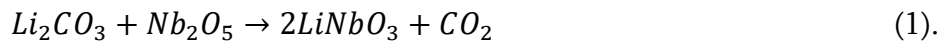


Figure 4: Schematic phase diagram of the  $Li_2O - Nb_2O_5$  of the congruent and stoichiometric compositions of LN crystal [9].

According to the diagram of  $Li_2O - Nb_2O_5$  system LN is a material with a variable composition exhibiting wide non-stoichiometry in the Li/Nb cation ratio. The chemical reaction indicating the development of  $Li_2O$  from the  $Li_2CO - Nb_2O_5$  system can be expressed as:



The liquidus - solidus curve illustrates a diffuse maximum for  $X_m = [Li]/([Li] + [Nb]) = 48.4 \div 48.6$  congruent composition, which corresponds to the single point where both the melt and the crystal are identical with respect to the composition [10,11]. The nonstoichiometric solid solution (deficient of Li or excess Nb) is up to 6 mol% at  $T > 1150^\circ C$  for congruent composition. The congruent composition contains an excess of Nb ions compared to the Li-enriched composition. The deviation from stoichiometry is related to the density of nonstoichiometric defects. During grow process the melt composition varies with the crystallization of the lithium niobate causing a non-uniformity in the grown crystal composition. To achieve 50 mol%  $Li_2O$  in the crystal the LN must be grown from Li-enriched melt with the composition equal to about of 58.5 mol% [12]. The commercial congruent LN crystals usually are grown by Czochralski method by pulling from a melt, which is known as the most common growth method [13, 14]. The mixture of initial materials lithium carbonate ( $LiCO_3$ ) and niobium pentoxide ( $Nb_2O_5$ ) powders is annealed at  $700-800^\circ C$  for drying. The mixture after sintering at  $1050^\circ C$  for 2-4 hours and grounding at room temperature is melted in platinum crucible. The rotating LN crystal seed is located in the melt having the temperature slight higher of melting point and the crystal growth process is started when the seed rod is taken out slightly from the melt. The crystal is grown on the seed parallel to the crystallographic axis of seed. The temperature of crucible influences on the diameter of the growing crystal and the crystallization starts faster when the crucible temperature is close to the melting point of  $LiNbO_3$ . For growth process does not need the special atmosphere.

To achieve a near-stoichiometric composition in the crystal the vapor transport equilibration (VTE) growth technique was suggested in 1992 by Bordui et al [15]. Later, Malovichko, Kokanyan et al. proposed the other method according to which the crystal with stoichiometric composition was grown from the congruent melt by adding  $K_2O$  to the melt [16]. Also Polgar et al reported the technique named top-seeded solution growth (TSSG) by using potassium mixture as a high temperature solution [17]. Kitamura et al. proposed double crucible Czochralski method (DCCZ) method to grow near stoichiometric crystal from Li-enriched melt [18].

**Intrinsic defects:** In Li deficient crystals the deviation from stoichiometry is accompanied by the formation of Li vacancies ( $V_{Li}^-$ ) creating consequently Nb antisite defects ( $Nb_{Li}^{5+}$ ) as  $Nb^{5+}$  ions occupy vacancies in Li site having the nearly equal ionic radius as  $Li^+$  ions [19,20,21]. In order to maintain the charge neutrality caused by charge difference of  $Li^+$  and  $Nb^{5+}$  ions the additional Li vacancies appear in non-stoichiometric crystal [21]. Along with  $V_{Li}^-$  vacancies and  $Nb_{Li}^{5+}$  ions, oxygen vacancies ( $V_O^{2-}$ ) and protons ( $H^+$ ) also exist. Nb ions by trapping electrons in their turn form the other defects: free polaron ( $Nb_{Nb}^{4+}$ ), bound polaron ( $Nb_{Li}^{4+}$ ) and bi-polaron ( $Nb_{Li}^{4+} - Nb_{Li}^{4+}$ ) [20]. On the other hand  $V_{Li}^-$  vacancies by trapping holes also create hole-polarons. For the first time self-trapped charge carriers so-called polaron term was used by Landau [22]. According to the investigation of Landau in alkali halides due to the strong electron-phonon interaction formed charge carriers (electrons or holes) distort the neighboring lattice through the short-range and Coulomb interactions [23]. The displacement (shift) of surrounding ions results to a potential well where free charge carriers can be localized. For the first time in ionic (polar) substance discovered the quasiparticle formed by the electron-phonon coupling was referred to us as polaron consist of the self-trapped carrier and the resulting ionic displacements [24]. According to the coupling strength two kinds of polarons are well-known: large and small [25]. For large polaron the polaronic radii is larger compared to the lattice constant, whereas in the case of small polaron the increase of the coupling strength and the reduction of the polaronic radius restrict the potential well to a single lattice site [20]. Thus, the self-trapping of the charge carrier at this single site induces a small polaron due to the sufficiently strong short range interaction of the charge carrier with the neighboring lattice. After the displacement the vibration of the surrounding ions around new equilibrium positions leads to the lower energy than the half width of the energy band expecting from the tunnelling between the equivalent sites. Consequently for small polaron the tunnelling effect is strongly extinguished resulting to the lattice distortion. Various types of small polarons can be found in LN crystals [20,21,23].

Free small electron polaron composes electrons localized at Nb site. The self-trapping of electron at the regular  $Nb_{Nb}^{5+}$  ions forms the most simple type of polaron referred as “small free polaron”  $Nb_{Nb}^{4+}$  which is also the most shallow trap in LN crystals [20, 26]. Free small polarons were found only in Mg or Zn doped LN crystals above the threshold concentrations as bellow them the deeper traps  $Nb_{Li}$  exist yet [27].

Bound small electron polaron or simply bound polaron forms when electron are captured at the  $Nb_{Li}^{5+}$  antisites resulting to the locally lattice distortion. Due to the bounded electron to this site this defect is so-called bound small polaron. They can play the crucial role in photorefractive effect influencing on the photoconductivity [23]. Both free and bound small polarons are unstable at room temperature as they can be barely populated in the case of availability of enough electrons. This situation is supported by reduction treatment or by optical excitation of electrons to the valence band.

Bound bipolaron  $Nb_{Li}^{4+} - Nb_{Nb}^{4+}$  forms due to the accommodation of two electrons at the nearest neighbor couples  $Nb_{Li}^{5+} - Nb_{Nb}^{5+}$ . This polarons can be stabilized mainly by replacing the ions along the lattice mode towards each other [20, 28] and can be stable at room temperature in reduced LN samples. However they are dissociated optically and thermally, particularly optical dissociation of bound bipolaron turns onto the  $Nb_{Li}^{4+}$  and  $Nb_{Nb}^{4+}$  polarons. All mentioned types of small polarons compose electrons increasing the Fermi level of the substance by reduction treatment or by appropriate illumination.

Small bound hole polaron forms thanks to the irradiation of the material with the high photon energy. With the excitation of electrons to the conduction band the holes can be created in the valence band. The capturing of this holes by Li vacancies leads to the formation of stable small bound hole polaron  $V_{Li} - O^-$  [29].

The absence of free or bound polarons leading to the storage of all the charge is considered in LN:Fe crystals. Due to the photon absorption by the  $Fe^{2+}$  donor center formed small polaron realize a certain number of jump on  $Nb_{Nb}$  or  $Nb_{Li}$  sites. This hop occurs until the polaron is captured at the deep  $Fe^{3+}$  acceptor center consequently determine the final distance of the movement of the polaron.

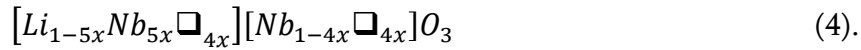
Historically, three different models have been proposed to explain the defect structure of LN crystals: the oxygen vacancy model [30] and the cation substitution models: corresponding to the niobium vacancy [31] and to lithium vacancy [32] models. The oxygen vacancy model have been proposed by Fay et al. assuming the charge neutrality via oxygen vacancies consequently resulting the decrease of the density of the crystal and the lattice parameters. The LN crystal structure is given by:



where □ denotes the vacancies. Unfortunately, this model was not able to explain the dependence of the density on the crystal composition. For Lerner et. al [31] the increase of the density of the non stoichiometric phase with the decrease of the stoichiometry could not be interpreted by oxygen model and Li vacancy model was suggested and recently supported by Iyi et al.[33]. Due to the close ionic radius of Li and Nb ions the relative  $Li_2O$  deficiency in crystal leads to the incorporation of Nb ions onto Li site referred to as Nb antisites [34]. According to the proposed Li-vacancy model by Lerner et al. [31] for the charge neutrality caused by the difference valence of Nb ions in Li site the Li deficiency is accompanied by the formation of Li-vacancies in Li site. Every Nb antisite creates four Li vacancies ( $V_{Li}$ ), thus, the theoretical chemical composition equation corresponding to Li site vacancy model can be expressed as:



Later, Abrahams and Marsh [32] X-ray diffraction experiments for crystals with congruent and near-stoichiometric composition proposed the niobium vacancy model where the vacancies are located at Nb site. The composition equation for niobium vacancy model can be given as:



According to the later investigation realized the Donnenberg et al. [33,35] the compensation of  $Nb_{Li}$  antisites by Li vacancies is energetically feasible thus, nowadays lithium vacancy model is more valid for defect reconstructions in LN crystal. Taking into account this fact we computed the amount of intrinsic defects (Nb antisites and Li vacancies) for our under study Fe doped LN samples by using the proposed Li-vacancy model by Lerner et al. Eq. 3 [31].

According to the calculation of some structural characteristics given in Table 2 the amount of intrinsic defects (Nb antisites and Li vacancies) reduces with the increase of Li content in LN crystals.

Table 2: Composition dependence of LN crystals calculated by Li vacancy model [31].

$x_c, \%$	$Li_{1-5x}$	$V_{Li}$	$Nb_{Li}$ antisite	Formula Li site vacancy model
48.45	0.95	0.04	0.01012	$[Li_{0.950}Nb_{0.0101}\square_{0.040}][Nb]O_3$
48.58	0.95355	0.03716	0.00929	$[Li_{0.954}Nb_{0.0093}\square_{0.037}][Nb]O_3$
49.59	0.9864	0.010874	0.0027185	$[Li_{0.986}Nb_{0.0027}\square_{0.011}][Nb]O_3$

**Extrinsic defects:** To control the defect content LN crystals are usually doped either by transition metals (Fe, Cu, Cr, Mn, Ni) or by rare earth elements (Er, Nd, Yn) or by non photorefractive ions (Mg, Zn, Hf, Sn, In, Zr) forming so-called extrinsic defects. In doped crystals the resulted charge compensation leads to the satellite centers depending on the relative location of the impurity ions. Dopant ions depending on the concentration and valence state usually occupy either Li site or Nb site or both Li and Nb sites [36]. Whereas the main part of dopant ions are populated on the Li site independent of charge although the ionic radius of  $Nb^{5+}$  and  $Li^+$  are similar [37]. The charge compensation is not necessary for monovalent  $Me_v^+$  ions. For divalent impurity ions  $Me^{2+}$  the charge excess can be compensated by additional  $O^{2-}$ . However, the increase of Li content is preferable in the LN crystals doped with divalent ions than the increase of amount  $O^{2-}$  due to the larger ionic radius compared to the sizes of the octahedral and tetrahedral vacancies. Trivalent cations  $Me_v^{3+}$  incorporating onto Li site in the structural vacancy are compensated both  $V_{Li} (Me^{3+} - 3V_{Li})$ ,  $V_{Nb} (5Me^{3+} - 3V_{Nb})$  or by interstitial oxygen ions ( $2Me^{3+} - 3O_2$ ) nevertheless not by  $Nb_{Li}$  antisites and oxygen vacancies.

### ***References-Introduction***

1. B. T. Matthiar and J. P. Remeika, "Ferroelectricity in the Ilmenite Structure", *Phys. Rev.* 76, pp. 1886-1887 (1949).
2. B.K. Vainshtein, "Modern Crystallography 1", Springer Ser. Solid-State Sci., Vol. 15 (Springer, Berlin, Heidelberg, New York 1981).
3. S.C. Abrahams, J.M. Reddy, J.L. Bernstein, "Ferroelectric Lithium Niobate. 3. Single Crystal X-Ray Diffraction Study at 24°C", *J. Phys. Chem. Solids* 27, pp. 997-1012 (1966).
4. S.C. Abrahams, W.C. Hamilton, J.M. Reddy, "Ferroelectric Lithium Niobate. 4. Single Crystal X-Ray Diffraction Study at 24°C\*", *J. Phys. Chem. Solids* 27, 1013-1018 (1966).
5. "Standards on Piezoelectric Crystals," 49 IRE 14.51, *Proc. IRE* 37, 1378-1395 (1949). *Proc. IRE* 37, pp. 1378-1395 (1949).
6. R.S. Weis and T.K. Gaylord, "Lithium niobate: Summary of physical properties and crystal structure" *Appl. Phys. A* 37, pp. 191-203 (1985).
7. R. Hsu, E. N. Maslen, D. Du Boulay, N. Ishizawa, "Synchrotron X-ray Studies of LiNbO<sub>3</sub> and LiTaO<sub>3</sub>", *Acta. Cryst. B* 53, pp. 420-428, (1997).
8. G.D. Boyd, R.C. Miller, K. Nassau, W.L. Bond, A. Savage, "LiNbO<sub>3</sub>: An Efficient Phase Matchable Nonlinear Optical Material", *Appl. Phys. Lett.* 5(11), pp. 234-236 (1964).
9. H. Hatano, Y. Liu, K. Kitamura, in "Photorefractive Materials and Their Applications 2, Materials", ed. by P. Gunter, J.P. Huignard, no. 114 in Springer Series in Optical Sciences (Springer, 2007), pp. 127-164.
10. P. F. Bordui, R. G. Norwood, C. D. Bird, G. D. Calvert, "Compositional uniformity in growth and poling of large-diameter lithium niobate crystals" *J. Cryst. Growth* 113, pp. 61-68, (1991).

11. I. Baumann, P. Rudolph, D. Krab, R. Schalge, "Orthoscopic investigation of the axial optical and compositional homogeneity of Czochralski grown LiNbO<sub>3</sub> crystals" *J. Cryst. Growth* 128, pp. 903-908 (1993).
12. K. Kitamura, Y. Furukawa, H. Hatano, K. Macfarlane, H. Guinther, "Stoichiometric LN Material Potential for Holographic Data Storage", Edited by Kazuo Kuroda, first published 2002 by Taylor & Francis, "Progress in Photorefractive nonlinear optics". 11 New Fetter Lane, London EC4P4EE.
13. H. M. O'Bryan, P. K. Gallagher, and C. D. Brandle, "Congruent Composition and Li-Rich Phase Boundary of LiNbO<sub>3</sub>" *J. Am. Ceram. Soc.* 68(9), pp. 493-496 (1985).
14. K. Nassau, H. J. Levinstein, and G. Loiacono, "Ferroelectric lithium niobate. Growth, domain structure, dislocations and etching", *J. Phys. Chem. Solids* 27, pp. 983-988 (1966).
15. P.F. Bordui, R.G. Norwood, D.H. Jundt, M.M. Fejer, "Preparation and Characterization of Offcongruent Lithium Niobate Crystals", *J. Appl. Phys.* 71, pp. 875-879 (1992).
16. G.I. Malovichko, V.G. Grachev, L.P. Yurchenko, V.Y. Proshko, E.P. Kokanyan, V.T. Gabrielyan, "Improvement of LiNbO<sub>3</sub> Microstructure by Crystal Growth with Potassium", *Phys. Stat. Solidi (a)* 133, pp. K29-K32 (1992).
17. K. Polgár, A. Péter, L. Kovács, G. Corradi, Z. Szaller, "Growth of Stoichiometric LiNbO<sub>3</sub> Single Crystals by Top Seeded Solution Growth Method", *J. Cryst. Growth* 177, pp. 211-216 (1997).
18. K. Kitamura, Y.K. Yamamoto, N. Iyi, S. Kimura, T. Hayashi, "Stoichiometric LiNbO<sub>3</sub> Single Crystal Growth by Double Crucible Czochralski Method Using Automatic Powder Supply System", *J. Cryst. Growth* 116, pp. 327-332 (1992).
19. T. R. Volk and M. Woehlecke, "Lithium Niobate: Defects, Photorefraction and Ferroelectric Switching" Springer: Berlin, Germany, Vol. 115 (2008).

20. O.F Schirmer, M.Imlau, C Merschjann. B. Schoke, "Electron Small Polarons and Bipolarons in LiNbO<sub>3</sub>" . J. Phys. Condens. Matter 21, 123201, pp.1-29 (2009).
21. O.F.Schirmer, O. Thiemann, M. Wohlecke, "Defects in LiNbO<sub>3</sub>—I. Experimental Aspects", J. Phys. Chem. Solids, Vol. 52, pp. 185-200 (1991).
22. L. D. Landau, "Über die bewegung der elektronen im kristallgitter," Phys. Z. Sowjetunion 3, pp. 664 – 665, 1993.
23. M. Imlau, H. Badorreck and C. Merschjann, "Optical Nonlinearities of Small Polarons in Lithium Niobate", Appl. Phys. Reviews, pp. 040606/1- 040606/26 (2015).
24. S. I. Pekar, Sov. Phys. JETP 16, 335 (1946).
25. D. Emin, "Polarons", Cambridge University Press, 2013.
26. C. Merschjann, D. Berben, M. Imlau, and M. Wohlecke, "Evidence for Two-path Recombination of Photoinduced Small Polarons in Reduced LiNbO<sub>3</sub>", *Phys. Rev. Lett.* 96, pp. 186404/1-186404/4 (2006).
27. B. Faust, H. Muller, and O. F. Schirmer, "Free Small Polarons in LiNbO<sub>3</sub>", *Ferroelectrics* 153, pp. 297-302 (1994).
28. J. Koppitz, O. F. Schirmer, and A. I. Kuynetsov, "Thermal Dissociation of Bipolarons in Reduced Undoped LiNbO<sub>3</sub>", *Europhys. Lett.* 4 (9), pp.1055-1059 (1987).
29. O. F. Schirmer and D. Von der Linde, "Two-photon- and X-Ray-Induced Nb<sup>4+</sup> and O-small Polarons in LiNbO<sub>3</sub>", *Appl. Phys. Lett.* 33, pp. 35-38 (1978).
30. H. Fay, W. J. Alford, H. M. Dess, "Dependence of Second-harmonic Phase-matching Temperature in LiNbO<sub>3</sub> Crystals on Melt Composition", *Appl. Phys. Letters* 12, pp. 89-92, (1968).
31. P. Lerner, C. Legras, P. J. Dumas, "Stoichiométrie des Monocristaux de Métaniobate de Lithium", *J. Cryst. Growth* 3/4, pp. 231-235, (1968).

32. S. C. Abrahams, P. March “Defect Structure Dependence on Composition in Lithium Niobate” *Acta. Crystallogr. B* 42, pp. 61-68, (1986).
33. H. Donnenberg, S. M. Tomlinson, C. R. A. Catlow, O. F. Shirmer “Computer-Simulation Studies of Extrinsic Defects in LiNbO<sub>3</sub> Crystals” *Phys. Rev. B* 44, pp. 4877-4883, (1991).
34. R. D. Shanon, “Revised Effective Ionic Radii and Systematic Studies of Interatomic Distances in Halides and Chalcogenides” *Acta Cryst. A* 32, pp. 751-767(1976).
35. N. Iyi, K. Kitamura, F. Izumi, J.K. Yamamoto, T. Hayashi, H. Asano, S. Kimura, “Comparative Study of Defect Structures in Lithium Niobate with Different Compositions”, *J. Solid State Chem.* 101, pp. 340-352 (1992).
36. V. Grachev, G. Malovichko, O. Schirmer, “Structure of Point Defects in Lithium Niobate”, ISSN 0503-1265, *Ukr. J. Phys.* V. 49, N5, pp. 438-447 (2004).
37. T. R. Volk and M. Woehlecke. *Ferroelectrics Review* 1, 195 (1998).

# Chapter 1.

## Samples for research

## Chapter 1. Samples for research

### § 1.1. Growth of crystals

We remember that the LN crystals understudied in this work are iron doped ones with different crystal composition, zirconium and indium doped congruent composition crystals. These crystals were grown by modified Czochralski grown technique [1] with the use of “Donetsk type growth set-up in air atmosphere in a platinum crucible with dimensions of 50mm×3mm×50mm. As a heating module a rf (radio frequency) furnace was utilized order to decrease the vertical temperature gradient in the growth system and after-heater consisting of a cylindrical platinum tube with dimensions of 50mm × 1mm × 100mm was placed above the crucible. After the growth process the crystal was pulled into the after-heater where, at a given rate, the temperature was decreased till the room temperature. All crystals were pulled along the  $c$  axis. The pulling rate and the rotation speed were 1mm/hour and 20 rpm respectively. The scheme of the furnace of the Czochralski grown method is given in Figure 1.1.

Except for the series of congruent LN:Fe samples with different iron concentration described in Chapter 4, in order to obtain the single domain crystal directly during the grown process as well as to get a homogenous distribution of the impurity ions along the grown axis an external DC electric current with 12 A/m<sup>2</sup> density was applied to the crystal-melt system during the grown process These crystals were grown in the Institute for Physical Researches of the National Academy of Sciences Armenia.

Iron doped congruent composition crystals with different concentration of iron ions were grown in the University of Padua in the group of Prof. Marco Bazzan and kindly provided for the investigation. The samples were grown by Czochralski technique pulling up the seed with the speed about of 2 mm/h. Initial mixture consists of commercial congruent  $LiNbO_3$  (Sigma Aldrich 99.999) and  $Fe_2O_3$  powders with the varied Fe concentrations: 0.1 mol%, 0.05 mol%, 0.02 mol% (see the Table 1.2.1). In order to grow the crystal with the homogeneous and planar solid-liquid interphase, the seed has been rotated around its axis with the constant value of speed between 30 and 5 rotate per minute [2]. As-grown samples contain not uniformly polarized domain thus, the poling treatment after the growth process has been utilized to overcome this problem. An electric current equal to some tenths of mA has been applied to

the crystal boule along the  $c$  axis with the help of platinum wire connection heating the boules  $50^\circ\text{C}$  above Curie temperature ( $T_c = 1150^\circ\text{C} \div 1210^\circ\text{C}$  for the crystal composition varied from the congruent to stoichiometric). After the polling process taking around an hour the current was switched off and the crystal cooled down to the room temperature.

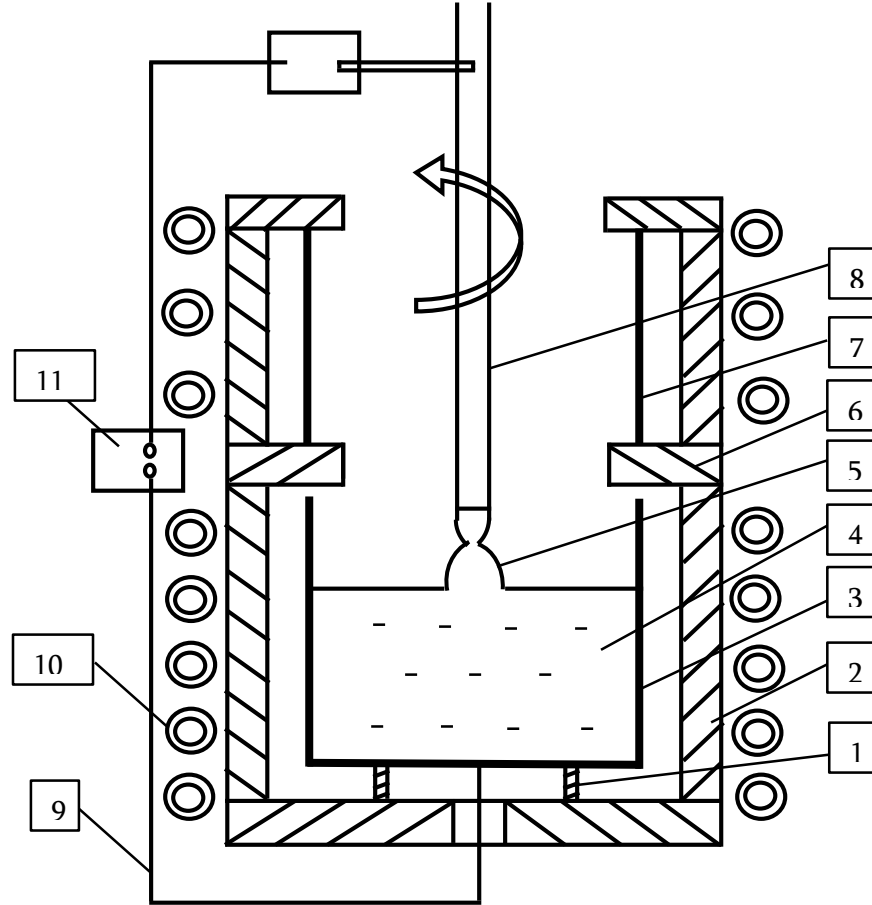


Figure 1.1: The scheme of the growth scheme for the Czochralski growth.

1-Ceramic plate, 2-Ceramic after heater, 3-Platinum crucible, 4-LN melt, 5-Grown crystal, 6-Ceramic diaphragm, 7-Platinum after heater, 8-Platinum rod as seed holder, 9-Platinum electrode, 10-Copper inductor, 11- Current source.

The grown LN samples can be separated in two main groups: correspondingly doped with transition metal ( $Fe^{2+}$  and  $Fe^{3+}$ ) and non-photorefractive ( $Zr^{4+}$  and  $In^{3+}$ ) Ions. The samples of the first group are LN:Fe boules grown from melt having the different Li contents equal to  $x_m = 48.45\text{mol}\%$ ,  $50.0\text{ mol}\%$ , and  $54.5\text{ mol}\%$  and doped with a fixed  $0.11\text{ mol}\%$  of iron concentration. They may be considered as samples with a fixed deep trap concentration whereas with a different amount of shallow trap centers (i.e. niobium antisites). High-purity powder compounds of  $Nb_2O_5$  from Johnson-Mattley, and  $Li_2CO_3$  from Merck (the same

compounds also for below discussed LN:Zr and LN:In samples), were used as the starting materials for sintering of the lithium niobate charges of various composition, through solid state reaction. The appropriate content of iron ions was added to the initial charges of LN in the form of  $Fe_2O_3$  oxide (Merck) and thoroughly mixed. During the growth process, the composition of the produced off-congruent crystals can be varied along the growth direction therefore the samples for investigations were cut at the same height in their respective grown boules. Besides, it should be noted that that the composition of the off-congruent samples will not be the same that of the melt and needs to be measured or estimated. The corresponding compositional characterization is discussed in Chapter 2. In the considered composition range and iron concentration in the melt, the distribution coefficient of the last is assumed to be equal to 0.9 [3] resulting to an iron concentration to be equal to 0.11mol% in crystal.

In the second group two series of congruent LN samples have been doped with zirconium and indium ions, respectively as photorefractive resistant ions. The  $ZrO_2$  compound with the 0.625 mol%, 0.75 mol%, 0.875 mol%, 1.00 mol%, 1.25 mol%, 1.50 mol%, 2.00 mol%, 2.50 mol% contents was added into the melt. As the distribution coefficient of  $ZrO_2$  is close to one thus, the concentration of Zr is accepted to be the same in the melt and the crystal.

In the second series of samples, the concentration of indium oxide  $In_2O_3$  in the melt was equal to 0.12at %, 0.25at%, 0.5at %, 1.7at % which corresponds to the content of the last in the crystal respectively to 0.24 at %, 0.5 at %, 0.9 at %, 2.1 at % [4].

### ***§ 1.2. Preparation of samples***

The handling of the grown crystals includes the orientation and cut of the boule along the selected crystallographic  $c$  axis. The grown boules after cutting the shoulder and the bottom were glued to a special goniometric sample holder and oriented taking into account the boule morphology and the seed axis. The grown crystals were obtained by cutting the shoulder and the bottom of the boule. In order to obtain the miscut angle between the cut surface and the chosen crystallographic axis a small piece of the boule was cut and analyzed by X –Ray diffractometer. The crystal axis orientation was performed with the aid of Laue method. This required results was used to control the crystal orientation on the cutting machine.

The final preparation stage is the surface lapping and polishing at optical grade. Due to the lapping some part of material was removed to obtain a smooth unpolished surface. In order to produce a scratch-free specular surface the polishing was performed with a diamond particles resulting to a flat surface with roughness in the nanometer range. Finally the optical polishing provides the rectangular samples on all the surfaces illustrating an optical facets perpendicular to the crystallographic axis. The dimensions of prepared samples are given in Table 1.2.1.

Table 1.2.1: Characterizations of the utilized samples.

Number of samples	Impurity concentration, mol %	$C_{Li}$ in the melt, mol %	$C_{Li}$ in the crystal, mol %	Dimensions ( $x \times y \times z$ ), $mm^3$
LN:Fe1-1	0.11	48.45	48.45	9.8×2.1×4.5
LN:Fe1-2	0.11	50	48.58	9.8×3.6×4.5
LN:Fe1-3	0.11	54.5	49.59	6.0×2.8×4.0
LN:Fe2-1	0.02	48.45	48.45	9.8×2.1×4.5
LN:Fe2-2	0.05	48.45	48.45	9.8×2.1×4.5
LN:Fe2-3	0.1	48.45	48.45	9.8×2.1×4.5
LN:Zr1	0.625	48.45	48.45	10×4×6.5
LN:Zr2	0.75	48.45	48.45	10×4×6.5
LN:Zr3	0.875	48.45	48.45	10×4×6.5
LN:Zr4	1	48.45	48.45	10×4×6.5
LN:Zr5	1.25	48.45	48.45	10×4×6.5
LN:Zr6	1.5	48.45	48.45	10×4×6.5
LN:Zr7	2	48.45	48.45	10×4×6.5
LN:Zr8	2.5	48.45	48.45	10×4×6.5
LN:In1	0.12	48.45	48.45	10×4.2×6.5
LN:In2	0.25	48.45	48.45	10×4.2×6.5
LN:In3	0.5	48.45	48.45	10×4.2×6.5
LN:In4	1.7	48.45	48.45	10×4.2×6.5

### ***§ 1.3. Conclusion-Chapter 1***

The understudy LN samples have been grown by using Czochralski grown technique pulling along the crystallographic  $c$  axis. In general the growth LN samples can be separated onto two groups: doped with transition metal ( $Fe^{2+}$  and  $Fe^{3+}$ ) and non photorefractive ( $Zr^{4+}$  and  $In^{3+}$ ) ions. The samples of the first group can be sorted in two series in their turn: LN samples with different  $Li_2O$  content (48.45 mol%, 50.00 mol%, 54.50 mol% in the melt) doped with the fixed Fe concentration equal to 0.11 mol% in the melt and the congruent LN samples doped with the various impurity concentration (0.02 mol%, 0.05 mol%, 0.1 mol%) numbered as LN:Fe1-1 ÷ LN:Fe1-3 and LN:Fe2-1 ÷ LN:Fe2-3 respectively. In the second group two series of congruent LN samples have been doped with the different contents of Zirconium oxide  $ZrO_2$  (0.625 mol%, 0.75 mol%, 0.875 mol%, 1.00 mol%, 1.25 mol%, 1.50 mol%, 2.00 mol%, 2.50 mol% in the melt) and Indium oxide  $In_2O_3$  (0.12at %, 0.25at%, 0.5at %, 1.7at % added to the melt) numbered as correspondingly LN:Zr1 ÷ LN:Zr8 and LN:In1 ÷ LN:In4. After the growth, the samples have been cut along the crystallographic axis, oriented, lapped and optically polished in order to obtain the samples with the smooth polished surfaces owing an optical facets perpendicular to the crystallographic axis.

### *References-Chapter 1*

1. R. N. Balasanyan, V. T. Gabrielyan, E. P. Kokanyan, I. Foldvarj, “The Composition and Homogeneity of LiNbO<sub>3</sub> Crystals Interconnected with Growth Conditions. I. The Influence of Electrical Field”, *Sov. Kristallografiya*, Vol.35, No6, pp. 1540-1544 (1990).
2. L. Vittadello, “Microscopic Insights in Photo-Induced Charge Transport in Fe : LiNbO<sub>3</sub>”, PhD thesis, (2017).
3. A. Raüber, “Chemistry and Physics of Lithium Niobate”. In: Kaldis E, editor. *Current topics in Materials Science 1*. Amsterdam: North-Holland, pp. 481–601 (1978).
4. T. R. Volk, N. M. Rubinina, “A New Optical Damage Resistant Impurity in Lithium Niobate Crystals: Indium”, *Ferroelectrics Lett.* 14:1-2, pp. 37-43 (1992).



# Chapter 2.

## Structure and composition of doped LN crystals

## Chapter 2. Structure and composition of doped LN crystals

### § 2.1 X-ray diffraction. Lattice parameters of crystals

#### Literature Review

The results on structural investigation of undetermined composition lithium niobate (LN) with the help of X-Ray diffraction (XRD) has been reported for the first time in [1, 2]. Belonging to the rhombohedral lattice system with the space group  $R3c$  was confirmed investigating the positional atomic coordinates of single LN crystals at 24 ° C temperature [1]. The stability of atomic arrangement in a temperature range from 24 ° C to 1200 ° C and the change of ferroelectric phase  $R3c$  to paraelectric phase  $R\bar{3}c$  at Curie temperature ( $T_C \approx 1210^\circ\text{C}$ ) have been demonstrated realizing polycrystal X-ray diffraction between 24 ° C and Curie temperature [2].

Later applied explorations of the lattice structure by X-ray and neutron diffraction of single crystals or powder emphasized the decrease of the lattice parameters  $a$  and  $c$  with the increase of stoichiometry [3-7]. Abrahams and Marsh analyzing the single crystals with the well investigated congruent and stoichiometric compositions by single XRD proposed the Nb-site vacancy model [3]. In contrast to this model Iyi et al. [4] applying X-Ray single crystal and powder neutron diffraction methods for single crystals arranging from highly nonstoichiometric ( $C_{Li} = 47\text{mol } \%$ ) to near stoichiometric ( $C_{Li} = 49.8\text{ mol } \%$ ) supported more recognized Li-site vacancy model suggested by Lerner [8]. In 2006, Abdi et al. [9] proposed a model to describe the structure of intrinsic defects in nominally pure  $LiNbO_3$  based upon the coexistence of both Nb and Li vacancies in non-congruent crystals, and predicts an intermediate crystal composition for which the amount of one kind of vacancies (Li or Nb) vanishes. They show that the Li vacancies are dominant in the defect structure of non-congruent crystals. Recently, the results of performed measurements for congruent LN samples by using powder XRD [5], X-Ray and powder neutron diffractions [6] can be explained completely by Li-site vacancy model.

Recently it was also shown the dependence of lattice parameters on the introduction of dopant ions [7, 10]. Malovichko et al. carried out investigation of lattice parameters with the help of powder XRD for pure LN with different Li content (43, 47.4; 48.46; 54.5% in the melt) and the ones grown from congruent melt (48.46%) doped with varied concentrations of  $K_2O$ , for congruent melt containing potassium and co-doped with Fe as well as for congruent melt

doped by different concentrations of Mg [7]. Lattice parameters illustrate the decrease with the increase of content of potassium whereas they increase with the increase of Mg concentration. This behavior was confirmed by Abdi et al. in Ref [11]. The introduction of iron ions in the samples grown from congruent melt containing potassium increases the lattice constants comparing to the results obtained for samples with the same content of  $K_2O$  (11 mol% in the melt) but without co-doping with Fe .

### **Theory**

X-Rays detected by Wilhelm Rontgen in 1895 [12] are electromagnetic radiations with ( $\lambda = 0.01 - 100\text{\AA} = 10^{-10} - 10^{-6}cm$ ) relatively short wavelength lying between ultraviolet light and Gamma rays in the electromagnetic spectrum [13]. Electric field of X-Rays is expressed as [14]:

$$\mathbf{E}(\mathbf{r}, t) = \hat{\mathbf{e}}\mathbf{E}_0e^{i(\mathbf{k}\cdot\mathbf{r}-\omega t)} \quad (2.1.1),$$

where  $\hat{\mathbf{e}}$ -is the unit vector describing the polarization of the electric field,  $\mathbf{k}$ -is wave vector along propagation direction,  $\mathbf{E}_0e^{i(\mathbf{k}\cdot\mathbf{r}-\omega t)}$ -the amplitude of electric field, when wave propagates along  $c$  axis. As X-rays are transverse electromagnetic waves, so:

$$\hat{\mathbf{e}} \cdot \mathbf{k} = 0 \text{ and } \mathbf{k} \cdot \mathbf{E} = \mathbf{k} \cdot \mathbf{H} = 0 \quad (2.1.2).$$

Here  $\mathbf{H}$ -is the magnetic field.

The interaction of X-rays and the matter containing many molecules or atoms, generates the following options:

- Reflection
- Scattering
- Absorption
- Refraction
- Transmittion

Basically there are two types of scattering:

- Coherent scattering- Thomson diffusion (elastic)  $h\nu = E_{binding}$ .
- Incoherent scattering- Compton diffusion (inelastic)  $h\nu > E_{binding}$ .

Classically, the scattered phonons preserve the wavelength of the incident wave.

Thomson scattering length or classical radius of electron is given as:

$$r_0 = \left( \frac{e^2}{4\pi\epsilon_0 mc^2} \right) = 2.85 \cdot 10^{-5} \text{Å} \quad (2.1.3).$$

Thomson length is the distance from the point charge  $e$ , where the Coulomb energy is  $\frac{e^2}{4\pi\epsilon_0 r}$ ,  $mc^2$ -is the dimensionally energy.

In quantum-mechanics the scattered photon obtains a lower energy comparing to the incident beam. The energy decreases due to the protection of momentum and energy during the collision with the atom or molecule. The scattering amplitude is expressed as:

$$F^{crystal}(\mathbf{Q}) = \sum_j \overbrace{f_j(\mathbf{Q})e^{i\mathbf{Q}\mathbf{r}_j}}^{\text{Unit cell structure factor}} \sum_n \overbrace{e^{i\mathbf{Q}\mathbf{R}_n}}^{\text{Lattice sum}} \quad (2.1.4),$$

$$\mathbf{R}_n = n_1 \mathbf{a}_1 + n_2 \mathbf{a}_2 + n_3 \mathbf{a}_3 \quad (2.1.5).$$

$\mathbf{R}_n$ -are lattice vectors defining the lattice,  $\mathbf{r}_j$ -is the position of atoms attitude toward any particular lattice site,  $\mathbf{a}_1, \mathbf{a}_2, \mathbf{a}_3$  are basis vectors of the lattice,  $n_1, n_2, n_3$  are integers. The position of atom is given by  $\mathbf{R}_n + \mathbf{r}_j$ . The Compton scattering length is defined by:

$$\lambda_C = \frac{h}{mc} = 3.86 \cdot 10^{-3} \text{Å} \quad (2.1.6).$$

The relationship is constant between Thomson scattering length and Compton scattering length:

$$\alpha = \frac{r_0}{\lambda_C} \approx \frac{1}{137} \quad (2.1.7).$$

During the coherent scattering, the intensity of the scattering results of the sum of different processes: scattering by electron and by an atom [15, 16]. The electrons in each atom interact with the oscillating electric field of the X-ray with the same phase scattering coherent light described by Thompson equation:

$$I = \frac{I_0}{r^2} \left[ \frac{e^2}{m_e c^2} \right]^2 \frac{1 + \cos^2(2\theta)}{2} \quad (2.1.8),$$

where  $I_0$  is the intensity of the incident beam,  $r$  is the interval between the detector and the scattering electron,  $e$ -electron charge,  $m_e$ -mass of electron,  $c$  is the light speed. Scattering by an atom is the sum of the scattering of the electron “cloud” and the strength of the scattered

beam is proportional to the number of electrons around the nucleus. Thus, each atom can be considered as a coherent point scatterer. X-rays are partially scattered by atoms striking the surface of a crystal as they consist of planes of atoms spacing a distance apart and the remained part of the X-ray which is not scattered simply passes through the next layer of atoms, where again part of the X-ray is scattered. By this way the other non-scattered part passes through to the next layer. As X-rays have a wavelengths on the order similar to the interatomic distances in crystalline solids thus the elastic scattering results to the coherent constructive interference (when two beams so-called “in phase” keep a phase difference of  $n\lambda$  is equivalent to  $2d \sin\theta$ , where  $(n \in \mathbb{Z})$ ) at specific angles diffused from each atom of the periodic structure of the matter and creating consequently X-ray diffraction. The diffraction angle of x-rays depends on the spacing between the adjacent layers of atoms or ions. X-rays “in phase” collide the adjacent layers and result to the production of the constructive interference of waves on a detector plate describing by Bragg’s law which is the general relationship between the wavelength  $\lambda$  of the incident X-rays, the incident angle of the beam  $\theta$  and the spacing  $d$  between the crystal lattice planes of atoms. (Figure 2.1.1)[17].

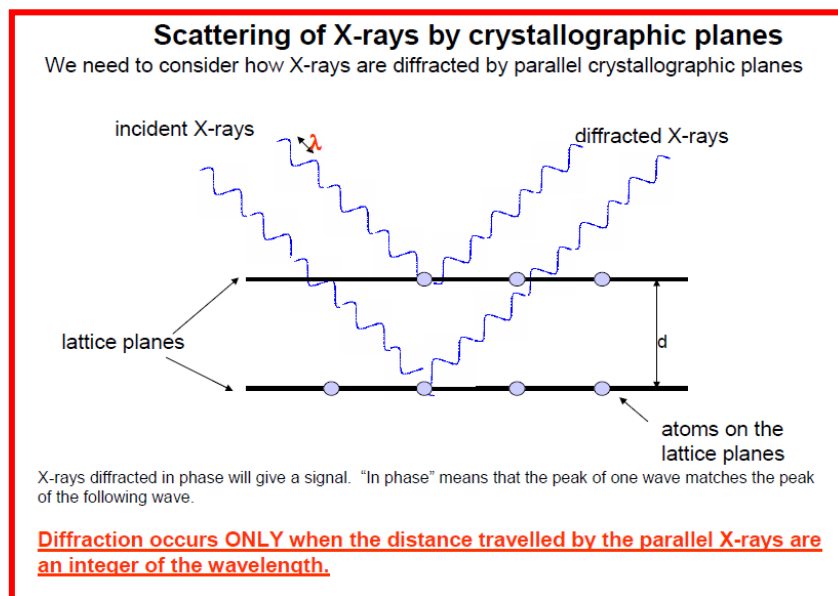


Figure 2.1.1. X-ray diffraction from lattice planes of crystals.

The reflected beams combining form a diffraction beam with the equal phase difference to a whole number of wavelength is defined:

$$n\lambda = 2d \sin \theta. \quad (2.1.9)$$

The expression 2.1.9 has been observed by Bragg in 1912 illustrating that the diffraction pattern is due to the reflection of the incident beam from lattice planes. Bragg's law gives a possibility to determine the spacing between the atomic planes and to investigate the crystalline structure of material as well. From atoms, electrons and planes scattering X-rays caused an overall diffraction pattern contain the information about the atomic arrangement within the crystal.

X-rays are generated by bombarding a metal target (in our case Cu) with a beam of electrons emitted from a hot filament (tungsten) [14]. The incident beam will ionize electrons from the  $K$ -shell ( $1s$ ) of the target atom and X-rays are emitted as the resultant vacancies are filled by electrons dropping down from the  $L$  ( $2P$ ) or  $M$  ( $3P$ ) levels (Figure 2.1.2). This gives rise to  $K_\alpha$  and  $K_\beta$  lines. Electrons are slowed down and lose energy forming the X-rays [13, 15]. The probability of filling an electron from  $L$  to  $K$  is more than  $M$  to  $K$  resulting to the higher intensity of  $K_\alpha$  than  $K_\beta$ . As X-ray powder diffraction experiments need monochromatic radiation thus the filters usually to keep only  $K_\alpha$  lines. For Cu X-ray source with  $K_\alpha$  line, the wavelength is equal to  $1,5418 \text{ \AA}$  [18]. The frequency is associated with the difference between the atomic energy levels of the target atoms.

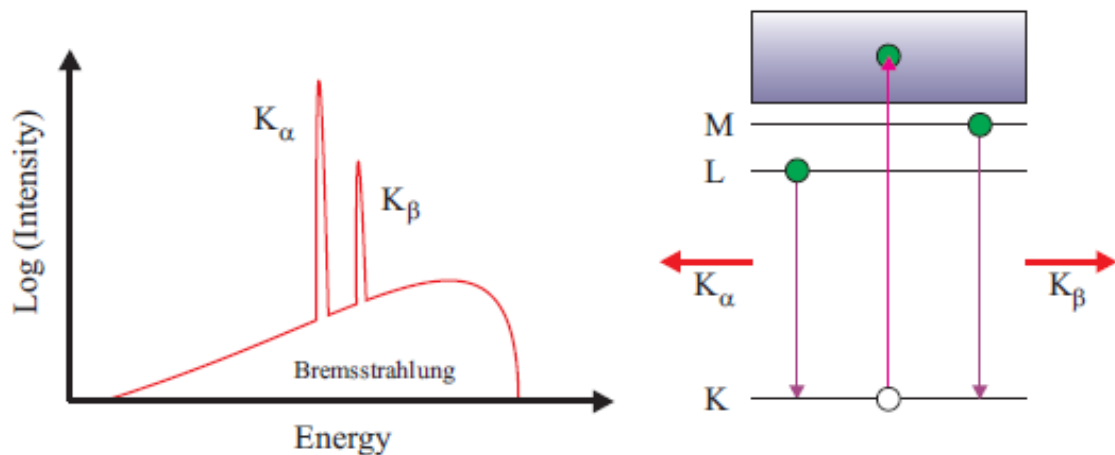


Figure 2.1.2: X-ray emission spectrum of X-ray source used and the origin of  $K_\alpha$  and  $K_\beta$  lines resulted  $K_\alpha$  line from transitions between  $L$  and  $K$  shell, when  $K_\beta$  creates due to the transition from an  $M$  to  $K$  shell.

### ***§2.1.1. Experimental Technique***

Powder X-ray diffraction (PXRD) [17] is one of the most potential characterization tools to identify the phases in powder specimens, phase composition, the crystal structure, unit cell parameters and the crystalline space group as well. PXRD illustrates the numerous advantages like non-destructive nature, high sensitivity, reliability, depth profiling (glancing incident angle), easy sample preparation, operational procedure (effective resolution, easy data interpretation) that could be used for both qualitative and quantitative analysis, in wide range of applications. In order to perform the powder X-ray diffraction, the sample must be crystalline and the spacing between the atom layers must be close to the radiation wavelength. Systematic study including the influences of intrinsic defects and the introduction of Fe iron was not performed, thus the main intention of our investigation by means of X-ray powder diffraction is to reveal the dependence of lattice parameters on this two factors.

The powder samples from above mentioned LN:Fe1-1÷LN:Fe1-3 samples have been used for X-ray diffraction analysis (See Chapter 1). The sample preparation is one of the important requirements in the analysis of the powder specimen. As the X-ray absorption may reduce the intensity of peaks with angle thus, in Bragg-Brentano geometry a smooth flat surface of "infinitely" thick sample, having the randomly oriented grains/crystallites with the lesser size than 10 microns, is the basic contribution for the diffraction. Due to the variation of the experimental angle the X-rays interacting with the grains detect all possible interatomic planes. By this way the possible diffracted peaks from powder are recorded by the detector to estimate the relative intensities. In order to achieve a good signal-to noise ratio (to avoid a fluctuation in intensity) and to minimize the preferred orientation the powder samples were extremely fine grained. The specimen preparation involves a number of steps such as grinding, dilution, drying, mounting as a sample should contain a large number of tiny crystals (or grains) randomly oriented in three dimensional space. The amorphous material (glass) has been used as the sample holder, in order not to have a periodic array with long-range order, so not to produce any significant peak in diffraction pattern. The pictures of powder sample are given in Figures 2.1.1.1 and 2.1.1.2 [19].



Figure 2.1.1.1: The powder of Fe:LN crystal.

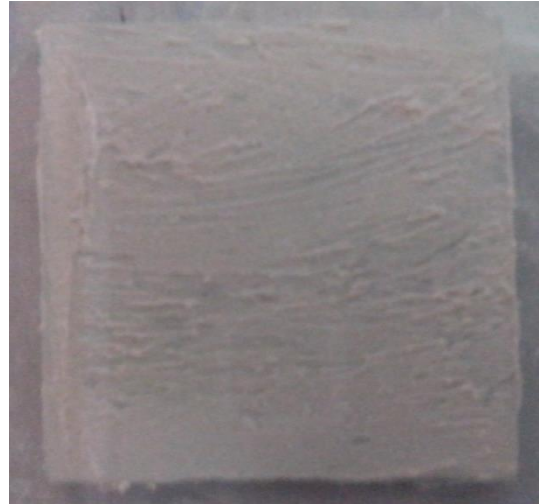


Figure 2.1.1.2: Prepared Fe:LN powder specimen onto the piece of non-transparent glass.

The basic features of XRD experiments are: production of X-rays, diffraction of X-rays, detection of diffracted beams and finally interpretation of the results of diffraction. The lattice parameters measurements have been performed with the help of Philips MRD (Material Research Diffractometer) diffractometer by utilizing  $\text{Cu } K_{\alpha}$  radiation with wavelength  $\lambda=0.1540598$  nm and operating in the reflection configuration with Bragg–Brentano geometry (shown in Figure 2.1.1.3).

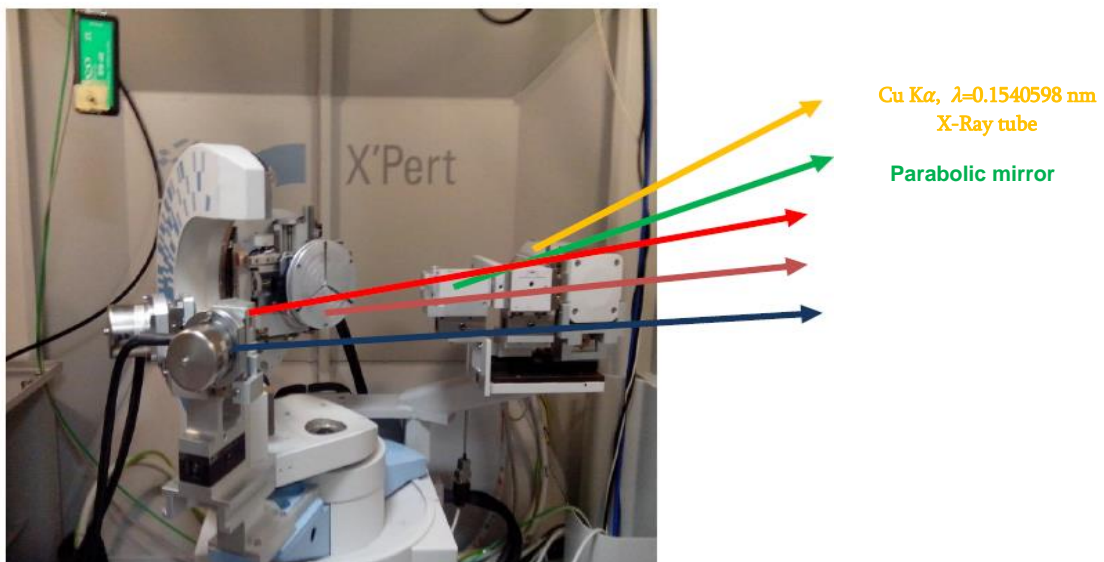


Figure 2.1.1.3: The structure of the Philips MRD.

Diffractionmeter contains the following parts: X-ray tube with Cu  $K_{\alpha}$  radiation with wavelength  $\lambda=0.1540598$  nm, incident-beam optics (DS- divergence slit, SS-soller slit, RS-receiving slit, "parallel-beam optics"), the sample holder (located between the X-ray source and the detector), and detector operating in the base of ionization of the atoms of argon gas irradiated by an X-ray beam (to count the number of X-rays scattered by the sample).

X-rays are produced in the vacuum tube where 40 kV voltage is applied between the filament cathode and anode target metal [13]. The used metal is copper, which can be kept cool easily, due to its high thermal conductivity. X-rays are generally filtered to a single wavelength (made monochromatic) and collimated to a single direction before collision to the crystal. The filtering simplifies not only the data analysis, but also removes undesirable radiation which degrades the crystal without contributing useful information. Most of the kinetic energy (about 98%) is converted into heat, so the target metal must be cooled externally. The operating value of  $U = 40kV$  voltage and  $I = 40mA$  current of X-ray tube is typically selected to optimize the emission of characteristic radiation, as it is a source of monochromatic radiation. When the electrons strike the target copper metal, X-rays are given off producing strong  $K_{\alpha}$  line.

In Bragg-Brentano ( $\theta - 2\theta$ ) geometry the X-ray source is fixed and the sample rotates around the own goniometric axis at a speed  $\omega$ . Interactions between the incident X-ray beam and the sample produce intense reflected X-rays by constructive interference when conditions satisfy Bragg's Law. The gas-filled detector scans at a speed  $2\omega$  around the sample along a circle in order to collect all X-ray beams scattered (diffracted) by lattice planes at  $2\theta$  angles and records the intensities of beam peaks diffracted at  $\theta$  angle [16, 17]. The schematic drawing of the principle of the Bragg-Brentano geometrical arrangement of X-ray source, specimen and detector is given in Figure 2.1.1.4.

The collimation of the incident and diffracted beams are realized with the help of optics for incident and diffracted beams [17]. As X-rays produced in tube are divergent, containing the multiple characteristic wavelengths, thus neither of these conditions suit an ability to use X rays for analysis. According to the divergence the sample does not diffract a single wavelength of radiation, but rather several wavelengths of radiation with the illumination by photons with a range of incident angles.

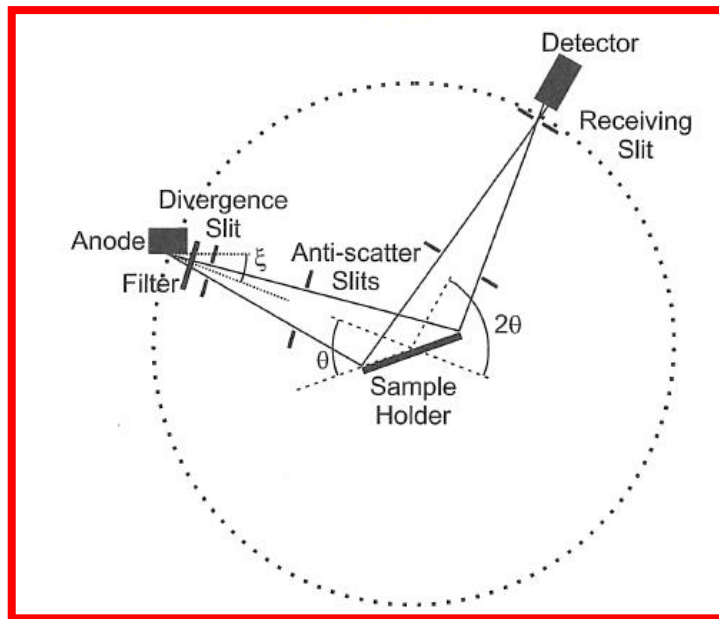


Figure 2.1.1.4: Scheme of the principle of “Bragg–Brentano” geometry.

Consequently, a single set of crystallographic planes will produce the several diffraction peaks instead of one diffraction peak. Thus the functions of applied optics are: to limit the divergence of the X-ray beam, to refocus X rays into parallel paths, to remove the unwanted wavelengths. The divergence slits is applied to control the size of the incident angle. Soller slit is a series of closely spaced parallel plates which are parallel to the diffractometer circle. SS is designed to limit the “axial divergence” of the beam. The receiving slit is replaced on the diffractometer circle.

To refocus X-rays into parallel paths are used: "parallel-beam optics", parabolic mirrors and lenses. As well as monochromators,  $K_{\beta}$  filters are used to remove unwanted wavelength of X-rays.

Monochromators mounting between the tube and sample (incident-beam) or between the sample and detector (diffracted-beam) delete the unwanted wavelengths of radiation from the incident or diffracted X-ray beam eliminating 99% of  $K_{\beta}$ . Diffraction from a monochromator crystal can be used to select one wavelength of radiation and provide energy discrimination. A diffracted-beam monochromator will provide the best signal-to-noise ratio, but data collection will take a longer time. Parallel plate collimator like the Soller slits blocks the divergent X-rays, but do not restrict the beam size like a divergent slit.

A diffraction pattern plotting the intensities and the positions of the diffracted peaks of radiation against the angular  $2\theta$  position of the detector, produces a two dimensional pattern called diffractogram which typically contains many distinct peaks, each corresponding to a different interplanar spacing. In a diffraction pattern, the peak positions depending upon the wavelength and determine interatomic distances thus, the position of a diffraction peak is determined by the size and shape of unit cell of the crystalline phase. The intensity illustrating the relative strength of the diffraction is proportional to the number of X-ray photons of a particular energy that have been counted by the detector for each angle  $2\theta$  determining an atom types and position. Peak size broadening gives information about the instrumental factors, the presence of defects, differences in strain, size of the crystallites.

### ***§ 2.1.2. Results and discussion.***

The diffractograms of LN samples LN:Fe1-1, LN:Fe1-2, LN:Fe1-3, obtained by detector resulting of X-ray diffraction are shown in Figures. 2.1.2.1a-2.1.2.1c [19].

X-ray diffraction data analysis requires the separation of the sample signal from the background and noise. Thus, to improve the signal/noise ratio the measurements have been done for long time increasing the counting time. In order to analyze the X-ray spectrum to obtain lattice parameters a and c the peak positions were observed comparing the experimental diffractograms with the calculated spectrum from the ICSD "Inorganic Crystal Structure Database" with the help of Maud (Materials Analysis Using Diffraction) computer program produced by Luca Lutterotti written in Java resulting to the automatic determination of lattice parameters together with the instrumental parameters [20]. The calculated diffraction pattern of pure LN crystal with detailed crystal structure data serves as a reference in database. The automatic procedure Maud needs to input the spectrum obtained by the detector and to select the calculated model from the database as a reference. Then both experimental and reference spectra have been compared resulting to the automatic determination of lattice parameters together with the instrumental parameters. In the diffractograms all expected reflections should be exist, otherwise it is not a valid match.

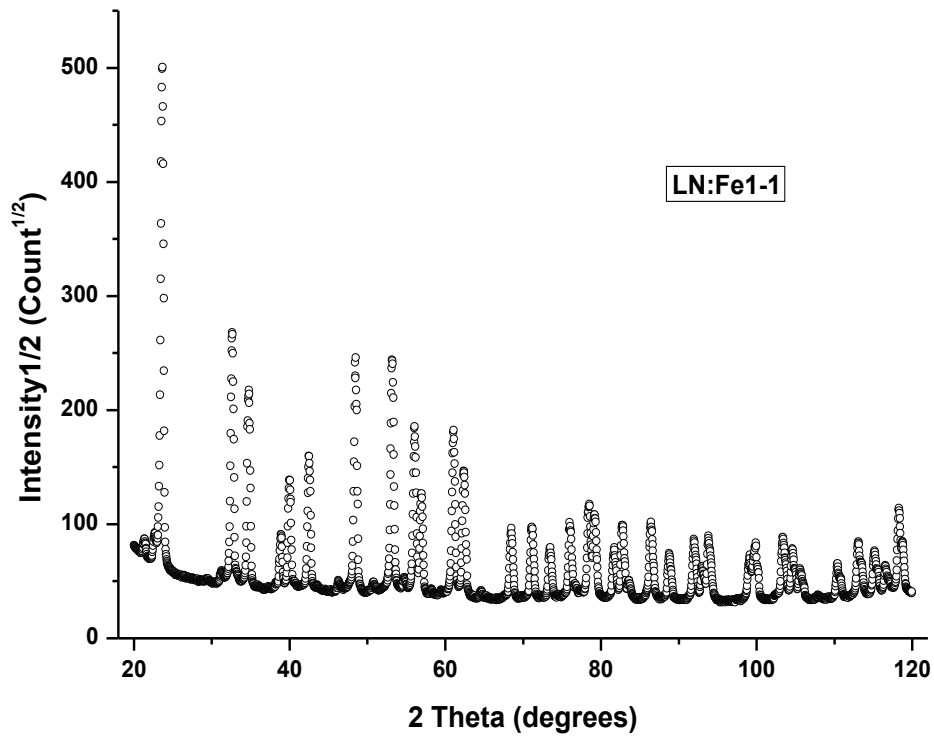


Figure. 2.1.2.1 a: XRD spectrum for sample LN:Fe1-1.

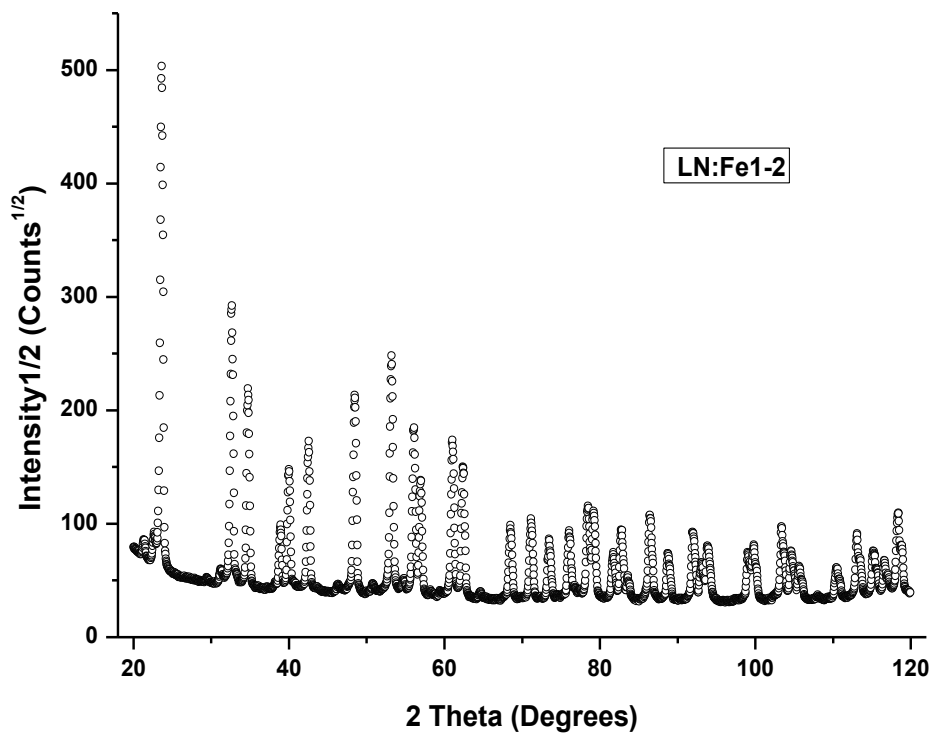


Figure. 2.1.2.1 b: XRD spectrum for sample LN:Fe1-2.

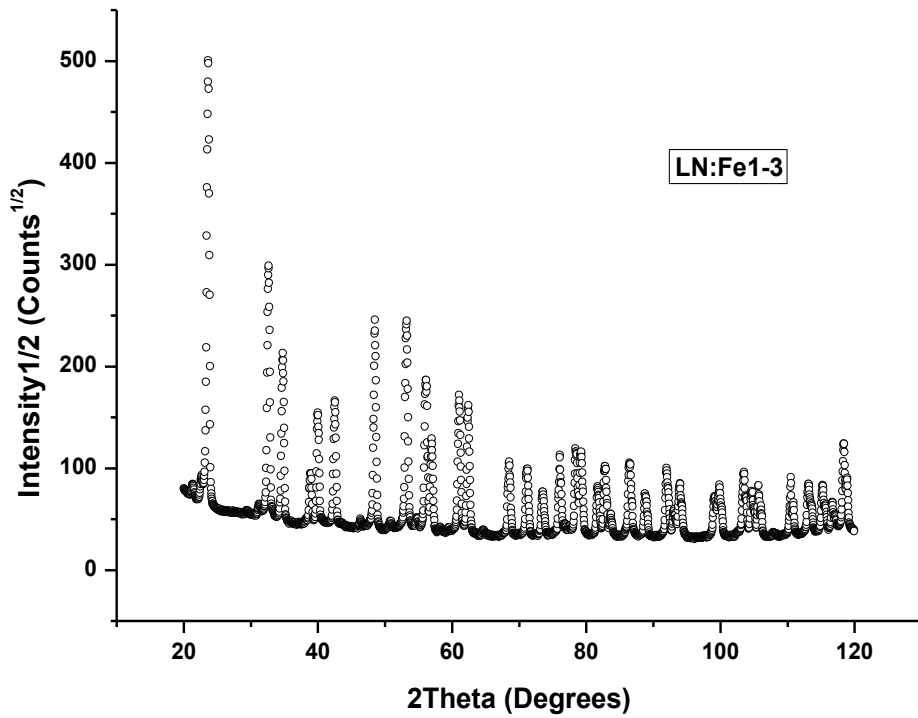


Figure. 2.1.2.1 c: XRD spectrum for sample LN:Fe1-3.

The results of the comparison of experimental diffractograms of samples LN:Fe1-1, LN:Fe1-2, LN:Fe1-3 with the computed spectrum for a LN crystal from the ICSD "Inorganic Crystal Structure Database" indexed in COD-2101175 are given in Figures 2.1.2.2a-2.1.2.2c. [3, 4, 7, 8, 19].

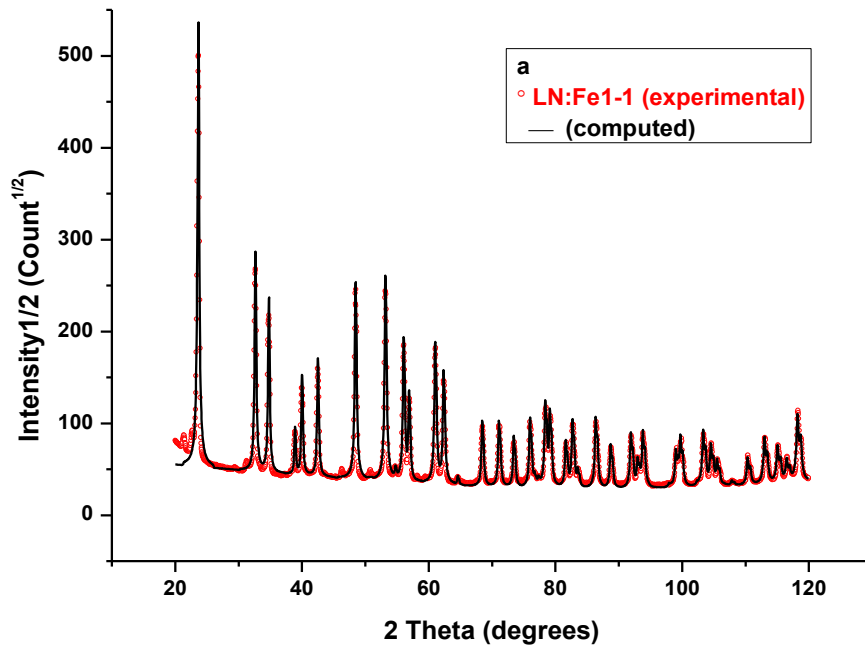


Figure 2.1.2.2 a: The results of the comparison of the experimentally obtained XRD spectrum for sample LN:Fe1-1 with the reference for pure LN crystal from the ICSD.

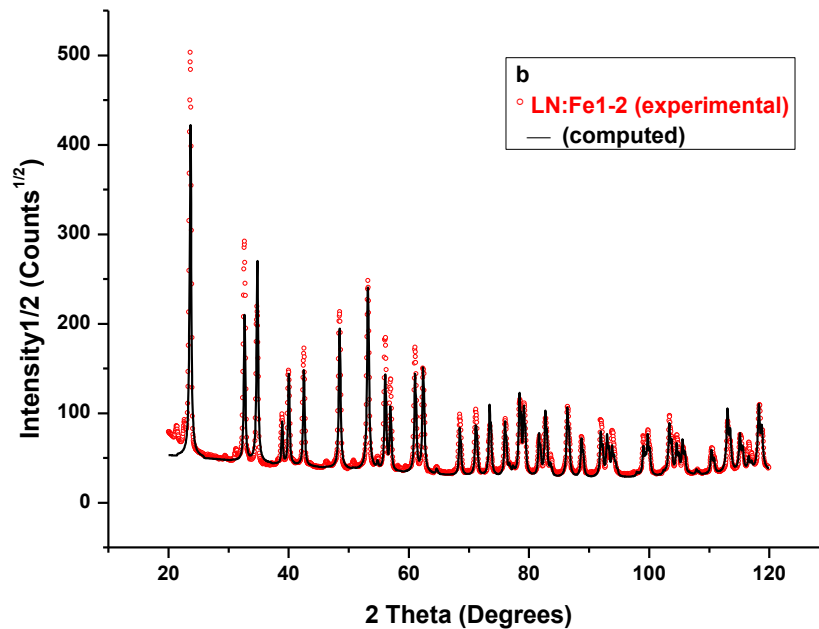


Figure 2.1.2.2 b: The results of the comparison of the experimentally obtained XRD spectrum for sample LN:Fe1-2 with the reference for pure LN crystal from the ICSD.

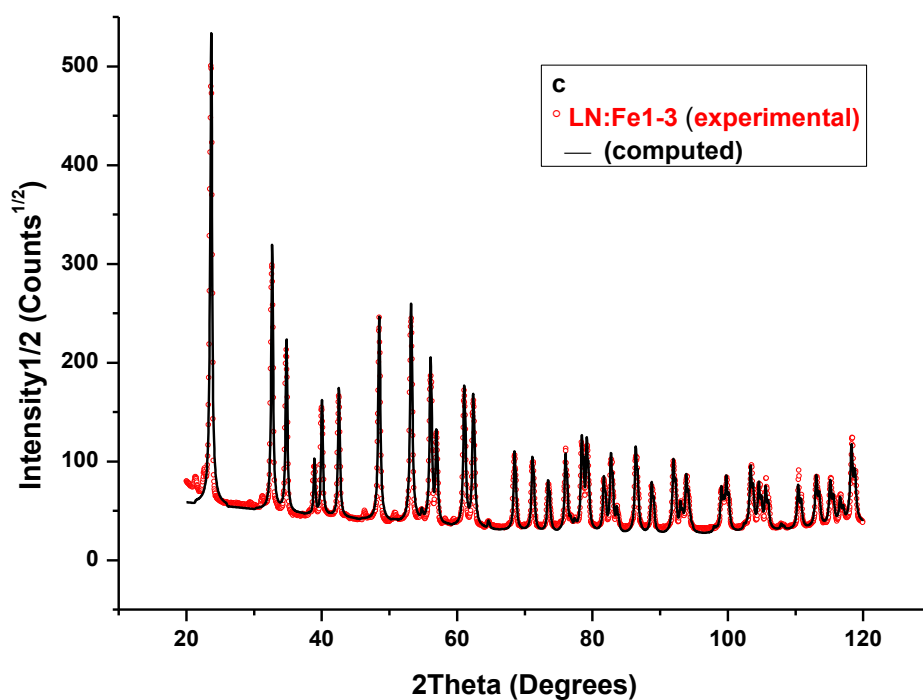


Figure 2.1.2.2 c: The results of the comparison of the experimentally obtained XRD spectrum for sample LN:Fe1-3 with the reference for pure LN crystal from the ICSD.

The obtained values of lattice parameters  $a$  and  $c$  for all samples under study are shown in Table 2.1.2.1 and in Figure 2.1.2.3 (dependence of lattice parameters on  $LiO_2$  content in the melt).

Table 2.1.2.1: Lattice parameters  $a$  and  $c$ [19].

Sample	$C_{Li}$ in the melt mol %	Lattice parameters	
		$a, \text{\AA}$	$c, \text{\AA}$
LN:Fe1-1	48.45	$5,1506 \pm 2 \times 10^{-4}$	$13,8673 \pm 7 \times 10^{-4}$
LN:Fe1-2	50.00	$5,1497 \pm 2 \times 10^{-4}$	$13,8620 \pm 7 \times 10^{-4}$
LN:Fe1-3	54.50	$5,1482 \pm 2 \times 10^{-4}$	$13,8599 \pm 8 \times 10^{-4}$

In Figure 2.1.2.4 are shown the results of the comparison of the obtained lattice constants in the understudy LN:Fe1 samples (the  $LiO_2$  content in the mentioned crystals has been obtained by Raman backscattering spectroscopy) with the ones known from the literature [19].

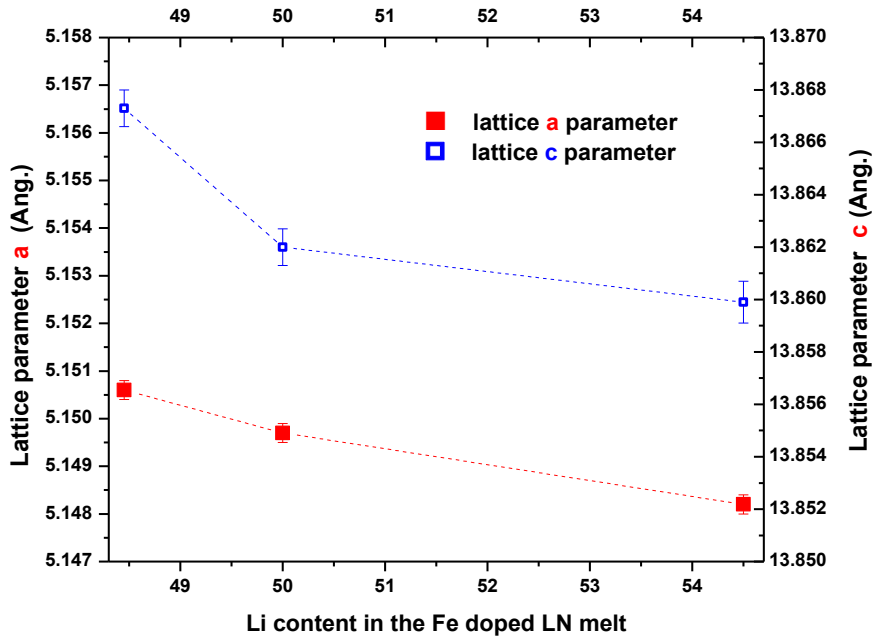


Figure 2.1.2.3: Lattice  $a$  and  $c$  parameters obtained for LN:Fe1-1, LN:Fe1-2, LN:Fe1-3 samples.

The variation of lattice constants has a similar behavior compared to results obtained for nominally pure LN crystals [3, 4, 7, 8]. This change demonstrates the dependence on the difference of the intrinsic defects concentration as it decreases with the increase of lithium content. Both lattice constants decrease with the increase of crystal stoichiometry underlining the smaller concentration of intrinsic (non stoichiometric) defects in the crystals with the compositions varying from congruent to near stoichiometry. In addition a slight decrease of lattice parameters is noticed in Fe:LN crystals compared to the pure LN crystals with the same composition. One can assume that the main part of Fe ions occupies Li sites [21, 22] which were captured by  $Nb^{5+}$  cations. In any case this change is negligible with the comparison to the change coming from the change of intrinsic defects in the crystal due to the small amount of iron ions. Thus, the decrease of both lattice parameters  $a$  and  $c$  is caused by the decrease of intrinsic defects due to the change of initial composition of the melt.



## § 2.2 Raman spectroscopy.

### *Literature review*

The light inelastic scattering phenomenon first has been detected by Smekal [23]. This phenomenon is popular as Raman spectroscopy since it was experimentally investigated by the Indian physicist Sir Chandrasekhara Venkata Raman and Kariamanikkam Srinivasa Krishnan [24].

First time Raman scattering from LN crystals was explored by discussion only transverse three  $A_1(TO)$ , seven  $E(TO)$  and longitudinal one  $E(LO)$  phonons [25]. Later electro-optic coefficients were measured by analyzing the contributions of four  $A_1(TO)$  and nine  $E(TO)$  modes [26]. Recently, the frequencies were calculated for four  $A_1(TO)$ , five  $A_2(TO)$  and nine  $E(TO)$  which were estimated experimentally [27].

The photorefractive effect influence on the Raman spectrum of the LN crystals especially doped with photorefractive-enhancing impurities via the generated space charge field. Raman experiments were performed with an excitation laser line of a  $Kr^+$  laser beam at  $\lambda=647.1$  nm. The decrease of the intensity of  $A_1(TO)$  and  $E(TO)$  Raman modes correspondingly at  $632\text{ cm}^{-1}$  and  $578\text{ cm}^{-1}$  frequency ranges in  $Y(ZZ)X$  and  $Y(XZ)X$  configurations were recorded due to the defocusing of the laser line inside the LN crystals doped by iron ions [28]. The scattering laser intensity is higher in the center and the probability of the capturing of photon excited electrons by  $Fe^{3+}$  ions is smaller, thus those electrons staying in the conduction band going away from the focus of laser beam. This phenomenon built up the strong space charge field generating the modulation of refractive index. Consequently the divergence of laser beam photons rises from the optical axis decreasing the intensity of Raman phonons.

The appearance of  $A_1^*(TO)$  forbidden mode was noted above  $50\text{ W/cm}^2$  of 633 nm wavelength of He-Ne laser beam at about  $150\text{ cm}^{-1}$  in the  $Y(XZ)Y$  configuration for LN:Fe crystals (0.05 wt%) [29]. The interpretation of the activation of forbidden mode depending on the laser beam intensities is based on the photovoltaic effect, which increases due to the carriers. The light-induced photovoltaic effect originates space charge field which varies the refractive index through electro-optic effect in his turn. Since the space charge field is created along the  $c$  axis, consequently the generated nonlinear polarization along  $c$  axis creates the additional  $ZZ$  components in Raman tensor bringing up the activation of  $A_1^*(TO)$  forbidden line.

The effect of photoinduced space charge field on the frequency shift of  $A_1(TO_4)$  Raman phonon was estimated for iron doped LN crystals by using 632.8 nm He-Ne laser beam [30]. 0.03 mol%, 0.05 mol%, 0.1 mol% Fe doped LN crystals were used for Raman Backscattering spectroscopy in the  $X(ZZ)X$  configuration and for Raman Forward investigations in the  $X(YZ)X$  configuration, respectively. The value of space charge field is one order of magnitude higher in the case of forward measurements comparing to the results obtained by backscattering spectroscopy as space charge field depends on the absorption coefficient. The photoinduced space charge field induces the refractive index variation via the electro-optic Pockels effect as well as the strain via the piezo-electric effect. Since Raman spectroscopy is sensitive to the crystal piezo-electric strain originated by space charge field, Raman modes exhibit the frequency shift. The space charge field consequently the Raman frequency shift illustrates the dependence of concentration of  $Fe^{3+}$  ions which was controlled by reduced and oxidized treatments [31].

Nowadays the Raman scattering spectroscopy is considered as a powerful technique for the determination of composition and the structure of crystals [32, 33]. The broadening of Raman spectrums was recorded when the concentration of lithium decreases [34, 35]. The Raman lines become more intense and better resolved, frequency damping decreases with the change of crystal composition from sub-congruent to stoichiometric [14].  $E(TO_2)$  and  $E(TO_9)$  modes appear for stoichiometric crystals instead of wide bands in congruent crystals, which are connected to the activation of phonon by the intrinsic defects. Mainly Li/Nb concentration ratio of LN crystal is estimated by analyzing the full width at half maximum (FWHM) of  $A_1(TO_1)$  and  $E(TO_1)$  phonons which are attributed to Nb/O vibration along z axis (considered that oxygen sites are completely occupied and fully) [35-39] The Raman spectrum parameters as a function of temperature was investigated at the large temperature range [34,35,37]. The Raman lines expanded with the increase of temperature from the room temperature up to about Currier temperature (297K-1224K) [34]. FWHM decreased with the decrease of temperature down to T=70K. Below this temperature it stays stable [37].

### ***Theory***

During the interaction between the laser beam and the material, the electron orbits are oscillated periodically with the same frequency of the electric field of the incident electromagnetic wave. The perturbation of electron cloud leads to a periodic charge separation referred as a generated dipole moment. Thus, the oscillation generating the dipole moment induces the light scattering. The strength of the dipole moment is expressed as [40]:

$$\mathbf{P} = \alpha \bar{\mathbf{E}} \quad (2.2.1),$$

where  $\alpha$ -is the polarizability and is the function of instantaneous position of molecules,  $\bar{\mathbf{E}}$ -is the incident electric field and gives by:

$$\bar{\mathbf{E}} = \mathbf{E}_0 \cos(\omega t) \quad (2.2.2),$$

$\omega$ -is the frequency of the incident beam.

The vibrational energy of the specific mode characterizing the oscillation of atoms is expressed as:

$$E_v = (j + \frac{1}{2}) \hbar \omega_v \quad (2.2.3),$$

$j = 0, 1, 2 \dots$ -is the vibrational quantum number,  $\omega_v$ -is the vibrational frequency of the molecule,  $\hbar$ -is the Planck constant.

The displacement  $dQ$  of atoms from the equilibrium position is given by:

$$dQ = Q_0 \cos(\omega_{vib} t) \quad (2.2.4),$$

where  $Q_0$  is the maximum displacement from the equilibrium position.

In the case of small displacements the polarizability can be expressed by a Taylor series:

$$\alpha = \alpha_0 + \frac{\partial \alpha}{\partial Q} dQ \quad (2.2.5),$$

$\alpha_0$ -is the polarizability of the phonon at equilibrium position.

The induced dipole moment can be expressed as:

$$\mathbf{P} = \alpha_0 \mathbf{E}_0 \cos(\omega_0 t) + \left( \frac{\partial \alpha}{\partial Q} \frac{Q_0 \mathbf{E}_0}{2} \right) \{ \cos[2\pi(\omega_0 - \omega_v)t] + \cos[[2\pi(\omega_0 + \omega_v)t] \} \quad (2.2.6).$$

According to this equation the dipole moment can be generated at three frequencies:  $\omega_0$ -Mie or Rayleigh and  $\omega_0 - \omega_\nu$ ,  $\omega_0 + \omega_\nu$ -frequencies of inelastic (Raman) scatterings. Raman scattering is a non-linear phenomenon, when an incident photon generates or annihilates one or more particles with modulated energy [41]. The interaction of the matter and monochromatic laser beam results to elastic scattering referred as Rayleigh scattering, where the scattered beam keeps the same frequency of incident field. Only one of  $10^3$  or  $10^4$  photons illustrates the exchanged energy and frequency it is said to be inelastic or Raman scattering. The scattering with lower frequency ( $\omega_0 - \omega_\nu$ ) than the incident electromagnetic wave is called Stokes-Raman scattering and the scattered beam with higher frequency ( $\omega_0 + \omega_\nu$ )-is referred as Anti-Stokes scattering (Figure (2.2.1)).

The intensity of Raman phonon may be expressed as:

$$I \propto (n(\omega) + 1) \left| e_i \frac{\partial \alpha}{\partial Q} e_s \right|^2 f(\omega) I_0 \quad (2.2.7),$$

$e_i$ -is the polarized vector of incident beam, whereas  $e_s$ -is the polarized vector of scattered beam,  $I_0$ -is the intensity of incident beam taking into account the experimental parameters.  $n(\omega)$ -is the thermal population of Anti-Stokes scattering determined by Bose-Einstein factor, when  $n(\omega) + 1$ -is the population factor of Stokes scattering:

$$n(\omega) = \frac{1}{\exp(\frac{\hbar\omega}{k_B T} - 1)} \quad (2.2.8).$$

Here  $k_B$ -is the constant of Boltzman,  $\hbar$ -is the Planck constant.

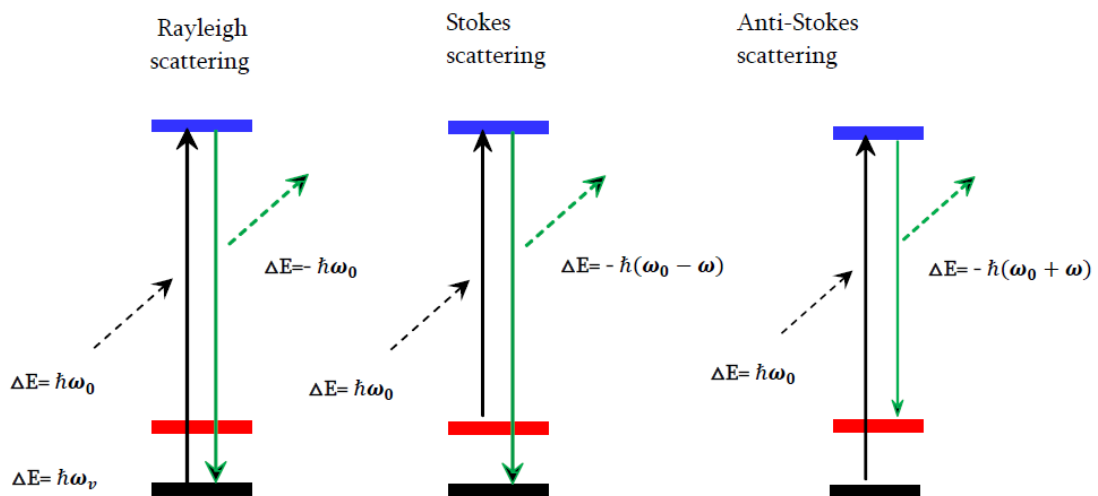


Figure 2.2.1: Interaction of photons with the substance.

$f(\omega)$  function related to the Raman bands may be expressed as:

$$f(\omega) = \frac{S\omega_0^2\gamma\omega}{(\omega_0^2 - \omega^2)^2 + \omega^2\gamma^2} \quad (2.2.9).$$

The angular phonon frequency of the incident phonon  $\omega_0$ , phonon damping  $\gamma$  defined by the full width at half maximum (FWHM) of Raman mode and the oscillator strength  $S$  are phonon characteristics detected by the fitting process. The oscillator strength  $S$  estimated by the peak intensity of Raman lines. A larger frequency  $\omega_0$  is associated with a stronger chemical bond thus it is sensitive to the variation of local stress or strain [35]. The higher linewidth is related to the incorporation of impurity or dopant ions, inhomogeneity, domains, crystal imperfection, structural damages. Especially the frequency shift of  $A_1(TO_4)$  phonon is concerned with the internal space charge field caused by photorefractive effect through the piezo effect [30]. The intensity corresponds to the polarizability of ions [42].

The Rayleigh beam has the thousandth of the incident beam intensity, whereas the Raman phonon obtains a millionth of intensity of the incident wave.

Indeed, at room temperature lithium niobate (LN) crystals belong to the  $R_3C$  space group ( $C_3V$  or  $3m$  point group), thus, the representation of the phonons at Brillouin zone center  $q \approx 0$ , are given as:  $5A_1 + 5A_2 + 10E$ , where one  $E$  and  $A_1$  are acoustic phonons and the all remaining phonons are optical.  $E$  and  $A_1$  optical modes are active, whereas  $A_2$  phonons are inactive.  $E$  optical modes contribute to the dipole moment along  $x$  or  $y$  when  $A_1$  optical phonons are associated to dipole moment along  $z$  axis. Raman optical modes are referred as transverse optical ( $TO$ ) and longitudinal optical ( $LO$ ) lines depending on the perpendicular or parallel polarization respectively, to the propagation direction of phonon. The Raman tensors are expressed as:

$$A_1(Z) = \begin{pmatrix} a & 0 & 0 \\ 0 & a & 0 \\ 0 & 0 & b \end{pmatrix}; E(X) = \begin{pmatrix} 0 & c & d \\ c & 0 & 0 \\ d & 0 & 0 \end{pmatrix}; E(Y) = \begin{pmatrix} c & 0 & 0 \\ 0 & -c & d \\ 0 & d & 0 \end{pmatrix}.$$

The  $X, Y, Z$  letters denote the direction of ionic vibration thus, the phonon polarization. The non-zero components are related to the  $x, y, z$  coordinate system. Expected optical phonons of lithium niobate crystals due to the selected rules are given in Table 2.2.1[43].

Table 2.2.1: Expected optical phonons of lithium niobate crystals due to the selected rules.

Configuration	Expected phonons according to selection rules
$X(YY)\bar{X}$	$A_1(TO)+E(TO)$
$X(YZ)\bar{X}$	$E(TO)$
$X(ZY)\bar{X}$	$E(TO)$
$X(ZZ)\bar{X}$	$A_1(TO)$
$Y(XX)\bar{Y}$	$A_1(TO)+E(LO)$
$Y(XZ)\bar{Y}$	$E(TO)$
$Y(ZX)\bar{Y}$	$E(TO)$
$Y(ZZ)\bar{Y}$	$A_1(TO)$
$Z(YX)\bar{Z}$	$E(TO)$
$Z(XY)\bar{Z}$	$E(TO)$
$Z(XX)\bar{Z}$	$A_1(LO)+E(TO)$
$Z(YY)\bar{Z}$	$A_1(LO)+E(TO)$

The  $A_1(TO_1)$  and  $E(TO_1)$  Raman phonons correspond to the vibrations of Nb ions (B site) along  $z$  and  $x$  (or  $y$ ) directions respectively against oxygen octahedron [25] (shown in Figure 2.2.2).  $A_1(TO_2)$  and  $E(TO_6)$  modes are attributed to the effective mass is sensitive to the out of phase motion of ions in Li (A) site and is related to the strengthening of  $A - O$  bond [43].  $A_1(TO_3)$  phonon is attributed to the distortions of the rotation of oxygen octahedron around  $c$  axis, whereas  $A_1(TO_4)$  and  $E(TO_8)$  modes correspond to the  $O/O$  oxygen octahedron stretching vibration (deformation) normal to  $z$  axis.

**Raman shift.** Most commonly Raman shifts are recorded in wavenumbers expressing in the units of inverse length, particularly is ( $cm^{-1}$ ) related directly to energy. The relation between the wavenumbers of the Raman phonon shift and the spectral wavelength can be reported as:

$$\Delta\omega = \frac{1}{\lambda_0} - \frac{1}{\lambda_1} \quad (2.2.10).$$

Here  $\Delta\omega$  is the Raman shift expressed in wavenumber,  $\lambda_0$  is the excitation wavelength when  $\lambda_1$  is the Raman spectrum wavelength. Taking into account this fact that the wavelength is usually reported in units of nanometers (nm) whereas wavenumbers are expressed in inverse centimeters, Equation 2.2.10 can be rewritten as:

$$\Delta\omega(cm^{-1}) = \left( \frac{1}{\lambda_{0(nm)}} - \frac{1}{\lambda_{1(nm)}} \right) \times \frac{10^7(nm)}{(cm)} \quad (2.2.11).$$

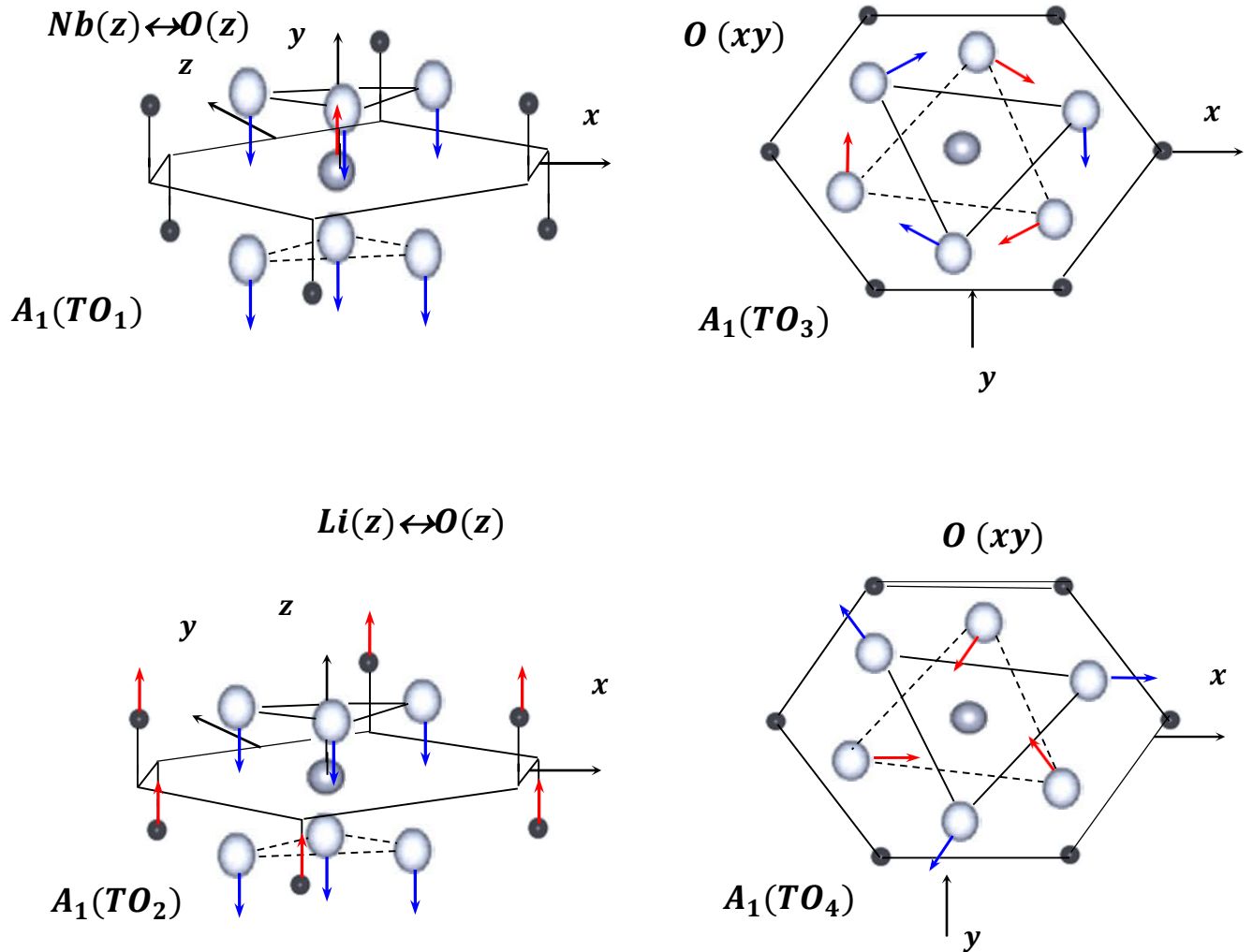


Figure 2.2.2: Vibration of  $A_1(TO)$  phonons interacting with LN.

### § 2.2.1. Experimental Technique

Raman backscattering spectroscopy was used to characterize the crystal composition as a function of the full width at the half of maximum (FWHM) of the Raman modes as well as

check the reliability of the obtained results for intrinsic defects (Table 2.2.2.1) connecting with the linewidth and frequency shift of the particular vibrational phonons. The measurements were performed by using LabRAM HR Evolution Raman Spectrometer permitting an access to the small frequencies down to  $5\text{cm}^{-1}$ . In this spectrometer the incident power (by means of neutral filter), cutoff filters, polarizers and analyzers, confocal diaphragm are controlled fully automatically. Three solid lasers are operated at visible wavelengths (with 532 nm, 638 nm, 785 nm wavelengths) switching by automatic control in the Raman device. The laser beam with 785 nm wavelength beam has been utilized with 200 mW power at room temperature (Figure 2.2.1.1). We gave preference to the  $A_1(TO)$  phonon in the  $Y(ZZ)Y$  backscattering configuration as it is more sensitive our under study  $x$ -cut ( $y$ -cut) crystals on the other hand in the same measurements conditions  $A_1(TO)$  phonon is more intense than  $E(TO_1)$  mode [37].



Figure 2.2.1.1: LabRAM HR Evolution Raman spectrometer.

The spectrometer contains a laser source, a sample holder, an optical system to collect the scattered light and to couple with the spectrum analyzer (spectrometer), an optical separator, a light sensitive CCD (Charge coupled Device array) detector and the electronics for acquisition and treatment of spectral data. The principle of the Raman backscattering spectroscopy is shown in Figure 2.2.1.2. In the optical part as the objective was used the lense with  $\times 100$  magnitude. The diameter of the focused light was  $1\mu\text{m}$ . Between the laser source and the optical system the polarizer was located to polarize the light beam. Polarized incident laser beam interacting with sample was scattered and was guided to the analyzer via the objective. The notch filter allowing to remove a small band in the spectrum was used to obtain

only the anti-Stoke scattering related to the increase of energy due to the inelastic scattering from the crystal. The notch filter cut a beam start  $50\text{ cm}^{-1}$  up to  $5000\text{ cm}^{-1}$  frequency. The measurement wavelength range was extended from  $100\text{ nm}$  to  $1000\text{ nm}$ . The monochromator was used, which is a grating with  $1800\text{ g/mm}$ , for the separation the Raman spectrum from the incident laser (Rayleigh) part. The Raman signal was recorded by the CCD (Charge coupled Device array) detector due to the diffraction after the separation.

Laser source

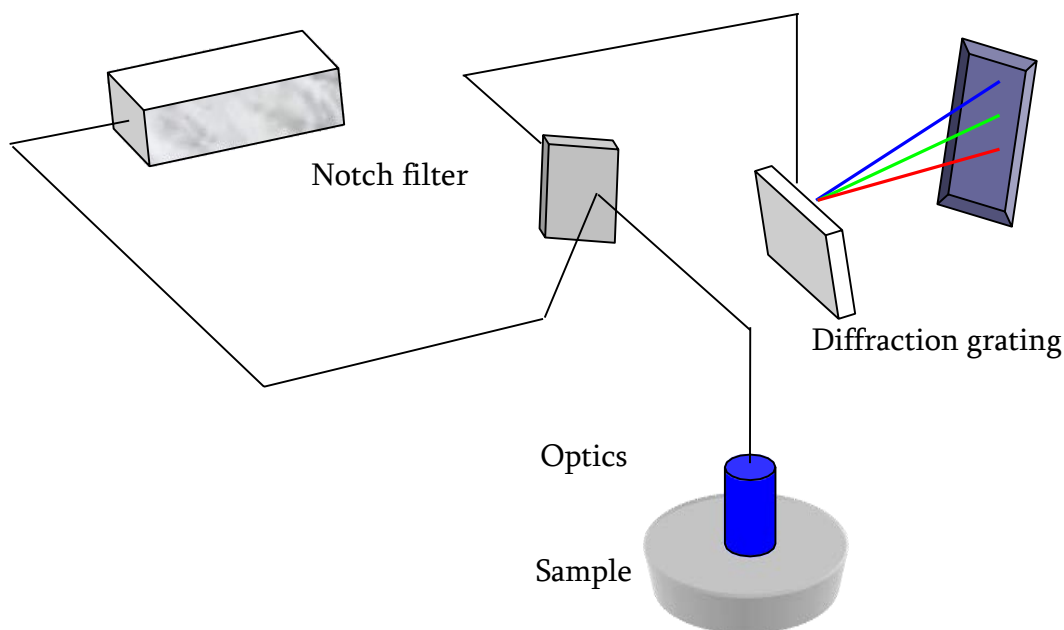


Figure 2.2.1.2: The principle of the Raman backscattering spectroscopy.

The Raman phonon at  $521\text{ cm}^{-1}$  of silicon crystal was used for the spectral calibration of the spectrometer.

### ***§ 2.2.2. Results and Discussion.***

Taking into account the instrumental resolution equal to be  $0.2\text{ cm}^{-1}$  depending on the wavelength of the laser focal length, the crystal composition error was calculated to be about of  $0.03\text{ mol}\%$ . Raman spectrum of  $A_1(TO)$  mode in  $Y(ZZ)Y$  configuration is given in Figure 2.2.2.1.

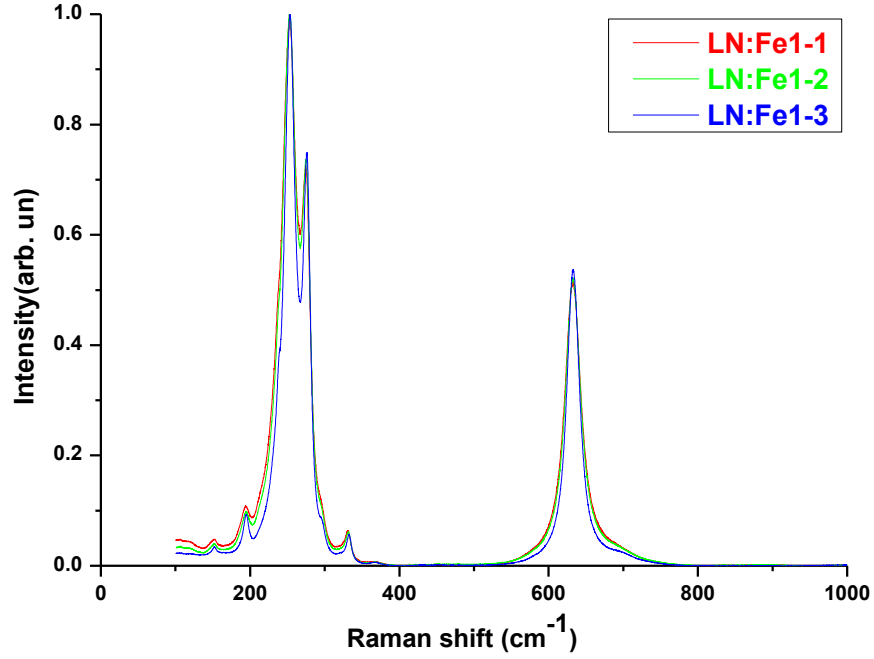


Figure 2.2.2.1:  $A_1(TO)$  Raman spectrum of Fe:LN crystals in the  $Y(ZZ)Y$  configuration.

The full width at the half of maximum (FWHM) for  $A_1(TO_1)$  phonon given in Figure 2.2.2.1 has been used to characterize the crystal composition by Zhang method [19, 39, 44]. The dependence  $\Gamma_{A_1(TO_1)} = f(X_c)$  was estimated by using the following equations [39]:

$$\Gamma_{A_1(TO_1)} = 18.00 + 8.086(50\% - X_c) \quad (2.2.2.1),$$

$$C_{Li}(mol\%) = 52.226 - 0.1237\Gamma(cm^{-1}) \quad (2.2.2.2).$$

The results of FWHM of  $A_1(TO_1)$  Raman phonon versus  $Li_2O$  concentration in the melt for iron doped LN samples are given in Table 2.2.2.1 and Figure 2.2.2.2.

Table 2.2.2.1: The results of FWHM of  $A_1(TO_1)$  Raman phonon and the shift of  $A_1(TO_1)$  mode in the  $Y(ZZ)Y$  configuration various  $Li_2O$  concentration in the melt for iron doped LN LN:Fe1-1, LN:Fe1-2, LN:Fe1-3 samples, as well as calculated values of  $Li_2O$  content in the crystal.

Samles	$C_{Li}$ in the melt (mol%)	$C_{Li}$ (mol%)	FWHM of $A_1(TO_1)$ Raman phonon	$A_1(TO_1)$ ( $cm^{-1}$ ) in $Y(ZZ)Y$ config.
LN:Fe1-1	48.45	$48,45 \pm 0,03$	14.5955	252.477
LN:Fe1-2	50.0	$48,58 \pm 0,03$	14.0660	253.334
LN:Fe1-3	54.5	$49,49 \pm 0,03$	10.3765	253.678

From the results it is noticeable that the linewidth of  $A_1(TO_1)$  phonon decreases with the increase of Li content, especially for close-stoichiometric sample the abrupt reduction is recorded. On the other hand the analyzing of the FWHM of  $A_1(TO_1)$  Raman spectra testifies that content of lithium  $C_{Li}$  decreases mainly during crystallizing. Only the lithium concentration remains invariable for sample with the congruent composition ( $C_{Li} = 48.45 \text{ mol}\%$ ).

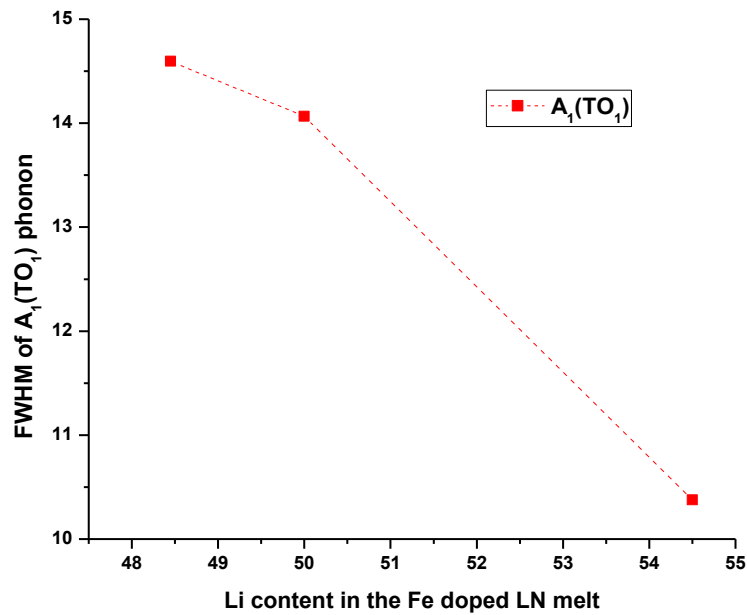


Figure 2.2.2.2: The full width at the half of maximum (FWHM) for  $A_1(TO_1)$  phonon as a function of melt composition for Fe:LN crystals obtained in  $Y(ZZ)Y$  configuration by 785 nm wavelength laser beam.

$A_1(TO_1)$  Raman phonon is activated at the  $254\text{ cm}^{-1}$  in the  $Y(ZZ)Y$  configuration for undoped congruent LN. However, the shift of frequency from  $254\text{ cm}^{-1}$  was induced due to the different composition and the presence of iron ions. The values of activated frequencies of  $A_1(TO_1)$  Raman line for samples are given in Table 2.2.2.1.

The frequency shift of  $A_1(TO)$  modes as a function of crystal composition derived from Raman backscattering measurements for iron doped crystals with different composition varying from congruent to near stoichiometry is shown in Figure 2.2.2.3.

It is visible from the graphs that the variation of frequency shift of all  $A_1(TO)$  phonons illustrate the same behavior: it increases with the increase of Li content in iron doped LN crystals consequently the force constant of  $B - O$ ,  $A - O$  bonds parallel to the  $z$  axis as well as the respectively rotation and deformation of oxygen octahedron perpendicular to  $c$  axis increase monotonously. The increase of frequency shift of  $A_1(TO_1)$  and  $A_1(TO_2)$  phonons related to the introduction of iron ions can be explained by the following hypothesis: It is considered that iron ions with valence  $Fe^{2+}$  or  $Fe^{3+}$  incorporate onto both A (lithium) and B (niobium) sites. On the other hand is reliable that  $Fe^{2+}$  ions occupy A site, whereas  $Fe^{3+}$  ions sit in B sites due to the valence state  $Li^+$  and  $Nb^{5+}$  respectively. In general A site occupied by  $Li^+$  ions and caused by Li deficiency. If iron ions with  $Fe^{2+}$  or  $Fe^{3+}$  valence states incorporate onto A site it can occupy place of  $Li^+$  or  $Nb^{4+}$  antisites.

Here two scenarios can be discussed. Scenario 1: The occupation of Li places by  $Fe^{2+}$  or  $Fe^{3+}$  ions would decrease the force constant of  $A - O$  bond due to the slight higher ionic radii in the case of  $Fe^{2+}$ , or smaller ionic radius for  $Fe^{3+}$  ions, whereas about nine times higher atomic mass of Fe compared to the values of Li [24] (see Table 2.2.2.2), also taking into account differ valence state. Vice-versa we have strengthening of this bond (Figure 2.2.2.3) thus, the first scenario related to the occupation of Li places in A site by iron ions is refused. Scenario 2: It may be considered that Fe ions ( $Fe^{2+}$  or  $Fe^{3+}$ ) ions occupy the places of  $Nb^{4+}$  antisites in A site and  $Nb^{5+}$  ions in their natural B site. Thanks to the higher ionic radii, smaller atomic mass and valence state than for Nb ions, the incorporation of places of Nb antisites by iron ions strengthens  $A - O$  bond increasing the frequency shift of  $A_1(TO_2)$  phonon. On the other hand

this occupation in A site push out Nb ions from A site to their natural site strengthening also  $B - O$  bond consequently frequency shift of  $A_1(TO_1)$  mode increases.

Due to the above discussed characteristics this incorporation increases additionally the frequency shift of  $A_1(TO_1)$  related to B-O bond which is proved by results given in Figure 2.2.2.3. Thus, it can be concluded that Fe ions incorporate onto both A and B sites occupying the places of Nb ions. With the variation of composition from congruent to near-stoichiometric the increase of Li content in A site gives rise to the probability that more amount of iron ions will occupy B site. Thus, the increase of Li content strengthens the  $A - O$  and  $B - O$  bond proved by the increase of  $A_1(TO_1)$  and  $A_1(TO_2)$  modes respectively (Figure 2.2.2.3).

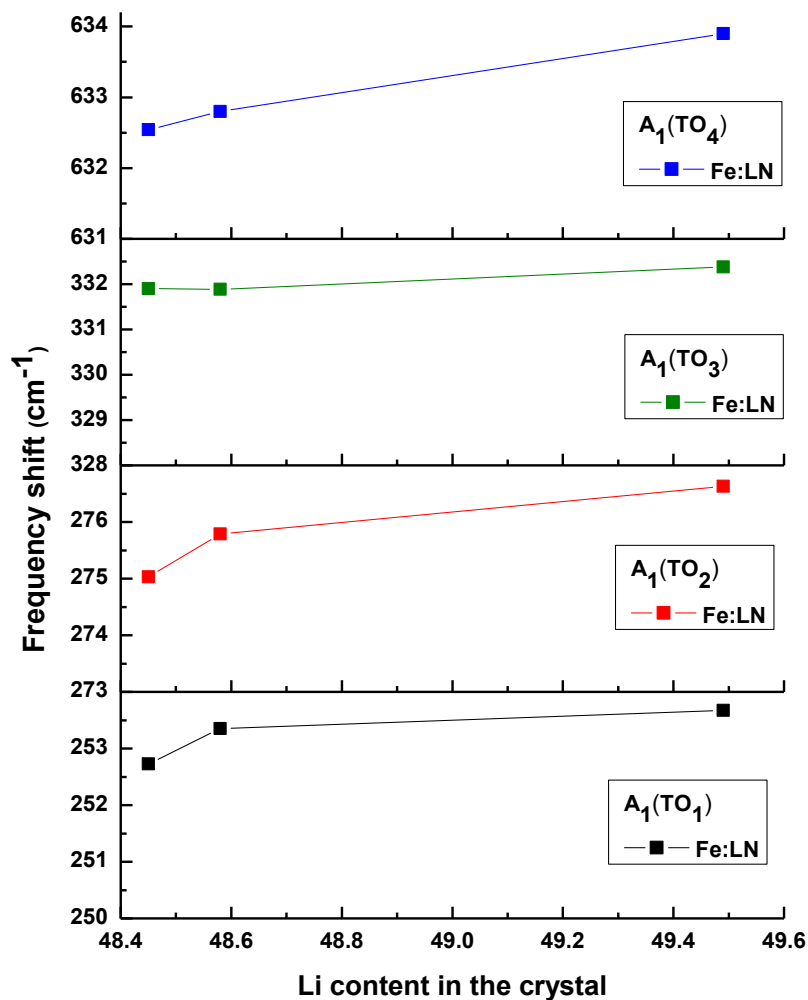


Figure 2.2.2.3: Frequency shift of  $A_1(TO)$  phonons as a function of crystal composition for iron doped LN samples with various composition.

Table 2.2.2.2: Ionic radius and mass [45].

Ions	$Li^+$	$Nb^{5+}$	$Fe^{2+}$	$Fe^{3+}$
Ionic radius, $r_i$ (pm)	76	64	78	64.5
Atomic mass, $A_r$	6.941	92.906	55.845	

The increase of  $A_1(TO_3)$  and  $A_1(TO_4)$  modes is associated with the hardening of oxygen octahedron (Figure 2.2.2.3). In congruent crystals the oxygen ions are able to the motions easily around their positions due to the higher concentration of Nb and Li vacancies in their natural sites. With the increase of composition as well as due to the presence of iron ions the content of Li and Nb vacancies decreases complicating the motions of oxygen ions.

### ***§ 2.3. Optical absorption***

#### ***Theory***

The photons with higher energy than band gap ( $E_g$ ) can be absorbed transmitting this energy to the photo-induced electrons due to the optical absorption processes. Photo-generated charge carriers move from donor centers ( $Fe^{2+}$  in our case) to the conduction band and after migration trapping in the acceptor centers (mainly  $Fe^{3+}$ ) [46,47]. The excitation and migration in conduction band is controlled by diffusion, photo-voltaic and drift mechanism [31]. Optical absorption process may be investigated by measuring the intensity of initial beam  $I_0$  propagated via the crystal with length  $L$  and the transmitted beam intensity  $I_t$  after the medium [48]. Since  $Fe^{2+}$  ions compared to  $Fe^{3+}$  centers expand the absorption band in the visible range [47] thus, the intensity of absorption band ( $I_t$ ) is proportional to the concentration of  $Fe^{2+}$  ions. Therefore, in order to determine the  $Fe^{2+}$  concentration, an optical absorption measurements have been performed. The relationship between the intensities of incident  $I_0$  and transmitted beams  $I_t$  with wavelength  $\lambda$  is expressed as:

$$I_t = I_0 \gamma 10^{-\alpha d} \quad (2.3.1.1),$$

where  $d$  is the sample thickness,  $\gamma(\lambda)$  is a function comprising the instrumental constants and the Fresnel reflection losses [49],  $\alpha$  is an absorption coefficient depending on the wavelength of beam. This coefficient rises up for wavelengths shorter than  $\lambda_c$  corresponding to the band gap energy ( $\lambda_c = \frac{hc}{E_g}$ ). The absorption coefficient is used to estimate the intensity losses due to the absorption process and light scattering.

#### ***§ 2.3.1. Experimental Technique***

The main parameter of optical absorption measurement is the determination of the transmittance of samples, shown as:

$$T_S = \frac{I_t(\lambda)}{I_0(\lambda)} \quad (2.3.1.1).$$

For optical absorption measurements Jasco V670 spectrophotometer (Figures 2.3.1.1, 2.3.1.2) has been used in transmission mode, with beam polarized in 330-850 nm range and with bandwidth 1nm.

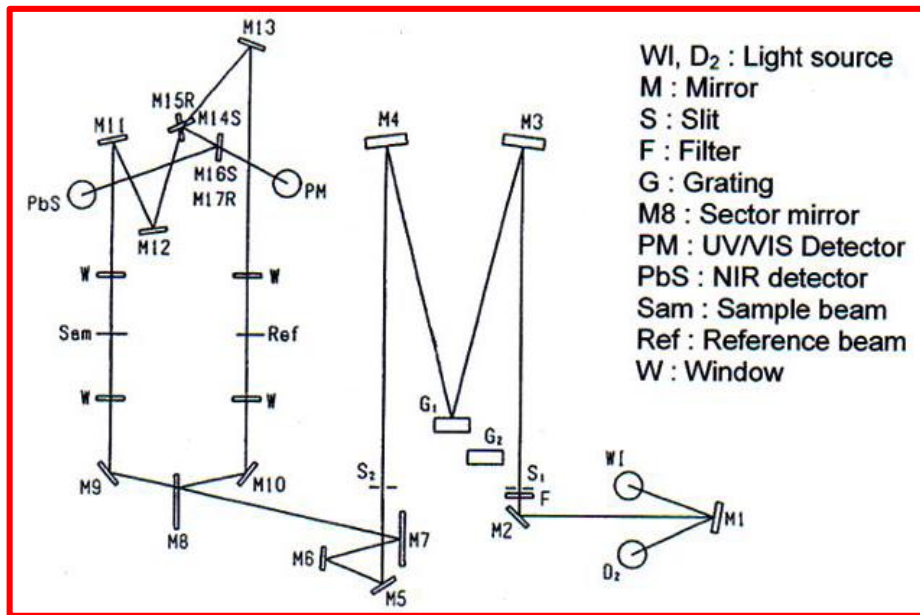


Figure 2.3.1.1: Scheme of the Jasco V670 spectrophotometer used for optical absorption measurements. It is a double beam spectrophotometer operating in a wide range of wavelengths from 200 to 3200 nm. It is equipped with two lamps (deuterium lamp from 190 to 350 nm, halogen lamp from 330 to 3200 nm), a dual-grating monochromator, two detectors (a photomultiplier tube and a Peltier-cooled PbS detector). It is equipped also with an optional rotating sample holder, and an optional polarizing window made of a Glan-Taylor calcite prism.



Figure 2.3.1.2: Jasco V670 spectrophotometer.

The spectra were detected in ordinary polarization thus, the electric field was perpendicular to the ferroelectric axis. For measurements series of undoped LN and Fe doped LN samples were used. The each obtained spectrum was normalized to the spectrum taken for pure LN

samples to avoid the reflection contribution at the crystal interfaces. The spectra of the optical absorption due to  $Fe^{2+}$  ions are shown in the Figure 2.3.1.3.

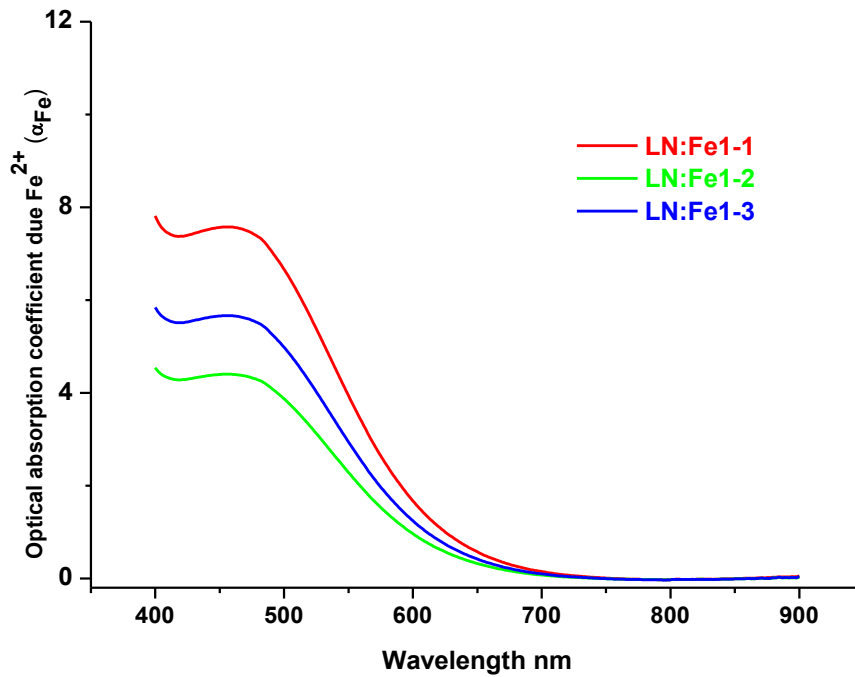


Figure 2.3.1.3: Transmission of the iron doped LN crystals of different composition.

The transmittances  $T_{1,2}$  of two pure, undoped congruent LN samples with a thicknesses  $d_1 = 0.5$  mm and  $d_2 = 1$  mm were also measured and used as a standard.

$$T^1(\lambda) = \gamma(\lambda) \cdot 10^{-[\alpha_{LN}(\lambda)]d_1} \quad (2.3.1.2),$$

$$T^2(\lambda) = \gamma(\lambda) \cdot 10^{-[\alpha_{LN}(\lambda)]d_2} \quad (2.3.1.3),$$

where  $\alpha_{LN}$  – is the intrinsic absorption of the lithium niobate. The ratio of transmittances for two pure samples can be expressed as:

$$\frac{T^2(\lambda)}{T^1(\lambda)} = 10^{-[\alpha_{LN}(\lambda)](d_2-d_1)} \quad (2.3.1.4).$$

From these values the intrinsic absorption of pure LN is calculated as:

$$\alpha_{LN} = -\log\left(\frac{T_2(\lambda)}{T_1(\lambda)}\right) \frac{1}{d_2-d_1} \quad (2.3.1.5).$$

And

$$\log(\gamma) = \log(T^1(\lambda)) + \alpha_{LN}d_1 \quad (2.3.1.6).$$

For small Fe concentration, the absorption coefficient  $\alpha$  is proportional to the  $Fe^{2+}$  concentration:

$$\alpha(\lambda) = \sigma(\lambda)[Fe^{2+}] \quad (2.3.1.7).$$

Where  $\sigma(\lambda)$  is the absorption cross section [50]. In particular,  $\sigma(532nm) = (3.95 \pm 0,08) \times 10^{-18}cm^2$  [51]. However, there may be a contribution due to intrinsic LN absorption. The absorption considering only the contribution of Fe ions ( $\alpha_{Fe}$ ) can be determined by using the following equations:

$$\frac{T_s(\lambda)}{T^1(\lambda)} = 10^{-(\alpha_{LN} + \alpha_{Fe})d_s - \alpha_{LN}d_1} = 10^{-(\alpha_{LN}(d_2 - d_1) + \alpha_{Fe}d_s)} \quad (2.3.1.8),$$

$$\log\left(\frac{T_s(\lambda)}{T^1(\lambda)}\right) = -[\alpha_{LN}(d_2 - d_1) + \alpha_{Fe}d_s] \quad (2.3.1.9).$$

Thus, the absorption coefficient due only to the  $Fe^{2+}$  ions:

$$\alpha_{Fe} = -\frac{1}{d_s} [\log\left(\frac{T_s(\lambda)}{T^1(\lambda)}\right) + \alpha_{LN}(d_s - d_1)] \quad (2.3.2.10).$$

The  $[Fe^{2+}]$  concentration was calculated from the cross section of  $Fe^{2+}$  at 532 nm [52]:  
According to the (2.3.1.7) equation:

$$C_{Fe^{2+}} = \frac{\alpha_{Fe}}{\sigma(532nm)} \quad (2.3.1.12).$$

### ***§ 2.3.2. Results and Discussion***

The determination of concentration  $Fe^{3+}$  was attempted by measuring the total iron based on the measurement of the absolute absorption coefficient at 342 nm [46]. Whereas at this wavelength the transmittance of Fe:LN samples is so small that, even after decreasing their thickness up to 1 mm, the absorption coefficient could not be measured. The distribution coefficient of iron being closer to one [53] thus, assuming the total iron concentration in the crystal is equal to the known value in the melt,  $[Fe^{3+}]$  was estimated by subtracting of the amount of  $C_{Fe^{2+}}$  from the total  $C_{Fe}$  concentration in the crystals under study:

$$[Fe^{3+}] = [Fe] - [Fe^{2+}] \quad (2.3.2.1).$$

In the Figure 2.3.2.1 it is given the change of  $Fe^{3+}$  ions content in the crystal depending on the composition of the last.

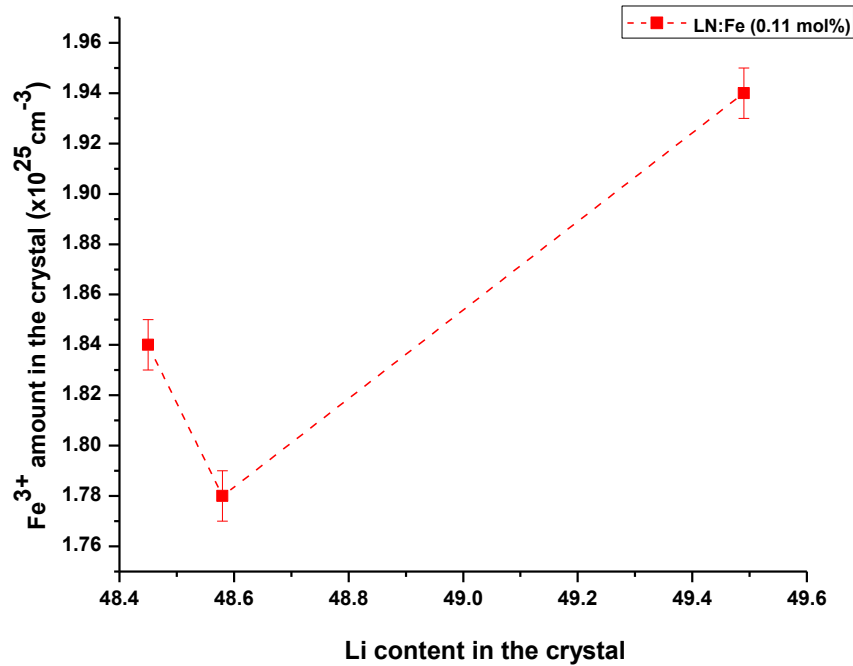


Figure 2.3.2.1:  $Fe^{3+}$  amount in the LN:Fe crystals of different compositions.

The results of the observation from optical absorption measurements are represented in the Table 2.3.2.1.

Table 2.3.2.1: The results of optical absorption measurements for  $C_{Fe^{2+}}$ ,  $C_{Fe^{3+}}$  and reduction degree:  $R = \frac{[Fe^{2+}]}{[Fe^{3+}]}$ .

	Nom. [Li] mol % in the melt	[Li] mol % In crystal	[Fe] · 10 <sup>25</sup> $m^{-3}$ (nom. )	[Fe <sup>2+</sup> ] · 10 <sup>3</sup> $m^{-3}$	[Fe <sup>3+</sup> ] · 10 <sup>3</sup> $m^{-3}$	R $= \frac{[Fe^{2+}]}{[Fe^{3+}]}$ · 100%
LN:Fe1-1	48.45	48,45±0,03	2.09	0.24±0,01	1.84	13.08±0,09
LN:Fe1-2	50	48,58±0,03	2.09	0.31±0,01	1.78	17.2±0,5
LN:Fe1-3	54.5	49,49±0,03	2.09	0.15±0,01	1.94	7.6±0,1

From the results given in Table 2.3.2.1 is visible that LN:Fe1-2 sample illustrates the greatest value for  $C_{Fe^{2+}}$ , while LN:Fe1-3 being close to stoichiometry consists of the smallest concentration of  $Fe^{2+}$ . Consequently, as the reduction degree ( $Fe^{2+}/Fe^{3+}$ ) is proportional to  $[Fe^{2+}]$ , repeat the same variation behavior. In all case, iron doped LN all samples, independent of the crystal composition ( $Li_2O$  content) and the Fe content, are in an almost completely oxidized state as the concentration of  $Fe^{3+}$  is one order of magnitude is higher. The reduction ratio ( $Fe^{2+}/Fe^{3+}$ ) can be modified by a reduction treatment. The effects of this treatment are more marked for samples containing more Fe. This suggests that the diffusion of electrons from the atmosphere proceeds more efficiently in samples with higher Fe concentration.

## § 2.4. Conclusion-Chapter 2

In LN:Fe1-1÷LN:Fe1-3 samples both lattice parameters  $a$  and  $c$  decrease with the variation of LN composition from congruent to near stoichiometry underlining the decrease of non stoichiometric intrinsic defects with the increase of  $Li_2O$  content. A slight decrease of lattice parameters of LN:Fe samples compared to the pure LN crystals with the same composition can be related to this assumption that the main part of Fe ions occupies Li sites captured by  $Nb^{5+}$  cations. However, this variation referred to the presence of iron ions is negligible due to the small amount of iron ions indicating that the main contribution of the change of the lattice parameters is related to the change of initial composition of the melt.

In LN:Fe1-1÷LN:Fe1-3 crystals  $Li_2O$  content decreases comparing to the corresponding value in the melts, except the congruent sample where  $Li_2O$  content remains the same in the melt and the crystal.

In iron doped LN crystals with the increase of  $Li_2O$  content the monotonous increase of the force constant of B-O, A-O bonds parallel to the Z axis as well as the respectively rotation and deformation of oxygen octahedron perpendicular to Z axis characterized by the frequency shift of  $A_1(TO)$  phonons is related to the incorporation of Fe ions onto both A and B sites occupying the places of Nb ions. Particularly, the increase of frequency shift of  $A_1(TO_1)$  and  $A_1(TO_2)$  phonons is referred to the occupation of Fe ions ( $Fe^{2+}$  or  $Fe^{3+}$ ) ions in the places of  $Nb^{4+}$  antisites in A site and  $Nb^{5+}$  ions in their natural B site respectively. The occupation of Fe ions in A site push out Nb ions from A site to their natural site strengthening also B-O bond increasing the frequency shift of  $A_1(TO_1)$  mode. Thanks to the higher ionic radii, smaller atomic mass and valence state than for Nb ions, the incorporation of places of Nb antisites by iron ions strengthens A-O bond increasing the frequency shift of  $A_1(TO_2)$  phonon. With the variation of composition from congruent to near-stoichiometric the increase of  $Li_2O$  content in A site gives rise to the probability that more amount of Fe ions will occupy B site. On the other hand in congruent crystals due to the higher concentration of Nb and Li vacancies in their natural sites the oxygen ions are able to the motions easily around their positions. With the increase of  $Li_2O$  content as well as due to the introduction of Fe ions the concentration of Li and Nb vacancies decreases hardening of oxygen octahedron consequently increasing the frequency shift of  $A_1(TO_3)$  and  $A_1(TO_4)$  modes.

Although the fixed iron total concentration in LN:Fe1-1÷LN:Fe1-3 samples, the amount of  $Fe^{2+}$  changes non-monotonously with the increase of  $Li_2O$  content. Meanwhile, the samples independent of crystal composition and  $Fe^{2+}$  iron ions concentration are in a completely oxidized state as  $Fe^{3+}$  concentration one order of magnitude is higher.

## ***References-Chapter 2***

1. S.C. Abrahams, J.M. Reddy, J.L. Bernstein, "Ferroelectric Lithium Niobate. 3. Single Crystal X-Ray Diffraction Study at 24°C", *J. Phys. Chem. Solids* 27, pp. 997-1012 (1966).
2. S. C. Abrahams, H. J. Levinstein and J. M. Reddy, "Ferroelectric Lithium Niobate. 5. Polycrystal X-Ray Diffraction Study Between 24°C and 1200 °C", *J. Phys. Chem. Solids* 27, pp. 1019-1026 (1966).
3. S. C. Abrahams and P. Marsh, "Defect Structure Dependence on Composition in Lithium Niobate", *Acta Cryst.* B42, pp. 61-68 (1986).
4. N. Iyi, K. Kitamura, F. Izumi, J.K. Yamamoto, T. Hayashi, H. Asano, S. Kimura, "Comparative Study of Defect Structures in Lithium Niobate with Different Compositions", *J. Solid State Chem.* 101, pp. 340-352 (1992).
5. A. P. Wilkinson, A. K. Cheetham and R. H. Jarman, "The defect structure of congruently melting lithium niobate", *J. Appl. Phys.* Vol. 74 No.5, pp. 3080-3083 (1993).
6. N. Zotov, H. Bovsen, F. Frev, T. Metzgar, E. Born, "Cation Substitution Models of Congruent LiNbO<sub>3</sub>, Investigated by X-Ray and Neutron Powder Diffraction", *J. Phys. Chem. Solids* Vol. 55, No 2, pp. 145-152 (1994).
7. G. Malovichko, O. Cerclier, J Estienne, V. Grachev, E. Kokanyan and C. Boulesteix, "Lattice Constants of K- and Mg-Doped LiNbO<sub>3</sub>, Comparison with Nonstoichiometric Lithium Niobate" *J. Phys. Chem. Solids* Vol. 56, No. 9, pp. 1285-1289 (1995).
8. P. Lerner, C. Legras, P. J. Dumas, "Stoéchiométrie des Monocristaux de Métaniobate de Lithium", *J. Cryst. Growth* 3/4, pp. 231-235, (1968).
9. F. Abdi, M.D. Fontana, M. Aillerie, P. Bourson "Coexistence of Li and Nb vacancies in the defect structure of pure LiNbO<sub>3</sub> and its relationship to optical properties" *Applied Physics A*, 83, 3, 427-434 (2006).
10. D. A. Bryan, R. Gerson and H. E. Tomaschenke, "Increased optical damage resistance in lithium niobate", *Appl. Ph. Lett.* 44, pp 847-849 (1984).

11. F. Abdi, M. Aillerie, P. Bourson, M. D. Fontana “Defect structure in Mg-doped LiNbO<sub>3</sub>: Revisited study” J. of Appl. Phys. 106(3), 033519 (2009).
12. W.C. Roentgen, “On a New Kind of Rays”, Science New Series (1896), Vol. 3, No. 59, pp. 227-231 (2015).
13. Ron Jenkins in “Encyclopedia of Analytical Chemistry R.A. Meyers (Ed.), X-ray Techniques”, Overview Ó John Wiley & Sons Ltd, Chichester, pp. 13269–13288 (2000).
14. Jens Als-Nielsen, Des McMorrow, “Elements of modern X-ray physics”, Second edition, John Wiley & Sons (2011).
15. A. K. E. Nobarzad, M. M. Khalilabad, K. Heirdari, “Phase Identification by X-ray diffraction”, pp. 1-18 (2014).
16. R. Guinebretière, “X-ray Diffraction by Polycrystalline Materials”, (2007).
17. R. E. Dinnibier and S. J. L. Billinge, “Powder Diffraction Theory and Practice”, (2008).
18. J. A. Bearden, “X-ray Wavelengths”, Rev. of Mod. Phys. Vol.39, pp.79-124(1967).
19. A. Danielyan, “Characterizing the lattice parameter in iron-doped lithium niobate crystals with different stoichiometry”, Bulletin (National Polytechnic University of Armenia), Part 1, pp. 59-64, (2018).
20. L. Lutterotti, P. Scardi and P. Maistrelli, J. Appl. Cryst., 25, pp. 459-462(1992).
21. L. Rebouta, M. F. DaSilva, J. C. Soares, et al. “Lattice Site of Iron in LiNbO<sub>3</sub>(Fe<sup>3+</sup>) by the PIXE/Channelling Technique”, Europhys. Lett.14, pp 557-561(1991).
22. V. Grachev, G. Malovichko and O. Schirmir, “Structures of Point Defects in Lithium Niobate”, Ukr. J. Phys. 49, N 5, pp. 438-447 (2004).
23. Smekal, A. Naturwissenschaften 11, pp. 873-875 (1923).
24. C. V. Raman and K. S. Krishnan, “A new type of secondary radiation”, Nature 121, pp. 501-502 (1928).
25. R. F. Schaufele and M. J. Weber, “Raman Scattering by Lithium Niobate” Phys. Rev. Vol. 152 pp. 705-708 (1966).

26. I. P. Kaminow and W. D. Johnston, "Quantitative Determination of Sources of the Electro-Optic Effect in LiNbO<sub>3</sub> and LiTaO<sub>3</sub>", *Phys. Rev.*, Vol. 160 pp. 519-522 (1967).
27. V. Caciuc, A. V. Postnikov and G. Borstel, "Ab Initio Structure and Zone-center Phonons in LiNbO<sub>3</sub>" *Phys. Rev. B* Vol.61 pp. 8806–8813 (2000).
28. M. Nippus and R. Claus, "The Influence of Photorefractive Index Change on Raman Scattering Intensities in LiNbO<sub>3</sub>" *Z. Naturforsch.* 33a, pp. 924-933 (1978).
29. R. Mouras, M. D. Fontana, M. Mostefa, and P. Bourson, "Photorefractive Properties Probed by Raman Spectroscopy in Fe-doped LiNbO<sub>3</sub>", *J. Opt. Soc. Am. B* Vol.23, No 9, 1867-1871 (2006).
30. M. Bazzan, N. Kokanyan, A. Zaltron, N. Argiolas, D. Chapron, M. D. Fontana, "Raman Frequency Shift Induced by Photorefractive Effect on Fe-doped Lithium Niobate" *J. of Appl. Phys.* 114, 163506/1-163506/6 (2013).
31. T. Volk and M. Wohlecke, "Lithium Niobate: Defects, Photorefracion, and Ferroelectric Switching" Springer, Berlin, 264 (2008).
32. S.M. Kostritskii, M. Aillerie, P. Bourson, D. Kip "Raman spectra and compositional inhomogeneities in lithium tantalate crystals of different stoichiometry compositions" *Appl Phys B: Lasers and Optics*, 95, 125–130 (2009).
33. A. Novoselov, A. Ruso, M. Ferriol, M. Cochez, N. Fressengeas, M. Aillerie "Micro-pulling-down growth and optical waveguide engraving in Fe-doped LiNbO<sub>3</sub> single crystal fibers" *Optical Materials*, Volume 32, Issue 3, ISSN 0925-3467, pp. 456-460 (2010).
34. Y. Okamoto, P-C. Wang and J. F. Scott, "Analysis of Quasielastic Light Scattering in LiNbO<sub>3</sub> Near T<sub>c</sub>", *Phys. Rev. B* Vol. 32 pp. 6787–6792 (1985).
35. G. I. Malovichko, V. G. Grachev, E. P. Kokanyan, O. F. Schirmer, K. Betzler, B. Gather, F. Jermann, S. Klauer, U. Schlarb and K. Wohlecke, "Characterization of Stoichiometric LiNbO<sub>3</sub> Grown from Melts Containing K<sub>2</sub>O" *Appl. Phys.* A56, pp. 103–108 (1993).
36. R. Ridah, M. D. Fontana, P. Bourson and G. Malovichko, "The Composition Dependence of the Raman Spectrum and New Assignment of the Phonons in LiNbO<sub>3</sub>" *J. Phys.: Condens. Matter* 9, pp. 9687–9693 (1997).

37. U. Schlarb, S. Klauer, M. Wesselman and M. Wöhlecke, "Determination of the Li/Nb Ratio in Lithium Niobate by Means of Birefringence and Raman Measurements", *Appl. Phys. A* 56 pp. 311–15 (1993).
38. F. Abdi, M. Aillerie, P. Bourson, M. D. Fontana and K. Polgar, "Electro-optic Properties in Pure LiNbO<sub>3</sub> Crystals from the Congruent to the Stoichiometric Composition", *J. Appl. Phys.* Vol. 84, No 4 pp. 2251–2254 (1998).
39. Y Zhang, L. Guilbert, P. Bourson, K. Polgar, M. D. Fontana, "Characterization of Short-range Heterogeneities in Sub-congruent Lithium Niobate by Micro-Raman Spectroscopy", *J. Phys.: Condens. Matter* 18 pp. 957–963 (2006).
40. A. Derek Long, "The Raman Effect: A Unified Treatment of the Theory of Raman Scattering by Molecules", John Wiley & Sons Ltd (2002).
41. R. Loudon, "The Raman effect in crystals" *Adv. Phys.* 13, pp. 423-482 (1964).
42. M. D. Fontana, K. Laabidi, C. Carabatos-Nedelec, "Correspondence Between Electro-optic Properties and the Raman Scattering in Oxydic Perovskites", *Ferroelectrics*, , Vol. 94, pp. 97-101 (1989).
43. M. D. Fontana and P. Bourson, "Microstructure and Defects Probed by Raman Spectroscopy in Lithium Niobate Crystals and Devices", *Appl. Phys. Rev.* 2, pp. 040602/1-040602/14 (2015).
44. L. Vittadello, M. Bazzan, A. Danielyan, E. Kokanyan, L. Guilbert, M. Aillerie, "A polaron approach to photorefractivity in Fe:LiNbO<sub>3</sub>" *Journal of Physics Communications*, vol. 2 , 125003/1-125003/12, (2018).
45. R. D. Shanon, "Revised effective ionic radii and systematic studies of interatomic distances in halides and chalcogenides", *Acta Cryst.* A32, pp. 751-767(1976).
46. G. E. Peterson, A.M. Glass, T.J. Negran, "Control of the Susceptibility of Lithium Niobate to Laser Induced Refractive Index Changes", *Appl. Phys. Lett.* 19, pp.130-132 (1971).
47. M.G. Clark, F.J. DiSalvo, A.M. Glass, G.E. Peterson, "Electronic Structure and Optical Index Damage of Iron Doped Lithium Niobate", *J. Chem. Phys.* Vol. 59, No. 12, pp.6209-6219 (1973).

48. M. Ciampolillo, A. Zaltron, M. Bazzan, N. Argiolas, C. Sada, M. Biancon, “Lithium Niobate Crystals Doped with Iron by Thermal Diffusion: Relation Between Lattice Deformation and Reduction Degree”, *J. Appl. Phys.* 107, pp. 084108/1-084108/5 (2010).
49. L. Kovacs, G. Ruschhaupt, K. Polgar, G. Corradi, and M. Wöhlecke, “Composition Dependence of the Ultraviolet Absorption Edge in Lithium Niobate”, *Appl. Phys. Lett.* Vol. 70, No. 21, pp. 2801-2803 (1997).
50. F. Träger, “Handbook of Lasers and Optics”, Springer, 2007.
51. D. Berben, K. Buse, S. Wevering, P. Herth, M. Imlau, and Th. Woike, “Lifetime of Small Polarons in Iron-Doped Lithium–Niobate Crystals”, *J. Appl. Phys.* Vol. 87, No. 3, pp. 1034-1041 (2000).
52. H. Kurz, E. Kratzig, W. Keune, H. Engelmann, U. Gonser, B. Dischler, and A. Rauber, “Photorefractive Centers in LiNbO<sub>3</sub>, Studied by Optical-, Mossbauer- and EPR-methods”, *J. Appl. Phys.*, Vol. 12, No. 4, pp. 355–368 (1977).
53. K. Peithmann, A. Wiebrock, and K. Buse, Photorefractive Properties of Highly-doped Lithium Niobate Crystals in the Visible and Near-infrared, *Appl. Phys. B*, Vol. 68, No. 5, pp. 777–784 (1999).

# Chapter 3.

## Electro-optical Properties

## Chapter 3. Electro-optical properties

### *Electro-Optic Effect*

The electro-optic effect is the application of an external electric field to a medium creates the electric dipole due to the displacement of the ions in the lattice and the electron orbits from their orientations and positions [1, 2]. This effect referred to us as the electro-optic (EO) effect can be represented as a variation of the optical dielectric properties of a material (commonly change of the refraction index) due to an applied electric field which results to the redistribution of the bond charges and the possibility of a slight deformation in the ion lattice (manifesting as the electric polarization  $\mathbf{P}$ ). According to the quantum theory of solids, the optical dielectric impermeability tensor depends on the charge distribution in the crystal. Thus, the electro-optic effect is a variation of the  $\Delta\mathbf{B}_{ij}$  components of the impermeability tensor  $\mathbf{B}$  being proportional to an electric field:

$$\mathbf{B}_{ij} = \left(\frac{1}{\varepsilon}\right)_{ij} = \left(\frac{1}{n^2}\right)_{ij} \quad (3.1).$$

Here  $\varepsilon$ -dielectric permittivity of the crystal and  $n$ -refractive index. The directions of the polarization as well as the corresponding refractive indices (i.e. the propagation velocity) of normal modes are most easily characterized using the index ellipsoid. The index ellipsoid is assumed to be the simplest form in the principle coordinate system:

$$\frac{x^2}{n_x^2} + \frac{y^2}{n_y^2} + \frac{z^2}{n_z^2} = 1 \quad (3.2),$$

where the  $x, y, z$  directions are the principle axes.  $\frac{1}{n_x^2}, \frac{1}{n_y^2}, \frac{1}{n_z^2}$  are principal values of the impermeability tensor  $\mathbf{B}_{ij}$ . The electro-optic coefficients are determined traditionally as [1, 3, 4]:

$$\Delta\mathbf{B}_{ij}(\mathbf{E}) - \mathbf{B}_{ij}(0) \equiv \Delta\mathbf{B}_{ij} = r_{ijk}\mathbf{E}_k + s_{ijkl}\mathbf{E}_k\mathbf{E}_l = f_{ijkl}\mathbf{P}_k + g_{ijkl}\mathbf{P}_k\mathbf{P}_l \quad (3.3),$$

where  $\mathbf{E}$  and  $\mathbf{P}$  are vectors describing the applied electric and the polarization fields respectively,  $i, j, k$  are the Cartesian indices running from 1 to 3 .

The constants  $r_{ijk}$  and  $f_{ijk}$  are the linear (or Pockels) electro-optic and polarization-optic coefficients, whereas  $s_{ijkl}$  and  $g_{ijkl}$  are correspondingly the quadratic electro-optic and polarization-optic coefficients (or Kerr). The quadratic EO effect was discovered first in 1875 by J. Kerr, in optically isotropic media such as liquids and glasses. The Kerr quadratic EO effect

in liquids is associated mostly with the alignment of the anisotropic molecules with the presence of an electric field. The linear electro-optic effect was first investigated by F. Pockels in 1893. As the dielectric tensor  $\varepsilon_{ij}$  is a symmetric tensor, thus,  $\mathbf{B}_{ij}$  must also be a symmetric tensor, and therefore indices  $i$  and  $j$  may be permuted. As it was mentioned above that the electro-optic effect is due to the redistribution of charges related to the application of a dc electric field, it may be expected that EO effect depends not only of the applied external field, but also to the interatomic electric field binding the charge particles such as electrons and ions. In general, in the most practical EO applications, the applied external electric field is smaller compared to the electric field induced inside the atoms, which is typically in order of  $10^8 \text{ V/cm}$ . As an expected result, the quadratic effect is often neglected due to the lower value compared to the linear effect when it is present [5]. However, in crystals with centrosymmetric point groups, the linear EO effect disappears resulting to the domination of the quadratic effect. It is vice versa in EO crystal where the quadratic effect is usually neglected because of smaller value comparing to the linear effect.

As  $\mathbf{B}$  is a symmetric tensor, the indices  $i$  and  $j$  can be inverted, thus, it is conventional to introduced contracted index numbers defined as  $\{m = ij\} = \{1=11, 2=22, 3=33, 4=23=32, 5=13=31, 6=12=21\}$  [6]. This relationship leads to the existence of 18 independent components of  $r_{mp} = r_{ijp}$  for the linear tensor. Taking into account the point group symmetry of the crystal the form of the EO liner tensor usually can be derived.

The refractive indices of the normal modes are defined by using index ellipsoid as:

$$\mathbf{B}_{ij}x_i x_j = (x_1^2/n_1^2) + (x_2^2/n_2^2) + (x_3^2/n_3^2) = 1 \quad (3.4),$$

where  $x_1, x_2, x_3$  are principal axes of the crystal without the electric field and  $1/n_1^2, 1/n_2^2, 1/n_3^2$  are values of the impermeability tensor  $\mathbf{B}$ . In the case of applied electric field  $\mathbf{E}_p$  ( $p = 1, 2, 3$ ), the expression of the perturbed ellipsoid can be rewritten and will have the next form:

$$\begin{aligned} \mathbf{B}_{ij}(\mathbf{E})x_i x_j = & \left( \frac{1}{n_1^2} + r_{1p}\mathbf{E}_p \right) x_1^2 + \left( \frac{1}{n_2^2} + r_{2p}\mathbf{E}_p \right) x_2^2 + \left( \frac{1}{n_3^2} + r_{3p}\mathbf{E}_p \right) x_3^2 + \\ & + 2x_2 x_3 r_{4p}\mathbf{E}_p + 2x_1 x_3 r_{5p}\mathbf{E}_p + 2x_1 x_2 r_{6p}\mathbf{E}_p = 1 \end{aligned} \quad (3.5)$$

New axis of the perturbed ellipsoid also can be determined from the Eq. 3.2 when their dimensions and orientations depend on the direction of the applied field and the EO coefficients  $r_{mp}$ . As function of the non-zero elements of the EO tensor, the applied electric field can induce the two types of contributions of the perturbed index ellipsoid described by Eq. 3.5. At first, the voltage can generate a variation of the length of the semi-axes, when exists  $r_{mp}$  coefficient with  $m = 1, 2, 3$  ( $m=ii=jj$ ). Thus, the components of the impermeability tensor can be presented as:

$$\mathbf{B}_{ii} = \frac{1}{n_i^2} + r_{iip}\mathbf{E}_p \quad (3.6),$$

$$\mathbf{B}_{jj} = \frac{1}{n_j^2} + r_{jjp}\mathbf{E}_p \quad (3.7).$$

At second, an external electric field can generate a rotation of the principal axes when exists  $r_{mp}$  coefficients with  $m = 4, 5$  or  $6$  ( $m = i \neq j$ ). Thus, the crossed component of the impermeability tensor can be defined by the following expression:

$$\mathbf{B}_{ij} = r_{ijp}\mathbf{E}_p \quad (3.8).$$

When the beam propagates along the  $x_k$  axis ( $k = 1, 2, 3$ ), and is polarized in the  $x_i, x_j$  plane, where  $i \neq j \neq k$ , the solution of the Eq. 3.5 is found to be:

$$\mathbf{B}_{ii}x_i^2 + \mathbf{B}_{jj}x_j^2 + 2\mathbf{B}_{ij}x_ix_j = 1 \quad (3.9).$$

In order to transform Eq. 3.1.9 into a diagonal form, it is worthy to choose a new coordinate system  $x'_i, x'_j, x'_k$  with  $x_k = x'_k$ . Thus, to obtain this diagonal form, the transformation from  $x_i, x_j$  to  $x'_i, x'_j$  have to be expressed as:

$$x_i = x'_i \cos\alpha_{ij} - x'_j \sin\alpha_{ij} \quad (3.10),$$

$$x_j = x'_i \sin\alpha_{ij} + x'_j \cos\alpha_{ij} \quad (3.11),$$

where the angle  $\alpha_{ij}$  is defined as:

$$\tan(2\alpha_{ij}) = 2\mathbf{B}_{ij}/(\mathbf{B}_{ii} - \mathbf{B}_{jj}) \quad (3.12).$$

Replacing Eqs. 3.10 and 3.11 into the Eq. 3.9 for  $x_i, x_j$  system, taking the vanish of the  $\mathbf{B}_{ij}$  component of the impermeability tensor into account, the diagonal form can be found:

$$\mathbf{B}_{ii}' = (1/n_i')^2 = \mathbf{B}_{ii} + \mathbf{B}_{ij}\tan(\alpha_{ij}) \quad (3.13),$$

$$\mathbf{B}_{jj}' = (1/n_j')^2 = \mathbf{B}_{jj} - \mathbf{B}_{ij}\tan(\alpha_{ij}) \quad (3.14).$$

It is worth noting that the absolute or relative values of components  $\mathbf{B}_{ij}$  and  $\mathbf{B}_{jj} - \mathbf{B}_{ij}$  depend on the symmetry class and the optogeometric configuration of the crystal linked to the applied field and beam propagation directions. Moreover, it is also noted that the variation of the refractive index  $\delta n$  via the electro-optical effect is smaller compared to the refractive index value. Thus, the differential relation can be simplified as:

$$\delta n = -\left(\frac{1}{2}\right)n^3\delta(1/n^2) \quad (3.15).$$

According to the absolute or relative values of components  $\mathbf{B}_{ij}$  and  $\mathbf{B}_{jj} - \mathbf{B}_{ij}$  three cases can be found in Eq. 3.12 resulting the three different values of angle  $\alpha_{ij}$ .

For the first case the component  $\mathbf{B}_{ij}$  (Eq. 3.8) is zero or negligible comparing to the  $\mathbf{B}_{ii}$  and  $\mathbf{B}_{jj}$  leading to the absence of a rotation of the ellipsoid. The new values of refraction indices are determined due to the Eqs. 3.6, 3.7 and 3.15 as:

$$n_i' = n_i - (1/2)n_i^3 r_{iip} \mathbf{E}_p \quad (3.16),$$

$$n_j' = n_j - (1/2)n_j^3 r_{j jp} \mathbf{E}_p \quad (3.17).$$

Thus, when the polarization of the propagated beam along  $x_k$  is at 45° of the axis  $x_i$  and  $x_j$  the beam birefringence is expressed as:

$$\Delta n = \Delta n_{ij}' = n_j' - n_i' = \Delta n_{ij} - \left(\frac{1}{2}\right)(n_j^3 r_{j jp} - n_i^3 r_{i ip}) \mathbf{E}_p \quad (3.18).$$

In Eq. 3.18 the first term  $\Delta n_{ij}$  expresses the spontaneous or natural birefringence and the second term represents the birefringence due to the electric field.

According the above mentioned the effective combined electro-optic coefficient  $r$  is usually determined as:

$$r = r_{j jp} - \left(\frac{n_i^3}{n_j^3}\right)r_{i ip} \quad (3.19).$$

The second case exists in an uniaxial environment when  $\mathbf{B}_{ii}=\mathbf{B}_{jj}$  provided by  $\alpha_{ij} = \pi/4$ , when the direction of the beam is perpendicular to the isotropic plane of the unperturbed index ellipsoid defined by  $n_j = n_0$ , where  $n_0$  is the ordinary refractive index. For this configuration the new values of the refractive indices according to the Eqs. 3.6 and 3.7 equations can be obtained by using the differential expression 3.1.15:

$$n'_i, n'_j = n_{ij} \pm (1/2)n_i^3 r_{ijp} \mathbf{E}_p \quad (3.20).$$

The beam birefringence is determined as:

$$\Delta n = \Delta n'_{ij} = \Delta n_{ij} - n_i^3 r_{ijp} \mathbf{E}_p \quad (3.21).$$

In this case, the effective electro-optic coefficient  $r$  is equal to the crossed electro-optic coefficient  $r_{ijp}$ .

Finally, the third case, exists when the difference between components  $\mathbf{B}_{ii}$  and  $\mathbf{B}_{jj}$  is high and  $\tan(2\alpha_{ij}) = 2\alpha_{ij}$ . This approach is also valid for high voltage and thus, Eqs. 3.13 and 3.14 for the diagonal form can be rewritten as:

$$\mathbf{B}'_{ii} = \mathbf{B}_{ii} + \mathbf{B}_{ij}^2 / (\mathbf{B}_{ii} - \mathbf{B}_{jj}) \quad (3.22),$$

$$\mathbf{B}'_{jj} = \mathbf{B}_{jj} - \frac{\mathbf{B}_{ij}^2}{(\mathbf{B}_{ii} - \mathbf{B}_{jj})} \quad (3.23).$$

According to the Eqs. 3.6 and 3.7 the new values of the refractive indices for this configuration can be found again using the differential Eq. 3.15:

$$n'_i = n_i - \left(\frac{1}{2}\right) n_i^3 r_{iip} \mathbf{E}_p + n_i^3 / 2 \left(\frac{n_i^2 n_j^2}{n_i^2 - n_j^2}\right) r_{ijp}^2 \mathbf{E}_p^2 \quad (3.24),$$

$$n'_j = n_j - \left(\frac{1}{2}\right) n_j^3 r_{jjp} \mathbf{E}_p + n_j^3 / 2 \left(\frac{n_i^2 n_j^2}{n_i^2 - n_j^2}\right) r_{ijp}^2 \mathbf{E}_p^2 \quad (3.25).$$

For the third case the beam birefringence can be expressed as:

$$\Delta n = \Delta n_{ij} - \left(\frac{1}{2}\right) n_j^3 (r_{jjp} - (n_i^3 / n_j^3) r_{iip}) \mathbf{E}_p - \left(\frac{1}{2}\right) n^3 r_{ijp}^2 \mathbf{E}_p^2 \quad (3.26),$$

where

$$n^3 = (n_i^3 + n_j^3) \left(\frac{n_i^2 n_j^2}{n_i^2 - n_j^2}\right) \quad (3.27).$$

Eq. 3.26 illustrates that the linear electro-optic effect considering the variation in the birefringence keeps linear and quadratic dependences on quantity  $E_p$ . However, the variation in the birefringence depends only quadratically on the parameter  $E_p$ , when the diagonal coefficients  $r_{iip}$  and  $r_{jjp}$  are equal to zero. We can note that this quadratic dependence with the field is due to the linear electro-optic effect, and not the quadratic or Kerr effect. This configuration is not advantageous for modulation applications but have to be carefully considered in experimental characterizations.

### ***Electro-Optic Effect in Lithium Niobate (LN) Crystals***

LN is a material that is well known for its large EO coefficients and it is used in numerous devices, such as modulators, deflectors and switches. Owing to its high optical quality and properties, and beyond the need to know its own electro-optical properties depending on the composition and doping, on the one hand and external parameters such as the frequency of the electric field, the intensity and the laser wavelength, on the other hand, LN constitutes a reference material for the general study of electro-optical properties of dielectric crystals. As it was mentioned the LN crystal is an optically uniaxial rhomboedral crystal with point-group  $C_{3V} = 3m$  symmetry and its EO properties can be described by the linear tensor  $r$ , so the EO coefficients are in the form allowing to describe electro-optic properties by a linear tensor [1]:

$$r = \begin{pmatrix} 0 & -r_{22} & r_{13} \\ 0 & r_{22} & r_{13} \\ 0 & 0 & r_{33} \\ 0 & -r_{51} & 0 \\ r_{51} & 0 & 0 \\ -r_{22} & 0 & 0 \end{pmatrix} \quad (3.28).$$

where the four non-zero elements in contracted notation [7] are  $r_{13} = r_{23}$   $r_{22} = -r_{12} = -r_{61}$ ,  $r_{51} = r_{42}$ ,  $r_{33}$ .

When the electric field is applied along the crystallographic c axis of the crystal the index ellipsoid (Eq. 3.2) can be written:

$$x^2 \left( \frac{1}{n_o^2} + r_{13}E \right) + y^2 \left( \frac{1}{n_o^2} + r_{13}E \right) + z^2 \left( \frac{1}{n_e^2} + r_{13}E \right) = 1 \quad (3.29),$$

where ordinary ( $n_o$ ) and extraordinary ( $n_e$ ) refractive indices are related to optical beams polarized parallel to the z axis and to the x (y axes) of the crystal respectively respectively. The principal new axes of the new index ellipsoid remain unchanged. The lengths of the new semi axis can be expressed as:

$$n_x = n_0 - \frac{1}{2}n_0^3r_{13}E \quad (3.30),$$

$$n_y = n_0 - \frac{1}{2}n_0^3r_{13}E \quad (3.31),$$

$$n_z = n_e - \frac{1}{2}n_e^3r_{13}E \quad (3.32).$$

It should be noticed, that under the influence of electric field in the direction parallel to  $c$  axis, the crystal remains uniaxially anisotropic. Moreover, when a light beam propagates along the  $x$  axis, the beam birefringence can be reported as:

$$n_z - n_y = (n_e - n_0) - \frac{1}{2}(n_e^3r_{13} - n_0^3r_{13})E \quad (3.33).$$

### *Electro-Optic Phase Shift*

In birefringent crystals, the light propagation can be represented as a linear superposition of two single waves, such as the ordinary and extraordinary wave. The polarization directions for these eigen light waves are mutually orthogonal and are referred as "slow" and "fast" axes of the crystal for that propagation direction. The phase retardation can be expressed by the difference of components  $n_s$  and  $n_f$ :

$$\Gamma = (n_s - n_f) \frac{\omega L}{c} = \left(\frac{2\pi}{\lambda}\right) \Delta n \quad (3.34),$$

where  $n_s$  and  $n_f$  are refractive indices for "slow" and "fast" components respectively,  $\Delta n = n_s - n_f$  is the total birefringence of the crystal in the direction which is considered as a function of the involved effective EO coefficient regardless of the crystal symmetry and the geometrical configuration.  $\lambda_0$  is the wavelength of light beam in the vacuum,  $\omega$ - angular velocity and  $c$ -the light speed in vacuum,  $L$ -the length of the crystal.

When an electric field  $E$  is applied onto the sample (assumed to exhibit linear EO coefficients), the birefringence can be written as [8]:

$$\Delta n = \Delta n(0) + \Delta n(E) \quad (3.35),$$

where  $\Delta n(0)$  presents the spontaneous (or natural) birefringence, whereas  $\Delta n(E)$  is the external field-induced (or EO) birefringence [8, 9]. The electro-optic change in refractive index, equal to the difference of the refractive indices with and without an applied electric field onto the sample respectively, can be presented as [9, 10]:

$$\Delta n(E) = \frac{1}{2}n^3rE \quad (3.36).$$

Thus, the total phase retardation of the sample submitted to an external field  $E$  can be expressed:

$$\Gamma = \Gamma(0) + \Gamma(E) \quad (3.37),$$

where  $\Gamma(0)$  is the natural retardation due to the natural birefringence  $\Delta n(0)$  and  $\Gamma(E)$  is the electro-optic retardation generated by the electric field.

In general, to produce an external electric field  $E$ , two electrodes set in contact with two faces of the sample placed at a distance  $d$ , that when assuming that no (air) gap exists between electrode and sample,  $d$  correspond to the width of the sample. Consequently applying a voltage  $V$  to the sample via the electrodes it will hold  $E = V/d$ . Therefore the retardation induced by an applied electric field can be obtained as:

$$\Gamma(E) = \left(\frac{\pi}{\lambda_0}\right) L n^3 r E = \pi \left(\frac{V}{V_\pi}\right) \quad (3.38).$$

Where the half-wave voltage  $V_\pi$  is the corresponding voltage producing an EO phase shift  $\Gamma(E) = \pi$  expressed as:

$$V_\pi = \left(\frac{\lambda_0}{n^3 r}\right) \left(\frac{d}{L}\right) \quad (3.39).$$

$L$  is the length of the crystal along the beam-propagation direction,  $d$  is the sample thickness along the applied electric field direction,  $n$  is the refractive index corresponding to the propagation direction,  $\lambda_0$  is the beam wavelength.

### ***Dielectric properties of lithium niobate***

As mentioned above, LN crystal is an optically uniaxial rhomboedral crystal with point-group  $C_{3V} = 3m$  symmetry [1], the induced polarization  $\mathbf{P}$  depends on the direction and magnitude of an applied  $\mathbf{E}$  field by the expression:

$$\begin{aligned} P_x &= \varepsilon_0 (\chi_{11} E_x + \chi_{12} E_y + \chi_{13} E_z) \\ P_y &= \varepsilon_0 (\chi_{21} E_x + \chi_{22} E_y + \chi_{23} E_z) \end{aligned} \quad (3.40),$$

$$P_z = \varepsilon_0(\chi_{31}E_x + \chi_{32}E_y + \chi_{33}E_z)$$

where  $\varepsilon_0$  is free space permittivity. The magnitude of the electric susceptibility tensor  $\chi_{ij}$  with 3×3 array depends on the choice of the  $x, y, z$  axes relative to the crystal structure. Thus, the polarization depending on the direction can be expressed:

$$P_x = \varepsilon_0\chi_{11}E_x$$

$$P_y = \varepsilon_0\chi_{22}E_y \quad (3.41).$$

$$P_z = \varepsilon_0\chi_{33}E_z$$

These  $x, y, z$  directions are referred as the principle dielectric axes of the crystal. The dielectric response of the crystal characterized by the dielectric permittivity tensor  $\varepsilon_{ij}$ , is defined by:

$$D_x = \varepsilon_{11}E_x + \varepsilon_{12}E_y + \varepsilon_{13}E_z$$

$$D_y = \varepsilon_{21}E_x + \varepsilon_{22}E_y + \varepsilon_{23}E_z \quad (3.42).$$

$$D_z = \varepsilon_{31}E_x + \varepsilon_{32}E_y + \varepsilon_{33}E_z$$

Assuming

$$\mathbf{D} = \varepsilon_0\mathbf{E} + \mathbf{P} \quad (3.43),$$

and

$$\varepsilon_{ij} = \varepsilon_0(1 + \chi_{ij}) \quad (3.44).$$

Thus, Eq. 3.1.2.4 can be recorded in a tensor as:

$$D_i = \varepsilon_{ij}E_j \quad (3.45).$$

Taking into account the crystallographic structure and the symmetry properties of LN crystal, the dielectric permittivity tensor, in the orthogonal cell, can be written in a form of a  $3 \times 3$  matrix. Nine quantities  $\varepsilon_{11}, \varepsilon_{12}, \dots$  are values of dielectric permittivity of the medium and constitute the dielectric tensor, where only diagonal components exhibit non zero values:

$$\varepsilon = \begin{pmatrix} \varepsilon_{11} & 0 & 0 \\ 0 & \varepsilon_{22} & 0 \\ 0 & 0 & \varepsilon_{33} \end{pmatrix} \quad 3.46.$$

Assuming the properties of uniaxial rhomboedral crystal related to the fact that in the range of optical frequencies the dielectric permittivity of a media is characterized in the terms of refractive index of this matter:  $n = \sqrt{\varepsilon}$ , for LN crystal  $\varepsilon_{11} = \varepsilon_{22}$ .

### ***Permittivity related Polarization Effects in Dielectric Materials***

Generally, several mechanisms or polarization effects related to their overall permittivity occur in dielectric materials. These mechanisms are summarized as function of their frequency in Figure 3.1. It is to be of note that, as EO coefficients are closely linked to the dielectric properties of materials, they follow the same evolutions with the frequency range considered in the material [11, 12]. An arrangement of electric charge carriers exists in a dielectric substance which can be displaced by an applied electric field. To compensate the electric field the charge carriers become polarized resulting to the movement of the positive and negative charges in opposite to each other directions [13]. At the microscopic level, in general three dielectric mechanisms contribute to the dielectric behavior (see Figure 3.1). Dipole orientation and ionic conduction dominate strongly at microwave frequencies. Atomic and electronic mechanisms are relatively weak, and assumed to be constant in the microwave range. Each dielectric mechanism has a characteristic “cutoff frequency.” The magnitude and characteristic “cutoff frequency” of each mechanism is unique for different materials.

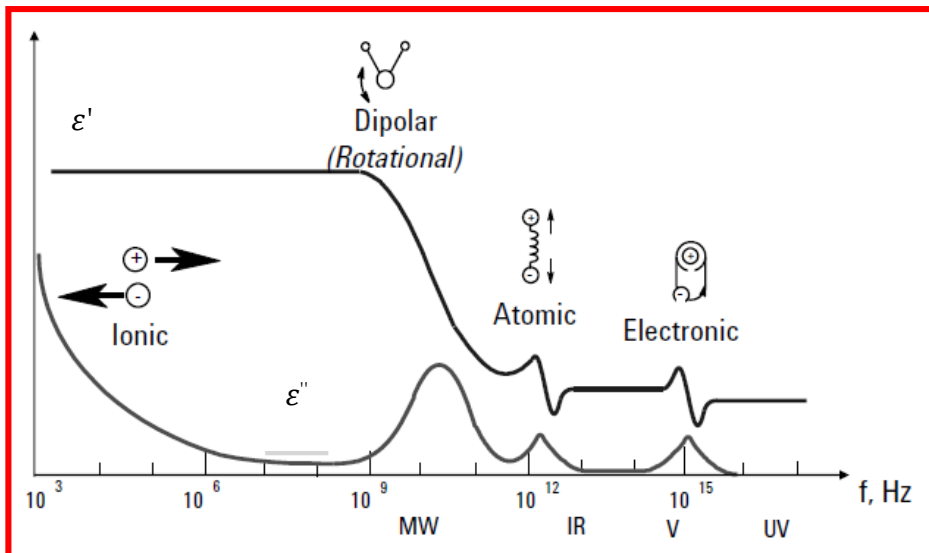


Figure 3.1: Frequency response of dielectric mechanisms.

The complex dielectric constant  $\epsilon = \epsilon' - j\epsilon''$  consists of a real  $\epsilon'$  and an imaginary  $\epsilon''$  parts related to the storage and the loss of the external electric field, respectively. The imaginary part of permittivity ( $\epsilon''$ ) being greater than zero whereas usually has a value much smaller comparing to the real part ( $\epsilon'$ ). The loss factor contains the effects contributed to the dielectric loss and conductivity. Drawing the complex permittivity as a simple vector diagram (Figure 3. 2), the real and imaginary components are  $90^\circ$  out of phase.

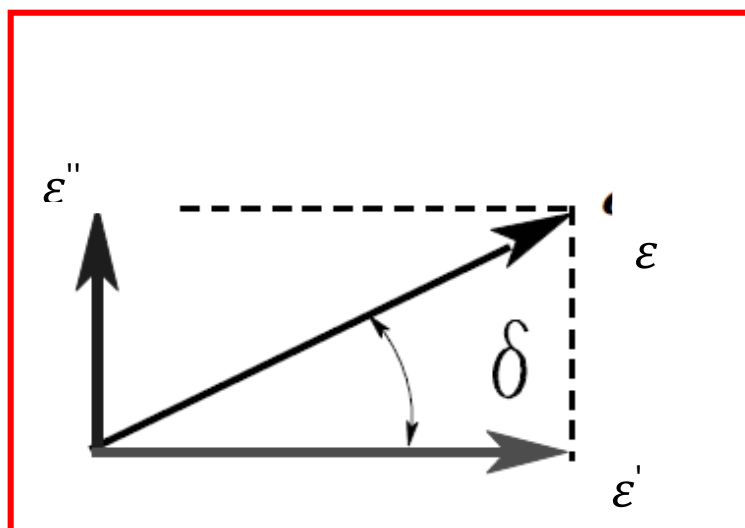


Figure 3.2: Loss tangent vector diagram.

The vector sum produces an angle  $\delta$  with the real axis ( $\epsilon'$ ). The relative “lossiness” of a material is the ratio of the energy lost to the energy stored. The loss tangent or dissipation factor ( $\tan \delta$ ) is determined as a ratio of the imaginary part of the dielectric constant to the real part:  $\tan \delta = \epsilon''/\epsilon'$ . For materials with tiny losses, since  $\tan \delta \approx \delta$ , thus, the loss tangent is expressed in angle units, milliradians or microradians.

With the increase of frequency, the slow mechanisms fall out in turn, leaving the faster ones contributing to  $\epsilon'$ . The loss factor ( $\epsilon''$ ) reaches peak value at each critical frequency. A resonance effect is usually associated with the electronic or atomic polarization whereas a relaxation effect is related to the orientation polarization.

### Orientation (dipolar) polarization.

In order to share one or more of their electrons the atoms combine resulting to the formation of molecule. This electrons rearrangement produces an imbalance in the charge distribution resulting to a permanent dipole moment in its turn. In the absence of an electric field these moments are oriented randomly consequently leading the absence of the polarization. The external electric field  $E$  realizes a torque  $T$  on the electric dipole shown in Figure 3.3, resulting the rotation of the dipole in order to align with the electric field causing the appearance of the orientation polarization. The torque also changes with the variation of the field direction.

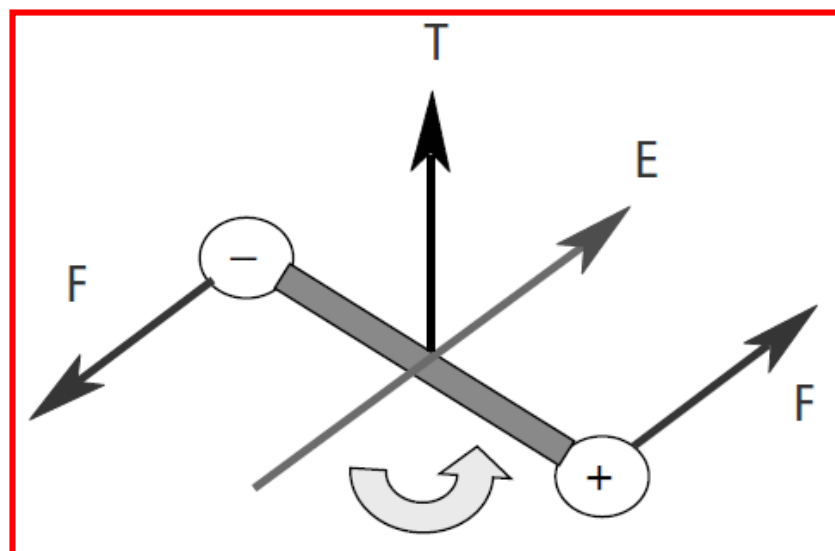


Figure 3.3: Dipole rotation in electric field.

The friction accompanying the orientation of the dipole contributes to the dielectric losses. The dipole rotation generates a variation of both  $\varepsilon'$  and  $\varepsilon''$  at the relaxation frequency usually being in the microwave frequency range.

### **Electronic and atomic polarization.**

Electronic polarization exists in neutral atoms if an applied electric field displaces the nucleus with respect to the surrounding electrons. However atomic polarization can be found when adjacent ions with positive and negative charges “stretch” under the influence of an external electric field. In the infrared and the visible light ranges the momentum of the orbiting electrons should be taken into account. Usually atoms may be modeled as oscillators with a damping effect which is similar to a mass system and mechanical spring. For different frequency values the amplitude of the oscillations is smaller than for the resonant frequency. Far below resonant frequency, the electronic and atomic polarizations are almost lossless as contribute only to a small constant amount of  $\varepsilon'$ . The resonant frequency is determined by a resonant response in factor  $\varepsilon'$  and by a peak of maximum absorption in factor  $\varepsilon''$ . Above the resonant frequency, the contribution of these mechanisms vanishes.

### ***Relationship between linear electro-optic coefficients and dielectric permittivity***

In piezo-electric crystals the relationship between electro-optic and dielectric properties is expressed as [14]:

$$d\varepsilon_{ij} = -\sum_k r_{ijk}(\omega)\varepsilon_{ii}\varepsilon_{jj}dE_k(\omega) \quad (3.47),$$

where  $E_k$ -is the component of the applied electric field tensor E depending on the frequency,  $r_{ijk}$ -component of EO tensor with the third rank,  $\varepsilon_{ii}$ ,  $\varepsilon_{jj}$ -components of dielectric permittivity tensor in optical frequency range. The difference between the values of dielectric permittivity for low and high frequency on both sides of piezo-electric resonances can be reported:

$$\Delta\varepsilon_{ij} = \varepsilon_{ij}^T - \varepsilon_{ij}^S = \sum_{kl} d_{ij,k}e_{kl} = \sum_{kl} d_{ij,k}C_{ijkl}^E d_{l,ij} \quad (3.48).$$

$\varepsilon_{ij}^T$ -unclamped dielectric coefficient in low frequency range including constant stress,  $\varepsilon_{ij}^S$ -clamped dielectric permittivity at high frequency containing constant strain,  $d_{ij,k}$ - component of piezo-electric tensor,  $e_{kl}$ -component of inverse piezo-electric tensor.

In low frequency range the crystal deformation is related to the mechanical contribution (Eq. 3.48), whereas in high frequency range the crystal is deformed via the piezo-electric effect due to the applied electric voltage (Eq. 3.49) [36, 44] :

$$r_{ijk}^S = \sum_{mn} P_{ijmn} \delta_{mnk} \quad (3.48),$$

$$r_{ijk}^T = r_{ijk}^S + \Delta r_{ijk}^d \quad (3.49),$$

where  $P_{ijmn}$  and  $\delta_{mnk}$  are elasto-optic and piezo-optic coefficients respectively, clamped EO coefficient  $r_{ijk}^S$  is attributed by ionic and electronic contributions [3, 12].

According to investigations reported in [3] the acoustic contribution to the EO coefficients can be estimated via elasto-optic (Pockels) coefficients  $P_{ijkl}^E$  at the stable electric field and the piezoelectric tensors  $d_{kij}$ , as well as the electro-mechanical contribution to the static permittivity  $\Delta\varepsilon_{ij} = \varepsilon^T - \varepsilon^S$  with the help of piezo-electric stress tensor  $e_T$ ,  $C^E$  elastic tensor at the stable electric field. Piezo-optic contribution  $\Delta r_{ijk}^a$  on both parts of acoustic resonances is recorded as:

$$\Delta r_{ijk}^a = \sum_{lm} P_{ij,lm}^S d_{lm,k} \quad (3.50).$$

$P^S$  is referred as the elasto-optic tensor (constant strain at high frequency). Taking photo-elastic tensor  $\pi$  (constant stress at low frequency) and elastic constant  $C$  into account, the piezo-optic contribution is expressed as:

$$\Delta r_{ijk}^d = \sum_{r,s,lm} \pi_{ij,rs} C_{rs,lm} d_{lm,k} \quad (3.51).$$

As LN crystals belong to the point group  $3m$  [7], the piezo-electric tensor  $d$ , elastic constant  $C$ , photo-elastic tensor  $\pi$ , elasto-optic tensor  $P$ , EO tensor  $r$  illustrate the symmetric properties thus, the electro-mechanical contribution to dielectric permittivity can be obtained with the help of Neumann's principles:

$$\Delta\varepsilon_{22} = 2d_{22}^2(C_{11}^E - C_{12}^E) - 4d_{22}d_{15}C_{14}^E + d_{15}^2C_{44}^E \quad (3.52).$$

The piezo-optic contribution to EO coefficient in  $r_{222}$  opto-geometric configuration can be reported as:

$$\Delta r_{222}^d = \pi_{14}C_{44}d_{15} - (\pi_{11} - \pi_{12})[(C_{11} - C_{12})d_{22} + C_{14}d_{15}] \quad (3.53),$$

or

$$r_{222}^d = -(p_{11}^E - p_{12}^E)d_{22} + p_{14}^E d_{15} \quad (3.54).$$

### ***Literature Review of the investigation of electro-optic (EO) effect in LN crystals***

First observations of the linear electro-optic coefficients have been explored for pure congruent LN crystals [15-21]. The experimental results of electro-optic coefficients obtained by using the different techniques are given in Table 3.1.

#### **EO coefficients in pure congruent LN crystals.**

For the first time in 1964, G. E. Peterson et al. recorded "patches switching" by investigated high-frequency electro-optic effect of multi domain LN crystals growth by Czochralski technique whereas the nature of the patches induced by the electric field were not clear at that time [15]. However, this patches were not obtained in the case of the quantitative low-frequency measurements for electro-optic coefficients  $r_{22}$  and  $|0.9r_{33}-r_{13}|$  in single-domain crystals performed by P. V. Lenzo et al [16]. The main electro-optic coefficients ( $r_{22}$ ,  $r_{61}$ , and  $r_c$ ) over a wide frequency range for pure congruent LN crystals illustrated compliance comparing together and with literature results [18-20]. For the first time Kaminow and Johnston [21] calculated the values of the EO coefficients by using the combined Raman, infrared, second-harmonic-generation data and comparing to the results measured directly by Turner [17] the dependence on frequency was recorded in the case of EO coefficient  $r_{22}$  when for the EO coefficients  $r_{13}$ ,  $r_{33}$  the frequency dependence was not detected.

#### **EO coefficients in pure LN crystals as a function of composition.**

The investigation of electro-optic coefficients for different compositions of pure LN crystals had shown a dependence of this parameters on the Li content which is associated with the concentration of intrinsic defects related to the deviation from stoichiometry to the sub-congruent[20, 22-25] (Table 3.1). Particularly,  $r_{33}$  increases with the increase of crystal stoichiometry and exhibits 20% larger value in stoichiometric crystal, whereas  $r_{13}$  has probably the same value as in congruent crystal [23, 25]:  $r_{33}=38.3\text{pmV}^{-1}$ ,  $r_{13}=10.4\text{pmV}^{-1}$  for stoichiometric crystal, and  $r_{33}=31.5\text{pmV}^{-1}$ ,  $r_{13}=10.4\text{pmV}^{-1}$  for congruent crystal[23]. However, the unclamped

values of third column are smaller in quasi-stoichiometric crystal compared to the congruent crystal [22, 24]:  $r_{33}=29.4\text{pmV}^{-1}$ ,  $r_{13}=9.25\text{pmV}^{-1}$  for quasi stoichiometric crystal and  $r_{33}=31.4\text{pmV}^{-1}$ ,  $r_{13}=10.49\text{pmV}^{-1}$  for congruent crystal. Combined EO coefficient  $r_c$  indicates non monotonous dependence on the crystal composition explored for crystals grown from the congruent melt ( $X_c=48.46\%$ ) by adding different content of  $K_2O$  to the melt to vary the stoichiometry in crystal [26]:  $r_c=20.4\text{pmV}^{-1}$  for congruent crystal, then it decreases again  $r_c=17.9\text{pmV}^{-1}$  for  $X_c=49.5\%$  crystal, then increases again for stoichiometric crystal  $r_c=19.9\text{pmV}^{-1}$ . EO coefficient indicates also strongly non symmetric dependence [20]:  $r_{22}=6.07\text{pmV}^{-1}$  for congruent crystal, then it decreases up to  $r_{22}=1.51\text{pmV}^{-1}$  for  $X_c=48.09\%$  composition, then increases again  $r_{22}=1.97\text{pmV}^{-1}$  starting from intermediary composition ( $X_c=49.09\%$ ). The largest value  $r_{22}$  demonstrates  $r_{22}=9.89\text{pmV}^{-1}$  for near stoichiometric crystal.

The origin of the absence of minimum value for  $r_{33}$  may be due to the specific anisotropy of electron-phonon interaction for particular EO tensor components [25]. At the first time the minimized value was related to the modification of the elastic constant [20] and later to the non-centrosymmetry in the electroelastic potential distribution around Nb-O<sub>6</sub> clusters which gives more than 50% contribution to the  $r_{22}$  [27]. Later, to give an explanation of the non symmetry variation of EO coefficients for mentioned pure crystal a new model of intrinsic defects was proposed by F. Abdi, M. Aillerie and the others [28] since existing several models not able to describe the complicated dependencies on the crystal composition shown by electro-optic coefficients. Due to the suggested two versions (Li and Nb vacancies model) of this new model when one kind of this vacancies disappears in the intermediate crystal, EO coefficients are affected by an amount and site occupation of niobium ions.

### **EO coefficients in non-photorefractive ions doped LN crystals**

Electro-optic properties illustrate a different variation behavior depending on the introduction and the concentration of non-photorefractive ions: divalent  $\text{Mg}^{2+}$  [29, 30, 31, 32] and  $\text{Zn}^{2+}$  [35-38], trivalent  $\text{In}^{3+}$  [39,40, 41], and  $\text{Sc}^{3+}$  [42] and tetravalent  $\text{Sc}^{4+}$  [43],  $\text{Hf}^{4+}$  [44-47] and  $\text{Zr}^{4+}$  [48].

Although the threshold concentration of magnesium was found to be about 5.5 mol%, whereas the exploration of the dependence of the electro-optic coefficients on the introduction and concentration of magnesium lead to the varied results obtained for the different series of

Mg:LN crystals [29, 30, 31, 32]: The introduction of Mg ions decreases EO coefficient  $r_{22}$  in congruent crystals:  $r_{22}=6.2 \text{ pmV}^{-1}$  in Mg:LN (5mol%) crystal when  $r_{22}=6.54 \text{ pmV}^{-1}$  in undoped crystal [29], especially by doping 6.1mol% Mg ions EO coefficient decreases about eight times:  $r_{22}=0.8 \text{ pmV}^{-1}$ [31]. The quasy stoichiometric crystals doped with smaller concentration (1.8 mol%) illustrate the bigger value:  $r_{22}=6.54 \text{ pmV}^{-1}$ [29], however the largest value of the electro-optic coefficient indicates 4 mol% Mg:LN crystals [32]. Mg:LN crystals doped with higher dopant concentration (10mol%) exhibit a comparability of third column of EO tensor to those in pure LN crystals [29]:  $r_{33}=36 \text{ pmV}^{-1}$ ,  $r_{13}=11.2 \text{ pmV}^{-1}$  in Mg:LN (10 mol%) and  $r_{33}=36.7 \text{ pmV}^{-1}$ ,  $r_{13}=11 \text{ pmV}^{-1}$  in undoped crystals. As well as EO coefficients  $r_{33}$ ,  $r_{13}$  decreases linearly with the decrease of Li content in LN crystals doped with the fixed Mg concentration (5mol%) [30]:  $r_{33}=34 \text{ pmV}^{-1}$ ,  $r_{13}=10.5 \text{ pmV}^{-1}$  in  $X_c=43.4\%$  Mg:LN,  $r_{33}=32.4 \text{ pmV}^{-1}$ ,  $r_{13}=9.8 \text{ pmV}^{-1}$  in  $X_c=43.9\%$  Mg:LN,  $r_{33}=30.6 \text{ pmV}^{-1}$ ,  $r_{13}=9.2 \text{ pmV}^{-1}$  in  $X_c=44.5\%$  LN:Mg. According to the defect model proposed by Grabmaier et al. [33] the increase of Mg concentration leads to the decrease of Nb antisites in Li sites varying the physical properties of LN:Mg: crystals as Mg ions incorporate onto Li sites. Above 4.5 mol% concentration Mg ions occupy both Li and Nb site accompanied by the decrease of Nb vacancies. Due to the other explanation [34] the oxygen octahedron is distorted with the increase of Mg concentration resulting to the change of physical properties of Mg doped LN crystal.

Due to the investigation, the EO coefficients  $r_c$ ,  $r_{22}$  illustrate a strong non-monotonic dependence on Zn content realized for Zn-doped LN crystals with the various doping concentration altering from 0 to 8 mol% [38]. For low Zn concentration EO coefficients decrease compared to the undoped LN crystal:  $r_{22}=3.5 \text{ pmV}^{-1}$ ,  $r_c=17 \text{ pmV}^{-1}$  for LN:Zn (2.87mol%), when  $r_{22}=6.3 \text{ pmV}^{-1}$ ,  $r_c=21 \text{ pmV}^{-1}$  for undoped crystal, due to the reduction of Li vacancies concentration related to the weaker deformability of  $NbO_6$  and  $LiO_6$  octahedras. EO coefficients reach their minimum value for the concentration of about 2 mol%, due to the lowest  $V_{Li}$  content. At higher Zn concentration the generation of new Li vacancies is accompanied by the increase of EO coefficients again indicated the highest value for 6.4mol.% Zn when  $V_{Li}$  concentration is the biggest:  $r_{22}=7.8 \text{ pmV}^{-1}$ ,  $r_c=25.5 \text{ pmV}^{-1}$ . Starting from 7.6mol.% concentration, Zn ions partially incorporate also on Nb site where the crystals illustrates a strong optical-damage-resistance:  $r_{22}=3.6 \text{ pmV}^{-1}$ ,  $r_c=20 \text{ pmV}^{-1}$  for LN:Zn (8.16mol%).

LN:Hf congruent crystals with different concentration of Hf ions (1mol%-5mol%) were used to investigate EO coefficients  $r_{33}$ ,  $r_{13}$ ,  $r_c$  and  $r_{22}$  as a function of the concentration of Hf ions [44-48]. Due to the results EO coefficients reveal a weak dependence on the Hf concentration of the crystals, which is attributed to the strain contribution related to the introduction of Hf ions. EO coefficient  $r_{33}$  exhibits values from 30 to 31  $\text{pmV}^{-1}$ , when  $r_{33}=32\text{pmV}^{-1}$  for pure LN as well as the coefficient  $r_{13}$  spanned from 8.9 to 9.5  $\text{pmV}^{-1}$ ,  $r_{13}=10\text{pmV}^{-1}$  for pure LN. The combined coefficient  $r_c$  varied from 19.3 to 20.7  $\text{pmV}^{-1}$  with the same trend of  $r_{33}$ , when  $r_c=21.5\text{pmV}^{-1}$  for pure LN. All EO coefficients reached their maximum values at the Hf concentration of 5 mol%:  $r_{13}=9.5\text{pmV}^{-1}$ ,  $r_{33}=31.7\text{pmV}^{-1}$ ,  $r_c=20.7\text{pmV}^{-1}$  and  $r_{22}=2.5\text{pmV}^{-1}$ . Meanwhile EO coefficient  $r_{22}$  was slightly smaller compared to the pure crystal:  $r_{22}=2.3\text{pmV}^{-1}$  for LN:Hf (1,4,8mol%),  $r_{22}=2.2\text{pmV}^{-1}$  for LN:Hf (3mol%), when  $r_{22}=2.6\text{pmV}^{-1}$  for pure LN. The piezo-optic contribution is larger in  $r_{22}$  than in  $r_c$  [47], which is related to the stronger electric field.

### EO coefficients in transition-metal ions doped LN crystals

A study of the dependence of EO coefficients of LN crystals on the concentration of transition metal impurities and crystal composition were performed for Cr [26, 49,50], Ti [51, 52] and Fe [53] doped LN crystals (Table 3.1). An increase of the third column of EO tensor more than 30% was achieved in LN crystals doped by Fe and Ce ions (less than 500 ppm) [25]. In crystals doped with higher Ce content the decrease of EO coefficients was obtained caused by the degradation of crystallinity. However EO coefficients  $r_{13}$ ,  $r_{33}$  are independent on the dopant concentration:  $r_{33}=43\text{pmV}^{-1}$ ,  $r_{13}=13\text{pmV}^{-1}$  for Fe:LN crystals, while  $r_{33}=44\text{pmV}^{-1}$ ,  $r_{13}=14\text{pmV}^{-1}$  for Ce:LN if  $r_{33}=38\text{pmV}^{-1}$ ,  $r_{13}=12\text{pmV}^{-1}$  for undoped crystal.

Combined EO coefficient  $r_c$  illustrates a monotonous reduction with the respect to the crystal stoichiometry in LN:Fe (0.05wt%) crystal grown from a congruent melt containing different content of potassium [53]:  $r_c=22 \text{ pmV}^{-1}$  for  $X_c=48.5\%$ ,  $r_c=20 \text{ pmV}^{-1}$  for  $X_c=49.2\%$ ,  $r_c=19.5 \text{ pmV}^{-1}$  for  $X_c=49.4\%$  and  $r_c=18 \text{ pmV}^{-1}$  for  $X_c=49.55\%$  crystals. However, EO coefficient  $r_c$  in LN:Cr (0.06at%) crystals grown from a congruent melt by adding  $K_2O$  in order to change the crystal composition demonstrates lower value than in Fe:LN crystals and a non-symmetric dependence on the crystal stoichiometry [26]:  $r_c=19 \text{ pmV}^{-1}$  for congruent crystal, then it decreases  $r_c=17.2 \text{ pmV}^{-1}$  for  $X_c=49.25\%$  and increases again  $r_c=20\text{pmV}^{-1}$  for  $X_c=49.85\%$  crystals.

The dependence of coefficient  $r_c$  on Cr content is much larger than on the composition of the crystal [26]. The shift due to Cr ions is about  $5 \text{ pmV}^{-1}$  for Li-rich crystals and  $12.5 \text{ pmV}^{-1}$  for congruent ones when Cr concentration varies from 0.06 at% up to 0.8 at%.

EO coefficients are governed by two mechanisms: non stoichiometric intrinsic defects varying ionic and electronic polarizability of Nb ions and lattice structure changing deformability of oxygen octahedron around Li ions. The first mechanism dominates in congruent crystal and the second one in stoichiometric crystal [26]. In crystals doped with small amount of Fe ions EO coefficients are governed by intrinsic defects related to the Li deficiency. The values of the combined coefficient are remarkably close to the results that had been found in undoped crystals with the same compositions correspondingly. This modification is noticeable for crystals with the near stoichiometric composition, containing the smallest concentration of intrinsic defects. Even a small amount of introduced impurity ions, impedes the crystal to reach the stoichiometry [53]. The introduction of small content of Cr ions affects the crystal composition resulting of the incorporation onto Li site, changing Nb antisites and reducing also EO coefficients due to the variation of ionic and electronic polarizabilities of Nb ions. In Cr doped Li-rich crystals EO coefficients are governed by deformability of the oxygen octahedron around Li and is unaffected by Cr small content.

The EO investigation of LN crystals illustrates the dependence of crystal composition, introduction of dopant impurities their concentration as well, whereas there is no exploration of EO coefficients as a function of Li/Nb ratio as well as presence of transition metal ions in addition.

#### **EO coefficients as a function of external parameters: 1- Wavelength.**

According to the results of investigations for EO coefficients as a function of wavelength performed for pure [5,6,7] as well for doped with Mg [8,9,10] and Fe LN crystals [11] with different composition of the crystal electro-optic coefficients demonstrate an increase with the shift of wavelength from long range to the short range. Particularly, the data of EO coefficients at 632.8 nm demonstrate a dispersion in short range [7,32,6,5,10,9].

## **EO coefficients as a function of external parameters: 2- Temperature.**

The application of the LN crystals in high-voltage systems based on the dependence of electro-optic effect on the temperature also had been investigated [15, 18, 54-58]. Mainly an increase of EO coefficients with the increase of temperature was found except the work of Zook et al. who found the linearly decrease of electro-optic coefficients  $r_{33}$ ,  $r_{13}$  with the increase of temperature [54].

### **EO coefficients in Rare-Earth ions doped LN crystals**

According to the investigations of the relationship between the values of EO coefficient  $r_{33}$  and the presence of rare Earth (RE) ions performed for LN crystals doped with different concentration of erbium (Er) [59-61] ions and codoped with erbium and ytterbium (Er+Yb) [59] the increase of the content of RE ions makes the electro-optic coefficient decreased. Before 0.2 mol% concentration erbium ions create the new defects, decreasing quadratically the EO coefficient. For higher concentrations erbium ions influence on the intrinsic defects forcing a linear decrease of the coefficient. These results suggest that the presence of Er ions reduces the concentration of the Nb antisites and Li vacancies incorporating always onto the same site, which is the similar effect obtained by increasing the stoichiometry of LN crystal [62].

As it is noted in literature, the influence of the crystal composition and the introduction of photorefractive ions on the EO coefficients analyzed in the view of their corresponding dielectric permittivity in iron doped lithium niobate (LN:Fe) crystals was earlier studied. Nevertheless, these published researches presented only the relative EO coefficients obtained in LN:Fe crystals grown with a modified Czochralski technique from congruent melt containing potassium. In fact the composition of the crystals mentioned in the publication had been changed by changing the concentration of potassium ions in the melt [49]. In addition for final correction of the composition different value of electric field had been applied to the crystal-melt system. Thus, even if the incorporation of potassium ions into the lattice of the LN crystals was negligible it would influence the charge compensation mechanism in the matrix. So, at least till the near stoichiometric composition to get pure experimental results for the influence of intrinsic defects on the EO properties of LN:Fe crystals it is preferable to

change the composition of the crystals by the change of the main components of the system, that is, lithium ions in the melt. Currently, EO coefficients of LN:Fe crystals with various composition are grown with the conventional Czochralski technique in which the final composition  $X_c$  of the crystal is achieved by changing the initial composition  $X_m$  in the melt (see Section 2). Thus, in these new LN:Fe crystals, it does not exist any influence of an electric field value or potassium concentration in the melt or residue in the final crystal composition.

Table 3.1: Literature data on measurements on EO coefficients of LN crystals at room temperature.

<b><math>r_{22}</math>, pmV<sup>-1</sup></b>	<b>composition</b>	<b>dopant</b>
3.4[17], 6.7[16], 3.95[21], 6.54[55], 6.4[12,18-20], 6,8[31], 6.3[31,18],6.07[20]	congruent	pure
4.5; 6.8[12],9.89[20]	stoichiometric	pure
6.2;6.97[29], 0.8[31]	congruent	Mg
<b><math>r_{33}</math>, pmV<sup>-1</sup></b>	<b>composition</b>	<b>dopant</b>
30.8[17],30.6[21], 36.0[41], 31.5[23], 31.4[22], 31.0[50]	congruent	pure
38.3[23]	stoichiometric	pure
36.6[51]	congruent	Ti
<b><math>r_{13}</math>, pmV<sup>-1</sup></b>	<b>composition</b>	<b>dopant</b>
8.6[17], 7.8[21],11.0[41], 10.5[24],10.49[22], 10.4, 10.0[40], 10.0[23]	congruent	pure
10.7[51]	congruent	Ti
10.4[23]	stoichiometric	pure
9.25[22]	quazi stoichiometric	pure
<b><math>r_c</math>, pmV<sup>-1</sup></b>	<b>composition</b>	<b>dopant</b>
20[12], 19.1[57] ,20.5[26, 53]	congruent	pure
18[12],20.2[26,53]	stoichiometric	pure
18.7[26]	congruent	Cr
19.9[26]	stoichiometric	Cr
20.3[53]	congruent	Fe
18.5[53]	stoichiometric	Fe
<b><math>r_{42}</math>, pmV<sup>-1</sup></b>	<b>composition</b>	<b>dopant</b>
28[17], 28.2[21]	congruent	pure

### § 3.1. Used experimental techniques.

#### § 3.1.1. Experimental technique for EO measurements.

##### § 3.1.1.1. One-Beam Senarmont-Type Ellipsometric Technique

In general, the one-beam Senarmont-type ellipsometric technique is applied for the observations of combined coefficient  $r_c$  and EO linear coefficient in  $r_{22}$  opto-geometrical configuration. The scheme and the picture of the Senarmont technique are shown correspondingly in Figures 3.1.1.1.1 and 3.1.1.1.2.

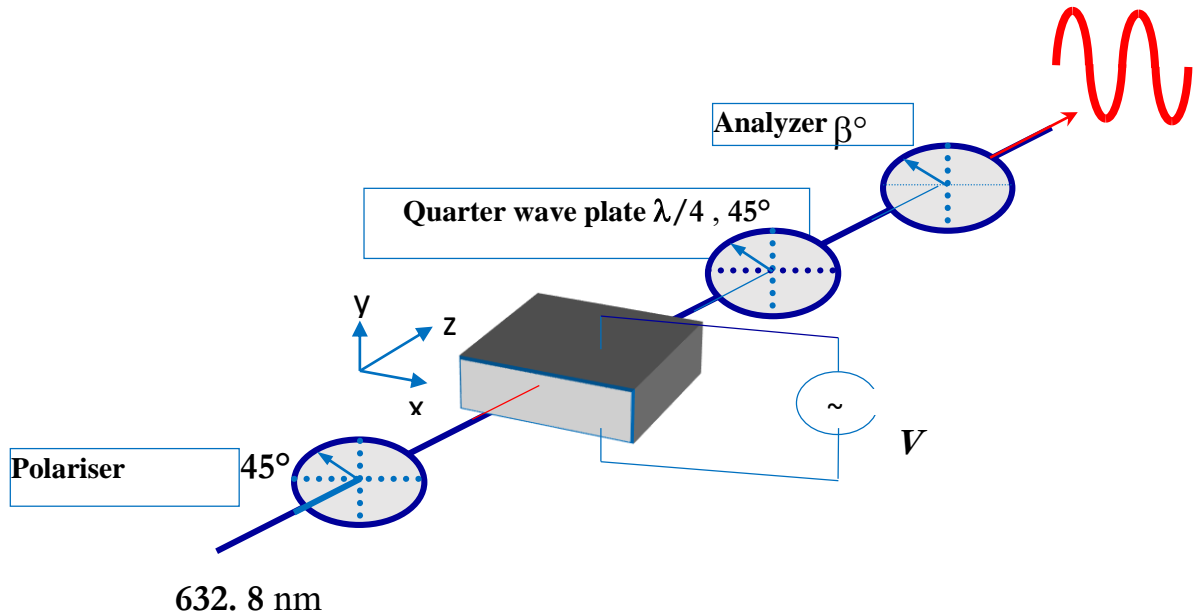


Figure 3.1.1.1.: Schematic Senarmont setup for measurements of EO  $r_{22}$ ,  $r_c$  coefficients" (Basic arrangement of the optical components in the PSCA type of modulator). In figure it is shown the arrangement for  $r_{22}$  opto-geometric configuration.



Figure 3.1.1.1.2: The Senarmont compensation one-beam ellipsometric setup (LMOPS laboratory).

For measurements of combined EO coefficient  $r_c$  and the principle coefficients of the third column of the tensor ( $r_{33}, r_{13}$ ) an external field is applied parallel to the  $z$ -axis of the crystal when the light propagates along the  $y$ -axis (equivalent  $x$ -axis). Whereas, for  $r_{22}$  opto-geometric configuration an applied external field is parallel to the  $y$  direction (or equivalently the  $x$ -axis) of the crystal and beam propagation is along the crystallographic axis ( $c$ ). The opto-geometric configurations are summarized in Table 3.1.1.4. Geometry of the incident beam and applied electric field for  $r_{22}$  opto-geometric configuration is shown in Figure 3.1.1.1.3.

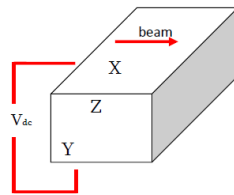


Figure 3.1.1.1.3: Geometry of the incident beam and applied electric field for  $r_{22}$  opto-geometric configuration.

The sample is sandwiched between a polarizer and a quarter-wave or  $\lambda/4$  retardation plate (compensator) if the neutral axes are oriented at  $45^\circ$  from the axes of the crystal obtaining a polarizer-sample-compensator-analyzer (PSCA) system [6, 9, 10, 63]. The uniaxial crystals (quartz, calcite) are used usually as a retardation plate cut in such a way that the  $c$  axis to be lied in the plane of the plate surfaces. Thus, the propagation direction of an incident beam is perpendicular to the crystallographic  $c$  axis. A quarter-wave plate has a phase retardation equal to  $\Gamma = \frac{1}{2}\pi$ . At first the input light beam propagating via a linear polarizer oriented at  $45^\circ$  from the axes of the crystal and then via the crystal induces a differential phase shift. It is possible to measure the variations of the phase shift induced by the applied electric field by rotating the analyzer arranged behind the quarter-wave plate. By this way an additional retardation (phase shift) of the external optical beam will be induced resulting to the electro-optic variation of refractive index [7, 8]. As a polarizer and analyzer are arranged with the polarization direction at  $\pi/4$  to the birefringence axis of the sample, the polarization direction of the analyzer is at an angle  $\beta$  to the fast birefringence axis of the sample obtained as the origin of azimuths. Taking these conditions into account, the optical transmission equation of the system without the quarter-wave plate can be reported as [9, 64]:

$$T = \left(\frac{I}{I_0}\right) = \left(\frac{T_0}{2}\right) [1 + \sin 2\beta \cos \Gamma] \quad (3.1.1.1.1),$$

where  $T$  is the transmission ratio or (optical) factor,  $I_0$  is the incident beam intensity (measured before the sample),  $I$  is the output light intensity and  $T_0$  is the transmission factor expressing the beam losses by reflection and/or absorption caused by the system.

If the polarizer and analyzer axes are parallel (i.e.  $\beta = \pi/4$ ) the Eq. 3.1.1.1.1 may be rewritten as:

$$T = \left(\frac{I}{I_0}\right) = T_0 \cos^2(\Gamma/2) \quad (3.1.1.1.2),$$

when the above mentioned axes are crossed (i.e.  $\beta = -\pi/4$  or  $3\pi/4$ ) the transmission ratio can be reported as:

$$T = \left(\frac{I}{I_0}\right) = T_0 \sin^2(\Gamma/2) \quad (3.1.1.1.3).$$

By using the quarter wave plate arranged with the axes at  $\pi/4$  to the axes of the understudy sample, an optical transmission ratio for Sénarmont system can be expressed as [6, 10, 65]:

$$T = \left(\frac{I}{I_0}\right) = T_0 \sin^2 \left[ \left(\frac{\Gamma}{2}\right) - \beta \right] \quad (3.1.1.1.4).$$

***The compensation of the natural retardation.***

The differential phase retardation created between the two polarization components of a light beam propagating through a birefringent crystal with refractive indices  $n_1$  and  $n_2$ , is ruled by the relation:

$$\Gamma = \left(\frac{2\pi L_{eff}}{\lambda_0}\right) \Delta n \quad (3.1.1.1.5)$$

where  $L_{eff}$  is the length of the crystal along the light beam,  $\lambda_0$  the wavelength of light in a vacuum and  $\Delta n = n_2 - n_1$ , the total birefringence of the sample for the direction considered. When an electric field  $E$  is applied onto a linear EO crystal or modulator, this birefringence can be rewritten as:

$$\Delta n = \Delta n(0) + \Delta n(E) = \Delta n(0) + \left(\frac{1}{2}\right) n^3 r_{eff} E \quad (3.1.1.1.6)$$

where  $\Delta n(0)$  and  $\Delta n(E)$  are the spontaneous or natural birefringence and the field-induced or electro-optic (EO) birefringence [1]. In this equation,  $r_{eff}$  is the effective EO coefficient of the crystal, for the direction under consideration as derived from the  $r_{ijk}$  components of the linear EO tensor [9].

Considering only the electro-optic contribution during the experiment, which could be possible if special cares associated to the differential measurements are done, we can deduce from Eqs. 3.1.1.1.5 and 3.1.1.1.6, that the total phase retardation of the crystal sample submitted to an electric field  $E$  can be expressed by:

$$\Gamma(E) = \left(\frac{\pi}{\lambda_0 d}\right) L_{eff} n^3 r_{eff} V \quad (3.1.1.1.7),$$

where  $\Gamma(E)$  is the EO phase retardation induced by the applied field  $E$ ,  $V$  is the voltage applied to the sample and  $d$  is the distance between the two electrodes in contact with two opposite facets of the crystal [1, 66, 67]. In the general case, when the applied voltage  $V$  is composed by a dc and an ac component, i.e. by  $V_{dc}$  and  $V_{ac}$  which create in the sample the dc and ac phase retardations  $\Gamma_{dc}$  and  $\Gamma_{ac}$ , respectively.

In what follows, more thoroughly the case of a typical IM-EO system must be considered, based on the classical one-beam Sénarmont ellipsometric setup in the transverse configuration i.e. when the applied electric field is normal to the light beam. Under the above conditions, the optical transmission throughout the entire system is ruled by the I- $\phi$  transfer function [61]

$$I(\phi) = \left(\frac{T_0 I_0}{2}\right) (1 - \sin \phi) \quad (3.1.1.1.8),$$

with a transmission factor  $T_0$  standing for the losses of light by the system's components,  $I_0$  and  $I(\phi)$ , correspondingly the incident and the emerging light intensities and with the phase shift controlled electro-optically with the azimuthal position of the analyzer  $\beta$ .

$$\phi = \Gamma - 2\beta \quad (3.1.1.1.9).$$

It is to be noted that in a Sénarmont arrangement, as shown by Eq. 3.1.1.1.9, the relation between  $\Gamma$  and  $\beta$  is strictly linear representing a huge advantage in the compensation process and in some relative methods for the determination of the EO coefficients, as we will see below. In an EO-modulation system the position of the operating point over its characteristic curve  $I = I(\phi)$  is established by the opto-electronical bias of the system  $\phi$  defined by  $\phi =$

$\bar{\Gamma} - 2\beta$  with  $\bar{\Gamma}$  denoting the static phase retardation of the crystal sample, including the spontaneous or natural retardation of the sample and the dc phase retardation. In one-beam systems the compensation of the natural retardation ( $0$ ) of the used EO crystal can be achieved either by applying a dc voltage onto the sample producing a phase shift  $\Gamma = - (0)$  or by setting the analyzer at an azimuthal angle.

Usually the experimental solution for the optical compensation is preferred due to the following advantages: a supplementary voltage source isn't required to avoid a damage of the sample or an electrical fatigue, on the other hand the relaxation effects are excluded allowing a precise compensation even varied in the measurements.

The applied external electric field induces a phase retardation ( $E$ ) resulting to the shift of the operating point along the transmission curve plotted in Figure 3.1.1.1.4. Here the transmission ratio can be expressed as a function of phase  $\Gamma$  retardation and applied voltage:  $V/T = I/I_0 = fct(\Gamma) = fct(V)$ .

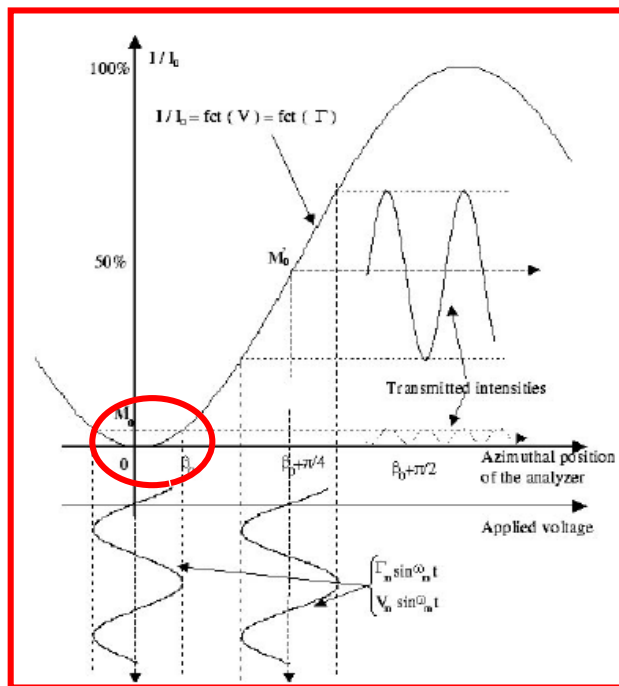


Figure 3.1.1.1.4: Characteristic EO curve  $T = I/I_0$  of optical setup used for linear electro-optic measurements as function of applied  $V$  voltage and as function of total phase  $\Gamma$  retardation.

Considering electro-optic characterizations or sensor applications, two kinds of points over the characteristic curve  $I = I(\phi)$  are specifically important. The position of these operating points over the EO characteristic curve can be chosen by changing either the optical bias, i.e., the azimuthal position  $\beta$  of the analyzer or the electrical bias, i.e. the static retardation by a change of the applied dc voltage.

#### ***§ 3.1.1.1.1. The frequency-doubling electro-optic modulation measurement method (FDEOM method)***

The first point  $M_0$  is the minimum-transmission or extinction point over the EO characteristic curve, at which  $I(\phi)$  is minimum (in Figure 3.1.1.1.4 the minimum working point is taken inside a red circle), hence  $dI/d\phi = 0$  with  $d^2I/d\phi^2 > 0$ . At this point, the EO modulator system provides an intensity-modulated light output  $I(t)$  that will contain practically only the second harmonic ac component of the applied voltage.  $M_0$  working point located at the midpoint of the curve is the lowest or minimum (theoretically zero) transmission point which is the maximum linearity point achieved by rotating the analyzer by an angle  $\beta_{2\omega}$ . At minimum transmission point the transmitted beam intensity is very low therefore only the noise of the receiving optoelectronic system exists and the photonic or quantum noise is absent practically. At this point often called the frequency doubling point the EO modulation produces clearly the output frequency-doubling waveform with frequency  $2\omega$  comparing to the frequency of the applied electric field. The doubling process is very sensitive thus, even a small displacement from the frequency-doubling position creates large and abrupt distortions in the shape of the output signal. This fact evidences non necessity of any measurements of light intensities or modulation depths. This minimum-transmission point, can be very precisely located when a very sharp narrow-band filter is used with a high-sensitivity oscilloscope for the observation of the frequency doubling of the output signal at the extinction shown very clearly on the oscilloscopic screen. This fact makes advantageous the location of the electro-optical arrangement at this operating point for the use of the so-called "Frequency doubling electro-optic modulation" or FDEOM method or one of other frequency-doubling techniques [63]. These methods was originally developed at the LMOPS laboratory to determine accurately the static phase retardation variation  $\bar{\Gamma}$  due to the natural birefringence

changes or to the various kinds of EO retardations including the static or dc phase retardation  $\Gamma_{dc}$  caused by the applied dc voltage  $V_{dc}$  onto the sample. It is to be noted that this determination of location of the operating point on the  $(I - \Gamma)$  characteristic is done without any intensity measurements but only by observation at an oscilloscope screen of the shape of the transmitted signal. Thus, when a sharp band-pass filter is used to amplify the detected output signal, adjusted at the double of the frequency of the modulating voltage, the resulting accuracy of methods based on this observation is hugely increased compare to methods based on intensity measurements. The FDEOM method will be used for the determination of the static EO coefficients of our samples under study [10, 63, 64, 68].

Due to the EO effect the induced differential static phase shift retardation  $\Gamma_{dc}$  by applied electric dc field via the crystal, generates a shift of the operating point from  $M_0$  on the EO characteristic curve in his turn. This phase shift  $\Gamma_{dc}$  is directly measured to full compensate (total restoration of the extinction) by azimuthal rotation of the analyzer by an angle  $\beta_{dc}$  given by the relationship:

$$\beta_{dc} = \beta_{2\omega} - \beta_{2\omega,0} = \Gamma_{dc}/2 \quad (3.1.1.1.1),$$

where  $\beta_{2\omega,0}$  is the angle of the analyzer required initially to compensate for the natural retardation  $\Gamma(0)$  before applying the (testing) dc voltage  $V_{dc}$ . The EO coefficients can be calculated as:

$$r_{eff} = \frac{\lambda d}{\pi n_{eff}^3 L} \cdot \frac{\delta\beta}{\delta V_{\pi}} \quad (3.1.1.1.2).$$

Here  $\lambda$ -vacuum wavelength,  $d$ -the distance between the electrodes,  $L$  -is the length of sample,  $n_{eff}$ -refractive index of the crystal along the propagation direction. Experimentally, with appropriate apparatus as an efficient band-pass filter, within the FDEOM method, the expected accuracy is better than 5% in the determination of the EO coefficients and can achieved 2% in best case in materials with high EO effect.

**§ 3.1.1.1.2. The modulation depth measurement method (MDM)**

The second important working position located at 50% transmission  $(I_{max} - I_{min})/2$  point yielding the linear replica of the ac voltage is corresponding to the middle point over the characteristic curve  $I = I(\phi)$ , i.e. at  $I = \frac{I_0}{2}$  allowing the maximum-linearity in the intensity modulation response  $I_m$  of the EO crystal and thus, containing practically only the fundamental ac component of the applied voltage (Figure 3.1.1.1.2.1). This fact makes advantageously the location of the electro-optical arrangement at this operating point for the application of the so-called "Modulation Depth Method" or MDM or other dynamic methods to determine the ac phase retardation  $\Gamma_{ac}$  due to the applied ac voltage  $V_{ac}$  onto the sample [6, 69].

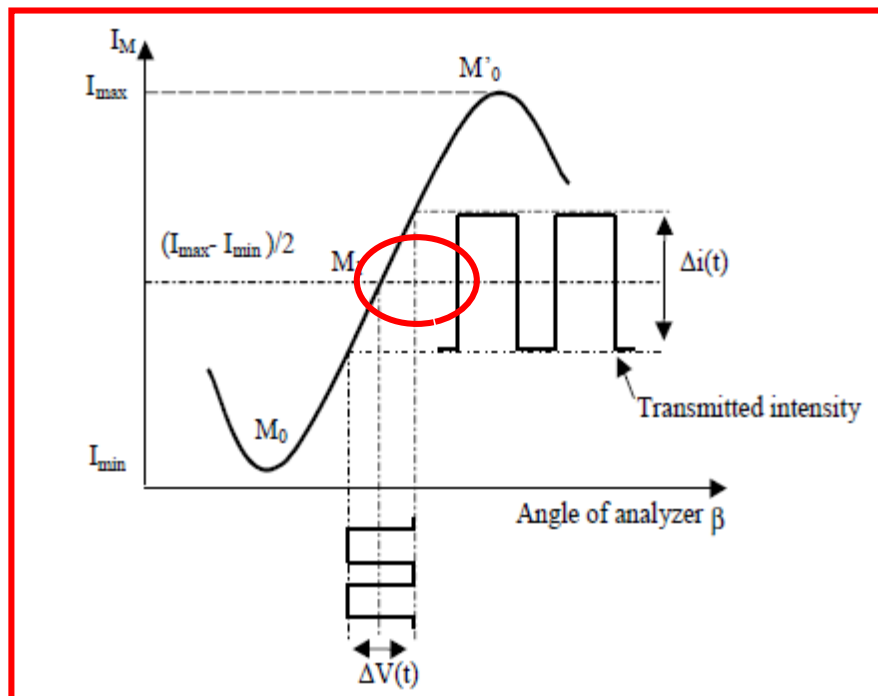


Figure 3.1.1.1.2.1: Optical transmission function of Sénarmont setup versus the angle of the analyzer  $\beta$  and applied voltage.

“Modulation Depth Method” (MDM)[6] can be used to determine the EO coefficient as a function of the modulated frequency from DC to 1 MHz defined by the specifications of power supply and signal acquisition electronic setup.

By measuring the peak-to-peak amplitude  $i_{pp}$  of the modulated signal at the point  $M_1$  the EO coefficient is obtained directly from the following equation:

$$r_{eff}(v) = \frac{\lambda d}{\pi n_{eff}^3 I_0 L} \cdot \frac{i_{pp}(v)}{v_{pp}(v)} \quad (3.1.1.1.2.1).$$

The effective EO coefficients can be written as

$$n^3 r_{eff}(v) = \frac{\lambda d}{\pi I_0} \cdot \frac{i_{pp}(v)}{L v_{pp}(v)} \quad (3.1.1.1.2.2).$$

The effective combine EO coefficient is given as:

$$n_e^3 r_c = n_e^3 r_{333} - n_o^3 r_{113} \quad (3.1.1.1.2.3).$$

Here,  $v_{pp}(v)$ -is the peak-to-peak amplitude value of the modulated ac voltage at the frequency  $v$ ,  $i_{pp}(v)$  - the peak-to-peak amplitude of the sinusoidal voltage,  $I_0 = I_{max} - I_{min}$  is the total intensity shift of the transmitted beam. The measurements of  $v_{pp}(v)$  and  $i_{pp}(v)$  quantities are carried out in ac regime whereas the measurements of  $I_{max}$  and  $I_{min}$  are done in dc regime.

For measurements of EO coefficient  $r_c$  the polarization of the incident beam is at  $45^\circ$  of the  $z$  axis, thus, the field-induced effective change in the birefringence can be reported as [1]:

$$\delta \Delta n(E) = -\left(\frac{1}{2}\right) n_e^3 r_c E_3 \quad (3.1.1.1.2.4).$$

Thus, the combined coefficient defined by the following relationship:

$$r_c = r_{33} - (n_o/n_e)^3 r_{13} \quad (3.1.1.1.2.5),$$

with  $n_o$  and  $n_e$  the ordinary and extraordinary refractive indices of the crystal.

It is important to note that the previous developments performed for a unique light beam propagating through a birefringent crystal in Sénarmont modulator configuration provide the same type of equations when a two beams arrangement in an interferometric configuration is employed. We have seen above that the differential phase retardation between the two polarization components of the beam propagating through the birefringent crystal is considered in Sénarmont modulator or setup.

It is to be of note that as this method and others associated ones are based on intensity measurements, the experimental accuracy in the determination of the EO coefficients is generally limited to about 10% in the best cases.

### § 3.1.1.2. Interferometric measurements

In order to measure the third column of EO coefficients  $r_{33}$  and  $r_{13}$  the Mach-Zehnder interferometry was employed (the scheme and the picture of the setup are given correspondingly in Figures 3.1.1.2.1 and 3.1.1.2.2).

In interferometric setup, the differential phase retardation of the beam passing through the crystal is considered relative to the phase of the polarization of the reference beam passing in the second arm of the interferometric setup. In the most common interferometric system, that is the Mach-Zehnder interferometer the transmission equation along the axis of the interferometer is similar to Eq. 3.1.1.1.5 and followings, where  $\Gamma$  is now the differential phase retardation at the output between the phases of the two beams in the active branch and in the reference branch. Within such setup, considering the total light intensity  $I_0$  entering the system assumed equally divided between the two branches, the  $I - \phi$  transfer function output fringes can be described by equations similar to Eq. 3.1.1.1.8. For this opto-geometrical configuration, the electro-optically controlled phase shift  $\phi$ , described by Eq. 3.1.1.1.9, represents now the distance  $y$  from the center in the plane of the fringe pattern via the following equation

$$\phi = \left(\frac{2\pi}{\lambda_0}\right) y \quad (3.1.1.2.1).$$

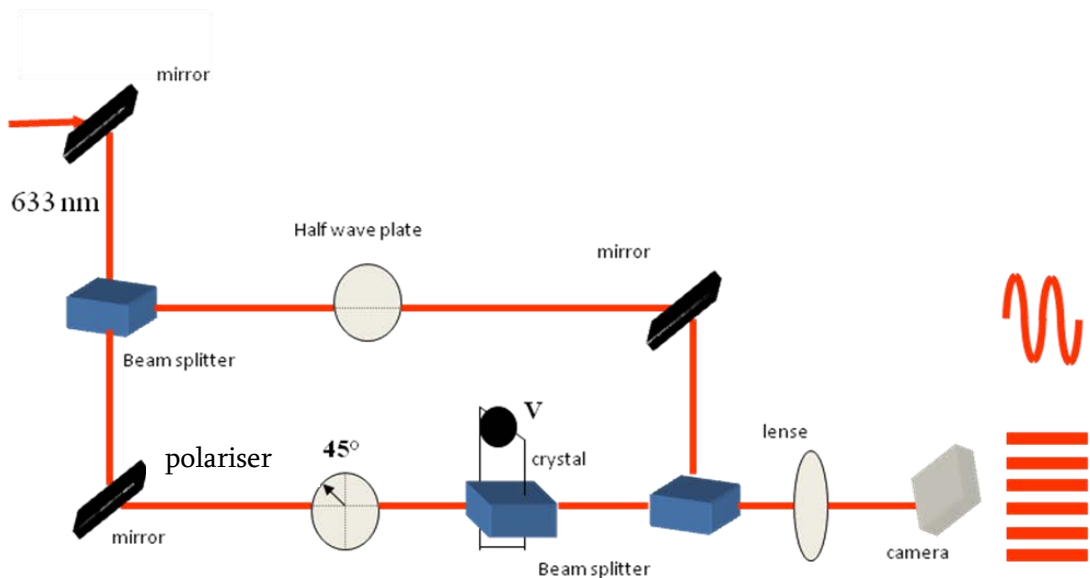


Fig. 3.1.1.2.1: Scheme of the Match-Zehnder interferometric setup.



Figure 3.1.1.2.2: Mach-Zehnder interferometric setup.

(With the hypothesis of small angle between the observe ray and the normal). Thus, to select during EO measurements a functioning point on the  $I - \phi$  characteristic in the fringe pattern plane, we can adjust the distance  $y$  of the observed point or introduce a retardation of the phase of the polarization in the reference arm. In our setup, this retardation is created by the mirror placed in this reference arm, mounted on piezo-electric translation.

The phase of the light wave propagated in the crystal was modulated by a dc voltage applied along the direction parallel to the optical axis  $c$  of the crystal (See Table 3.1.1.4). Considering that in the trigonal structure,  $r_{113} = r_{223}$ , it results that only two direct and one combined EO coefficients have to be determined. In interferometric measurements, with a light propagation along the  $y$  axis ( $x$  axis), the field induced effective change in the refractive index for each polarization component is [70]:

$$\delta n_o(E) = -\left(\frac{1}{2}\right) n_o^3 \delta \left(\frac{1}{n_o^2}\right) = -\left(\frac{1}{2}\right) n_o^3 r_{113} E_3 \quad (3.1.1.2.2)$$

and

$$\delta n_e(E) = -\left(\frac{1}{2}\right) n_e^3 \delta \left(\frac{1}{n_e^2}\right) = -\left(\frac{1}{2}\right) n_e^3 r_{333} E_3 \quad (3.1.1.2.3).$$

Laser beam dividing into two parts due to the beam splitter one part of the beam propagates directly then reflects by mirror and due to the analyzer the polarized beam passes through the EO crystal. In order to have a retardation of the phase dc voltage is applied to the crystal. To measure  $r_{33}$  EO coefficient the beam is polarized through z direction, for  $r_{13}$  is used polarized beam through  $x$  (or  $y$  direction). The second beam passes through half wave plate and then recombining after the crystal with the splitted first part of the beam. As half wave plate changes the phase of the beam, so after the sample the beams have phase shift, thanks to which the interferometric image is created on the detector. The lense is used to control the size of the fringes. The direction of the fringes could be changed due to the beam splitter after sample and due to the mirror after the half wave plate. To avoid the Fabry-Perot interferometer is used the diaphragm before the detector. The light part of the fringes is related to the maximum intensity of the transmitted beam and the dark one is corresponded to the minimum intensity of the transmitted beam. To move the fringes a piezo-electric mirror is used, which changes horizontally the position of the fringes on the detector. Amplitude value of the intensity could be obtained by applying ac voltage to the crystal. EO coefficients are calculated due to the following equations:

$$r_{33}(v) = \frac{2\lambda di_{pp}(v)}{\pi n_e^3 I_0 LV_{pp}(v)} \quad (3.1.1.2.4)$$

$$r_{13}(v) = \frac{2\lambda di_{pp}(v)}{\pi n_o^3 I_0 LV_{pp}(v)} \quad (3.1.1.2.5).$$

It is to remember that in one beam set-up, the electric phase contribution is measured as a phase shift between the components of the polarization crossing the sample, yielding to have the possibility to determine only combined EO coefficients or direct ones only when one term of the combination is equal to zero. The main advantage of the interferometric based methods is the possibility to obtain individually all direct EO coefficients as the electrical perturbed beam in the crystal is referred to the passive beam of the second arms of the interferometer. Nevertheless, the amplitude of the detected signal (interferometric pattern) at the output of the experimental two-beam set-up is low and the resulting accuracy in the determination of the EO coefficients is relatively poor, above 10%, within these techniques.

### § 3.1.1.3. Time Response method (TRM)

The method called “Time Response method” (TRM) usually is used to measure the clamped EO coefficients [6, 71]. Indeed, analogic method are often limited by the bandwidth of the electronic devices and apparatus limited to a few megahertz which in general, limits the determination of EO coefficients beyond the frequencies of acoustic resonances. Thus, digital experimental methods followed by mathematical and signal treatments need to be developed in a wide frequency range, allowing the determination of both clamped and unclamped EO coefficients. The specialty of this method is the application of the step voltage taking into account the acoustic contribution increasing the width of the step of voltage. On the other hand this method provides a large frequency range which decreases the rise time of the step of voltage to a few nanoseconds [71]. It was shown that thanks to Time Response method the frequency dispersion of Pockels coefficients in the large range from DC up to 500 MHz can be obtained. However the main limitation reason of this observation is the rising time of the voltage pulse [6]. The schematic diagram of experimental setup for TRM measurements is given in Figure 3.1.1.3.1.

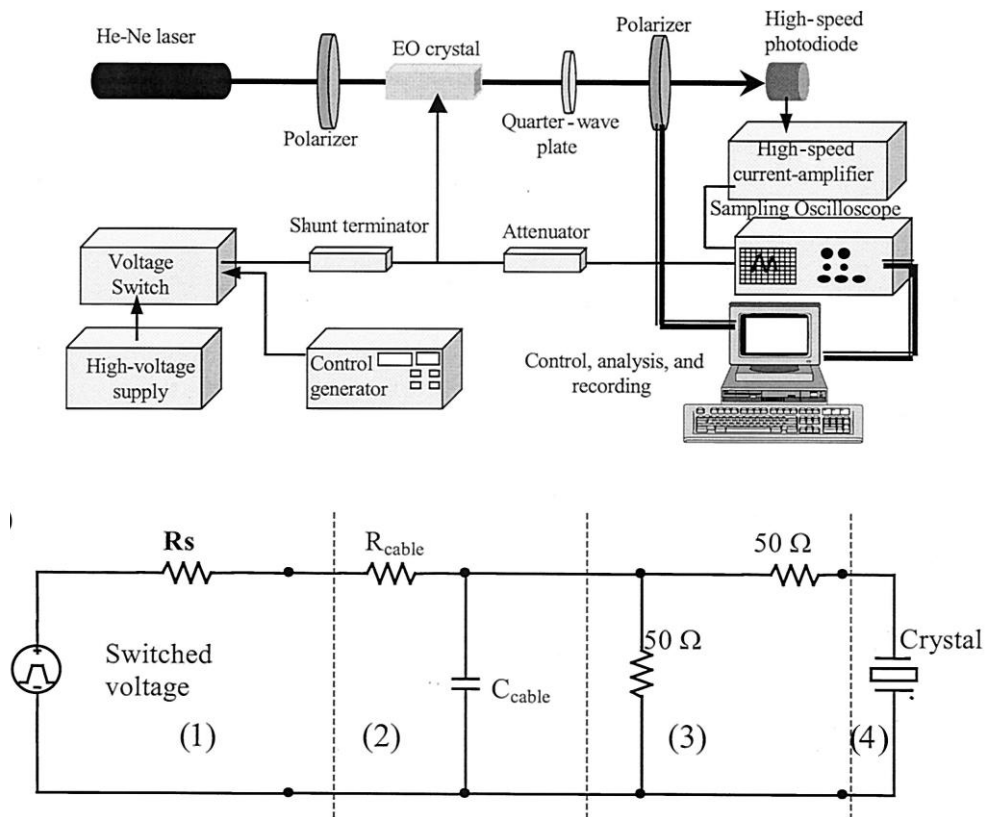


Figure 3.1.1.3.1: Scheme of the TRM experimental setup. The electrical part of experimental setup is shown below: 1)-pulse generator, 2) cable, 3) shunt terminator, 4) the sample [69].

Usually the unclamped EO coefficients can be measured by both MDM and TRM methods. Linear working point  $M_1$  (see Figure 3.1.1.1.2.1) where the transmission  $I_0 = (I_{max} - I_{min})/2$  is about 50% also used to observe the EO coefficients depending on time. The applied electric voltage  $\Delta v(t)$  generates the immediate variation of the intensity of transmitted beam  $\Delta i(t)$ . The electric field generated variation of intensity is the highest at the linear part of the transfer function. The intensity variation of the transmitted beam  $\Delta i(t)$  induced by voltage  $\Delta v(t)$  as a function of time at the working point  $M_1$  is given by:

$$\Delta i(t) = \frac{\pi L I_0 n_{eff}^3}{2 \lambda d} \cdot r_{eff}(t) \otimes \Delta v(t) \quad (3.1.1.3.1)$$

$\otimes$ -is the convolution operator. The time signals  $\Delta i(t)$  and  $\Delta v(t)$  have been exhibited and measured by using the oscilloscope. For observation of the frequency dispersion of the signals  $\Delta i(\vartheta)$  and  $\Delta v(\vartheta)$  Z-transformation of signals correspondingly  $\Delta i(t)$  and  $\Delta v(t)$  is used in TRM method. (shown in Figure 3.1.1.3.2).

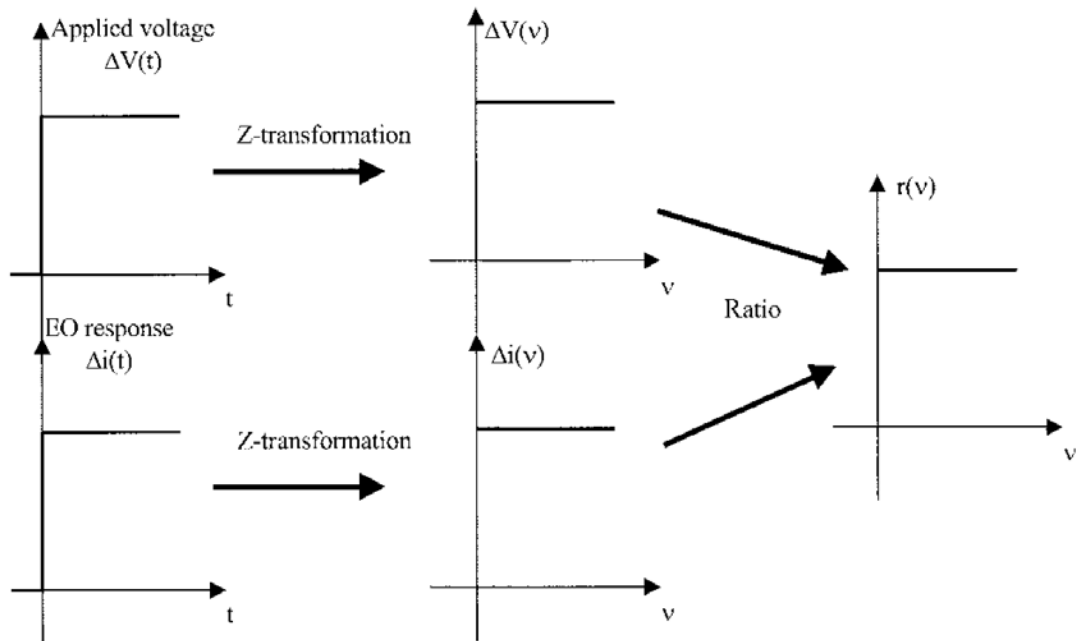


Figure 3.1.1.3.2: Z-transformation of signals correspondingly  $\Delta i(t)$  and  $\Delta v(t)$  to observe the frequency dispersion the signals  $\Delta i(\vartheta)$  and  $\Delta v(\vartheta)$ . The applied voltage illustrates a step form.

For Z-transformation signals  $\Delta i(t)$  and  $\Delta v(t)$  were considered as discrete functions  $\Delta i(t_n)$  and  $\Delta v(t_n)$  respectively for samples of N numbers obtained in period T. The relationship between time intervals for sampling time ( $t_n$ ) and successive samples  $\Delta \tau = T/N$  can be expressed:

$$t_n = n\Delta\tau \quad (3.1.1.3.2).$$

Thus, the Z-transform of signals  $\Delta i(t)$  and  $\Delta v(t)$  is given by:

$$\Delta i(\vartheta_m) = \sum_{n=0}^{N-1} Z^{-n} \Delta i(t_n) \quad (3.1.1.3.3),$$

$$\Delta V(\vartheta_m) = \sum_{n=0}^{N-1} Z^{-n} \Delta V(t_n) \quad (3.1.1.3.4),$$

where  $\vartheta_m = m/T$  is the frequency for number  $m$ ,  $m=0, 1, \dots, N$ .

$$Z = \exp\left(-2i\pi \frac{m}{N}\right) \quad (3.1.1.3.5).$$

The absolute values of effective EO coefficients was expressed as:

$$r_{eff}(v) = \frac{2\lambda d}{\pi n_{eff}^3 l_0 L} \cdot \frac{\Delta i(v)}{\Delta v(v)} \quad (3.1.1.3.6).$$

The effective EO coefficient can be expressed as:

$$n^3 r_{eff}(v) = A \frac{\lambda d}{\pi l_0} \cdot \frac{\Delta i(v)}{L \Delta v(v)} \quad (3.1.1.3.7),$$

where  $A=1$  or  $2$  correspondingly for Senarmont and two beam interferometric measurements.

It is to be noted that the use of this method is justified only when clamped EO coefficients are desired as the accuracy is lower and the procedure is more complex than the determination performed with analogic methods as presented above.

#### ***§ 3.1.1.4. The opto-geometric configurations required for EO measurements***

The opto-geometric configurations are summarized in Table 3.1.1.4.

Table 3.1.1.4: Opto-geometric configurations of the applied electric field ( $E$ ) and the propagated light beam directions relative to the crystal configuration ( $x, y, z$ ) used for the determination of the electro-optic coefficients.

EO coefficient	Configuration for applied electric field $E$ direction	Configuration light beam ( $k$ ) direction
$r_{33}, r_{13}, r_c$	$E // z$	$k // y (x)$
$r_{22}$	$E // y (x)$	$k // z$

In general the typical values for pure congruent crystal  $n_o = 2.20863$  and  $n_e = 2.2025$  at room temperature and at  $\lambda=632.8$  nm have been assumed for calculations of the EO coefficients. The small change in the value of the indices induced by a change of composition and by doping impurities will require a correction in the values of the EO coefficients that has been found in the order of 5%, which is below the accuracy of our measurements.

**§ 3.1.2 Experimental technique for dielectric measurements.**

The application of ac sinusoidal voltage  $V$  across the capacitor leads to the current  $I$  including a charging current  $I_c$  and a loss current  $I_l$  related to the dielectric constant (Eq. 3.1.2.1). Usually, the losses of the material are represented as a conductance ( $G$ ) parallel to a capacitor ( $C$ ) as shown in Figure 3.1.2.1 [13].

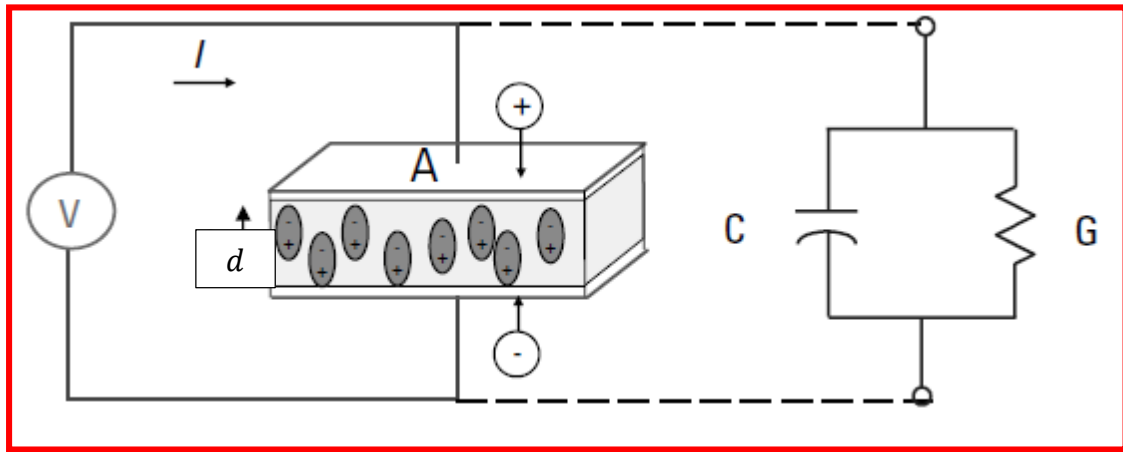


Figure 3.1.2.1: Parallel plate capacitor.

$$I = I_c + I_l = V(j\omega C + G) \tag{3.1.2.1}$$

If

$$G = \omega \varepsilon'' C_0 = \omega \varepsilon'' \varepsilon_0 \frac{S}{d} \tag{3.1.2.2},$$

$$C = \varepsilon' \varepsilon_0 C_0 = \varepsilon' \varepsilon_0 \frac{S}{d} \tag{3.1.2.3},$$

where

$$C_0 = \varepsilon_0 \frac{S}{d} \tag{3.1.2.4},$$

thus,

$$I = V(j\omega\varepsilon_0(\varepsilon' - j\varepsilon'')) = V\varepsilon(j\omega\frac{S}{d}) \quad (3.1.2.5).$$

Where  $\omega = 2\pi f$  is the angular frequency,  $S$  and  $d$  are the surface of the capacitor plates and the distance between them respectively (Figure 3.1.2.1).  $C$  and  $C_0$  are the capacitances with and without dielectric respectively,  $\varepsilon_0 = 1/36\pi \times 10^{-9} F/m = 8,85 \times 10^{-12} F/m$  is the free space permittivity.

To realize dielectric measurements at first two surfaces of the crystal must be covered by a silver as a material with high conductivity. To determine  $\varepsilon_{33}$  the surfaces with area of  $x$  and  $y$  were covered when the distance between them is  $d = z$ . To analyze a dielectric permittivity  $\varepsilon_{22}$  the surfaces with area of  $x, z$ , axes were covered when the distance is  $d = y$ .

By measuring the capacitance and the conductivity of the crystal correspondingly the real  $\varepsilon'$  and  $\varepsilon''$  imaginary parts of dielectric permittivity were calculated by using Eqs. 3.1.2.6 and 3.1.2.7 obtained from Eqs. 3.1.2.2 and 3.1.2.3:

$$\varepsilon' = \frac{Cd}{\varepsilon_0 S} \quad (3.1.2.6),$$

$$\varepsilon'' = \frac{Gd}{\varepsilon_0 \omega S} \quad (3.1.2.7).$$

## ***§ 3.2. EO and dielectric coefficients of LN crystals doped with non-photorefractive ions.***

### ***§ 3.2.1. Zr doped crystals***

#### ***§ 3.2.1.1. Details of Experiments***

##### ***Electro-Optic measurements***

The measurements of Pockels EO coefficients have been performed at room temperature using He-Ne laser beam with 632.8 nm wavelength [72]. Particularly,  $r_{113}$  and  $r_{333}$  linear EO coefficients have been measured with the help of interferometric Mach-Zehnder method whereas  $r_{222}$  and combined coefficient  $r_c$  have been measured using the one-beam Senarmont compensation ellipsometric technique.

In general the unclamped EO coefficient  $r_{eff}^T$  can be measured by both MDM [6, 73] and TRM methods [6, 71], nevertheless we used MDM method referred as “Modulation Depth Method”.

The sinusoidal ac voltage with the peak-to-peak amplitude equal to 250 V at 1 kHz was applied onto the sample to generate the modulation of amplitude for the output signal.

The measurements of clamped EO coefficient have been performed by the “Time Response method” (TRM) [6, 71] presented above, when the EO response is considered to be in the long time range. In order to define the time response of crystal to a voltage step the large range of voltage pulse up to 1kV passes across the sample. For the investigation of  $r^S$  the voltage pulse with short duration was used (nanoseconds), however in the case of  $r^T$  the larger pulse was applied (several microseconds). For our measurements of  $r^S$  coefficients the voltage pulse was equal to 300 V with the 5 ns duration and 10  $\mu$ s repetition rate.

The electrical voltage applied onto the sample contained a DC power supply with 0 to 1000 V and a high voltage switch, which decrease a rise time below 10 ns. The switching was controlled by pulse generator with pulse duration of 10  $\mu$ s and a rise time of 6ns. The output resistor of the pulse generator (50 $\Omega$ ) was used to escape the expansion of the voltage rising edge. Thus, to achieve this conditions the output of the voltage switch was connected to the sample trough the too shorter wire with 50 $\Omega$  providing the sample with shunt terminator of 50 $\Omega$ . The high-speed p-i-n photodiode with response time lower than 0.5 ns and the voltage-current amplifier with response time of 0.8 ns was used in the detection system. The oscilloscope with a sampling rate equal to 10 GSa/s and an analogical bandwidth equal to 500 MHz was applied to display the signals  $\Delta i(t)$  and  $\Delta v(t)$ .

Within in the conditions of the sample dimensions, realized optical and electric arrangements the uncertainty of EO coefficients is in order less than 10 % for LN:Zr crystals.

The recorded applied voltage and the optical signal at various time scale for opto-geometric  $r_{22}$  configuration is reported in Figure 3.2.1.1.1 for 0.8 mol% Zr doped LN crystal within TRM technique.

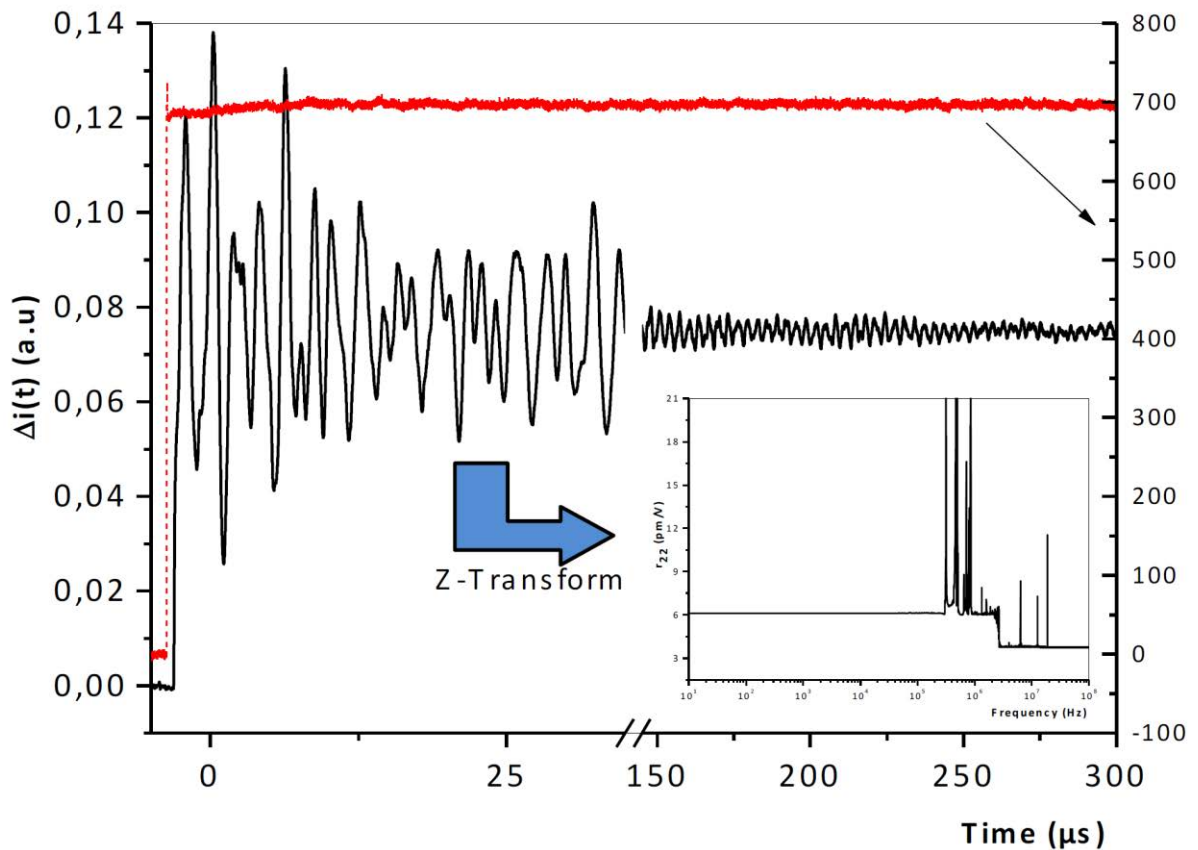


Figure 3.2.1.1.1: Time and frequency responses for  $r_{222}$  opto-geometric configuration for 0.8 mol% Zr:LN sample. By using Z-transform (the insert) the response of  $\Delta i(t)$  signal to one step of voltage  $\Delta v(t)$  at different time scales and frequency dependence was obtained by laser beam with 633 nm wavelength.

The response  $\Delta i(t)$  signal to the applied voltage  $\Delta v(t)$  and the frequency was obtained by the Z-transform (the insert in Figure 3.2.1.1.1). The measurements have been performed by using 632.8 nm laser beam. For long time the optical signal oscillation illustrates the periods of the piezo-electric frequency resonances. For LN:Zr crystals the time range shorter than 350 ns of the oscillations absents as the propagation of acoustic waves through the crystal more time requires. The intensity demonstrates a larger acoustic contribution as this value corresponding to the plateau is smaller for time below 350 ns compared to the value obtained for longer time than 200 $\mu$ s. Although the frequency dependence of the EO coefficient  $r_{222}$  was shown only for 0.8 mol% Zr:LN crystals, the investigations have been performed for all samples under study LN:Zr1-LN:Zr8 and all samples illustrate the same behavior depending on the frequency. In opto-geometric configuration  $r_{222}$  laser beam propagated along the  $c$  axis, when electric field was applied parallel to  $x$  (or  $y$ ) axis. The unclamped EO coefficients at constant stress in low

frequency range were investigated by both MDM and TRM methods whereas the clamped EO coefficient at constant strain in high frequency range was measured by MDM method using Senarmont compensation setup.

EO coefficients for  $r_{113}$  and  $r_{133}$  opto-geometric configurations were observed by Mach-Zehnder interferometric technique. Laser beam propagated along the  $x$  (or  $y$ ) axis, when electric field was applied parallel to  $y$  axis. The combined EO coefficient  $r_c$  investigated by Senarmont compensation method was compared to the calculated values.

As in  $r_{113}$  and  $r_{333}$  configurations the electric field is applied onto the crystal along the  $Z$  direction the contributions of piezo-optic effect is slightly thus,  $r_{xx3} = r_{xx3}^T = r_{xx3}^S$ , when  $xx = 11$  or  $33$ .

### ***Dielectric measurements***

According to the established relationship between EO and linear dielectric coefficients as well as depending of these mentioned parameters on the frequency and the temperature, EO coefficient reproduce the same behavior of dielectric permittivity [12]. The link between EO and dielectric coefficients presents with the variation of crystal composition and impurity concentration [3]. Thus, with the EO parameters the values of dielectric constants also have been measured for Zr and In doped samples (See 3.2.2). The measurements of  $\epsilon_{22}^T$ ,  $\epsilon_{22}^S$  and  $\epsilon_{33}^T$ ,  $\epsilon_{33}^S$  coefficients correspondingly for low and high frequency ranges at room temperature have been performed by utilizing the two impedance analyzers HP 4151 and HP 4191A in large frequency ranges correspondingly from 1 Hz up to 13 MHz and from 1 Mhz up to 1 GHz.

In addition optical absorption experiments were carried out.

The UV-Visible-NIR optical transmission spectra was recorded with the help of Perkin Elmer Lambda 900 spectrometer by using un-polarized light. For this measurements the samples were located with polished surfaces at normal incidence as well as the  $K$  vector of incident beam was parallel to the crystallographic  $c$  axis. The recorded transmission spectra for all samples illustrates the flat transparency response in the visible range and an absorption edges have been realized at the absorption coefficient of  $20\text{cm}^{-1}$ .

## ***§ 3.2.2 In doped crystals***

### ***§ 3.2.2.1 Details of Experiments***

#### ***Electro-Optic measurements***

The measurements of EO coefficients in opto-geometric configuration  $r_{222}$  for the samples LN:In1-LN:In4 have been performed at room temperature using  $\lambda = 632.8$  nm He-Ne laser beam. Laser beam propagated along the  $z$  axis, when electric field was applied parallel to  $x$  (or  $y$ ) axis. The unclamped EO coefficients at constant stress in low frequency range were investigated by both MDM and TRM methods whereas the clamped EO coefficient at constant strain in high frequency range was measured by MDM method using Senarmont compensation setup [74]. In the case of former MDM method the amplitude of the applied ac electric field was 220 V at 1 KHz. However, the amplitude of the pulse voltage applied onto the crystal was equal to 700 V in the TRM technique. In these conditions taking into account, the sample dimensions, realized optical and electric arrangements for measurements the error uncertainty of EO coefficients is in order of 6 %.

The time and frequency response of optical signal  $\Delta i(t)$  signal to one step voltage  $\Delta v(t)$  for EO coefficient  $r_{222}$  for LN:In4 (In:1.7 mol%) sample and congruent undoped LN crystal is reported in Figure 3.2.2.1.1. In the long time range the optical signal illustrates periodic oscillation corresponding to the piezo-electric frequency resonances. In the inset Figure 3.2.2.1 is given the EO response for the short time scales when the oscillations absent because for the propagation of the acoustic waves through the sample requires more time. In contrast to congruent pure LN crystal for LN:In crystals the signal level remains stable in the both short and long time ranges, which reveals the negligible amplitude of the acoustic contribution. According to the investigations of  $r_{222}$  opto-geometric configuration all crystals illustrate the same behavior depending on the frequency.

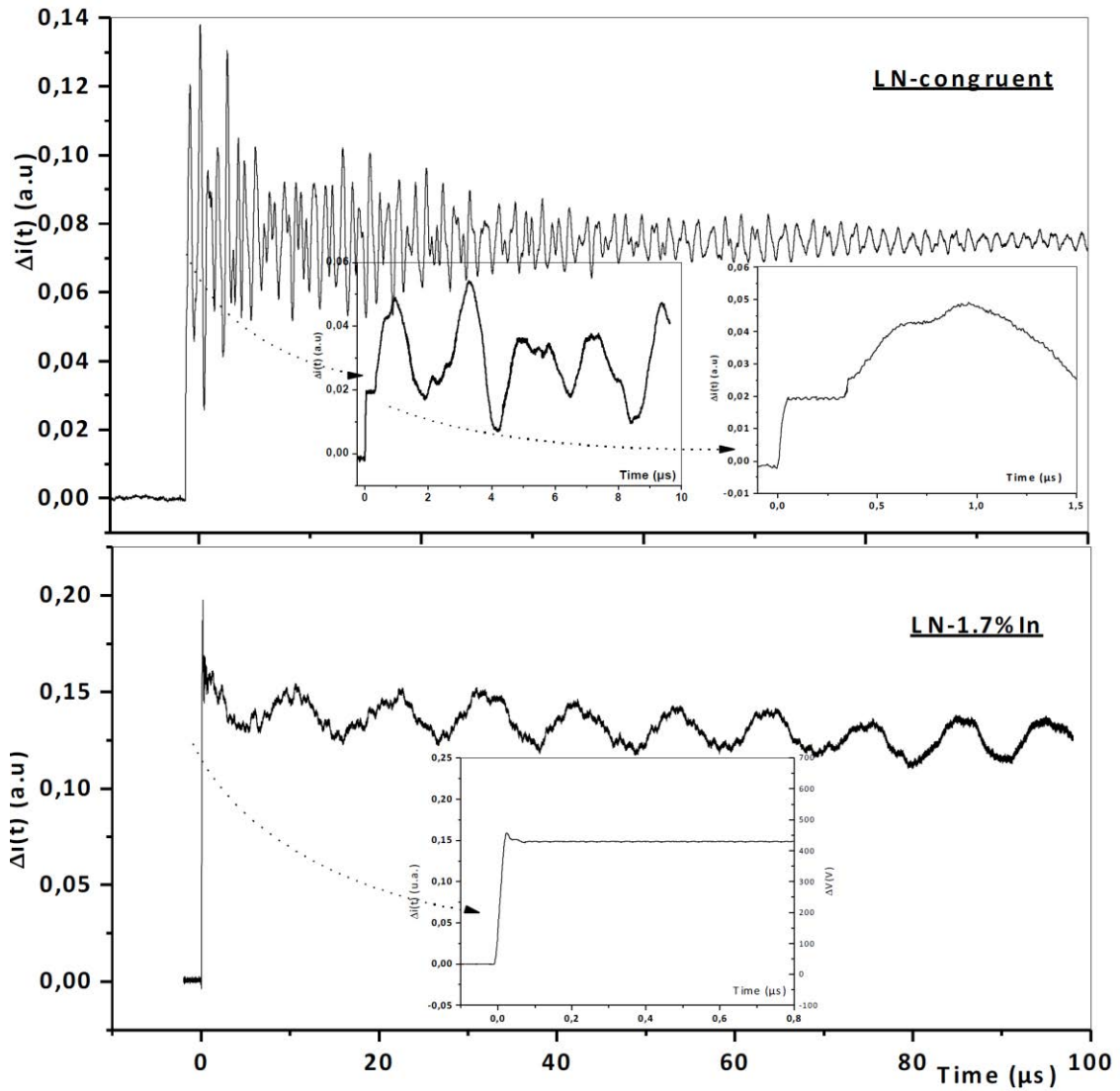


Figure 3.3.2.1.1: Time and frequency responses of EO coefficient  $r_{222}$  for LN:In4 (In:1.7 %) and pure congruent LN samples. Response of  $\Delta i(t)$  signal to one step voltage  $\Delta v(t)$  at different time scales and frequency dependence was obtained by laser beam with 633 nm wavelength.

### *Dielectric measurements.*

The investigations of the associated dielectric coefficients  $\varepsilon_{22}^T$ ,  $\varepsilon_{22}^S$  for low and high frequency ranges at room temperature as a function of frequency along the  $c$  axis for In:LN samples have been performed by using a low electric field equal to 1 V producing an electric field with 1 kV/m applied onto the sample. The two impedance analyzers HP 4151 and HP 4191A have been utilized in frequency ranges correspondingly from 1 Hz up to 13 MHz and from 1 Mhz up to 1 GHz.. The figure of merit  $\frac{n^7(r_{222}^S)^2}{\varepsilon_{22}^S} (pmv^{-1})^2$  was determined from the measured EO and dielectric results.

### ***§ 3.3. EO and dielectric coefficients of LN crystals doped with transition metal (Fe) ions.***

#### ***§ 3.3.1. Details of Experiments***

##### ***Electro-Optic Measurements***

The dependence of the linear EO coefficients on lithium niobate crystals composition  $X_c = [Li]/[Li + Nb]$  and the introduction of iron ions in various opto-geometric configuration was reported for samples LN:Fe1-1÷LN:Fe1-3 doped with fixed Fe ions with the crystal composition changing from  $X_c = 48.45$  mol %, i.e. congruent composition to  $X_c = 48.45$  mol % i.e. close to the stoichiometric composition [75]. The electro-optic coefficients  $r_{22}$  and combined  $r_c$  have been analyzed with the aid of the one-beam Sénarmont-type ellipsometric technique using the FDEOM or MDM methods, whereas to measure the elements of third column of EO tensor the Mach-Zehnder two beam interferometric setup was employed. In all EO measurements with the FDEOM or MDM methods, using either the Sénarmont or the interferometric setups, the samples were mounted in a transverse opto-geometric configuration. In the case of the  $r_{22}$  electro-optic coefficient, the external field is applied parallel to the  $y$  axis of the crystals and the light propagation along their  $z$  axis (see Table 3.1.1.4). A symmetrical configuration was used for  $r_{13}$ ,  $r_{33}$  and  $r_c$  with the external field applied along the  $z$  axis and the laser beam propagated parallel to  $y$  axis. Measurements were performed at room temperature using a He-Ne laser at  $\lambda=632.8$  nm. To decrease the influence of the photorefractive effect induced by the laser beam used for the measurements, an opto-geometric configuration have been chosen assuming a beam propagation along the  $y$  axis of the samples as their dimensions are smaller along that compared to  $x$  axes (§1, Table 1.2.1). On the other hand in order to minimize additionally the photorefractivity during the measurements, a non-focalized beam was used assuming a low power density in the crystal under study. Each coefficient was given from an average value provided by more than ten measurements after suppression of the extremum in the experimental results. Within this experimental protocol and even with a low dynamic in the output signal due to the low intensity of the beam, an accuracy of  $\pm 5\%$  was found for the final value given for all coefficients. In both MDM and FDEOM methods, the dynamic component of the EO response was produced by an ac sinusoidal voltage  $V = V_m \sin(2\pi ft)$  of maximum amplitude  $V_m$  variable up to 100V at a frequency  $f$  equal to 1kHz. In the FDEOM method the dc bias was induced in

the sample by adding in series with the ac voltage, a dc voltage amplitude varies between  $-270$  V and  $270$  V. It will be noted that as the acoustic resonances in LN appear at frequencies above the modulation one, with both methods, our measurements will concern to the unclamped EO coefficient  $r^T$ . The ac component of the output beam was detected by a photodiode followed by a current amplifier sets as narrow band-pass filter for measurements with the FDEOM method not requiring intensity measurements and as low-pass filter for measurements with the MDM method in which the dynamic modulated  $I_m$  and absolute  $I_0$  contributions of the laser beam intensity need to be determined.

### ***Dielectric Measurements***

Taking into account the correlation between, the EO coefficients and the linear dielectric permittivity as well as their respective behaviors with composition and other physical parameters as the temperature and the frequency to be closely linked in ferroelectric inorganic crystals for completely observation of the EO behavior the linear dielectric coefficients  $\epsilon_{22}$  ( $= \epsilon_{11}$ ) and  $\epsilon_{33}$  of all samples have been determined at room temperature as function of frequency. For the dielectric measurements, a low voltage equal to  $2$  V was used with a LCR analyzer HP4284A in frequency range from  $100$  Hz to  $1$  MHz.

## ***§ 3.4. Results and Discussion***

### ***§ 3.4.1. LN crystals doped with non-photorefractive ions.***

#### ***§ 3.4.1.1. Zr doped crystals***

##### **Optical absorption.**

The results for absorption edge as a function of Zr concentration are given in Table 3.4.1.1.1. According to the results the absorption edge replaces to the UV range with the increase of zirconium concentration up to  $2$  mol% related to the occupation of  $Zr^{4+}$  ions  $Nb_{Li}$  antisites positions in Li sites. However for crystals doped with higher content of Zr ( $2.5$  mol%) the absorption edge demonstrates the opposite replacement to the visible range of wavelengths referred to the incorporation of  $Zr^{4+}$  ions onto both Li and Nb site inducing the disorder necessary for charge compensation process. Thus, it is considered Zr concentration equal to  $2$

mol% corresponds to a threshold concentration, required for the reduction of the photorefractive effect in the LN crystal.

Table 3.4.1.1.1: Absorption edge as a function of Zr concentration in congruent LN doped samples (LN:Zr1-LN:Zr8) obtained from the absorption spectrum.

Number of samples		LN:Zr1	LN:Zr2	LN:Zr3	LN:Zr4	LN:Zr5	LN:Zr6	LN:Zr7	LN:Zr8
Zirconium concentration (mol%)	0	0.625	0.75	0.875	1	1.25	1.5	2	2.5
Wavelength of absorption edge (nm) at absorption coefficient of $20\text{cm}^{-1}$	326	322	319	318.75	318.5	318	317.7	315	316.3

### Electro-Optic Coefficients

The values of clamped and unclamped EO Pockels coefficients consequently for low and high frequency ranges as a function of Zr molar concentrations are represented in Figure 3.4.1.1.1 and in Tables 3.4.1.1.2, 3.4.1.1.3 respectively. The calculated values,  $n_e^3 r_c$  reported in this figure and tables are obtained from the direct  $n_e^3 r_{113}$  and  $n_e^3 r_{333}$  obtained with interferometric measurements.

For the understudy samples LN:Zr1-LN:Zr8 the effective combined EO coefficient was defined by direct Senarmont method and also calculated estimating the accuracy of the experimental and calculated methods. In Figure 3.2.1.2.1 all coefficients obtained for LN:Zr samples demonstrate the quazi-constant values with the error-bars for all dopant concentrations besides the 2 mol% LN:Zr crystal, which has a lower EO coefficients of about 20% compared to the values for other samples. This change is bigger than including amplitude of the uncertainty. Thus, 2 mol% is considered a threshold concentration if a doping-generated lattice reorganization is realized.

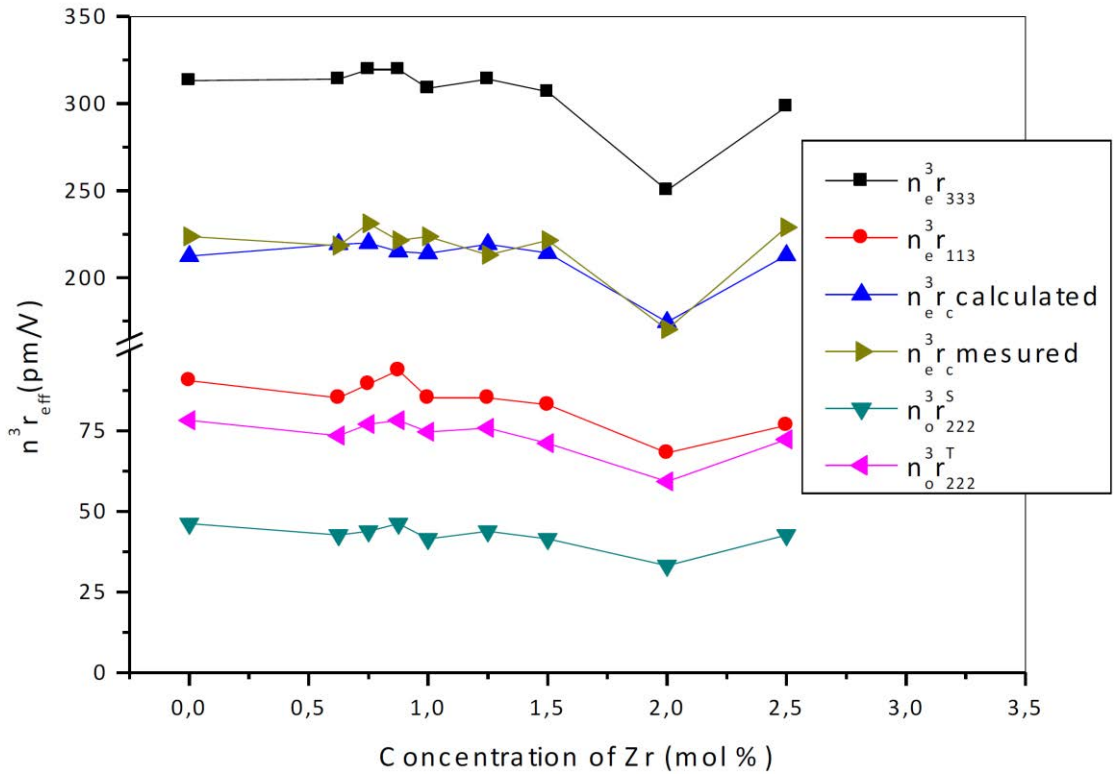


Figure 3.4.1.1.1: Clamped (for high frequency range) and unclamped (for lower frequency range) effective EO coefficients  $n^3 r_{eff}$  depending on zirconium concentration in LN congruent samples.

Table 3.4.1.1.2: Absolute values of EO coefficients for  $r_{222}$  opto-geometric configuration and associated dielectric permittivity for Zr doped LN samples as a function of zirconium molar concentration.

Number of sample	Impurity concentration	Senarmont compensation technique			Dielectric permittivity	
		TRM method		MDM method		
		$r_{222}^T pmv^{-1}$	$r_{222}^S pmv^{-1}$	$r_{222}^T pmv^{-1}$	$\epsilon_{22}^T$	$\epsilon_{22}^S$
	LN-Cg	$6.6 \pm 0.4$	$3.9 \pm 0.3$	$6.4 \pm 0.4$	$87 \pm 5$	$62 \pm 3$
LN:Zr1	0.625%ZrO <sub>2</sub>	$6.1 \pm 0.4$	$3.5 \pm 0.3$	$6.1 \pm 0.4$	$82 \pm 5$	$61 \pm 3$
LN:Zr2	0.75%ZrO <sub>2</sub>	$6.5 \pm 0.4$	$3.7 \pm 0.3$	$6.2 \pm 0.4$	$83 \pm 5$	$62 \pm 3$
LN:Zr3	0.875%ZrO <sub>2</sub>	$6.6 \pm 0.4$	$3.9 \pm 0.3$	$6.4 \pm 0.4$	$84 \pm 5$	$61 \pm 3$
LN:Zr4	1%ZrO <sub>2</sub>	$6.2 \pm 0.4$	$3.5 \pm 0.3$	$6 \pm 0.4$	$84 \pm 5$	$62 \pm 3$
LN:Zr5	1.25%ZrO <sub>2</sub>	$6.4 \pm 0.4$	$3.7 \pm 0.3$	$6.3 \pm 0.4$	$81 \pm 5$	$60 \pm 3$
LN:Zr6	1.5%ZrO <sub>2</sub>	$6 \pm 0.4$	$3.5 \pm 0.3$	$6.1 \pm 0.4$	$83 \pm 5$	$62 \pm 3$
LN:Zr7	2%ZrO <sub>2</sub>	$5 \pm 0.4$	$2.9 \pm 0.3$	$5.2 \pm 0.4$	$72 \pm 5$	$51 \pm 3$
LN:Zr8	2.5%ZrO <sub>2</sub>	$6.1 \pm 0.4$	$3.6 \pm 0.3$	$6 \pm 0.4$	$80 \pm 5$	$59 \pm 3$

Table 3.4.1.1.3: Absolute values of  $r_{113}$  and  $r_{133}$  EO coefficients and dielectric permittivity for Zr doped LN samples as a function of zirconium molar concentration.

Number of sample	Impurity concentration	Interferometric measurement			Senarmont compensation technique		Dielectric permittivity	
		TRM method			TRM method	MDM method		
		$r_{113}^{T,S} pmv^{-1}$	$r_{133}^{T,S} pmv^{-1}$	$r_c^{T,S} pmv^{-1}(\text{calc})$	$r_c^{T,S} pmv^{-1}(\text{meas.})$	$r_c^T pmv^{-1}(\text{meas.})$	$\epsilon_{33}^T$	$\epsilon_{33}^S$
	LN-Cg	8.5±0.6	29.4±2	20±2	3.9±0.3	20.7±1	87±5	35±2
LN:Zr1	0.625%ZrO <sub>2</sub>	8±0.6	29.5±2	20.6 ±2	3.5±0.3	20.3±1	82±5	34.5±2
LN:Zr2	0.75%ZrO <sub>2</sub>	8.4±0.6	30±2	20.7 ±2	3.7±0.3	21.3±1	83±5	35.5 ± 2
LN:Zr3	0.875%ZrO <sub>2</sub>	8.8±0.6	30±2	20.2 ±2	3.9±0.3	20.8±1	84±5	34.7±2
LN:Zr4	1%ZrO <sub>2</sub>	8±0.6	29±2	20.1 ±2	3.5±0.3	21.2±1	84±5	35±2
LN:Zr5	1.25%ZrO <sub>2</sub>	8±0.6	29.5±2	20.6 ±2	3.7±0.3	20.3±1	81±5	34.5±2
LN:Zr6	1.5%ZrO <sub>2</sub>	7.8±0.6	28.8±2	20.1±2	3.5±0.3	20.6±1	83±5	33.3±2
LN:Zr7	2%ZrO <sub>2</sub>	6.4±0.6	23.5±2	16.4±2	2.9±0.3	16.2±1	72±5	29±2
LN:Zr8	2.5%ZrO <sub>2</sub>	7.2±0.6	28±2	20±2	3.6±0.3	21.2±1	80±5	36±2

## Dielectric Permittivity

The results of dielectric constants of  $\epsilon_{22}^T$ ,  $\epsilon_{22}^S$  and  $\epsilon_{33}^T$ ,  $\epsilon_{33}^S$  obtained for understudy samples LN:Zr1-LN:Zr8 are reported in Figure 3.4.1.1.2 and tables 3.4.1.1.2, 3.4.1.1.3 respectively.

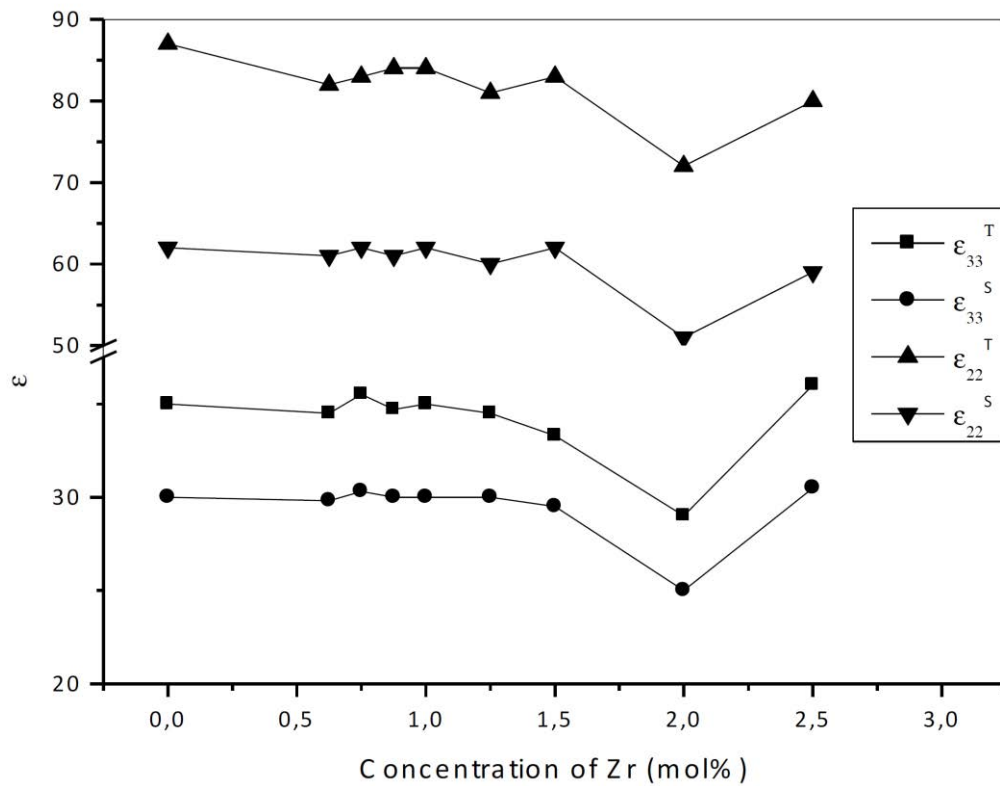


Figure 3.4.1.1.2: Values of dielectric permittivity for different configurations as a function of Zr molar concentration.

Due to the results the dielectric permittivity reproduces the same behavior of EO coefficients for all Zr and In doped (See 3.4.1.2) understudy samples. The  $\Delta\epsilon_{33} = \epsilon_{33}^T - \epsilon_{33}^S$  for LN:Zr is equal about 5 whereas the difference between  $r_c^T$  and  $r_c^S$  ( $r_c = r_c^T - r_c^S$ ) is smaller than the accuracy of EO methods. This difference of dielectric coefficients was generated by the elastic hardness during the electromechanical processes. It was shown that clamped and unclamped effective EO and dielectric coefficients illustrate a kink for Zr concentration equal to 2 mol%. This is the threshold concentration determined by the optical absorption investigation. However, according to the research of Kovacs et al [71] the crystal composition influence on the absorption edge. Thus, the shift of absorption edge to the shorter wavelength range can be attributed by the increase of Li/Nb ratio without increase of Li content due to the introduction of Zr ions. Zr ions incorporating onto the Li site, replace Nb antisites decreasing the Nb

concentration in Li site. The shift of absorption edge to the visible range for higher Zr concentration above threshold concentration leads to the generation of disorder due to the location of Zr ions in both sites (Li and Nb).

**§ 3.4.1.2. In doped crystals**

**Electro-Optic Coefficients.** The graph of frequency dispersions for  $r_{222}$  EO coefficients taken for pure congruent LN and 1.7 mol% LN:In4 samples is given in Figure 3.4.1.2.1. It is visible that the graph is smooth on both parts of piezo-resonances.

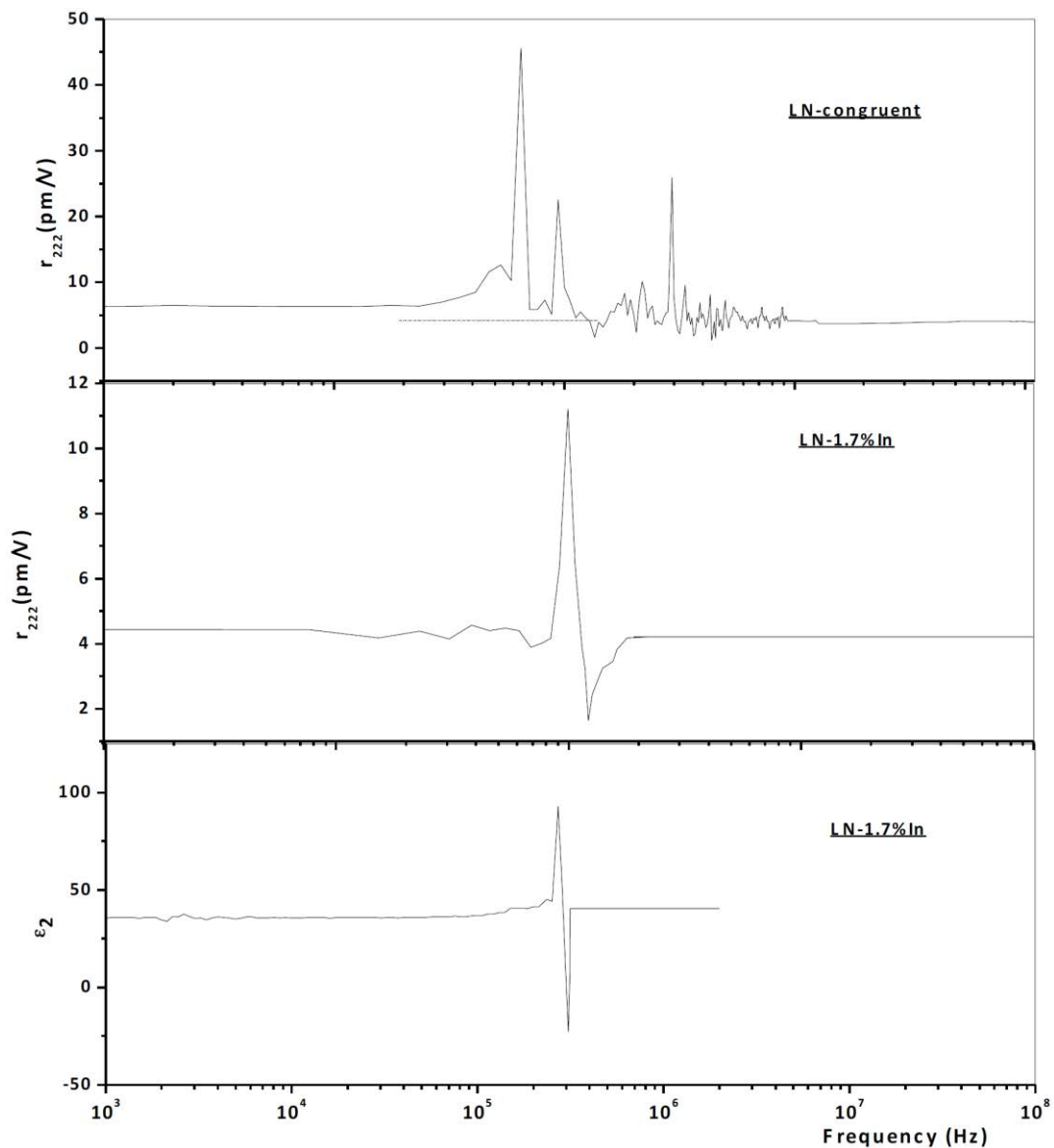


Figure 3.4.1.2.1: The frequency dispersions at  $r_{222}$  opto-geometric configuration for 1.7 mol% In doped LN:In4 and undoped congruent samples. Relationship between frequency dispersions for EO and dielectric coefficients in 1.7 mol% In:LN sample.

The clamped and unclamped EO coefficients as a function of In molar concentration are given in Figure 3.4.1.2.2 and in Table 3.4.1.2.1. According to these results the values obtained by different techniques are in good relationship together:  $r_{222}^S = 4.4 \pm 0.3 \text{ pmv}^{-1}$  for high frequency,  $r_{222}^T = 4.6 \pm 0.3 \text{ pmv}^{-1}$  for lower frequency obtained by TRM method and  $r_{222}^T = 4.8 \pm 0.3 \text{ pmv}^{-1}$  obtained by MDM method.

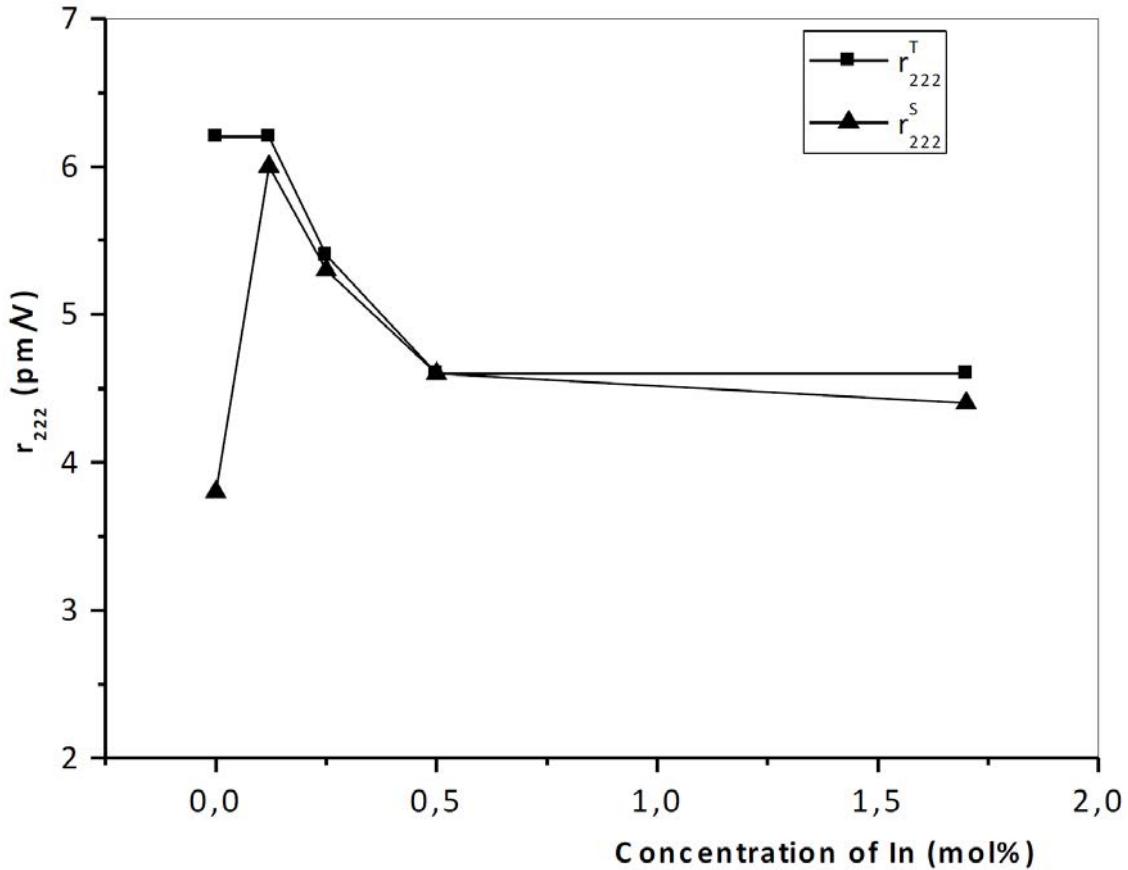


Figure 3.4.1.2.2: Unclamped and clamped EO coefficients as a function of indium molar concentration.

It is visible from Figure 3.4.1.2.2 that both clamped and unclamped EO coefficients illustrate non-monotonous dependence on the In ions and decrease with the increase of indium concentration, whereas a kink appears about at 1.0 mol% for In:LN crystals. For 1.7 mol% LN:In4 sample  $r_{222}^T = 4.6 \pm 0.4 \text{ pmv}^{-1}$ ,  $r_{222}^S = 4.4 \pm 0.4 \text{ pmv}^{-1}$ . This results evident the 25 % decrease of EO coefficients obtained for 0.1 % LN:In sample as well as preventing the high values of unclamped coefficients for In:LN crystals compared to the results for undoped LN crystal. Thus, the acoustic contribution is lower in samples LN:In1-LN:In4 due to the introduction of In ions.

Table 3.4.1.2.1: Absolute values of EO coefficients for  $r_{222}$  opto-geometric configuration and associated dielectric permittivity for LN:In1-LN:In4 samples as a function of indium molar concentration.

Number of sample	Impurity concentration	MDM method	TRM method		Acoustic contribution	Dielectric permittivity		Figure of merit
		$r_{222}^T pmv^{-1}$	$r_{222}^T pmv^{-1}$	$r_{222}^S pmv^{-1}$	$r_{222}^T - r_{222}^S (pmv^{-1})$	$\epsilon_{22}^T$	$\epsilon_{22}^S$	
	LN-Cg	$6.4 \pm 0.4$	$6.6 \pm 0.4$	$3.9 \pm 0.3$	$2.7 \pm 0.4$	$87 \pm 5$	$62 \pm 3$	79
	2%ZrO <sub>2</sub>	$5.2 \pm 0.4$	$5 \pm 0.4$	$2.9 \pm 0.3$	$2.1 \pm 0.4$	$72 \pm 4$	$51 \pm 3$	157
	LN:In4	$4.8 \pm 0.3$	$4.6 \pm 0.3$	$4.4 \pm 0.3$	$0.2 \pm 0.4$	$32 \pm 1$	$31 \pm 1$	200
	LN:In3	$4.6 \pm 0.3$	$4.6 \pm 0.3$	$4.5 \pm 0.3$	$0.1 \pm 0.4$	$32 \pm 1$	$30 \pm 1$	216
	LN:In2	$5.5 \pm 0.4$	$5.4 \pm 0.4$	$5.3 \pm 0.4$	$0.1 \pm 0.4$	$29 \pm 1$	$27 \pm 1$	333
	LN:In1	$6.4 \pm 0.4$	$6.2 \pm 0.4$	$6 \pm 0.4$	$0.2 \pm 0.4$	$34 \pm 3$	$33 \pm 2$	349

### Dielectric Permittivity.

The results of the dielectric measurements for clumped and unclamp coefficients  $\epsilon_{22}^T$ ,  $\epsilon_{22}^S$  for the understudy samples LN:In1-LN:In4 are given in Figure 3.4.1.2.3 and Table 3.4.1.2.1.

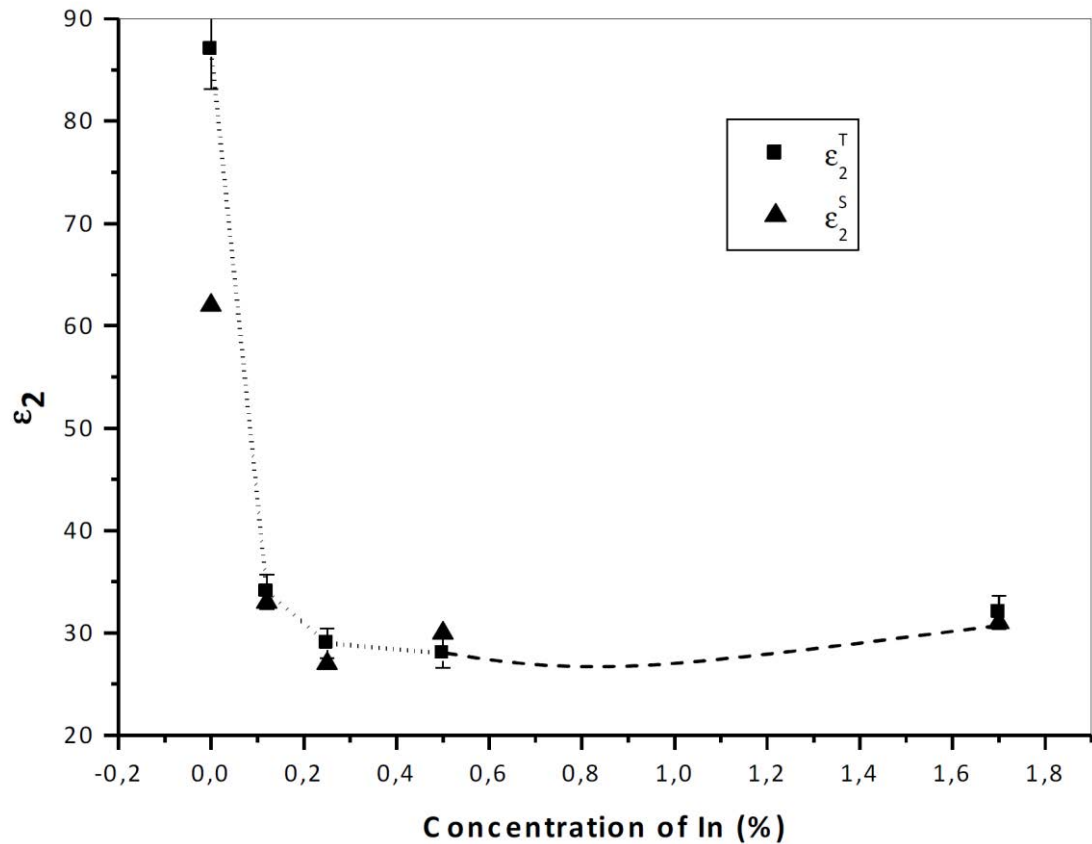


Figure 3.4.1.2.3: Dielectric unclamped ( $\epsilon_{22}^T$ ) and clamped ( $\epsilon_{22}^S$ ) permittivity versus Indium concentration (%) in LN congruent samples.

In LN:In crystals  $\varepsilon_{22}$  illustrates the stability and only a small jump presented across both parts of the piezoelectric resonances, which corresponds to the small electromechanical contribution of static coefficient  $\varepsilon^T$ , difference between  $\varepsilon_{22}^T$  and  $\varepsilon_{22}^S$ . In LN:In crystals the large value of EO coefficients for small frequency range attributed to the acoustic contribution [1], being the difference of values of EO coefficients obtained below and above the piezo-elastic resonances for undoped sample  $r_{222}^a = 2.7 \pm 0.4 \text{ pmv}^{-1}$ , for LN:In samples  $r_{222}^a = 0.2 \pm 0.4 \text{ pmv}^{-1}$ . One can assume a small dependence of EO coefficients on the acoustic contribution in LN:In crystals.

Taking into account the relationship between EO and dielectric effects [1] leading the acoustic contribution to the EO coefficients consequently applying the value of piezo-electric and elasto-optic coefficients  $r_{222}^a = 37 \text{ pmv}^{-1}$  for pure congruent LN crystal [76, 77] was defined, to be in a good agreement with the experimental value within the uncertainty equal to 10%. According to the experimental results, the  $r_{222}$  unclamped and clamped coefficients and dielectric permittivity decrease with the increase of In concentration and prevent a kink about 1 mol% of In concentration. The small jump between two parts of piezo-elastic resonance (low and high frequency range) is due to the absence of electromechanical contribution in LN:In crystal, whereas it is larger for congruent undoped LN sample. On the other hand  $C_{44}$  elastic constant is the highest also for congruent pure LN crystal. The specific small acoustic contribution being the difference between the values of the EO coefficients obtained below and above the piezoelastic resonances can also be linked to the noticeable decrease of the optical damage in LN:In. These phenomena were attributed to the fact that In ion being trivalent, it may be incorporated simultaneously in both lattice cation positions ( $\text{In}_{\text{Li}}^{2+}$  and  $\text{In}_{\text{Nb}}^{2-}$ ) providing a possibility for charge self-compensation [39]. This proves that  $\text{Nb}_{\text{Li}}$  antisites cannot co-exist with In ions or, in other words,  $\text{Nb}_{\text{Li}}$  is completely cancelled even at In concentration  $< 2$  mol% due to the simultaneous incorporation of In ions in both Li and Nb sites.

Indium being non-photorefractive ion, is attractive material due to the lowest threshold concentration, thus, it can be used to increase the photoconductivity [41]. The introduction of In ions the absorption edge remains invariable compared to the optical spectrum for pure LN crystals grown from the same charge.

### § 3.4.2. LN crystals doped with transition metal (Fe) ions

#### Electro-Optic Coefficients

As at room temperature  $LiNbO_3$  crystal belongs to an optically uniaxial rhombohedral crystallographic group with point-group symmetry  $C_{3v} = 3m$ . thus, the EO coefficients of interest are the direct  $r_{22}$ ,  $r_{13}$  and  $r_{33}$  EO coefficients and the  $r_c$  coefficient calculated from the relation 3.1.1.1.2.5.

Following the description of the setups and methods presented above, the coefficients of the third column of the EO tensor,  $r_{13}$  and  $r_{33}$ , plotted in Figure 3.4.2.1 versus the composition, were experimentally obtained applying the MDM method with the two-beams interferometric setup.

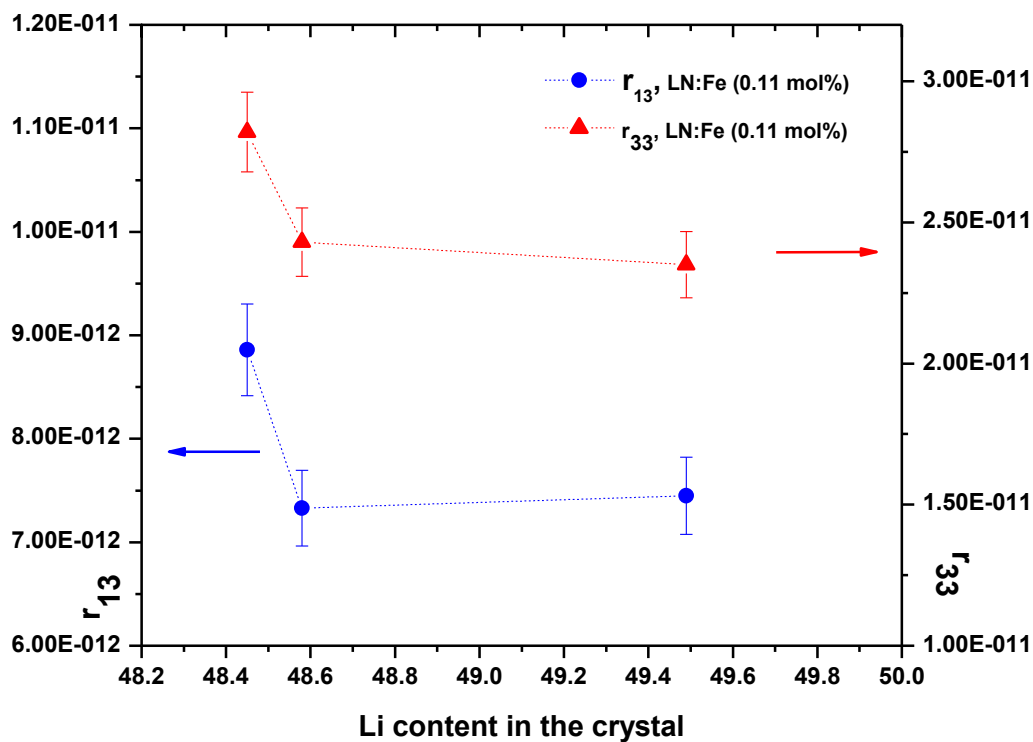


Figure 3.4.2.1: The  $r_{13}$  and  $r_{33}$  EO coefficients of iron doped LN crystals as function of the composition.

Measurements of the  $r_{22}$  EO coefficient of the various samples were done applying both FDEOM and MDM techniques with the one-beam Sénarmont setup. The  $r_{22}$  coefficient was plotted versus the composition in Figure 3.4.2.2.

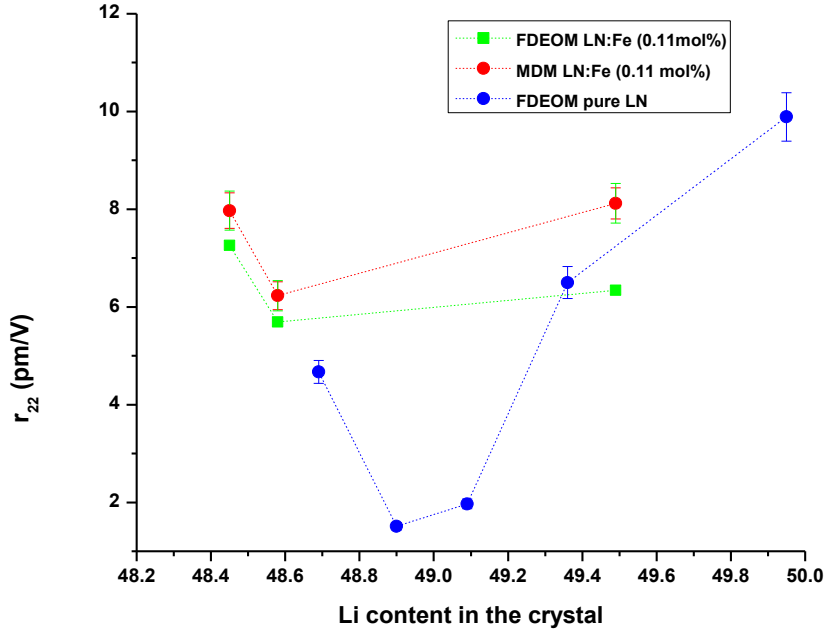


Figure 3.4.2.2: The  $r_{22}$  EO coefficient for un-doped and iron doped lithium niobate crystals as function of the composition determined by both the FDEOM and MDM methods.

It is to be of note that the lines in Figures 3.4.2.1 and 3.4.2.2 relying the experimental points are just guides for the eyes. Indeed, if we consider, Figure 3.4.2.2, the behavior of  $r_{22}$  with composition for pure crystals, we notice very low values of the coefficient for intermediary composition. In the iron-doped series, samples in this intermediary composition range were unfortunately absent. One can see that EO coefficients  $r_{22}$ ,  $r_{13}$  and  $r_{33}$  present the same behavior with the variation of the crystal composition with higher amplitude than the accuracy of the method. This behavior of the EO coefficients points out a slight increase for crystals with composition varied from congruent to near stoichiometric crystal. This non-monotonous dependence of the EO coefficients on the composition will be discussed further in view of dielectric properties. We also notice a discrepancy between results obtained with both methods in Figure 3.4.2.2. This discrepancy can be attributed to the effect of the bias dc field used in the FDEOM method than can induce some electrical polarization effects as an electric field screening due to residual space charges in crystals. Thus, even if currently, the electro-optic effect is considered relative to the external electric-field, i.e. with the values here obtained with the MDM method, the results obtained with the FDEOM method is important

when the internal electric field relative to the presence of space charge field has to be considered for the electro-optic effect instead of the external electric field as in photorefractive process or photorefractive applications.

In Figures 3.4.2.3, the  $r_c$  coefficient calculated from the relation Eq. 3.1.1.1.5 was compared to those experimentally determined by both FDEOM and MDM methods with the one-beam Sénarmont setup.

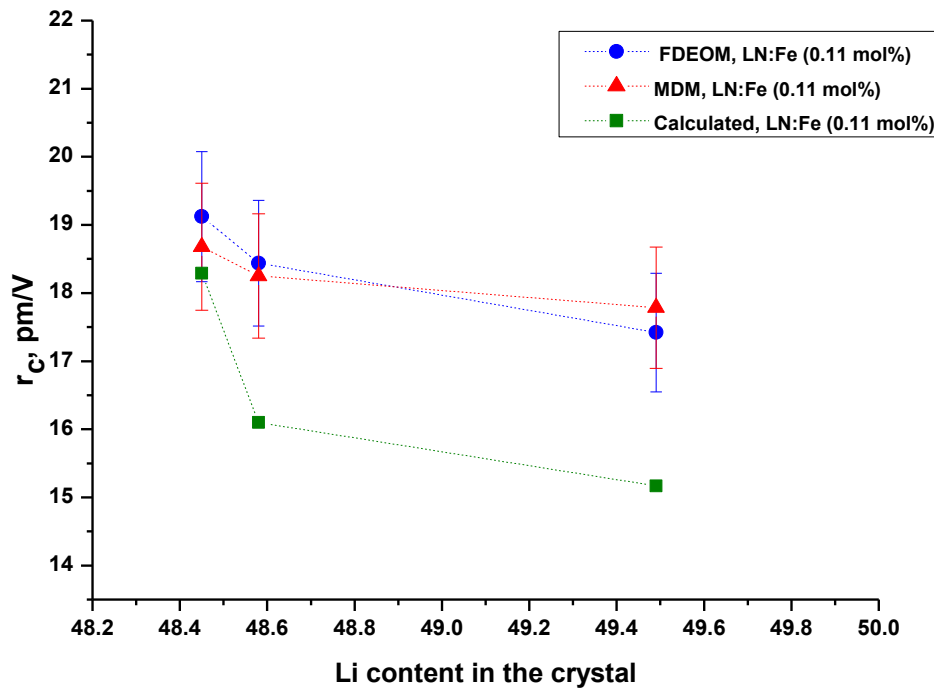


Figure 3.4.2.3: Comparison between the calculated  $r_c$  EO coefficients from  $r_{13}$  and  $r_{33}$  with the  $r_c$  coefficient experimentally determined by FDEOM and MDM methods as function of the understudy samples LN:Fe1-1 ÷ LN:Fe1-3.

The behaviors of  $r_c$  in Figure 3.4.2.3 present the same evolution with the composition and point a true agreement between calculated and measured values of  $r_c$  in the used accuracy range. From the Figure 3.4.2.3 it is noticeable that the EO coefficient  $r_c$  in Fe doped LN crystals monotonously diminishes when the crystal composition changes from congruent to intermediary and then it increases again for near-stoichiometry crystal. It is also obvious to remarks that this agreement also exists in calculated  $r_c$  by using the values of  $r_{13}$  and  $r_{33}$  experimental obtained by both FDEOM and MDM methods even if these two direct

coefficients present some discrepancies with the composition when they are individually considered as shown in Figure 3.4.2.2. This fact confirms that the applied dc electric field in the FDEOM method induces the same electrical polarization effects in all crystals of the series. With the hypothesis that this effect is due to the residual space charges in crystals, the amount of these charges is the same in all crystals, thus whatever is the composition.

Finally, our results point that only slight changes following the same behavior in all unclamped direct EO coefficients with the composition exist in iron doped LN crystal. In inorganic crystal the unclamped EO coefficient is expressed as:

$$r^T = r^I + r^a + r^e \quad (3.4.2.1),$$

with  $r^I$  the ionic contribution,  $r^a$  the acoustic contribution link to the piezo-optic effect and  $r^e$  the direct electronic contribution relative to the second harmonic contribution. It was previously shown that in congruent LN crystal,  $r_c^a$  is smaller than 1pm/V and  $r_c^e$  is around 5pm/V. Consequently, the ionic contribution is the most important contribution in the absolute value and in the relative change with the composition of the unclamped EO coefficients of the third column of the tensor. Applying the same approach concerning the behavior of  $r_{22}$  with the composition, we notice that in this opto-geometric configuration, the piezo-optic contribution, i.e.  $r_{22}^a$  is equal to 3.3 pm/V for the congruent composition, which is comparable to the ionic contribution  $r_{22}^I$ . Thus, the change observed in the unclamped EO  $r_{22}^T$  with the composition originates from both changes in the ionic and piezo-optic contributions.

### Dielectric Permittivity

The static dielectric permittivities  $\varepsilon_{11}$  and  $\varepsilon_{33}$  as function of composition of crystals LN:Fe1-1 ÷ LN:Fe1-3 are shown in Figure 3.4.2.4.

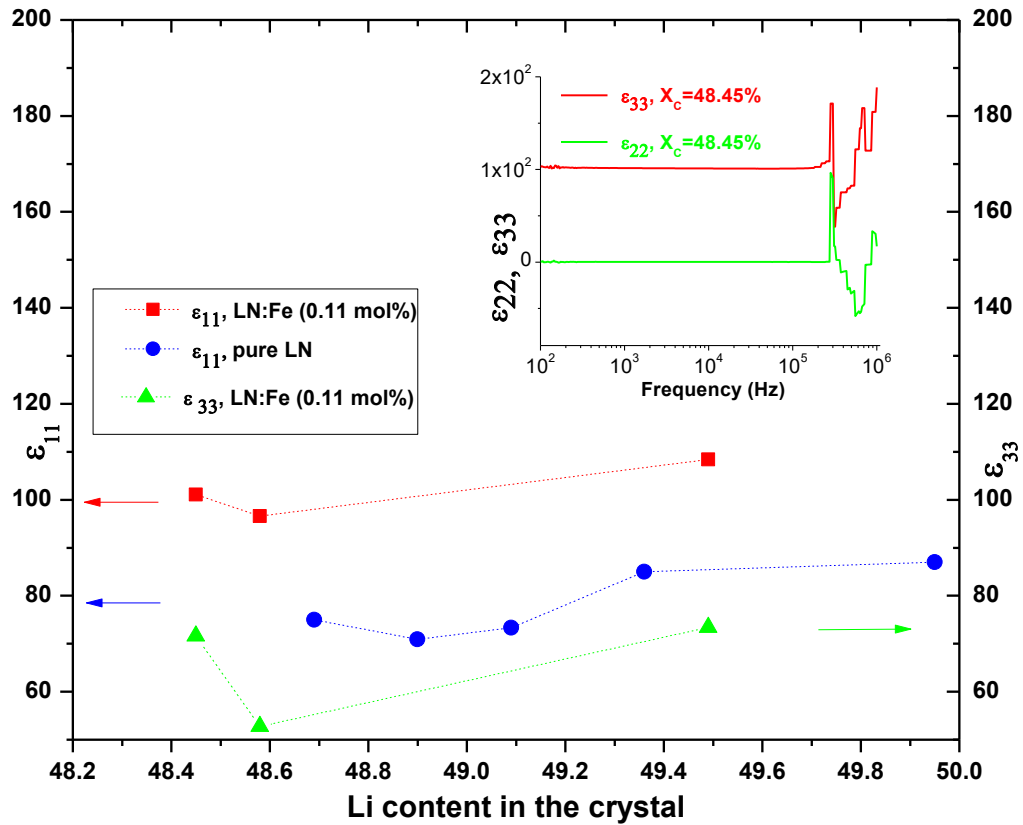


Figure 3.4.2.4: Static dielectric permittivities  $\epsilon_{11}$  ( $= \epsilon_{22}$ ) and  $\epsilon_{33}$  of iron doped lithium niobate crystals as function of the composition. Inset: Frequency dependence of the dielectric permittivity  $\epsilon_{33}$  of congruent iron doped crystal presented as example of experimental obtained response).

The dielectric permittivities for all crystals remain constant over a wide frequency range as presented for the congruent crystal in the inset of Figure 3.4.2.4. Experimentally and due to the limitation of the LC meter, we cannot obtain the high frequency dielectric permittivities at the upper side of the piezoelectronic resonances.

Nevertheless, as expected, we observed in Figure 3.4.2.4 that the dielectric permittivities remarkably reproduce the behavior of the corresponding EO coefficients.

In Table 3.4.2.1, we summarize the compositions and growing characteristics of melts and crystals and the electro-optic coefficients and dielectric permittivities obtained by experimental measurement in the current study.

Table 3.4.2.1: EO coefficients and corresponding dielectric permittivities of the understudy samples LN:Fe1-1÷LN:Fe1-3. In calculation of the EO coefficients, we assumed the typical values of the refractive indices for pure congruent crystal (at T=25°C and  $\lambda=632.8$  nm). See the text.

N°	$X_m$ = [Li] /[Li + Nb]	$X_c$ = [Li] /[Li + Nb]	$r_{22}$ (pm/V)		$r_{13}$ (pm/V)	$r_{33}$ (pm/V)	$r_c$ (pm/V)			$\epsilon_{22}$	$\epsilon_{33}$
			FDEOM meth.	MDM meth.			FDEOM meth.	MDM meth.	Calculation		
			interferometric								
LN:Fe1-1	48,45%	48.45	7.26	7,97	8.86	28.2	19.12	18.68	18.29	101,06	71,61
LN:Fe1-2	50,0%	48.58	5,69	6,23	7.33	24.3	18.44	18.25	16.10	96,57	52,74
LN:Fe1-3	54,5%	49.49	6.34	8.12	7.45	23.5	17.42	17.79	15.17	108,40	73,42

The non-monotonous behavior with the composition of the dielectric permittivity and EO coefficients have been reported with the variation of the composition of a crystal. The behavior of dielectric permittivity is remarkably similar to the change of electro-optical coefficients at variation of the composition. The coefficients of third column of EO tensor  $r_{13}$ ,  $r_{33}$  as well as combined EO coefficient  $r_c$  illustrate a variation with the increase of Li content. Furthermore EO Pockels coefficient for  $r_{22}$  opto-geometrical configuration and dielectric permittivities vary non monotonously as a function of crystal composition: it is the biggest for congruent Fe:LN sample, the lowest for off congruent sample LN:Fe1-2 and and it has the intermediate values for the near stoichiometric sample LN:Fe1-3.

In  $ABO_3$  compounds electro-optic coefficients are generally attributed to the ionic and electronic polarizabilities of the Nb ions (Li poor crystals) and the deformability of the oxygen octahedron around Li (Li rich crystals) [20, 26, 28, 50, 53]. Among them, the ionic polarizability plays a dominant role for the doping effect [38]. For LN crystals doped with a small amount of iron, the polarizability as well as Pockels EO coefficients are governed by the content of intrinsic defects [26,28] resulted by the Li deficiency, Nb antisite in A (Li) site and impurity ions as well.

For the linear EO coefficients  $r_{13}$ ,  $r_{33}$ ,  $r_c$  the role of the electro-mechanical contribution is negligible [78]. The mentioned EO and dielectric coefficients mainly depend on the variation of Nb ions polarizability mechanism along  $z$  axis due to the change in the charge compensation processes in crystal with varying composition from congruent to near stoichiometry. As mentioned above, we remind that photorefractive ions incorporate onto both A (Li) and B (Nb) sites. In Li-poor crystals (congruent crystal LN:Fe) Fe ions occupying A site displacing  $Nb_{Li}$  antisites from A site to their natural B site, thus increasing the polarizability of Nb ions consequently the Pockels EO coefficients  $r_{13}$ ,  $r_{33}$ ,  $r_c$  illustrate higher values [28]. Moreover, it also indicates that in LN:Fe crystals, the additional modulation of Nb ions polarizability exists comparing to the pure LN crystals due to the presence of impurity Fe ions changing the content of Nb antisites [20]. With the variation of crystal composition from congruent to near-stoichiometric due to the increase of Li content in A site Fe ions mainly incorporate onto B site decreasing the polarizability of Nb ions in their own site. Thus, due to the smaller

polarizability of Nb ions EO coefficients in  $r_{13}$ ,  $r_{33}$  optic-geometrical configuration and combined coefficient  $r_c$  decrease in near-stoichiometric crystals.

Concerning the EO coefficient  $r_{22}$  and its corresponding dielectric permittivity  $\epsilon_{22}$  for Fe:LN crystals, they are in the agreement with the results reported earlier for pure LN crystals with different compositions ( $X_c=48,51\div 49,95$ ) with the same non monotonous variations with the composition[18]. Whereas the iron doping effect modified the EO and dielectric coefficients compared to the results reported for pure LN crystals especially for one with close to stoichiometric composition. The EO coefficient  $r_{22}$  corresponds to a modulation of the birefringence consequently polarizability in the plane normal to the ferroelectric axis  $z$ , induced by the applied electric field along the axis  $y$  (or  $x$ ). Thus, a contribution for EO coefficient  $r_{22}$  is related to the crystal deformation induced via the piezoelectric effect which gives rise to a large piezo-optic contribution to the EO coefficient and a large electromechanical contribution to the dielectric permittivity as it observed at constant stress range (in the low frequency range from acoustic resonance up to 1 MHz). In ref. [20, 28], authors shown that the behavior of  $r_{22}$  and  $\epsilon_{22}$  are related to the elastic contributions, mainly the elasto-optic coefficient  $C_{44}$ , which is closely dependent to the Li content. They showed that this coefficient presents the same behavior of variation as EO and dielectric coefficients with composition [20,79]. For perfect crystal the elastic constant increases with the increase of defect points [80]. The reason of the non-symmetric dependence of elastic coefficients consequently observed dielectric and EO coefficients on the amount of intrinsic defects may be the presence of dislocations of main ions from their crystallographic positions due to the introduction of iron ions or density fluctuations  $C_{44} \sim \rho$  [81, 82]. In A site iron ions shift Li ions along Z axis proved by ENDOR, EPR measurements. As the A and B sites occupied by Fe ions introduced electronic and physical defects in the structure due to the different valence state, ionic radii and atomic mass compared to the natural Li and Nb ions [83-85] inducing a local disorder mainly caused by nearby charge-compensating effects. Thus, the change of the localization of iron ions with the composition will straightforwardly induce a non-monotonously variation of the  $r_{22}$  coefficient and related dielectric permittivity with the LN crystal compositions.

### § 3.5. Conclusion-Chapter 3

The unclamped (low frequency range) and clamped (high frequency range) components of third column of EO tensor  $r_{113}$  and  $r_{333}$ , combined EO coefficient  $r_c$  for zirconium doped LN crystals LN:Zr1-LN:Zr8 and EO linear coefficients for opto-geometric configuration  $r_{222}$  for both series of zirconium and indium doped LN:In1-LN:In4 samples have been investigated. Also the associated dielectric coefficients for low and high frequency ranges have been measured for both series of Zn and In doped crystals mentioned above as well as the piezo-optic contributions were calculated for samples LN:In1-LN:In4. All series of samples have been grown from congruent melt with varying impurity concentration. EO coefficients  $r_{113}$  and  $r_{333}$ , of samples LN:Zr1-LN:Zr8 were observed by Mach-Zehnder interferometric arrangement whereas coefficients  $r_c$  and  $r_{222}$  were investigated by using one-beam Senarmont setup with the help of MDM and TRM methods. The unclamped and clamped obtained results of EO coefficients and associated dielectric permittivity for all opto-geometric configurations emphasize the specific value of molar concentration of zirconium where the coefficients illustrate a kink. This concentration of 2 mol % is considered to be threshold concentration of zirconium where above mentioned coefficients decrease about of 20 %.

We have shown that in LN:In congruent crystals with  $In_2O_3$  concentration in the studied range, i.e. from 0.12 mol% to 1.7 mol%, the EO coefficient  $r_{222}$  and the dielectric coefficient  $\epsilon_{22}$  possess only a small acoustic contribution compared to pure congruent LN crystals or to LN:Zr congruent one due to the smaller deformation along  $x$  (or  $y$ ) axis generated by applied voltage. This specific small acoustic contribution being the difference between the values of the EO coefficients obtained below and above the piezoelastic resonances can also be linked to the noticeable decrease of the optical damage in LN:In. These phenomena were attributed to the fact that In ion being trivalent, it may be incorporated simultaneously in both lattice cation positions ( $In_{Li}^{2+}$  and  $In_{Nb}^{2-}$  providing a possibility for charge self-compensation. This prove that  $Nb_{Li}$  antisites cannot co-exist with In ions or, in other words,  $Nb_{Li}$  is completely cancelled even at In concentration  $< 2$  mol% due to the simultaneously incorporation of In ions in both Li and Nb sites.

EO coefficients of iron doped LN samples have been determined for two opto-geometric configurations as a function of crystal composition and an introduction of Fe ions at room

temperature using He-Ne laser beam with 632,8 nm wavelength. In the samples doped with a constant content of iron (0.06 wt%) the crystal composition was varied from congruent to near stoichiometric. In the first opto-geometric configuration involving  $r_{33}$  and  $r_{13}$  and  $r_c$  coefficients the external electric field was applied parallel to the crystallographic axis of the sample, when the laser beam propagated along the  $y$  (equivalent  $x$ ) axis. Vice versa in the second configuration employed for  $r_{22}$  the applied electric field was along the  $y$  ( $x$ ) direction, when the beam propagation was parallel to the  $c$  axis of sample. The one-beam ellipsometric Senarmont technique with FDEOM and MDM methods were utilized to measure EO coefficient in  $r_{22}$  configuration and combined  $r_c$  coefficient, whereas the components of the third column of EO tensor  $r_{33}$  and  $r_{13}$  was investigated with the aid of interferometric Mach-Zehnder optical arrangement applying MDM method. Besides the experimental analysis linear coefficient  $r_c$  was calculated using the relationship with  $r_{33}$  and  $r_{13}$  coefficients. Assuming the link between EO coefficients and the dielectric permittivity concerning their behaviors related to the composition, parameters such as temperature and the frequency, the linear dielectric constants  $\varepsilon_{22} = \varepsilon_{11}$  and  $\varepsilon_{33}$  have been measured at room temperature as a function of frequency. Taking the experimental details into account it can be assumed that the measurements concern the unclamped values of EO coefficients and dielectric permittivity.

The decrease of EO coefficients  $r_{13}$ ,  $r_{33}$  and  $r_c$  has been recorded with the increase of  $Li_2O$  content in the crystal with higher amplitude than the accuracy of the method. The measured and computed results of combined coefficient  $r_c$  being in a true agreement illustrate the same evolution in the accuracy range with the composition variation. In the variation of EO coefficients  $r_{13}$ ,  $r_{33}$  and  $r_c$  the variation of Nb ions polarizability mechanism places the key role caused by the change of the occupation site of iron ions. In Li poor sample Fe ions mainly occupy A site, however with the increase of Li content in sample composition Fe ions incorporate both A and B sites consequently decreasing the polarizability of Nb ions in their own B site.

However the non monotonous variation of EO coefficient  $r_{22}$  can be related to the intrinsic defects produced due to dislocations of main ions from their crystallographic positions related to the introduction of iron ions or a density fluctuations for the charge compensation. The non-monotonous variation of above mentioned coefficients with the change of sample

composition depends on the content of the intrinsic defects produced due to the charge compensation. As expected the results obtained for dielectric permittivity  $\epsilon_{33}$  and  $\epsilon_{22} = \epsilon_{11}$  remarkably reproduce the behavior of the corresponding EO linear coefficients  $r_{22}$  related to the crystal deformation generated through the piezo-optic contribution.

### ***References-Chapter 3***

1. A. Yariv, Pochi Yeh, "Optical Waves in Crystals: Propagation Control of Laser Radiation", John Wiley & Sons, New York, (1984).
2. J. A. Valdmanis, "Semiconductors and Semimetals", Vol. 28, Ultrafast Science Laboratory, University of Michigan, 1990.
3. I.P. Kaminov, "An Introduction to Electrooptic Devices", Academic Press, New- York, 1974.
4. M. Didomenico Jr., S.H. Wemple, "Oxygen-Octahedra Ferroelectrics. I. Theory of Electro-optical and Nonlinear Optical Effects", J. Appl Phys. Vol. 40, Numb. 2, pp. 720-734 (1969).
5. F. Abdi, M.D. Fontana, M. Aillerie: Non Linear Opt. 16, 65 (1996)
6. M. Aillerie, N. Theofanous, M. D. Fontana, "Measurement of the Electro-optic Coefficients: Description and Comparison of the Experimental Techniques", Appl. Phys. B 70, pp.317–334 (2000).
7. J.F.Nye, "Physical Properties of Crystals", Clarendon Press Oxford, 1957.
8. D. Eimerl, "Crystal Symmetry and the Electrooptic Effect", IEEE J. Quantum Electron. Vol. QE-23, No. 12, pp. 2104-2115 (1987).
9. I.P. Kaminow, E.H. Turner, "Electrooptic light modulators", Appl. Opt. Vol. 5, Issue10, pp. 1612-1628 (1966).
10. G.N. Ramachandran, S. Ramaseshan: In Handbuch der Physik, Springer, Berlin, Heidelberg, p. 217 (1961).
11. M. D. Fontana, K. Laabidi, B. Jannot, M. Maglione, P. Jullien, "Relationship Between Electro-Optic, Vibrational and Dielectric Properties in BaTiO<sub>3</sub>", Sol. St. Comm., Vol. 92, No. 10, pp. 827-830, 1994.
12. J. P. Salvestrini, M. D. Fontana, B. Wyncke, and F. Brehat, "Comparative measurements of the frequency dependence of the electrooptical and dielectric coefficient in inorganic crystals", Nonlinear Opt. 17, pp. 271-280 (1997).
13. Agilent Basics of Measuring the Dielectric Properties of Materials, Application Note, Printed in USA (2006).
14. S.H. Wemple, M. Di. Domenico, J, Appl. Solid State Science 3 (Edited by R. Wolfe), Academic Press, p. 264 (1972).

15. G. E. Peterson, A. A. Ballman, P. V. Lenzo, and P. M. Bridenbaugh, "Electrooptic Properties of LiNbO<sub>3</sub>", Appl. Physics Lett. Vol. No. 5, pp. 62-64 (1964).
16. P. V. Lenzo, E. G. Spencer, K. Nassau, "Electro-Optic Coefficients in Single-Domain Ferroelectric Lithium Niobate", J. Opt. Soc. Of Am., Vol. 56, Numb. 5, pp. 633-635 (1966).
17. E.H. Turner, "High-Frequency Electro-optic Coefficients of Lithium Niobate", Appl. Phys. Letters Vol. 8, Numb 11, pp. 303-304 (1966).
18. H. Iwasaki, H. Toyoda, N. Nizeki, H. Kubota, "Temperature and Optical Frequency Dependence of the DC Electro-optic Constant  $r_{22}^T$  of LiNbO<sub>3</sub>", Japanese J. Appl. Phys. Vol. 6, No. 14, pp. 1419-1422 (1967).
19. A. Chirakadze, S. Machavariani, A. Natsvlishvili, B Hvitia, "Dispersion of the Linear Electro-optic Effect in Lithium Niobate", J. Appl. Phys. 23 pp. 1216-1218 (1990).
20. F. Abdi, M. Aillerie, P. Bourson, M. D. Fontana, and K. Polgar, "Electro-optic properties in pure LiNbO<sub>3</sub> crystals from the congruent to the stoichiometric composition", J. of Appl. Phys. Vol. 84, Numb. 4, pp. 2251-2254 (1998).
21. I.P. Kaminov, W. D. Johnston, "Quantitative Determination of Sources of the Electro-Optic Effect in LiNbO<sub>3</sub> and LiTaO<sub>3</sub>", Phys. Rev. Vol 160, Numb. 3 (1967).
22. J. A. de Toro, M. D. Serrano, A. García Cabañes, and J. M. Cabrera, "Accurate Interferometric Measurement of Electro-optic Coefficients: Application to Quasi-Stoichiometric LiNbO<sub>3</sub>," Opt. Commun. 154(1-3), pp. 23-27, (1998).
23. T. Fujiwara, M. Takahashi, M. Ohama, A. J. Ikushima, Y. Furukawa, and K. Kitamura, "Comparison of electro-optic effect between stoichiometric and congruent LiNbO<sub>3</sub>", Electron. Lett. Vol. 35, Issue 6, pp. 499-501 (1999).
24. A. Méndez, A. García Cabañes, E. Diéguez, and J. M. Cabrera, "Wavelength dependence of electro-optic coefficients in congruent and quasi-stoichiometric LiNbO<sub>3</sub>", Electron. Lett. Vol. 35, No. 6, pp. 498-499 (1999).
25. Y. Kondo, T. Fukuda, Y. Yamashita, K. Yokoyama, K. Arita, M. Watanabe, Y. Furukawa, K. Kitamura and H. Nakajima, "An Increase of More Than 30% in the Electrooptic Coefficients

- of Fe-doped and Ce-doped Stoichiometric LiNbO<sub>3</sub> Crystals”, Jpn. J. Appl. Phys. Vol. 39 pp. 1477–1480(2000).
26. K. Chah, M. D. Fontana, M. Aillerie, P. Bourson, and G. Malovichko, “Electro-optic properties in undoped and Cr-doped LiNbO<sub>3</sub> crystals,” Appl. Phys. B: Lasers Opt. 67, pp. 65-71 (1998).
27. I.V. Kityk, M. Makowska-Janusik, M.D. Fontana, M. Aillerie, F. Abdi, “Band structure treatment of the influence of nonstoichiometric defects on optical properties in LiNbO<sub>3</sub>”, J. Appl. Phys. 90(11), pp. 5542-5549 (2001).
28. F. Abdi, M. D. Fontana, M. Aillerie, P. Bourson, “Coexistence of Li and Nb Vacancies in the Defect Structure of Pure LiNbO<sub>3</sub> and its Relationship to Optical Properties”, Appl. Phys. A 83, pp. 427–434 (2006).
29. K. Yonukera, L. Jin, and K. Takizawa, “Measurement of Wavelength Dependence of Electro-Optic Coefficients  $r_{22}$  of Non-doped and 5% MgO-doped Congruent LiNbO<sub>3</sub> Crystals and 1.8% MgO-doped Quasi-stoichiometric LiNbO<sub>3</sub> Crystal by Multiple Reflection Interference Method”, Opt. Rev. Vol. 14, No. 4 pp. 194–200 (2007).
30. W.-Y. Du, Z.-B. Zhang, Sh. Ren, W.-H. Wong, D.-Y. Yu, E. Yue-B. Pun, De-L. Zhang, “Note: Electro-optic Coefficients of Li-deficient MgO-doped LiNbO<sub>3</sub> crystal”, J. Rev. Sc. Instr. 87, pp. 096105/1-096105/3 (2016).
31. M. Aillerie, F. Abdi, M. D. Fontana, N. Théofanous, and E. Abarkan, “Accurate Measurements of the Electro-optic Coefficients and Birefringence Changes Using an External Modulation Signal”, Rev. Sc. Instr., Vol. 71, No.4, pp. 1627-1634 (2000).
32. B. Kang, B. K. Rhee, Gi-T. Joo, “Variation of Electro-optic Coefficients in MgO-doped LiNbO<sub>3</sub> Single Crystals”, Materials Letters 60, Issue 16/17, pp. 2306–2308 (2006).
33. B. C. Grabmaier, W. Wersing, W. Koestler, “Properties of Undoped and MgO-doped LiNbO<sub>3</sub>; Correlation to the Defect Structure”, J. Cryst. Growth, Vol. 110, Issue 3, pp. 339-347 (1991).
34. I.W. Kim, B.C. Park, B.M. Jin, A.S. Bhalla, J.W. Kim, “Characteristics of MgO-doped LiNbO<sub>3</sub> Crystals”, J. Mater. Lett. Vol. 24, Issue 1-3, pp. 157-160 (1995).

35. T.R. Volk, V.I. Pryalkin, N.M. Rubinina, "Optical-damage-resistant LiNbO<sub>3</sub>: Zn crystal". *Opt. let.*, 15(18), pp. 996-998 (1990)
36. Y. Kong, S. Liu, Y. Zhao, H. Liu, S. Chen, J. Xu, "Highly optical damage resistant crystal: Zirconium-oxide-doped lithium niobate". *Appl. Phys. Lett.*, 91(8), pp. 081908 (2007).
37. M. Aillerie, P. Bourson, M. Mostefa, F. Abdi, M.D. Fontana, "Photorefractive damage in congruent LiNbO<sub>3</sub>. Part I. Zinc doped lithium niobate crystals". *J. of Phys: Conf.e Ser.* 416(1), pp. 012001 (2013).
38. F. Abdi, M. Aillerie, M. Fontana, P. Bourson, T. Volk, B. Maximov, S. Sulyanov, N. Rubinina and M. Wohlecke, "Influence of Zn doping on electrooptical properties and structure parameters of lithium niobate crystals.", *Appl. Phys. B: Lasers Opt.* 68, pp. 795-799 (1999).
39. T. Volk, M. Wöhlecke, N. Rubinina, N.V. Razumovski, F. Jermann, C. Fischer, R. Böwer, "LiNbO<sub>3</sub> with the damage-resistant impurity indium", *J. Appl. Phys. A*, 60(2), pp. 217-225 (1995).
40. Y. Kong, J. Wen, H. Wang, "New doped lithium niobate crystal with high resistance to photorefractive-LiNbO<sub>3</sub>: In", *J. Appl. Phys. Lett.*, 66(3), pp. 280-281 (1995).
41. H. Qiao, J. Xu, Q. Wu, X. Yu, Q. Sun, X. Zhang, G. Zhang, T. R. Volk, "An Increase of Photorefractive Sensitivity in In:LiNbO<sub>3</sub> Crystal", *Opt. Mat.* Vol. 23, Issue 1-2, pp. 269-272 (2003).
42. M. Nakamura, S. Takekawa, Y. Liu, K. Kitamura, "Crystal growth of Sc-doped near-stoichiometric LiNbO<sub>3</sub> and its characteristics", *J. of Cryst. Gr.*, 281(2-4), pp. 549-555 (2005).
43. L. Wang, S. Liu, Y. Kong, S. Chen, Z. Huang, L. Wu, R. Rupp, J. Xu, "Increased optical-damage resistance in tin-doped lithium niobate", *J. Opt. let.*, 35(6), pp. 883-885 (2010).
44. F. Rossella, D. Grando, P. Galinetto, V. Degiorgio and E.Kokanyan, "Photoconductive and Electro-Optical Properties of Hf Doped Lithium Niobate Crystals", *Ferroelectrics*, 352, pp. 143-147, 2007.

45. V. Degiorgio, E.P. Kokanyan, L. Razzari, P. Minzioni, I. Cristiani, “High-photorefractive resistance of hafnium-doped, single-domain, and periodically-poled lithium niobate crystals”. In *Integrated Optics and Photonic Integrated Circuits*, 5451, pp. 59-67 (2004).
46. E.P. Kokanyan, L. Razzari, I. Cristiani, V. Degiorgio, J.B. Gruber, “Reduced photorefractive in hafnium-doped single-domain and periodically poled lithium niobate crystals”, *J. Appl. Phys. Lett.*, 84(11), pp. 1880-1882 (2004).
47. M. Abarkan, M. Aillerie, J.P. Salvestrini, M.D. Fontana, E.P. Kokanyan, “Electro-optic and Dielectric Properties of Hafnium-doped Congruent Lithium Niobate Crystals”, *J. Appl. Phys. B* 92 pp. 603–608 (2008).
48. G. Nava, P. Minzioni, W. Yan, J. Parravicini, D. Grando, E. Musso, I. Cristiani, N. Argiolas, M. Bazzan, M.V. Ciampolillo, A. Zaltron, C. Sada, V. Degiorgio, “Zirconium-doped lithium niobate: photorefractive and electro-optical properties as a function of dopant concentration”, *Opt. Mat. Exp.*, 1(2), pp. 270-277 (2011).
49. K. Chah, M. Aillerie, M.D. Fontana, G. Malovichko, E. Kokanyan, “Electro-optical properties of chromium-doped  $\text{LiNbO}_3$  crystals”, *J. Ferroelectrics* 186, pp. 13-16 (1996).
50. K. Chah, M. Aillerie, M.D. Fontana, G.I. Malovichko, K. Betzler, E. Kokanyan, “Influence of chromium doping on the electro-optic properties of lithium niobate”, *J. Opt. Comm.*, 136(3-4), pp. 231-234 (1997).
51. W. Y. Du, Z. B. Zhang, J. Q. Xu, W. H. Wong, D. Yu, Edwin Y. B. Pun and D. L. Zhang, “Electro-optic property of  $\text{Ti}^{4+}$ -doped  $\text{LiNbO}_3$  single crystal”, *Opt. Mat. Expr.*, Vol. 6, No. 8 pp. 2593-2599 (2016).
52. R. J. Holmes, Y. S. Kim, C. D. Brandle, D. M. Smyth, “Evaluation of Crystals of  $\text{LiNbO}_3$  Doped with  $\text{MgO}$  or  $\text{TiO}_2$  for Electrooptic Devices”, *Ferroelectrics*, 51, pp. 41-45 (1983).
53. K. Chah, M. Aillerie, M.D. Fontana, G. Malovichko, “Electro-optic Properties in Fe-Doped  $\text{LiNbO}_3$  Crystals as Function of Composition”, *Opt. Comm.* 176, pp. 261-265 (2000).
54. J. D. Zook, D. Chen, and G. N. Otto, “Temperature Dependence and Model of the Electro-optic Effect in  $\text{LiNbO}_3$ ”, *J. Appl. Phys. Lett.* Vol. 11, Numb. 5, pp. 159-161 (1967).

55. P. Gorski, K. Bondarczuk, and W. Kucharczyk, "Temperature Dependence of the Electrooptic Coefficients  $r_{22}$  and  $m_{22}$  in  $\text{LiNbO}_3$ ", *Opto-Electronics Rev.* Vol. 12, No. 4, pp. 459-461 (2004).
56. P. Gorski, R. Ledzion, K. Bondarczuk, and W. Kucharczyk, "Temperature Dependence of Linear Electrooptic Coefficients  $r_{113}$  and  $r_{333}$  in Lithium Niobate", *Opto-Electronics Rev.* Vol. 16, No. 1, pp. 46-48 (2008).
57. M. Aillerie, M. D. Fontana, F. Abdi, C. Carabatos-Nedelec, N. Theofanous, and G. Alexakis, "Influence of the Temperature-dependent Spontaneous Birefringence in the Electro-optic Measurements of  $\text{LiNbO}_3$ ", *J. Appl. Phys.* Vol. 65, No. 6, pp. 2406-2408 (1989).
58. C. Herzog, G. Poberaj, and P. Gunter, "Electro-optic Behavior of Lithium Niobate at Cryogenic Temperatures", *J. Opt. Comm.*, Vol. 281, pp. 793 - 796 (2008).
59. P. Nekvindova, J. Cervena, P. Capek, A. Mackova, V. Perina, J. Schrofel, J. Spirikova, "Features of APE Waveguides in Different  $\text{Er}:\text{LiNbO}_3$  and  $(\text{Er} + \text{Yb}):\text{LiNbO}_3$  Cuts: Electrooptical Coefficient  $r_{33}$ ", *Optical Materials* 24 pp. 527-535 (2003).
60. A. Petris, S. Heidari Bateni, V. I. Vlad, M. Alonzo, F. Pettazzi, N. Argiolas, M. Bazzan, C. Sada, D. Wolfersberger, E. Fazio, "The  $r_{33}$  Electro-optic Coefficient of  $\text{Er}:\text{LiNbO}_3$ ", *J. Opt.*, pp. 015205/1-015205/5 (2010).
61. Du W.Y., Zhang P., Zhang Z.B., Ren S., Wong W.H., Yu D.Y., Pun E.Y.B., Zhang D.L. 2017. Electro-optic coefficients  $r_{13}$  and  $r_{33}$  of singly  $\text{Er}^{3+}$ -doped and  $\text{In}^{3+}/\text{Er}^{3+}$ -codoped  $\text{LiNbO}_3$  crystals. *Journal of Physics and Chemistry of Solids*, 100, pp. 101-106.
62. N. Mkhitarian, J. Zaraket, N. Kokanyan, E. Kokanyan, M. Aillerie, "Electro-optic Properties of Singly and Doubly Doped Lithium Niobate Crystal by Rare Earth Elements for Optoelectronic and Laser Applications", *J. Eur. Phys. J. Appl. Phys.* Vol. 85, pp. 30502/1-30502/7 (2019).
63. N. Theofanous, M. Aillerie, M.D. Fontana, G. Alexakis, "A Frequency Doubling Electro-optic Modulation System for Pockels Effect Measurements: Application in  $\text{LiNbO}_3$ ", *Rev. Sci. Instrum.* Vol. 68, No. 5, pp. 2138-2143(1997).

64. H.G. Jerrard, D.B. Mc Neill, "In Theoretical and Experimental Physics", Chapman-Hall, London pp. 422–455 (1960).
65. M. Aillerie: Thesis, Metz-University (1991).
66. M. Aillerie, N. Théofanous, M.D. Fontana, "Measurement of the electro-optic coefficients: description and comparison of the experimental techniques", *J. Inv. Rev.Pap, Appl Phys B: Lasers and Optics*. 70, pp. 317-334 (2000).
67. A.S. Andrushchak, B.G. Mytsyk, N.M. Demyanyshyn, M.V. Kaidan, O.V. Yurkevych, A.V. Kityk, W. Schranz, "Spatial Anisotropy of Linear Electro-optic Effect in Crystal Materials: I- Experimental Determination of Electro-optic Tensor in LiNbO<sub>3</sub> by Means of Interferometric Technique", *Opt. and Las. in Eng.*, 47(1), pp. 31-38 (2009).
68. K. Takizawa, M. Okada, "Determination of Relative Signs of Electro-optic and Piezoelectric Coefficients by Measuring Optical Phase Shifts Caused by an Applied Electric Field", *J. Opt. Soc. Am. B Vol. 2, Issue 2*, pp. 289-296 (1985).
69. B.E. Benkelfat, E. H. Horache, Q. Zou, B. Vinouze, "An Electro-optic Modulation Technique for Direct and Accurate Measurement of Birefringence" *Opt. Comm.*, Vol. 221, Issue 4-6, pp. 271-278 (2003).
70. F.W.J. Olver, 'Handbook of Mathematical Functions', ed. by M. Abramowitz, I.A. Stegun Dover, New York (1968).
71. M. Abarkan, J. P. Salvestrini, M. Aillerie, M. D. Fontana "Frequency dispersion of electro-optical properties over a wide range by means of time-response analysis", *Appl. Opt.* Vol. 42, No. 13, pp. 2346 (2003).
72. M. Abarkan, A. Danielyan, N. Kokanyan, M. Aillerie, A. Movsesyan, S. Kostritskii E. Kokanyan, "The clamped and unclamped effective electro-optic coefficients of zirconium-doped congruent lithium niobate crystals", *Journal of Physics*, Vol. 879(1), pp. 012004/1-012004/9 (2017).
73. L. Kovacs, G. Ruschhaupt, K. Polgar, G. Corradi, M. Wohlecke, "Composition dependence of the ultraviolet absorption edge in lithium niobate", *Appl. Phys. Lett.* Vol. 70, No. 21 pp. 2801-2803 (1997).

74. M. Abarkan, A. Danielyan, S. Sewastianow, N. Theofanous, M. Aillerie, S. Kostritskii, E. Kokanyan, “The  $r_{22}$  electro-optic coefficients in indium-doped congruent lithium–niobate crystals”, *Journal of Physics* Vol. 879(1), pp. 012005/1-012005/1 (2017).
75. A. Danielyan, N. Kokanyan, S. Kostritskii, E. Kokanyan, M. Aillerie “Composition dependence of the electro-optic properties of iron- doped lithium niobate crystals mounted as bulk modulator” *Journal of American Ceramic Society*, Vol.102, Issue 6, pp. 3535-3546 (2018).
76. M. Jazbinsek, M. Zgonik, “Material tensor parameters of LiNbO<sub>3</sub> relevant for electro- and elasto-optics”, *Appl. Phys. B* Vol. 74, Issue 4-5, pp. 407-414 (2002).
77. R. W. Dixon, M. G. Cohen, “A New Technique for Measuring Magnitudes of Photoelastic Tensors and its application to Lithium Niobate”, *Appl. Phys. Lett.* Vol. 8, Numb. 8, pp. 205-208 (1966).
78. V. Grachev, G. Malovichko, O. Schirmer, “Structures of Point Defects in Lithium Niobate”, ISSN 0503-1265. *Ukr. J. Phys.* V. 49(5), pp 438-447 (2004).
79. M. Aillerie, M. Abarkan, S.M. Kostritskii, E.P Kokanyan, “Third column electro-optical coefficients of zirconium-doped congruent lithium niobate crystals”, *J. Opt. Mat., Elsevier*, 36 (7), pp.1238-1242 (2014).
80. N.W. Ashcroft, N.D. Mermin, *In Solid State Physics*, New York: Thomson Learning (1976).
81. A. Bernabe, C. Prieto, A. Andre, “Effect of stoichiometry on the dynamic mechanical properties of LiNbO<sub>3</sub>”, *J. Appl. Phys.* 79 (1), pp. 143-148 (1996).
82. R. Vacher, L. Boyer, “Brillouin Scattering: A Tool for the Measurement of Elastic and Photoelastic Constants”, *J. Phys. Rev. B* 6, pp. 639-673 (1972).
83. Y. Zhang, L. Guilbert, P. Bourson, K. Polgar, and M. D. Fontana, “Characterization of short-range heterogeneities in sub-congruent lithium niobate by micro-Raman spectroscopy,” *J. Phys.: Condens. Matter*, vol. 18, pp. 957-963 (2006).
84. T.H. Yeom, Y.M. Chang, S.H. Choh, C. Rudowicz, “Experimental and Theoretical Investigation of Spin-Hamiltonian Parameters for the Low Symmetry Fe<sup>3+</sup> Centre in LiNbO<sub>3</sub>”, *Phys. Stat. Sol. (b)*, 409-415 (1994).

85. L. Rebouta, M. E. Da Silva, J. C. Soares, M. Hage-Ali, J. P. Stoquert, P. Siffert, J. A. Sanz-Garcia, E. Dieguez and F. Agullo-Lopez, "Lattice Site of Iron in LiNbO<sub>3</sub> (Fe<sup>3+</sup>) by the PIXE/channelling Technique", J. Europhys. Lett. 14, pp. 557-561 (1991).

# **Chapter 4.**

## **Photorefractive properties of Lithium niobate crystals**

## Chapter 4. Photorefractive properties of Lithium niobate crystals

### § 4.1. Photorefractive effect

In 1966 at the Bell laboratories in New Jersey the light induced refractive-index variation ("optical damage") due to charge redistribution have been discovered by Ashkin et al [1]. At the same laboratory two years later refractive index variation referred as a "photorefractive effect" utilized by Chen [2] was recognized as the main attractive characterization for nonlinear performances such as holographic data storage. The photorefractive effect consists of excitation of charge carriers due to the inhomogenous illumination and appearance of modulated currents can be demonstrated by the following scheme (Figure 4.1.1) [3]:

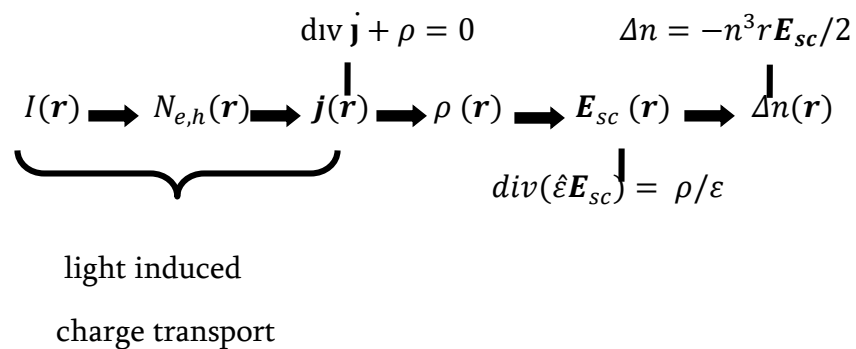


Figure 4.1.1: Photorefractive effect ( $I$  -light intensity,  $N_{e,h}$ -concentration of electrons/holes in the conduction/valence band,  $\mathbf{j}$  -current density,  $\rho$  -space charge density,  $\mathbf{E}_{sc}$  -space charge field,  $n$ -refractive index,  $\Delta n$  -refractive index change,  $\hat{\epsilon}$ -permittivity tensor,  $\mathbf{r}$  -special coordinate) [3].

The improvement of photorefractive performance of LN is controlled by crystal composition, by doping with the transition metal ions (TM) or non photorefractive ions.

#### Photorefractive effect as a function of crystal composition

The dependence of the optical damage on the crystal composition was investigated for the first time by Anghert et al [4] and more detailed by Furukawa et al. [5] discovering a larger optical damage for near stoichiometric crystals (NSLN). For relatively low intensity range the congruent LN crystals (CLN) exhibit more optical resistance comparing to the stoichiometric crystals (SLN) up to the certain threshold value of intensity [6] above which the situation is inversed and near stoichiometric LN crystals become more damage resistant than CLN [7]. Measured photorefractive characteristics are given in Table 4.1. The explanation of the smooth

increase of optical damage with the increase of light intensity and the steeply increase of photorefractivity in the high intensity range ( $I > 100 - 200 \text{ Wcm}^{-2}$ ) [7] for NSLN and CLN crystals respectively is the various dependence on the beam intensity which is responsible for the beam defocalization, electronic conductivity and bulk photovoltaic current.

In the high light intensity range the enhanced optical damage in CLN crystals is related to the photoinduced optical absorption via a non equilibrium population of shallow traps leading to the superlinearly dependence of the photovoltaic current on the intensity:  $j_{pv} \propto I^x (x > 1)$  explained in the framework of a two-center charge transport scheme [8] (described bellow).

### **Photorefractive effect in LN crystals doped with transition metal impurities**

Photorefractive effect also may be enhanced by using the transition metals (TM) (Fe, Cu, Ce, Mn, Ni) [9,10] and especially Fe illustrates the best photorefractive properties.  $TM^{3+}$  ions changing lattice position are partially placed at the Nb site resulting to the decrease of the capture cross-section of electrons by these centers thus, they discontinue to be as electron traps. Therefore, the density of potential electron traps is lesser in TM doped NSLN crystals than in CLN crystals due to the variation of lattice sites of  $TM^{3+}$  ions. Although Fe ions are usually present in LN crystals at several ppm levels, to maximize the holographic storage the intentional introduction of Fe ions is necessary for the existence of deep trap as Fe ions capture from the shallow levels decreasing the photoconductivity. The electron migration from small polaron  $Nb^{4+}$  to  $Fe^{3+}$  decreases the lifetime of the intermediate level increasing the velocity of the holographic writing in the digital data storage. Particularly, Fe doped LN stoichiometric crystals illustrate about an order of magnitude higher photorefractive sensitivity required for holographic volume storage [11].

The one center model was formed to give explanation for the holographic recording in photorefractive crystals [12]. In the case of relatively low light intensity ( $I < 1 \text{ Wcm}^{-2}$ ) the photoexcited charge transport is usually described in the frame of a band model with one-center charge transport model (the scheme is given in Figure 4.1.2) which has been developed in the first time of the investigation of photorefractive effect. Photo-generated free conduction band electrons from filled traps (donor centers),  $C^0$  migrating in the conduction band are captured by empty traps  $C^+$ , and transform them to the filled traps,  $C^0$ . The photo-induced

charge transport in LN:Fe and LN:Cu crystals is described via one center transport model at low intensity range [13].

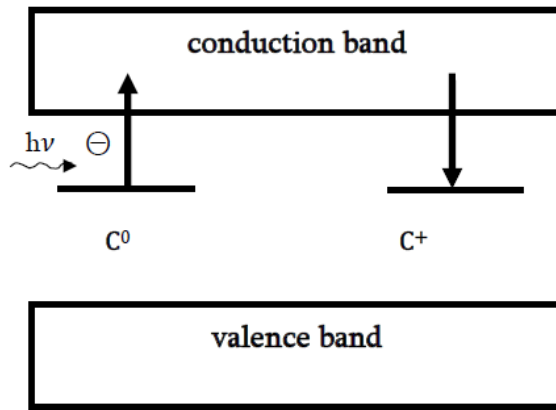
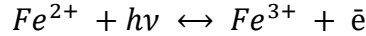


Figure 4.1.2: One-center charge transport model.  $C^0$  and  $C^+$  are filled and empty electron traps,  $h\nu$  is photon energy [12].

The photorefraction is defined by the appearance of photovoltaic effect due to the presence of TM impurities creating photo-induced space charge field. Due to the one center charge transport mechanism TM impurities are in two charge states states ( $Fe^{2+}$  and  $Fe^{3+}$ ,  $Cu^+$  and  $Cu^{2+}$ ,  $Mn^{2+}$  and  $Mn^{3+}$ , etc.) [9] illustrated by the following scheme:



where  $Fe^{2+}$  and  $Fe^{3+}$  ( $Cu^+$  and  $Cu^{2+}$ ) are electron donors and traps correspondingly. Photorefractivity increases with the increase of  $[Fe^{2+}]/[Fe^{3+}]$  ratio [16].

In LN crystals doped by TM impurities photovoltaic current depends on the donor concentration [9]:

$$j_{pv} = K_G S_{ph} [Fe^{2+}] I \quad (4.1.1).$$

The saturation value of photorefractive index  $\delta\Delta n$  is proportional to  $E_{pv} = j_{pv}/\sigma \propto [Fe^{3+}]$  [14]. In the higher intensity range ( $> 10^2 Wcm^{-2}$ ) the non linear dependence obtained between photoconductivity and light intensity  $\sigma_{ph} \propto I_x (x < 1)$  in BaTiO<sub>3</sub> crystals by Valley [15] leads to the need of two (or more) center scheme whereas the thermal generation rates was not considered. In higher intensity range ( $> 10^2 Wcm^{-2}$ ) when laser pulses and focused laser beam is used, the explanation of the superlinearly increase of photoconductivity with the increase of intensity, the refractive index changes depending on the light intensity, light-induced absorption variations can be given by two-center charge transport model where intrinsic defects  $Nb_{Li}^{4+/5+}$  Li site are also taken into account. In the model proposed by Jerman

and Otten (Figure 4.1.3) [16], a secondary hypothetically shallow traps  $Nb_{Li}^{4+/5+}$  were assumed with the traditional centers  $Fe^{2+/3+}$  as a deep centers. This model is actual also for other TM dopants.

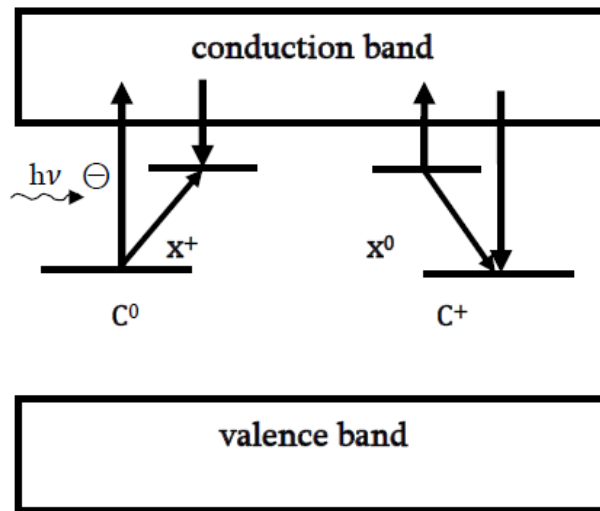


Figure 4.1.3: Two-center charge transport model.  $C^0$  and  $C^+$  are filled and empty deep electron traps,  $x^0$  and  $x^+$  filled and empty shallow electron traps,  $h\nu$  is photon energy [16].

#### Photorefractive effect in LN crystals doped with non-photorefractive ions

LN crystals are also excellent candidates to use as Pockels cells for laser Q-switches as these crystals illustrate a good transmission and light extinction ratio with half wave voltage requiring to develop EO linear properties of LN crystals. In LN Pockel cells the external electric field generates a mechanical compression through the piezo-electric effect, which doesn't vanish after removing the voltage in his turn modulating the refractive index through the elasto-optic effect. Whereas the high photorefractivity is the greatest drawback for LN Pockels cells limiting the applications for Q-switch laser system with the high power [17].

The optical damage resistant impurities ( $Mg^{2+}, Zn^{2+}, Sc^{3+}, In^{3+}, Hf^{4+}, Zr^{4+}$ )[5,18-121] provide a reduction of photorefractivity from two up to four orders of magnitude due to the high suppression against the light induced scattering[22]. The results of investigation of photorefractive effect depending on the threshold concentration of non-photorefractive ions are given in Table 4.1.1. For the first time Zhong and et al.[23] reported hundredfold increase of resistance against the optical damage in congruent LN crystals doped with 4,6 mol% Mg.

This result was confirmed by Bryan by investigating Mg:LN crystals with varying impurity concentration and with different stoichiometry [24]. In Li-enriched Mg:LN crystals the decrease of threshold concentration of Mg up to 0.67 mol% [25] or 0.5 mol% [26] is caused by the decrease of content of Li vacancies and Nb antisites in Li site [27]. Volk et al. suggested Zn and In ions [28] as the new members of family of optical damage resistant impurities analogous Mg ion to reduce the photorefractive damage in LN crystal. In Zn doped LN crystals the optical damage resistance was obtained at 7 mol% Zn for congruent melt [29], whereas later a threshold concentration of about 6 mol% Zn was found. This result for resistance of optical damage is two order of magnitude larger than in pure LN crystal and is similar for Mg:LN (5mol%) [29,30]. In crystals with lower Zn (<7 mol%) Zn ions incorporating onto the Li site ions replace Nb antisites in Li site, whereas at concentrations above threshold concentration Zn ions leads to the generation of disorder due to the location in both sites (Li and Nb) . The In doped crystals exhibit a similar optical damage resistance as Zn:LN (7.5 mol%) crystals which is smaller of results obtained for pure congruent LN crystal or for Fe:LN (0.07 wt%) crystals [31]. E. Kokanyan et al. suggested to dope LN crystals with tetravalent ions Zr and Hf as new optical damage resistant dopants to achieve a reduction of refractivity with more than 2 times lower concentration than in the case of divalent impurities [26, 32-35]. The threshold concentration of In ions was found to be less than 2 mol% [22,31,36]. Photorefractive damage decreases with the increase of Sc concentration in Sc:LN crystals and it reached a saturated value at 1.5 mol% of Sc, which is larger than for 5 mol% Mg:LN crystal but smaller than in pure congruent crystals [37,38]. Thus, the threshold concentration of non-photorefractive ions depends on the valence state: for divalent ions ( $Mg^{2+}, Zn^{2+}$ ) the threshold concentration is equal to 5-7 mol%, for trivalent ( $Sn^{3+}, In^{3+}$ ) and tetravalent ions ( $Hf^{4+}, Zr^{4+}$ ) is about 2-1 mol%.

### **Photorefractive effect in co-doped in crystals**

In LN:Fe crystals co-doped with non-photorefractive ions having a concentration even a little larger than the threshold one the photorefractive effect controlled by  $Fe^{3+}$  centers loss their acceptor properties thus the saturation value of refractive index decreases by one order of magnitude, as in LN:Zn:Fe (6.5 mol%), In:Fe:LN (1.5 mol%)  $\delta\Delta n < 5 \cdot 10^{-5}$  whereas above 7.2 mol% Zn concentration  $\delta\Delta n < 5 \cdot 10^{-6}$  [28] thus, the value of threshold concentration

Table 4.1.1: Photorefractivity of LN crystals

Composition	Dopant	Conc. mol%	$\delta\Delta n \times 10^{-4}$
Congruent	pure		2[26],0.239[22],0.394[31],2[7]
Congruent	Fe	0.01wt%	0.1[36]
Congruent,as grown	Fe	0.1wt%,	3[7]
Congruent, reduced	Fe		1.11[7]
Congruent	Fe	0.07wt%	0.68[31]
Congruent	Mg	1	0.15[22]
Congruent	Mg	2	0.182[22]
Congruent	Mg	4	0.033[22]
Congruent	Mg	5	0.275[22]
Congruent	Mg	6	0.2[26]
Congruent	Mg	6.5	0.078[34]
Congruent	Mg	7	0.197[22]
Congruent	Mg	9	0.335[22]
Stoichiometric	Mg	0.5	0.39[26]
Congruent	Hf	2	0.22[34]
Congruent	Hf	4	0.14[26],0.087[34]
Congruent	Hf	6	0.323[22],0.084[34]
Congruent	Zr	2	0,3[42]
Congruent	Zn	5	0.175[22]
Congruent	Zn	7	0.426[22]
Congruent	Zn	7.5	0.118[31]
Congruent	Zn	9	0.467[22]
Congruent	In	1	0.091[22],0.289[31]
Congruent	In	3	0.116[22],0.169[31]
Congruent	Fe:In	0.01wt%:1.5	0.5[28]
Congruent	In	5	0.224[20],0.089[31]

decreases [39] (Table 4.1.1). The enhanced resistance is due to the decrease of amounts of Nb antisites and Li vacancies [40]. Below the threshold concentration the optical damage resistant ions only incorporate onto the Li site decreasing the intrinsic defects which are removed at the threshold concentration [19]. Thus, for low concentrations optical damage resistant

impurities considered as intrinsic defects controller (non photorefractive ions) and are analogous to Li enrichment. Due to the possibility of partial incorporation of optical damage resistant impurities also upon Nb site above threshold concentration (completely remove Nb antisites) [10] a modification of charge compensation requires. An explanation of the variation of values for threshold concentration may be given by the change compensation effect for di-, tri- and tetravalent optical damage resistant impurity ions[41].

Photorefractivity is sensitive also to the beam intensity [42] and is larger for higher intensity for undoped crystals whereas it decreases with the increase of non-photorefractive ions concentration [35,42].

### **§ 4.2. Photogalvanic effect**

Free charge carriers (electron/holes) excited by the inhomogeneous illumination (intensity  $I/r$ ) migrate to the conduction/valence band because of drift, bulk photovoltaic effect and the diffusion, which can be expressed by the following equation (4.2.1):

$$j = j_{ph} + j_{drif} + j_{diff} \quad (4.2.1),$$

where  $j_{drif}$  is the drift current obeyed Ohms law results from the Coulomb interaction of charge carriers with a electric field, the diffusion transport of photocarriers  $j_{diff} = \sigma(E_{ext} + E_{int})$  occurs under a non homogeneous illumination and rises by the external or internal fields. The photoexcited charge carriers scattering, thermalizing, lose their directional properties and contribute to the drift and diffusion currents but no to the bulk photovoltaic current. The bulk photovoltaic effect related to the photoexcitation and recombination processes can be expressed as

$$j_{pv,i} = \beta_{ijk} e_j e_k I \quad (4.2.2),$$

where  $e_j, e_k$  are unit vectors of polarization of the light wave,  $I = |a^2|$  is the light intensity. The complex photovoltaic tensor  $\beta_{ijk} = \beta_{ijk}^*$  contains four components, that are not equal to zero:  $\beta_{311} = \beta_{322}, \beta_{333}, \beta_{222} = -\beta_{211}, \beta_{113} = \beta_{223}$ . The components  $\beta_{311}$  and  $\beta_{333}$  having the same order of magnitude are larger than  $\beta_{222}$ . The photovoltaic tensor element  $\beta_{113} = \beta_{131}^*$  showing a new type of holographic recording, thus it is called anisotropic recording. The linear

dependence of the photovoltaic current  $j_{ph}$  on the concentration of the filled traps was proposed by Glass et al [12,43] and usually is presented by the scalar form, as:

$$j_{ph} = K_G \alpha I \quad (4.2.3),$$

where  $K_G$  is the Glass constant,  $I$  is the intensity,  $\alpha = sN$  is Lambert-Beer absorption coefficient,  $s$ - the cross section and  $N$ -the concentration of the photogalvanic centers.

Due to the component values of the tensor, probably the same current is detected by using a linearly polarized beam parallel to one of the three axes of the crystal which results to a 1D problem. In iron doped LN crystals the initial part of the photorefractive effect is related to the not well known phenomenological parameters: the photogalvanic length  $L_{PG}$  and the photogeneration efficiency factor  $\phi$  (referred also as quantum efficiency). The former parameter is the average position of the center where the polaron is created due to the condensation of the charge emitted recently from the donor center. As characterized the photogalvanic effect, this average varies from zero even when the external electric field is not applied. According to the second phenomenological parameter all the absorbed photons not generate a polaron resulting to the photogalvanic process. Thus, taking also 1D problem, the photogalvanic current directed along the crystallographic axis can be rewritten including the experimental quantities [44,45]:

$$j_{PG} = q s N \frac{I}{h\nu} \phi L_{PG} \quad (4.2.4),$$

where  $q$ -the charge of the photo-excited carriers,  $h\nu$ -photon energy,  $L_{PG}$ -photogalvanic length,  $\phi$  -photogeneration efficiency factor (referred also as quantum efficiency). The product  $\phi L_{PG}$  is an effective average distance at which a carrier appears after being kicked-out by a photon.

Obtaining experimental value of  $j_{PG}$  it is convenient to normalize it attitude toward the charge generation rate  $G$  (as it includes all the parameters), the effective photogalvanic length can be determined:

$$L_{PG}^{eff} = \frac{j_{PG}}{G} = \phi L_{PG} \quad (4.2.5).$$

$G = q\alpha I/h\nu$  the generation rate is proportional to the beam intensity and to the concentration of filled traps producing the charge carriers. Due to the interpretation of the photogalvanic

effect within polaron model [45] in LN:Fe crystals the initial direction of the emitted charge as a Bloch wave is defined by the Fermi golden rule, as well as the varied matrix elements of the transition are given by the geometrical arrangement of the neighbored ions of the donor center. Thus, in this condition, the photogalvanic length in Eq. (4.2.5) is related to the average meaning of the distance traveled in different directions along the c-axis leads the polaron creation. It is assumed, that along the c axis an electron travels the several  $Nb_{Nb} - Nb_{Nb}$  spacings coherently before the surround lattice relaxation to generate  $Nb_{Nb}^{4+}$  small polaron. After the initial polaron formation stage, there are two possible choices for polaron to continue a life: to travel away or to return the same initial formation position. Both actions are thermally activated whereas with a varied energy barrier which gives a possibility for the microscopic interpretation of the quantum efficiency in Eq. (4.2.5), indicating the probability no return of the polaron to the generation site [46]. In this condition those surviving polarons after an essentially long time are the successful in the jumping away and those ones lost any memory about the starting site. The parameter  $\phi$  illustrates the temperature dependent as it can be identified by thermally activated processes.

### ***§ 4.3. Photoconductivity***

The term photoconductivity is the result of the excitation of the free charge carriers via the absorption of light and in the frame of a band model with one-center charge transport model photoconductivity is characterized as [9,13]:

$$\sigma_{ph} = nq\mu = q\mu\tau qN\phi \frac{I}{h\nu} = G\tau q\mu = \frac{q\mu q S_{ph} N_D}{h\nu \gamma N_C} I \quad (4.3.1),$$

where  $n$  is the density,  $q$  is the electron charge,  $\phi$  is the quantum efficiency of excitation of an electron via absorption of photon,  $\alpha = S_{ph}N_D$  is optical absorption coefficient,  $S_{ph}$  is photon absorption cross section depending on the light polarization and wavelength,  $I$  -light intensity,  $h\nu$  is the photon energy,  $\gamma$  is the recombination coefficient,  $N_D$  and  $N_C$  concentrations of donor and acceptor centers respectively,  $\mu$  is the charge carrier mobility illustrating how quickly an electron can move in an electric field which is independent of the impurity centers and determined by the band structure,  $\tau = 1/\gamma N_C$  is life time of carriers in the conduction band and is inversely proportional to the concentration of empty traps capturing the charge carriers. Impurity centers are considered as filled or empty traps which are not much varied by

excitation or trapping processes. The Eq. (4.3.1) requires two important assumptions: the charge carriers  $q$  are normally diffusing particles described by a time-independent mobility  $\mu$ , the decay time of the carriers is established by an equation  $dn/dt = -\frac{1}{\tau}nN^+$ , where  $N^+$  is the ionized donors concentration considering as deep traps

The specific conductivity  $\Sigma$  can be obtained normalizing the total conductivity for the photogeneration ratio:

$$\Sigma = \frac{\sigma}{G} = \frac{\sigma_{dark} + \sigma_{ph}}{G} = \phi(\Lambda + \Lambda_{dark}) \quad (4.3.2).$$

The quantities drift coefficient  $\Lambda$ ,  $\Lambda_{dark} = \sigma_{dark}/\phi G$  and photogalvanic efficiency  $\phi$  are discussed in paragraphs 4.6.2.3.1, 4.6.2.3.2 and 4.6.2.3.3 respectively.

The total conductivity of the LN crystal is expressed as a sum of dark  $\sigma_{dark}$  and photo conductivity  $\sigma_{ph}$ :

$$\sigma = \sigma_{dark} + \sigma_{ph} \quad (4.3.3).$$

The former demonstrates the dominant role only in high temperature regime thus, this term can be neglected [47].

Taking into account the significance of the photoconductivity as one of the observed quantities the essential literary results of the past investigations are given below.

### **Photoconductivity as a function of crystal stoichiometry**

The most efficient resistance of the optical damage is to increase the photoconductivity, which can be achieved in Li-enriched crystals [8,48] as well as by adding nonphotorefractive impurities to the crystal composition [6]. In near stoichiometric LN crystals as well as crystals doped by nonphotorefractive ions (Mg, Zn, In, Sc, Hf) for an increase of photoconductivity two possible explanations exist: the decrease of the trapping rate (coefficient  $\gamma$  is reduced) and the longer movement of photo-excited charge carriers in the band. An alternative explanation is the increase of the charge carriers mobility due to the less intrinsic defects ( $V_{Li}$  vacancies and  $Nb^{5+}$  ions in Li site) disturbing the charge transport and resulting to the increase of the charge carrier mobility  $\mu$ . In the relatively low intensity range with the increase of refractive index change the decrease of photoconductivity would be obtained for stoichiometric crystals whereas photoconductivity demonstrates the rise with the increase of stoichiometry [49]. The characterization of photoconductivity as function of crystal composition is given in Table 4.3.1.

### **Photoconductivity in LN crystals doped with transition metal impurities**

Photoconductivity is highly sensitive to the presence of defects contributed to the crystalline structure of the material and as well as the impurities in a crystal. The major processes corresponded to the photoconductivity are optical absorption leading to the production and increase of free carriers which may be due to the intrinsic photoexcitation effect from the valence band to the conduction band by which free carriers are created. The electrical transport of free carriers in the conduction band, capture of them leading to recombination, and the thermal excitation trapped carriers to the nearest band contribute to the electrical conductivity.

Photoconductivity is governed by the photo-excited electron transport between donor and acceptor centers in the frame of one center charge transport model where photoconductivity is linearly proportional to the light intensity for relatively low intensity range ( $< 10^3 Wm^{-2}$ ) and to the reducing degree at the same time [50]. However, in the higher intensity range ( $> 10^2 Wm^{-2}$ ) the photoconductivity exhibits the non-linear (quadratic) dependence on the light intensity  $\sigma_{ph} \propto I_x (x < 1)$  [51]. For high intensity range, the additional centers are largely populated, and transitions from these centers significantly affect the light-induced charge transport. They become filled in a wide range of the impurity concentrations, however, are no more valid in very highly doped LN:Fe crystals. Additional evidence of  $Nb_{Li}$  antisites as shallow electron traps with the traditional  $Fe^{2+}$  donor and  $Fe^{3+}$  acceptor centers is given by an enhanced  $\sigma_{ph}$  in stoichiometric crystals where  $Nb_{Li}$  content is reduced up to the minimum value. An increase of  $\sigma_{ph}$  in Li-enriched crystals may be caused by a partial incorporation of  $Fe^{3+}$  ions onto the Nb site thus,  $Fe^{3+}$  loses its electron acceptor properties and the charge transport scheme was changed [8]. At higher intensities the photoconductivity is always proportional to the concentration ratio  $N_{Fe^{2+}}/N_{Fe^{3+}}$  [52]. According to the two center model the nonlinear dependence of  $\sigma_{ph}$  on the intensity [51,53] can be explained by the lower concentration of  $Fe^{3+}$  and removing of  $Nb_{Li}$  in crystals doping with non-photorefractive ions.

### **Electron and hole competition and the dependence of photoconductivity on the reducing degree**

Orlowski and Kratzig by beam-coupling measurements illustrated the possibility of electron and hole contributions to photoconductivity simultaneously [54]. Physically different models describing charge carriers transport were proposed by Valley [15] and by Strohkendl, Jonathan

and Hellwarth [55]. The first model considers one center model when valence band electrons thermal and light-induced excite into  $C^0$  and recombined from  $C^-$  with valence band holes. The second model considers two centers, when electrons or holes predominate in every center. In the visible spectral range electrons exciting from the impurity donor centers ( $Fe^{2+}$ ,  $Cu^+$ ) migrate in the conduction band by giving rise to the photovoltaic effect, then trapped by acceptor impurity centers ( $Fe^{3+}$ ,  $Mn^{2+}$ ,  $Cu^{2+}$ ) [13,41]. In the near UV spectral region the additional second mechanism is determined by optical excitation electrons from oxygen  $\pi$  orbitals forming valence band to  $Fe^{3+}$  or  $Cu^{2+}$ . The generated holes migrate in the valence band until they trapped by acceptor centers ( $Fe^{2+}$ ,  $Cu^+$ ). The electron/hole life time is reciprocally proportional to the acceptor concentration. In crystals doped with transition metal ions the main transport mechanism is the bulk photovoltaic effect and electrons predominate [54].

Photoconductivity is proportional to the reducing degree  $C_{Fe^{2+}}/C_{Fe^{3+}}$  [54,56,57] which is the ratio between the concentration of filled ( $Fe^{2+}$ ) and empty ( $Fe^{3+}$ ) electron traps in the band transport model and it increases with the rise of this ratio whereas it doesn't depend on the entire Fe-content for the concentrations smaller than 0.1 wt.% [58]. On the other hand another holographic exploration for Fe doped LN crystals with different impurity concentrations bigger than 0.1 wt.% illustrated photoconductivity as a function of the total iron concentration thus photoconductivity increases with the increase of iron concentrations exceed  $C_{Fe} = 0.06$  wt. %. In pure oxygen atmosphere the increase of the temperature of about 1000°C oxidizes the iron ions to  $Fe^{3+}$ , whereas the heating in argon atmosphere or vacuum (low oxygen partial pressure) reduces the Fe ions to  $Fe^{2+}$ .

In highly iron-doped and strongly oxidized ( $C_{Fe^{2+}}/C_{Fe^{3+}} > 0.01$ ) LN crystals the hole transport predominates at shorter wavelengths (near UV spectral range) whereas for smaller iron concentration ( $C_{Fe^{2+}}/C_{Fe^{3+}} < 0.08$ ) electron process predominates [54]. The results of holographic measurements to estimate the different charge carrier contributions to the photoconductivity are determined also for oxidized and reduced Fe:LN and LN:Cu crystals with different impurity concentration by direct photoconductivity experiments realized. In the visible spectra range [13,58] the electron charge transport predominates over the entire oxidization/reduction range for oxidized and reduced Fe:LN and Cu:LN crystals and in the near UV region the dominant electron transport was obtained only for reduced crystals with

(( $C_{Fe^{2+}}/C_{Fe^{3+}} > 0.1$ ). Whereas for crystals with ( $C_{Fe^{2+}}/C_{Fe^{3+}} < 0.1$ ) the hole contribution predominates demonstrating the increase with the decrease of reducing ratio. In the visible region photoconductivity can be increased by reduction treatment, in the near UV region it can be increased by oxidation [58].

### **Non photorefractive impurity-controlled photoconductivity**

As mentioned above to increase photoconductivity, which is the dominant reason for the optical damage resistance, LN crystals usually are doped by Mg, Zn, In, Sc, Hf, Zr non photorefractive ions [22,26,32,48,59,60]. The values of photoconductivity depending on the threshold concentration of non-photorefractive ions is given in Table 4.3.1. In LN crystals the presence of optical damage resistant ions increases the photoconductivity by two orders of magnitude compared to the stoichiometry pure LN crystals. Especially the value of threshold concentration of non-photorefractive ions is lower in crystals with stoichiometric composition [5,26] than in congruent crystals [22,49]. In crystals doped with non-photorefractive ions above threshold concentration the photoconductivity increases with the growth of optical damage resistant ions concentration leading to the increase of hole contribution to the photoconductivity, thus the photovoltaic current decreases as it is related to the photo-excited electrons only [22,59].

Due to dependence of  $\sigma_{ph}$  on the free charge carriers the threshold value corresponds to the incorporation of resistant ions onto the Nb site and the minimizing of Li vacancies. The increase of  $\sigma_{ph}$  is related to the decrease of  $Nb_{Li}$  centers as electron traps [8]. As at the threshold concentration non-photorefractive ions incorporate partially onto the Nb site for self compensation minimizing Li vacancies content, thus above threshold concentration deep  $Fe^{3+}$  and shallow  $Nb_{Li}$  traps as well as  $V_{Li}$  disappear. On the other hand the electron contribution to the  $\sigma_{ph}$  increases below threshold value, whereas above threshold concentration the hole contribution increases with the increase of concentration of non photorefractive ions and above threshold value the disappearance of Li vacancies which are the most hole traps, results to the increase of the hole  $\sigma_{ph}$ .

### **The incorporation of TM and non photorefractive ions**

With the development of two-color holographic recording the influence of lanthanide ions ( $Ln^{3+}$ ) with the transition metal ions on the PC effect also was observed. The occupation of LN lattice by TM and  $Ln^{3+}$  ions was the debated subject for research groups as these ions seem

to keep either Li, Nb, empty oxygen octahedron or interstitial sites. Iron ions with two valence charges  $Fe^{2+}$  and  $Fe^{3+}$  are localized in the band gap and the ratio between charge state can be varied by reducing and oxidation annealing treatments [19].  $Fe^{2+}$  ions incorporate only onto the Li site, however  $Fe^{3+}$  ions partially localized in Nb site (EPR spectra for  $Tm^{3+}$  and  $Ln^{3+}$ ) or in Li site for congruent crystal [61]. Unlike TM impurities  $Ln^{3+}$  (Nd, Er) mainly incorporate onto Li site less depend on the crystal composition.

In co-doped crystals photoconductivity by a factor about four is larger than in Fe:LN crystals for certain  $[Fe^{2+}]/[Fe^{3+}]$  ratio [57]. With the increase of non photorefractive ions concentration additional  $Fe_{Nb}^{3+}$  centers appear. Feng et al [62] proposed that appearance of  $Fe_{Nb}^{3+}$  new centers is due to the remove of  $Nb_{Li}$  centers by Mg ions. The partial incorporation of  $Fe^{3+}$  ions onto Nb site with the possible self compensation  $[Fe_{Li}^{3+}]'' - [Fe_{Nb}^{3+}]''$  was found above the threshold concentration for non photorefractive ions which is equal to 4.6-6% for Mg, whereas that the location of  $Fe^{2+}$  in Li site is independent with the presence of non photorefractive dopants. The steep increase of photoconductivity was found in non photorefractive ions co-doped LN:Fe crystals although the ratio  $[Fe^{2+}]/[Fe^{3+}]$  is lesser because of the hampering of the Fe ions incorporation onto Li site resulting to the  $Fe^{2+}$  lower concentration. Above the threshold concentration of non photorefractive ions the  $Fe^{3+}$  centers are no more electron trap centers thus the origin of electron traps is varied however  $Fe^{2+}$  centers remain as electron donors. Thus the threshold concentration of non photorefractive ions is lesser in co-doped crystals with transition metals [53,57,63] (Table 4.3.1). Above the threshold concentration of non photorefractive ions the  $Fe^{3+}$  centers are no more electron trap centers thus the origin of electron traps is varied however  $Fe^{2+}$  centers remain as electron donors.

According to the explorations of the structure of  $Ln^{3+}$  and non photorefractive ions codoped crystals the partial incorporation of  $Nd^{3+}$  ions onto the Nb site was found at 5% Mg concentration in Mg:Nd:LN crystals whereas at the same time the partial incorporation of Nd ions onto the empty oxygen octahedra also was found at high Mg concentration [64].

The increase of  $\sigma_{ph}$  above threshold concentration of non photorefractive ions may be caused by the increase either the mobility or capture cross section or lifetime or variation of free charge carriers. In the framework of one center scheme the dependent of  $\sigma_{ph}$  on the mobility  $\mu$  was proposed by Sommerfeld et al. [57] as electron mobility rises above the threshold

concentration depending on the scattering of the doping carriers changed by Mg or Zn ions. However Garcia et al. [64] proposed the independence of  $\mu$  for  $\sigma_{ph}$  by studying LN, Mg 5%:LN, Fe:Mg 5%:LN crystals.  $\sigma_{ph}$  as a function of temperature is described by the following expression:

$$\sigma = 1620 \exp(-E_a / kT) \quad (4.3.5),$$

with  $E_a = 1,2 \text{ eV}$  activation energy. Thus, it was assumed that the  $\sigma_{ph}$  increase was not related to the change of  $\mu$ .

The other reason of an increase of  $\sigma_{ph}$  is the decrease of a capture cross section of electrons by  $\text{Fe}^{3+}$  at high Mg (or Zn) doping concentration more than two orders of magnitude.

### **Photoconductivity as a function of temperature**

According to the investigations of the photoconductivity as function of temperature performed for large temperature range it increases with an increase of the temperature [65, 66]. The growth of photoconductivity was found at higher temperatures and above  $1000^\circ\text{C}$  it remains constant. The origin of the completely ionic photoconductivity at the high temperature is the decrease of refractive index by about two orders of magnitude obtained by the holographic experiments with continuous wave light [67]. Besides photoconductivity, the photovoltaic current also increases with the increase of the temperature whereas current density is proportional to the concentration of donors and it was assumed that optical excitations of electrons to the conduction band from impurity centers in donor states gives rise to a bulk photovoltaic effect.

Table 4.3.1: Characterization of photoconductivity in LN crystals.

Composition	Dopant	Conc. mol%	$\sigma_{ph} \times 10^{-11} [\Omega m]^{-1}$	$\sigma_{ph}/l \times 10^{-12} cm [\Omega m]^{-1}$
Congruent	pure		0.17[32], 0.47[26],	2.31[22], 3.32[59],
Stoichiometric	pure		0.2[49],	
Congruent	Fe		0.00177[53],	
Congruent	Mg	1		9.22[22],
Congruent	Mg	2		9.57[22],
Congruent	Mg	4		10.8[22],
Congruent	Mg	5		82.6[22],
Congruent	Mg	6	0.83[32], 41[26],	
Congruent	Mg	7		110[22],
Congruent	Mg	9		278[22],
Stoichiometric	Mg	0.5	5.6[32], 18[26],	
Stoichiometric	Mg	2	6[49],	
Congruent	Zr	6	1.1[32]	
Congruent	Zr:Fe	2	0.00329[53],	
Congruent	Zr:Fe	4	0.007[53],	
Congruent	Zr:Fe	5	0.0083[53],	
Congruent	Hf	2	1.3[60],	
Congruent	Hf	4	0.42[32], 12[26] , 5.6[60],	105[22],
Congruent	Hf	6		120[22],
Congruent	Hf	8	5.5[60],	
Congruent	Zn	5		52.7[22], 10.6[59],
Congruent	Zn	7		237[22], 25.2[59],
Congruent	Zn	9		255[22], 57.3[59],
Congruent	In	1		1.42[22], 1.59[59],
Congruent	In	3		33.7[22], 7.46[59],
Congruent	In	5		98.8[22], 12.9 [59],

#### § 4.4. Space charge field

The photoexcited carriers from donor centers transported in the conduction/valence band are captured by acceptor centers resulting space charge field  $E_{sc}$  which leads to a variation of the

refractive indices in the illuminated part via the linear EO effect. In LN crystals taking into account that the photovoltaic mechanism is dominant photo-induced refractive index change can be represented as [68]:

$$\delta\Delta n = R_{eff} E_{sc} = R_{eff} \frac{j_{PG}}{\sigma_{ph} + \sigma_d} \quad (4.4.1),$$

$R_{eff}$  is the effective electro-optic coefficient. Here it is considered that the diffusion current is negligible and the photogalvanic current is represented as:

$$j_{drift} = \sigma E \quad (4.4.2).$$

The development of the electric space charge field for 1D geometry which accepts the form of a saturated exponential time evolution can be scalar approximated [68,69]:

$$E(t) = E_{sat} (1 - \exp(-\frac{t}{\tau_d})) \quad (4.4.3).$$

The dielectric relaxation time  $\tau_d$  can be expressed via the conductivity and the dielectric coefficient as:

$$\tau_d = \frac{\epsilon\epsilon_0}{\sigma_{dark} + \sigma_{ph}} \quad (4.4.4).$$

Upon reaching the diffusion-drift equilibrium the saturation value of the space charge field  $E_{sc}$  can be presented as:

$$E_{sat} = \frac{j_{PG}}{\sigma} = \frac{K_G \alpha I}{\sigma_{ph} + \sigma_d} \quad (4.4.5).$$

For low light intensity ( $\sigma_{ph} > \sigma_d$ )  $\sigma_{ph} \propto I$  thus, the space charge field illustrates the independence of intensity.

Taking into account the saturation results from Eqs. (4.2.5, 4.3.2), the Eq. (4.4.3) for the saturation value of the space charge field can be rewritten as:

$$E_{sat} = \frac{L_{PG}}{\Lambda + \Lambda_{dark}} \quad (4.4.6).$$

#### ***§ 4.5. The used experimental technique***

The aim of the photoconductivity measurements:

- Exploration of the temperature dependence of charge carrier transport in iron doped Fe:LN crystals.

- Investigation of the effect of doped LN defect structure on the charge transport.

The determination of the photoconductivity can be expressed as a combination of three steps.

1. Production of interferogram of understudy samples via the digital holographic technique
2. Reception of wrapped phase map from the interferogram due to the Fourier transformation
3. Obtainment of unwrapped phase map from wrapped phase map using Miguels algorithm

#### ***§ 4.5.1. Digital holographic technique***

The dependence of the photorefractive characterization has been performed on the concentration of the deep and shallow trap centers and on the temperature in range from 150K to room temperature. Employing the digital holography the phase difference was obtained and the light-induced refractive index variations were visualized consequently in photorefractive crystals [70,71]. The advantages of the used holographic technique are related to the insensibility toward mechanical vibration as well as is uninfluenced of the beam fanning effect caused by photorefractivity [69]. This mentioned advantages can be achieved due to the very slow measurements. The schematic figure and the photo of the setup based on a pump-probe scheme are given in Figures 4.5.1.1, 4.5.1.2.



The green laser beam with 543 nm wavelength and 4 mW power emitting by a He-Ne laser was expanded (BE) and formed with the aid of Gauss- to -top hat optics (GTH), resulting to the formation of the beam with nearly uniform intensity. The cylindrical lens (CL) focusing the beam guiding to the sample created a vertical strip of beam with a uniform intensity profile along the vertical ( $y$ ) direction and keeping a nearly Gaussian shape along the horizontal ( $x$ ) direction (Figure 4.5.1.3).

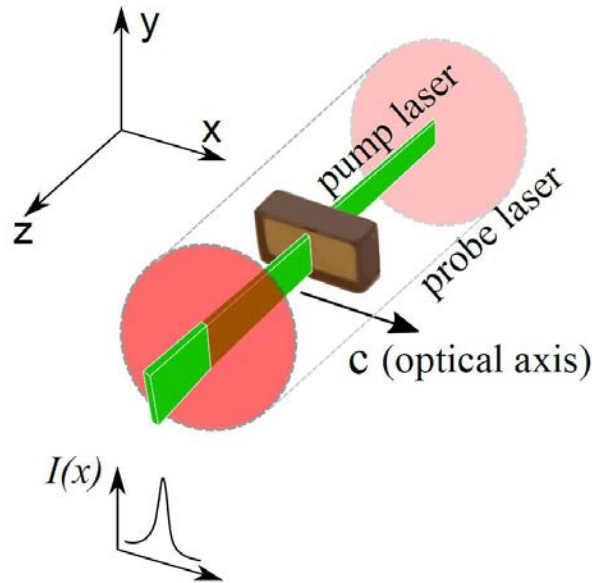


Figure 4.5.1.3: The scheme of the 1D illumination on the sample.

In accordance with these conditions the intensity profile at the input surface of the sample can be expressed as:

$$I(x) = I_0 \exp\left(-\frac{x^2}{2w^2}\right) \quad (4.5.1.1)$$

with a waist of  $w = (75 \pm 1) \mu\text{m}$ .

Eq. (4.5.1.1) describes a Gaussian beam with essentially different diameters along  $x$  (thin) and  $y$  (thick) axes propagates parallel to the  $z$  axis. Gaussian beam extent assumed to be infinite in the perpendicular direction to the  $z$  axis of the sample. The beam is perpendicularly polarized to the  $z$  axis. In Eq. (4.5.1.1) the diffraction and absorption of the beam due to the smaller thickness of the sample compared to the Rayleigh range of the beam is neglected. The Rayleigh range of the green laser beam is approximately 1 cm and the profile of the beam is assumed to be almost stable inside the sample as the crystal was located in the middle part of the beam.

To cancel a parasitic charge condensation at the sample surface it is short-circuited by a covering the conductive paste on the edges. To create, keep and control as well the homogeneous temperature in the range from room temperature to 150 K the sample was placed in the internal chamber of the nitrogen optical cryostat with a 0.1 K stability and the laser beam penetrated through the quartz window onto the crystal. The peak green beam intensity on the sample surface has been measured considering the losses caused to the cryostat window which was equal  $I_0 = 280W/m^2$ . Due to the realized low intensity regime the photoactive donor  $Fe^{2+}$  centers may be proposed as a single photo-excited charge carrier source. Before every measurement the LED (light emission diode) of incoherent light covering the whole surface of the sample was switched to clean all the information of previously measurements. The duration of the cleaning process depends on the temperature and is faster at room temperature. According to the photorefractive effect, the green beam pattern was turn into a refractive index pattern [72].

1. Production of interferogram of under study samples via the digital holographic technique.

The holograms including the information about the refractive index changes depend on the time are formed by Mach-Zehnder interferometer, which is considered the second part of the setup.

In order to create and visualize the fringes in the two-dimensional CCD camera (charge coupled device),  $\lambda = 632.8$  nm wavelength He-Ne laser beam source with 5 mW power was used, which was spatially filtered (SF) and was attenuated not to change the refractive index variation  $\Delta n$  formed by 543 nm green laser beam. The 632.8 nm laser beam was splitted (BS) onto two parts: object and reference beams making up a Mach – Zehnder interferometer. The object beam superimposing to the 543 nm laser beam was transmitted via the crystal with the help two dichroic mirrors (DM). After the sample object beam was recombined with the reference beam due to the second beam splitter (BS) resulting to the interferogram by using the CCD camera with  $1280 \times 7800$  pixels array (pixel dimension is  $3 \mu m$ ). In order to produce an image of the output surface of the tested sample on the CCD target plane a set of lenses with  $4 f$  system was arranged supporting the near field conditions for measurements to avoid the distortion of laser beam caused by the photorefractive effect. A polarizer was placed in front of the CCD camera only to select the extraordinary component of the varied refractive index

$\Delta n$ . The shutters were utilized to control the time exposure of the two lasers and of the LED. In order to obtain a picture of the sample corresponding to a time step set by the experimenter the CCD camera was connected directly to the photo-camera. The control of the temperature of the cryogenic system was performed with the help of the computer, which allows to monitor the temperature at each time frame.

According to the object beam containing an information about the phase shift after the sample the complex amplitude equal to  $U(Z)e^{i\varphi(x,y)}$  on the CCD target plane [73] where  $\varphi(x,y)$  phase difference caused by the sample can be in the range  $[0; 2\pi]$ :  $\Delta\varphi \in [0, 2\pi]$  the crystal considering as a pre phase object thus the photorefractivity influences only on the phase. The period of the visualized fringes depends on the wavelength and the angle between the object and reference beams  $\Lambda \sim \frac{1}{\sin\theta}$  as the beam wavelength  $\lambda=632.8$  nm is constant.

In the case of using only an object beam in the CCD detector would be formed only bright spot instead of fringes as CCD camera records only the intensity of the beams, on the other hand, an intensity is proportional to the square of amplitude.

$$I \propto |U(Z)e^{i\varphi(x,y)}|^2 = |U|^2 |e^{i\varphi}|^2 = |U|^2 \quad (4.5.1.2).$$

Whereas due to the interference of reference and object beams, the total complex amplitude (the scheme is given in figure 4.5.4) is expressed as:

$$U_{TOT} = U(Z) + U(Z)e^{i\varphi(x,y)} \quad (4.5.1.3).$$

The resultant intensity of the hologram on the CCD plane is equal to:

$$I(x,y) = |U_{TOT}|^2 = |U(Z) + U(Z)e^{i\varphi(x,y)}|^2 = |U(Z)|^2 + |U(Z)e^{i\varphi(x,y)}|^2 + UU^*e^{-i\varphi} + UU^*e^{i\varphi} \quad (4.5.1.4).$$

Where the last items  $UU^*e^{-i\varphi} + UU^*e^{i\varphi}$  demonstrate the phase shift due to the crystal.

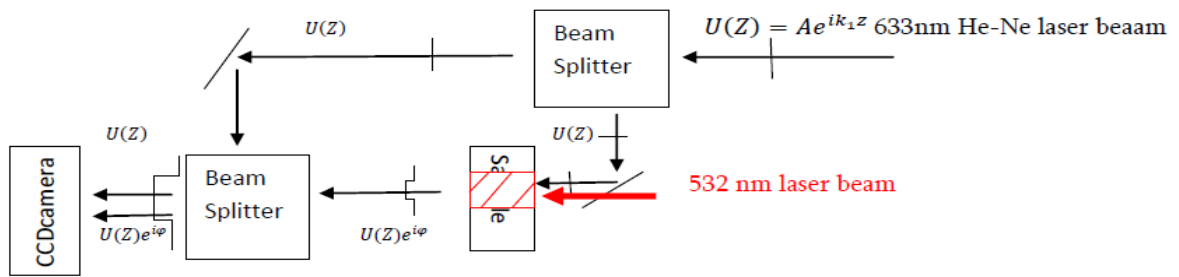


Figure 4.5.1.4: Schematic pattern of the creation of the fringes.

### § 4.5.2. The phase shift modeling

All process was controlled completely by Matlab computer program permitting series of measurement in different temperature ranges. The interferograms are stored in a computer as a function of time starting from the moment the green laser is switched on. The duration of the measurement must correspond to the complete evolution of  $\Delta n$  to reduce the error of the estimation of the saturation refractive index. A typical interferograms formed on the CCD target plane at the beginning of measurements and after the several time switching the green laser beam when the refractive index change is visible are illustrated in Figure 4.5.2.1.

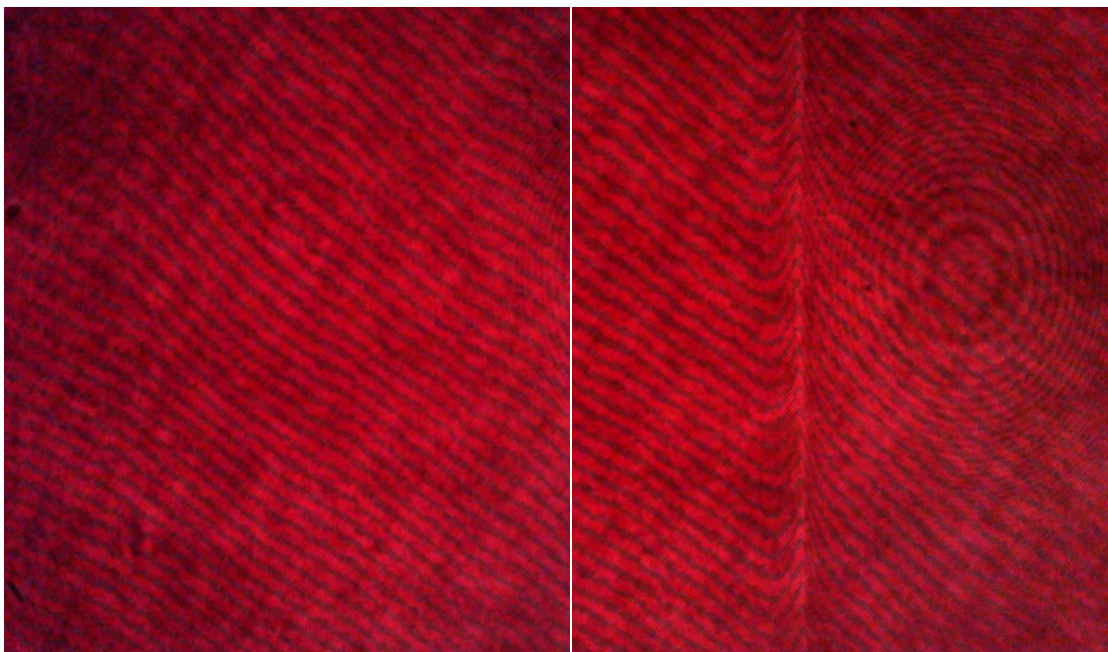


Figure 4.5.2.1: Interferograms without refractive index change and with the changing of the shape of fringes because of to the variation of refractive index due to the 543 nm laser beam.

### Reception of wrapped phase map from the interferogram due to the Fourier transformation.

To obtain phase shift all images of the interferograms were analyzed automatically by the following processes [70]:

Preprocessing of the input image

Fourier transformation

Filter function

Inverse Fourier transform

Wrapped phase shift

Taking the Fourier transformation of resultant intensity  $I(x,y)$ (Eq. 4.5.1.4) the spatial frequency of the hologram was obtained. In the frequency space three main peaks are located shown in Figure 4.5.2.2.

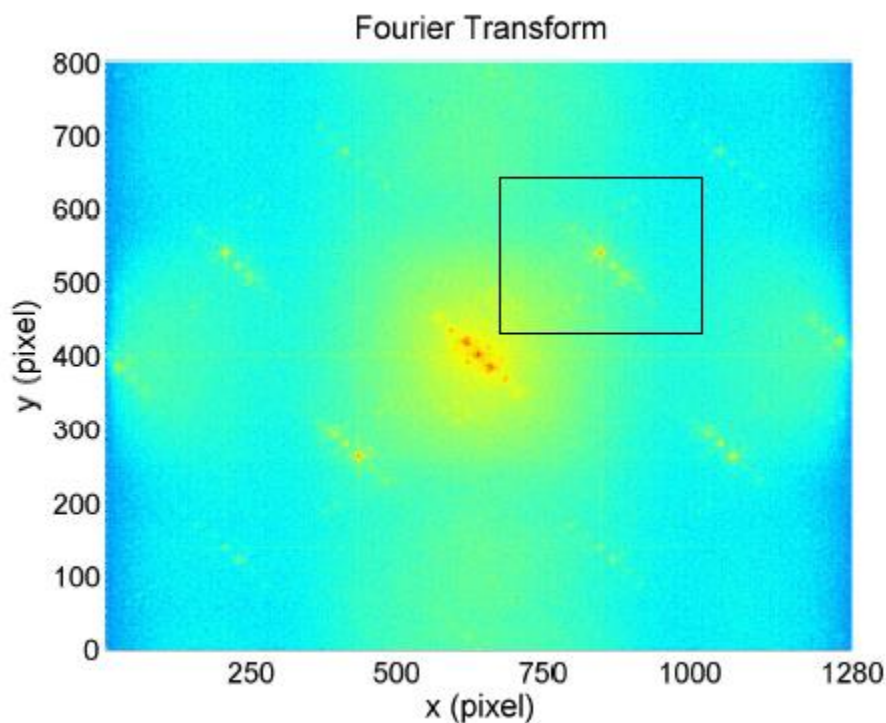


Figure 4.5.2.2: Fourier transform of the interometric image applying the bandwidth filter to the central peak.

The central main peak at  $\mathbf{k} = 0$  is related to the spatial average of the interferometric image, the other two dots with  $\mathbf{k} = \pm\mathbf{k}_0$  wave vector symmetrically placed on both sides of the

central peak contain the information about  $\Delta\varphi$ . As fringes of the obtained interferometric image in real space are tilted by  $45^\circ$  angle from the vertical direction thus, in the Fourier image this two satellite dots were placed also at the same angle. In the frequency space the other dots were also located which were related to the other interferometric patterns in the real space. Then the bandwidth filter was applied in the frequency space to separate the domain frequency from the whole special frequency spectrum of the holograms. By replacing the window with  $k_0$  to the center of the Fourier space the reconstruction of the object beam  $o(x, y)$  was realized with the help of the inverse Fourier transform of the object beam frequency spectrum  $O(\xi, \eta)$  [74]. This reconstructing process can be expressed as

$$o(x, y) = \frac{1}{r_0} F^{-1}\{r_0 O(\xi, \eta)\} \quad (4.5.2.1),$$

where  $F^{-1}\{r_0 O(\xi, \eta)\}$  is the inverse Fourier transformation and  $r_0$  is the amplitude of the object beam and demonstrates the constant value. Therefore, 2D wrapped phase of the objective beam can be obtained from the following equation:

$$\varphi(x, y) = \arctan \left\{ \frac{Im[o(x, y)]}{Re[o(x, y)]} \right\} \quad (4.5.2.2),$$

where  $Im[o(x, y)]$  and  $Re[o(x, y)]$  are correspondingly imaginary and real parts of the phase of the objective beam. The Fourier transformation was performed by using Micro Manager MM studio computer program, due to which the Fourier space was obtained from the real space of the image of fringes to determine wrapped phase map [75].

#### **Obtainment of unwrapped phase map from wrapped phase map using Miguels algorithm.**

According to the FFT transformation the wrapped phase map was obtained and then it was transformed on to the unwrapped map with the help of Miguel 2D unwrapper computer program using the 2D-SRNCP algorithm [76]. The information about the phase shift depends on the beam phase front shape, surface defects as well as the intrinsic transmittivity of the crystal thus to avoid this problem, a reference image obtained before the refractive index variation was considered as background and was subtracted from others.

The phase of the object beam is varied from 0 up to  $2\pi$ , then from  $2\pi$  to 0 and the variation continues with the same temp:  $\Delta\varphi \in [0, 2\pi]$  (Figure 4.5.2.3).

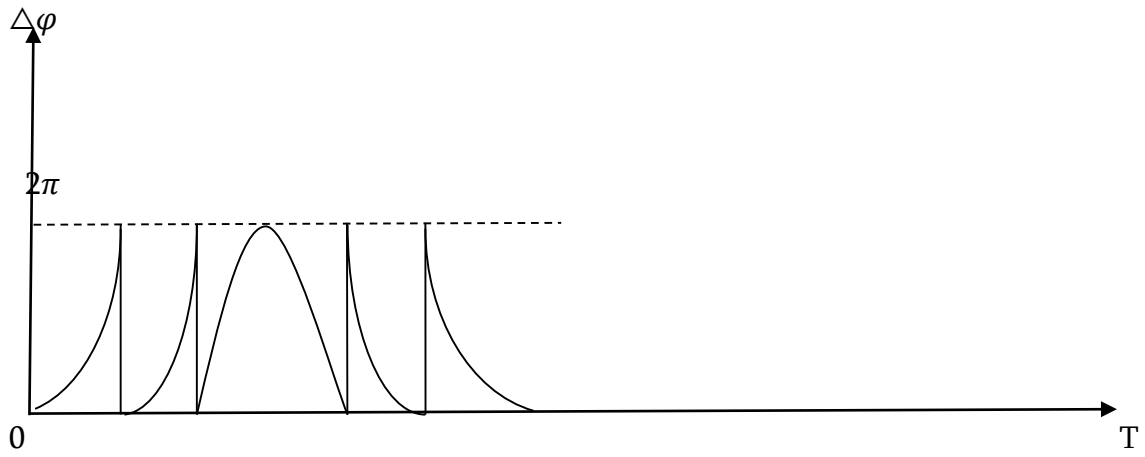


Figure 4.5.2.3: Wrapped phase map.

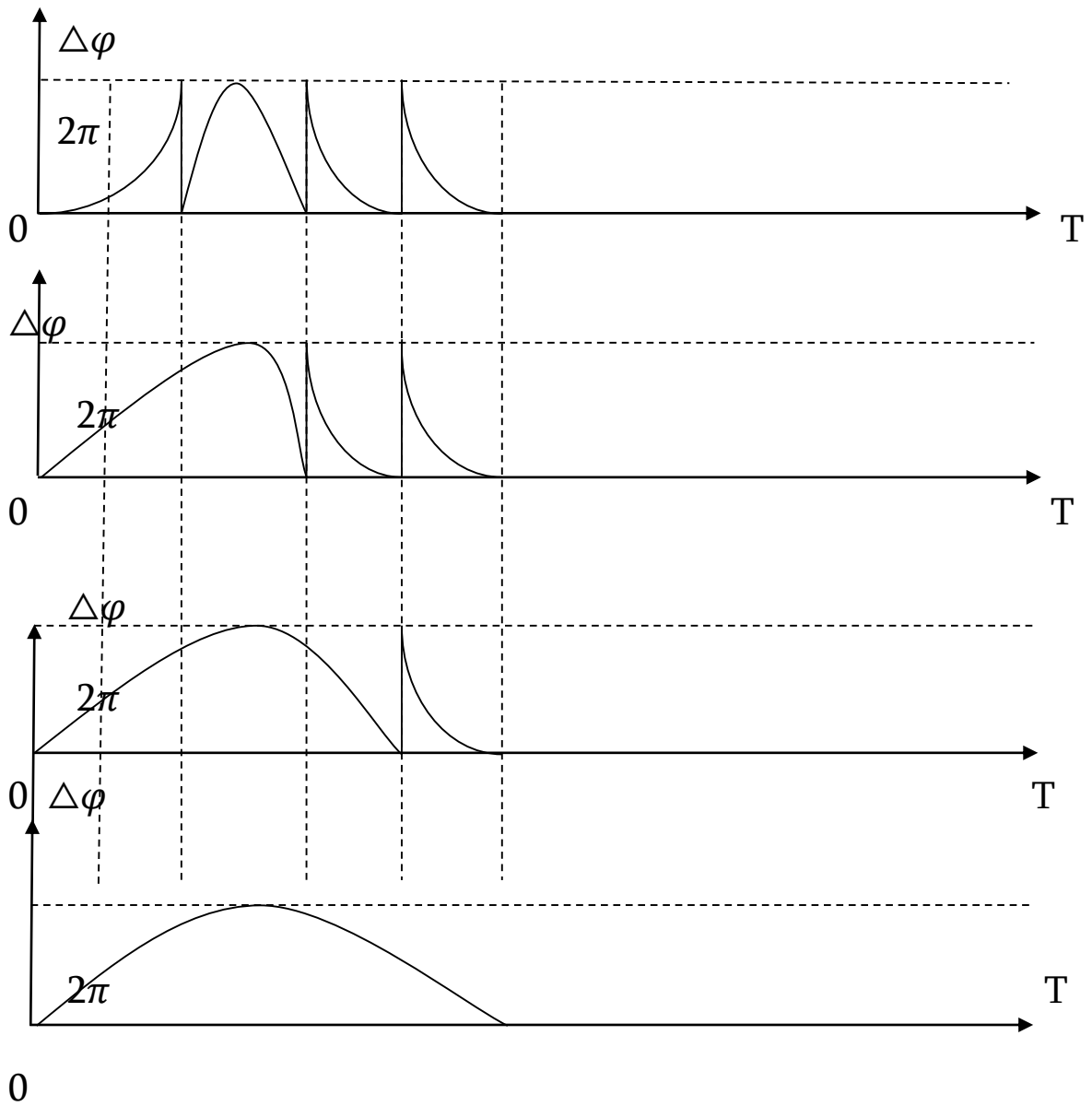


Figure 4.5.2.4: The process of phase unwrapping

Although the phase has a value at the  $[0, 2\pi]$  range, the refractive index change  $\Delta n$  has the arbitrary (non discret) values, thus the phase shift diagram is wrapped [77,78]. To observe the continuous value of the  $\Delta n$  the phase  $\Delta\varphi$  diagram was substituted to the unwrapped [79] (Figure 4.5.2.4).

All the process to obtain  $\Delta\varphi(x, y, t)$  map depending on the time was automatized fully in Matlab. The typical results of the refractive index change corresponding to the phase delay maps obtained at the beginning of the measurements and after the several time switching the green laser beam are illustrated in Figure 4.5.2.5.

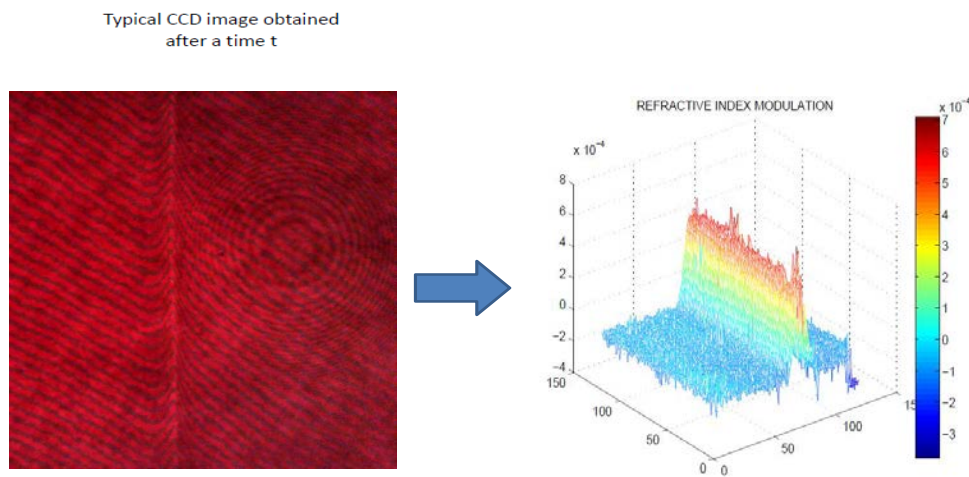


Figure 4.5.2.5: Receipt of the map of the refractive index modulation from CCD fringes image.

To analyze the phase shift delay, the measured  $\Delta\varphi$  along  $y$  was averaged, due to this fact that the beam is invariant along this direction by construction and finally a 1D phase profile  $\Delta\varphi(x)$  is obtained. To obtain a 1D profile  $\Delta\varphi(x, t)$  the phase profile given in Figure 4.5.2.5 is integrated along the vertical direction improving the signal to noise ratio. During the measurements for each temperature due to the 543 nm wavelength laser beam the phase modulation becomes bigger reaching the saturated value. All the frames reported during measurements were analysed to obtain the corresponding 1D profile.

After unwrapping the information about the refractive index modification can be determined including in the phase shift of the fringe pattern of the interferogram in the 150 K-300 K temperature range described by the following expression:

$$\Delta n = \frac{\lambda \Delta \varphi}{2\pi D} \quad (4.5.2.3).$$

where  $\lambda = 534 \text{ nm}$  is the wavelength of the probe laser beam,  $\Delta\varphi$ -is the phase shift,  $D$ -is the thickness of the crystal.

Eq. (4.5.1.1) can be used when the intensity profile of the beam is stable along the propagation distance. Taking into account the absorption of the understudy samples the equation of the intensity can be rewritten:

$$I(x, z) = I_0 \exp\left(-\frac{x^2}{2w^2} - \alpha z\right) \quad (4.5.2.4),$$

where  $\alpha$  –is the measured absorption coefficient (See Section 1). Thus, the space charge field as a function of the space and time, can be expressed as [80]:

$$E(x, t) = -E_{sat} \left[ \frac{I(x)}{I(x)+I_D} \right] \cdot \left[ 1 - \exp\left(-\frac{t}{\tau_d(x)}\right) \right] \quad (4.5.2.5).$$

To solve analytically the problem of the instability of the parameters which depend on the intensity is very hard [81], however the solution for 1D model can be found rewriting the Eq. (4.5.2.5) as:

$$E(x, z, t) = -E_{sat} \left[ \frac{\sigma_{ph}(x,z)}{\sigma_{ph}(x,z)+\sigma_{dark}} \right] \cdot \left[ 1 - \exp\left(-\frac{t}{\tau_d(x,z)}\right) \right] \quad (4.5.2.6).$$

Eq. (4.5.2.6) demonstrate the dependence of the parameter  $E(x, z, t)$  on the  $z$  direction. Here the “local” approximation [80] was used, when the parameters which indicate the dependence on the intensity were expressed by the “local” intensity value in the case of the uniform illumination or/and slow variation of the illumination profile. According to the linear electro-

optic effect the refractive index variation can be expressed via the space charge field taking into account the dependence of the last parameter on the z direction:

$$\Delta n(x, z, t) = \frac{1}{2} r_{33} n_e^3 E(x, z, t) \quad (4.5.2.7).$$

Here the values of the unclamped linear EO coefficient  $r_{33}$  were used as a function of temperature [82] for large range (7K-300K) with 632.8 nm wavelength illustrating 20% decrease with the slow decrease of the temperature from 300 K to 10K.  $n_e$ -is the extraordinary refractive index for the probe laser wavelength. Along the sample thickness integrating the measured total phase shift accumulated by the beam which propagates via the region of the sample with the refractive index variation:

$$\Delta\varphi(x, t) = \frac{2\pi}{\lambda} \int_0^d \Delta n(x, z, t) dz \quad (4.5.2.8).$$

Where  $\lambda = 632.8 \text{ nm}$  is the probe beam.

## ***§ 4.6. Data Analysis***

### ***§ 4.6.1. Experimental results***

The measurements of the recordation of the space charge field formation under the continuous illumination for large temperature range from 150K to the room temperature have been performed for two series of the samples LN:Fe1 and LN:Fe2 (see Table 1.2.1). The first series of samples have the constant deep trap ( $Fe^{3+}$ ) content and a different shallow trap ( $Nb_{Li}$ ) concentration meanwhile the last series of samples are with the fixed antisite concentration and a various deep trap concentration. In order to characterize the obtained results for the samples the following convention is adopted: Series/Deep Traps/ Shallow traps (see the Figures 4.6.1.3, 4.6.1.4, 4.6.1.5, 4.6.1.6, 4.8.1, 4.8.2, 4.8.4 and 4.8.5). The Series are expressed by letters A and B related to the samples LN:Fe2-3 and LN:Fe1-3 respectively and the concentration of traps (deep and shallow) are given in  $\times 10^{25} m^{-3}$ .

The fitting of the set of 1D profiles (Figure 4.5.2.5) one by one with the peak function leads to a determination of the dependence of the peak maximum  $\Delta\varphi_{MAX}(t)$  on the time. The typical

1D profile of the evaluation at room temperature and the example of the saturation of the phase shift at  $T = 140\text{ K}$  are given correspondingly in Figures 4.6.1.1a and 4.6.1.1b.

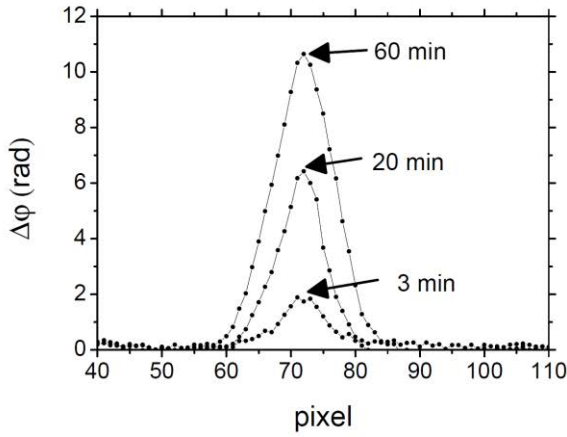


Figure 4.6.1.1a: 1D profile obtained from the integration of image given in Figure 4.5.2.5 along the vertical direction at room temperature.

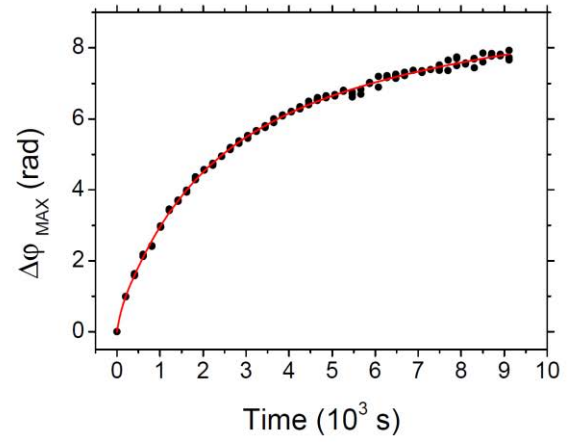


Figure 4.6.1.1b: The maximum amplitude of the phase map as a function of time obtained at  $T = 140\text{ K}$ , the red line corresponds to the fit.

Eq. (4.5.2.8) solving for the central illumination profile where  $\sigma_{ph}(0, z) \gg \sigma_{dark}$ , the value of the phase shift in the center of the probe beam depending on the time can be obtained:

$$\Delta\phi_{MAX}(t) = \frac{2\pi}{\lambda} \Delta n_{sat} \left\{ d + \frac{1}{\alpha} \left[ \mathcal{E} \left( \frac{t e^{-\alpha d}}{\tau_d(0,0)} \right) - \mathcal{E}_i \left( \frac{t}{\tau_d(0,0)} \right) \right] \right\} \quad (4.6.1.1).$$

Here  $\mathcal{E}_i(x) = -\int_{-x}^{\infty} \frac{e^{-t}}{t}$  is the exponential integral function. By fitting the experimental value of the phase shift at  $z = 0$  related to the beam intensity  $I_0$  reported in Eq. (4.5.2.4) the refractive index modulation for the stationary situation  $\Delta n_{sat}$  with  $\tau_d(0,0)$  was calculated using Eq. 4.6.1.1. During the measurement for every temperature value due to the 543 nm wavelength laser beam the refractive index modulation corresponding to the phase shift becomes bigger reaching the saturated value. The examples of the evaluation and the saturation of the refractive index change for certain temperature are reported in Figure 4.6.1.2a and 4.6.1.2b respectively. With the decrease of the temperature the duration to reach  $\Delta n_{sat}$  value becomes longer. As the estimated material parameters depending on the crystal composition were below experimental accuracy [83] thus, this dependence was neglected.

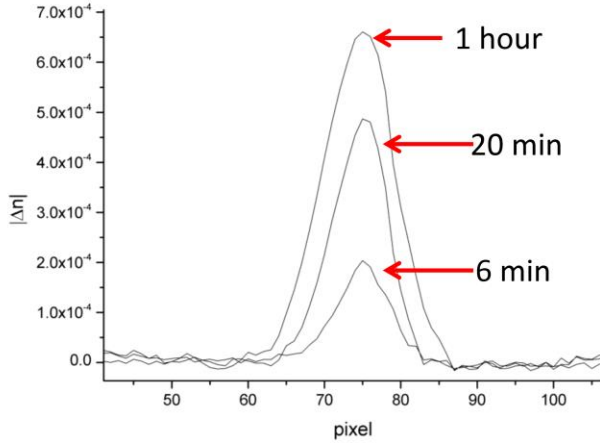


Figure 4.6.1.2a: Temporal evolution of refractive index profile T=280K.

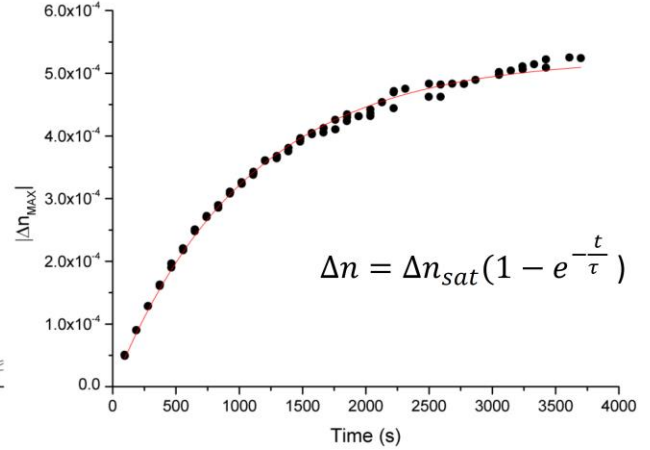


Figure 4.6.1.2b: Temporal behavior of maximum refractive index T=300K.

### Saturation space charge electric field

The next step was the computation of the saturation values of the space charge field by using the Equation:

$$\Delta n_{sat} = \frac{1}{2} r_{33} n_e^3 E_{sat} \quad (4.6.1.2).$$

Here  $r_{33}$  is the linear coefficient of third column of EO tensor. To calculate the saturation space charge field the values of  $r_{33}$  as a function of crystal composition were used measured by us at room temperature [84], however for the other temperatures the values of  $r_{33}$  were used investigated by C. Herzog et al. [82] as a function of temperature.

The experimental results (dots) of the saturation space charge field depending on the temperature given in Figures 4.6.1.3 a and 4.6.1.3 b illustrate the monotonous increase with the decrease of the temperature corresponding to the previous reports [85].

The calculated values (lines) of  $E_{sat}$  (Eq. 4.4.6) are reported in Figures 4.6.1.3 and 4.6.1.4 obtained for LN:Fe2-1 ÷ LN:Fe2-3 and LN:Fe1-1 ÷ LN:Fe1-3 series of samples.

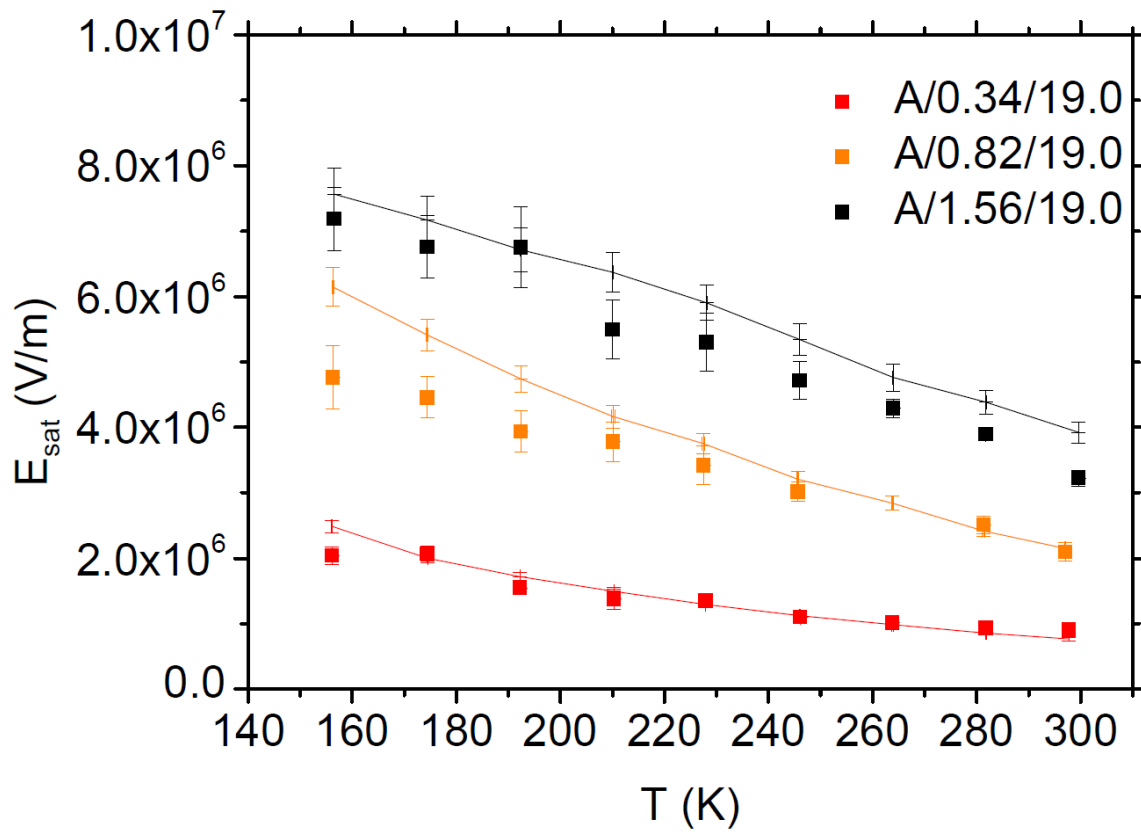


Figure 4.6.1.3: Saturation space charge field depending on the temperature for Fe:LN samples with series A. Dots: experimental results, Lines: simulation results for  $L_{PG} = (1.44 \pm 0.05) \text{ \AA}$  and  $\Lambda_{dark} = (1.69 \pm 0.07) \times 10^{-17} \text{ m}^2/\text{V}$  (detailed below).

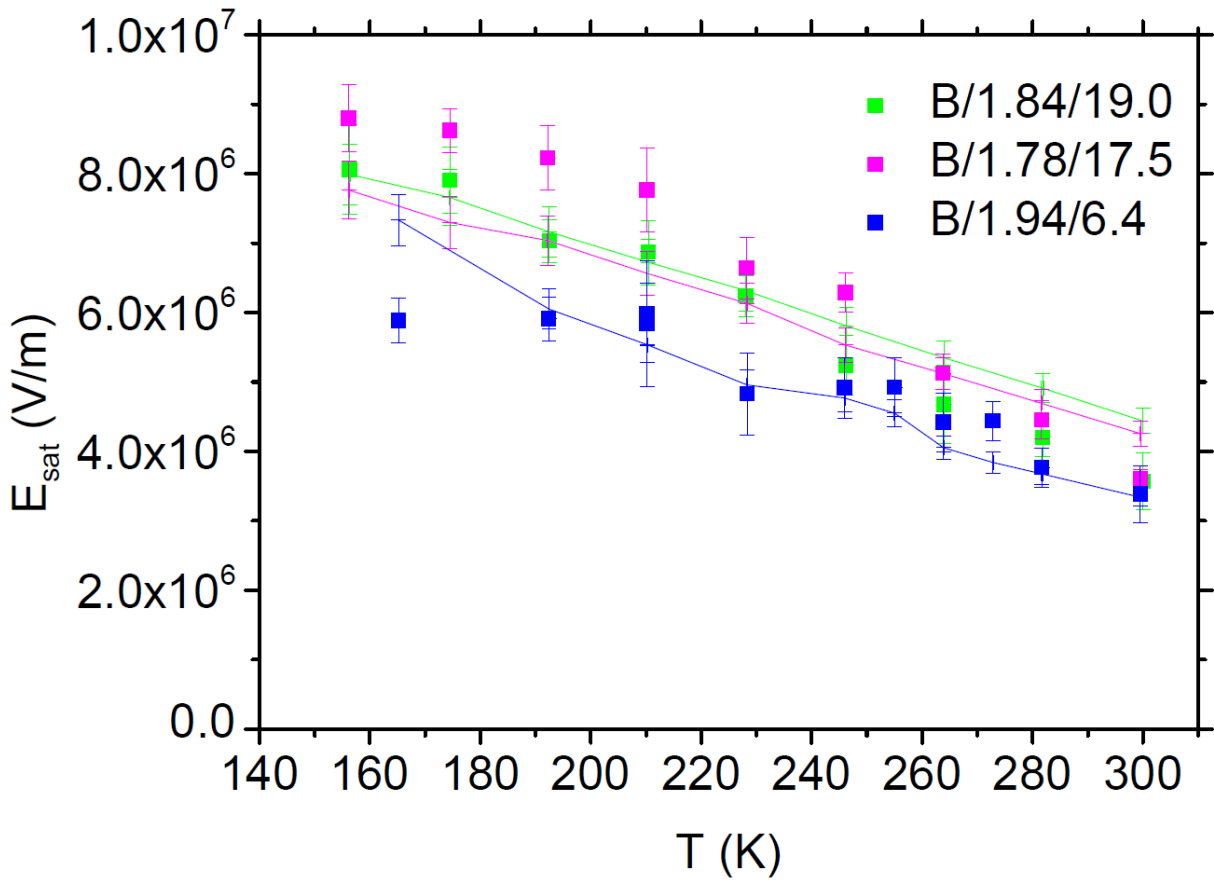


Figure 4.6.1.4: Saturation space charge field depending on the temperature for Fe:LN samples with series B . Dots: experimental results, Lines: simulation results for  $L_{PG} = (1.44 \pm 0.05) \text{ \AA}$  and  $\Lambda_{dark} = (1.69 \pm 0.07) \times 10^{-17} \text{ m}^2/\text{V}$  (detailed below).

It is also visible from the results that saturation space charge electric field  $E_{sat}$  is proportional to the  $[Fe^{3+}]$  concentration reported earlier [86], which is expectable from the photoconductivity measurements. However, the obtained values at room temperature were smaller compared to the previous results [87] paying attention on the variation of Fe concentration. This difference emphasizes the fact that dark conductivity  $\sigma_{dark}$  of the probed samples keeps the nonzero value (Eq. 4.4.5).

## Photoconductivity

From the results of the dielectric relaxation time (Eq. 4.4.4) the experimental values of photoconductivity were obtained as:

$$\sigma_{ph} = \frac{\varepsilon\varepsilon_0}{\tau_d} \quad (4.6.1.3).$$

The variation of the dielectric constant depending on the temperature and the crystal composition was ignored due to the below experimental accuracy [82,83]. Taking into account the drift coefficient  $\Lambda$  the photoconductivity can be normalized with the respect to the photogeneration rate  $G$ :

$$\Sigma = \frac{\sigma_{ph}}{G} = \phi\Lambda \quad (4.6.1.4).$$

The experimental results of the specific conductivity are given in Figures 4.6.1.5 and 4.6.1.6 (dots) demonstrating the monotonous decrease with the decrease of the temperature.

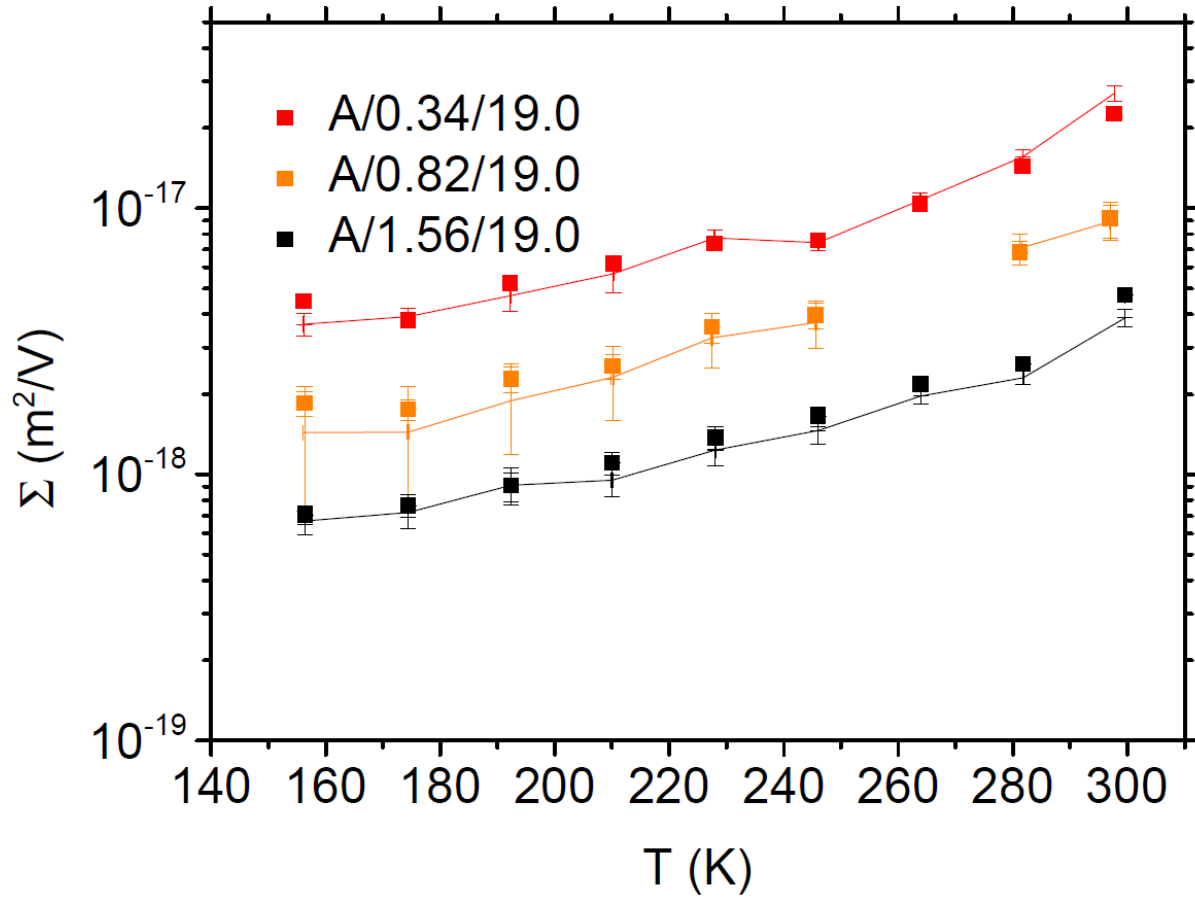


Figure 4.6.1.5: Empirical results (dots) for specific photoconductivity  $\Sigma$  as a function of temperature correspondingly for samples series A. By comparison the results obtained from simulation corrected for the experimental values  $\phi$  and  $\Lambda_{dark}$ .

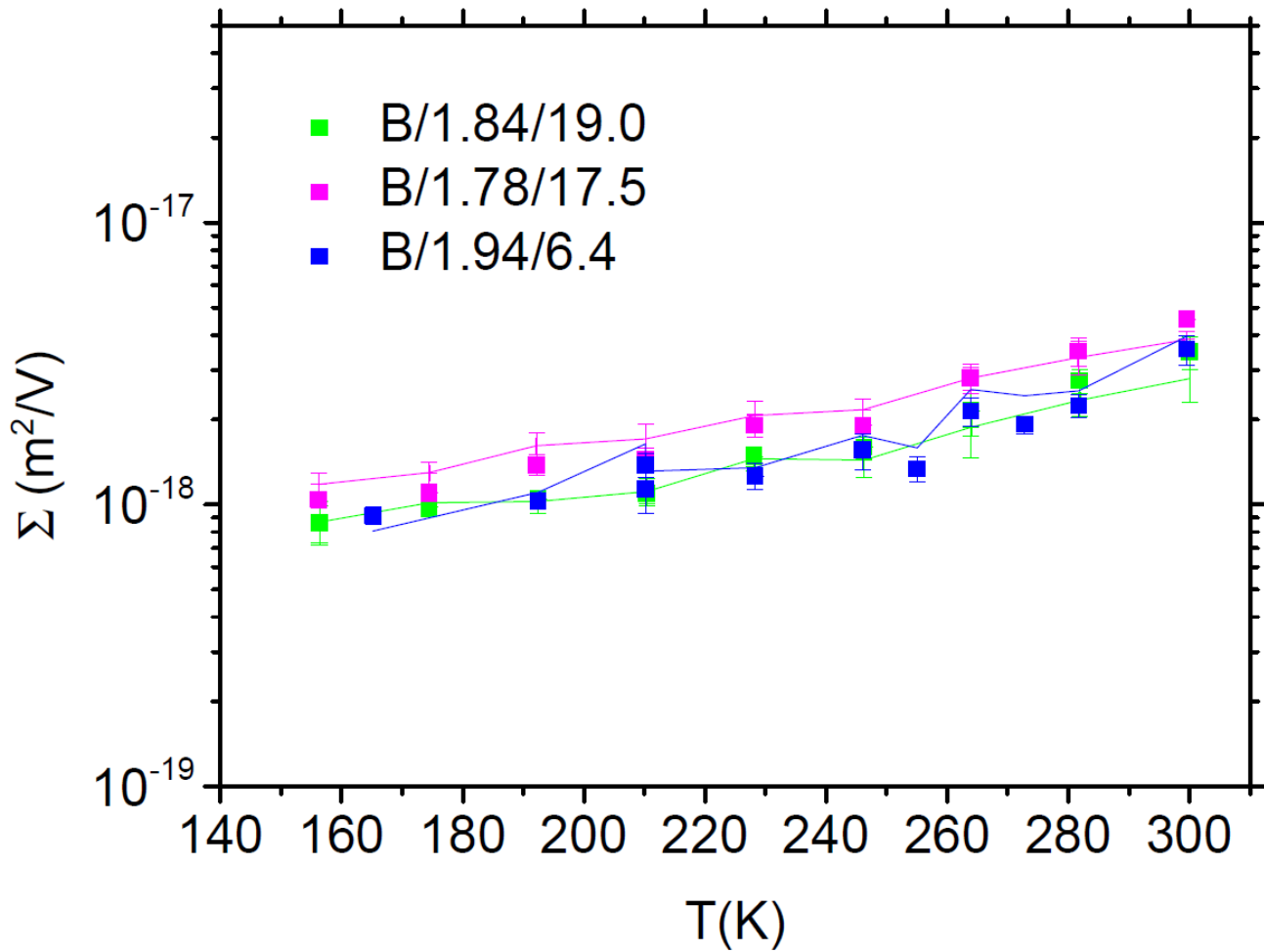


Figure 4.6.1.6: Empirical results (dots) for specific photoconductivity  $\Sigma$  as a function of temperature correspondingly for samples series B. By comparison the results obtained from simulation corrected for the experimental values  $\phi$  and  $\Lambda_{dark}$ .

## § 4.7. Simulation

### § 4.7.1. Marcus-Holstein polaron hopping model

Marcus-Holstein model was used to characterize the incoherent non-adiabatic hopping between small polarons in Fe:LN crystals in order to describe the photon induced charge transportation caused by photorefractive effect [88,89]. This simplest model proposed by Holstein based on the mechanism for electron transfer reactions [89]. According to the mentioned model the hopping can be realized between both sites with the same electron energy facilitating the tunneling effect of electrons from the initial site to the final one. The transition of electrons between sites with different values of energy is mediated by phonons after which the relaxation of the lattice neighboring the final site leads to the formation of the polaron again. The hopping of small polaron may be represented by the three-step. The hopping starts between atoms with thermal vibration due to the extraordinarily large atomic displacements close to a self-trapped carrier. The large-amplitude fluctuations permit to transfer the self-trapped charge carriers between sites. Then the transitory large-amplitude atomic shifts relax scattering the energy to the vibrations of neighboring atoms. In small polarons. The strong self-trapping of electron at one site permits electron transitions to the surrounding site.

The non-adiabatic jump frequency for hop from initial site to the final site ( $i \rightarrow f$ ) is defined [88-90]:

$$w_{i,f}(R, T) = \frac{1}{2} \left( \frac{\pi}{kT\lambda_{i,f}} \right)^{\frac{1}{2}} \frac{I_{i,f}^2}{\hbar} \exp\left(-\frac{r}{a_{i,f}} - \frac{U_{i,f}}{kT}\right) \quad (4.7.1.1),$$

where  $r$  is the spacing between initial  $i$  and final  $f$  sites,  $kT$  is the absolute temperature expressed in energy unit,  $\lambda_{i,f}$  the reorganization energy in Marcus theory related to the required energy for the lattice rearrangement is equal to the sum of the elastic energies of two polarons ( $E_i + E_f$ ),  $a_{i,f}$  an orbital parameter characterize the overlapping of electronic wave functions at the starting and final sites. The presence of the  $\frac{1}{2}$  factor is caused by the argument that Eq. (4.7.1.1) illustrate the individual rate related to the certain final site as well is equal to

a half of the total rate of the molecular chain in Holstein theory [70]. The hopping barrier  $U_{i,f} \neq U_{f,i}$  can be expressed as [91,92]:

$$U_{i,f} = \frac{(2E_i + \varepsilon_i - \varepsilon_f)^2}{4(E_i + E_f)} \quad (4.7.1.2),$$

where  $\varepsilon_i$  and  $\varepsilon_f$  are the pre-localization energies of the electrons at starting and final sites when the deformation is absent. In the case of the hopping between the same type sites ( $i = f$ ), the hopping activation energy is equal to the one half of the polaron energy [93-95].  $I_{i,f}$  pre-exponential factor defined by the selection of the combination ( $i, f$ ) characterize the jump between the chosen two sites. Due to the Marcus-Holstein polaron model the centers based on polarons ( $Nb_{Li}$  and  $Nb_{Nb}$ ) and  $Fe^{2+/3+}$  as well as the chosen hopping combination between them can be characterize by the set of the certain parameters.

Table 4.7.1.1: For the simulation used parameters.

<i>Parameter</i>	<i>Value</i>	<i>Unit</i>	<i>Ref.</i>	<i>Note</i>
$E_{FP}$	0.545	eV	[94]	Free polaron energy
$E_{GP}$	0.75	eV	[96]	Bound polaron energy
$E_{Fe}$	0.7	eV	[94]	Fe defect energy
$\varepsilon_{FP}$	0	eV		Free polaron pre-localization energy
$\varepsilon_{GP}$	0.2	eV	[96]	Bound polaron pre-localization energy
$\varepsilon_{Fe}$	1.22	eV	[94]	Fe defect polaron pre-localization energy
$\alpha_{FP,FP} = \alpha_{GP,GP} = \alpha_{GP,FP} = a$	1.6	eV	[96]	Hopping parameter
$\alpha_{FP,Fe} = \alpha_{GP,Fe} = c$	1.3	eV	[96]	Trapping parameter
$I_{FP,FP} = I_{FP,GP} = I_{GP,GP} = I$	0.1	eV	[97]	Transfer integral pre-factor

Choosing the initial and final sites all the required parameters can be obtained for the description of the possible jumps in iron doped LN crystals. The required parameters such as: 1) two energetic parameters, the polaron energy  $E_i$  and the pre-localization energy  $\varepsilon_i$ , 2) six orbital parameters ( $a_{i,f} = a_{f,i}$ ), 3) six pre-factors determine the transfer integral ruling the possible jumps are given in Table 4.7.1.1.

To illustrate the influence of the space charge field  $\mathbf{E}$  on the hopping frequency in Eq. 4.7.1.1 to the parenthesis at the numerator the potential energy  $q(\mathbf{r}_i - \mathbf{r}_f) \cdot \mathbf{E}$  gained by the polaron with the position vectors  $\mathbf{r}_i$  and  $\mathbf{r}_f$  related to the correspondingly initial  $i$  and final  $f$  sites is added. To support the random diffusion in the simulation the space charge field must be not too strong, which means that the term  $q(\mathbf{r}_i - \mathbf{r}_f) \cdot \mathbf{E}$  must be smaller compared to the absolute temperature  $kT$ . For the investigation of the measurable displacement this above mentioned compromise is maintained setting the value of field at  $5 \times 10^6 \text{ V/m}$  along the crystallographic  $c$  axis for all values of the temperature. As the approximation (4.7.1.1) is correct only for non-adiabatic hopping frequency [90] thus, the lattice must keep an essential thermal energy leading the charge motion as well as it assuming reliable for temperatures above the one half of the Debye temperature  $\theta_D/2$ , when  $\theta_D \approx 503 \text{ K}$  for lithium niobate crystals [98]. Nevertheless, according to the experimental results investigated by Faust et al [99] the non-adiabatic approximation can be preserved at least down to 150 K temperature, as the Arrhenius plot of the mobility in LN crystals without antisites is maintained before above mentioned temperature.

### ***§ 4.7.2. Monte Carlo simulation***

The small polaron theory based on Marcus-Holstein's model was used in Monte Carlo algorithm which is considered the simplest numerical approach to simulate the hopping model consist of one single electron at time. This approach is related to low electron density system thus, the interaction between electrons is ignored. At the initial site  $N_{\text{Nb}}$  electron places randomly performs a jump in a structure reproduced randomly. Although the final position

for every jump is randomly, but it is weighted by hopping frequency to each possible destination sites. According to the main approach the generation of polaron in a random position is considered for LN:Fe lattice. The random motion as well as randomly hops among the different sites have been investigated. The rest time on each visited site and the next destination site as well were computed by using the Marcus-Holstein hopping frequency. The relaxation time, as well as the type and the number of sites visited before polaron is trapped by a perfect trap ( $Fe^{3+}$  trap) also the final position have been calculated by a classical Gillespie algorithm [91]. All the simulation is repeated with a high number of polarons in order to reach the satisfactory statistics for the average distance along the field direction for running particles before trapping. The computed results have been used for the explanation of the experimental results.

Within band model both assumptions are justified, however more careful verification is necessary in the case of polaron transportation. For example, normal diffusion laws may not be tested [100] for a jumping polaron on a defective lattice with a distance- and energy – dependent hopping frequency (Marcus-Holstein polaron hopping model). As well as an equation described the polaron trapping rate in the frame of band models should be related to the monoexponential decays of a polaron population which are formed by a short beam pulse, meanwhile the decays of the polaron are characterized by a Kohlrausch - Williams- Watt law corresponding to a heavy-tailed distribution of the capturing times [93] . To avoid above described problems is more reasonable to observe as a parameter product  $\mu\tau$  than those separately. According to the physical meaning, this product is the average drift length (the displacement of the hopping particle)  $\langle z \rangle$  which is a polaron runs from the formation site up to the captured place under a unit electric field. The ratio of the mentioned parameters  $\langle z \rangle$  and the electric field  $E$  is referred as an operative definition such as the drift coefficient:

$$\Lambda = \langle z \rangle / E \quad (4.7.2.1).$$

In general, this definition is useful as the parameter  $\langle z \rangle$  remains proportional to the electric field magnitude even in the case of the anomalously diffusing particles [100].

### § 4.8. Yields

#### The drift coefficient

As discussed above the fundamental result of Monte Carlo simulation is the drift coefficient  $\Lambda$  which is the spacing that run the polaron from its generation to the capturing due to the influence of the unitary electric field. In Figures 4.8.1, and 4.8.2 are shown the results of  $\Lambda$  parameter in the same conditions which were used to obtain the results of the space charge field (Figures 4.6.1.3 and 4.6.1.4).

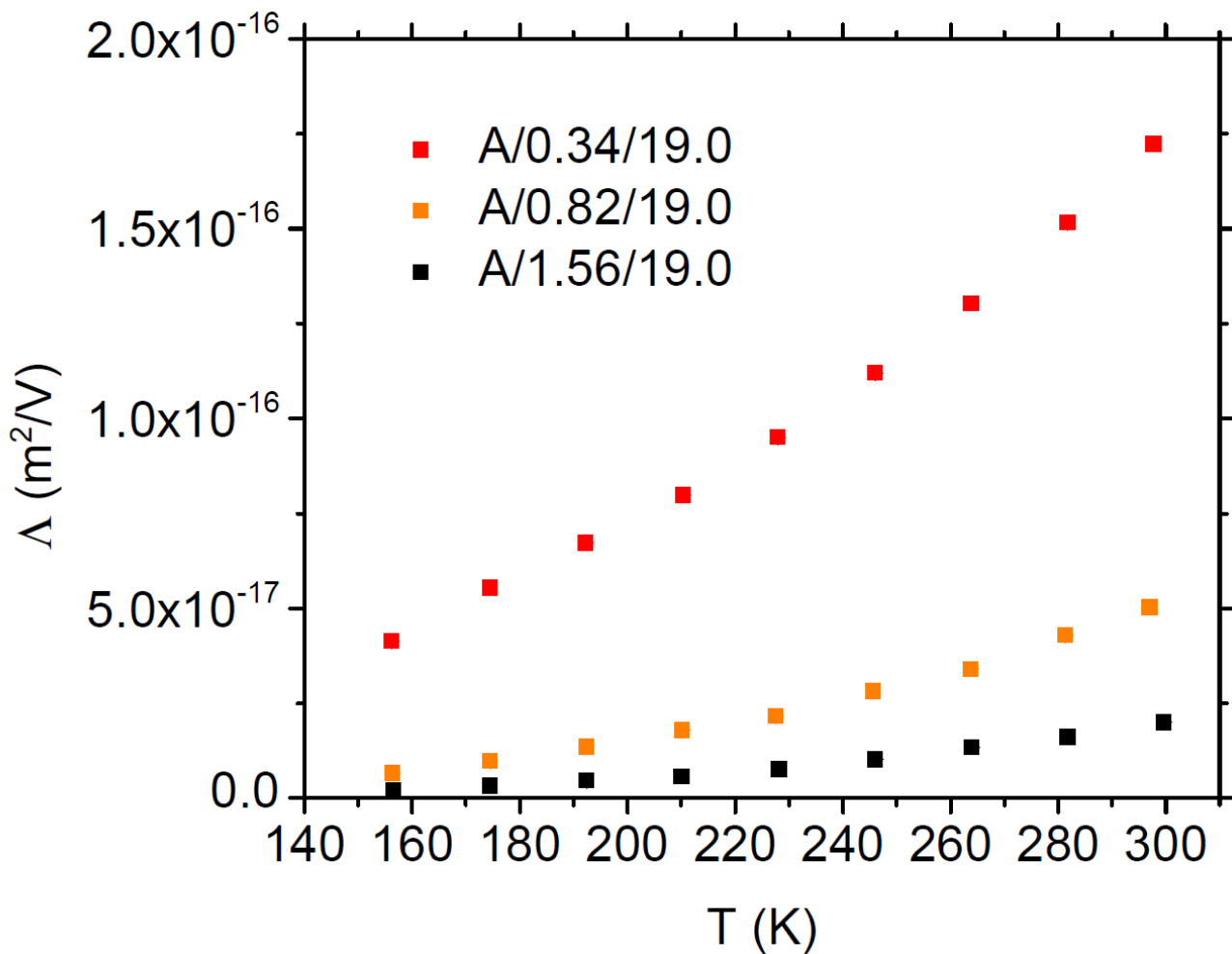


Figure 4.8.1: Simulated drift coefficient  $\Lambda$  for series A.

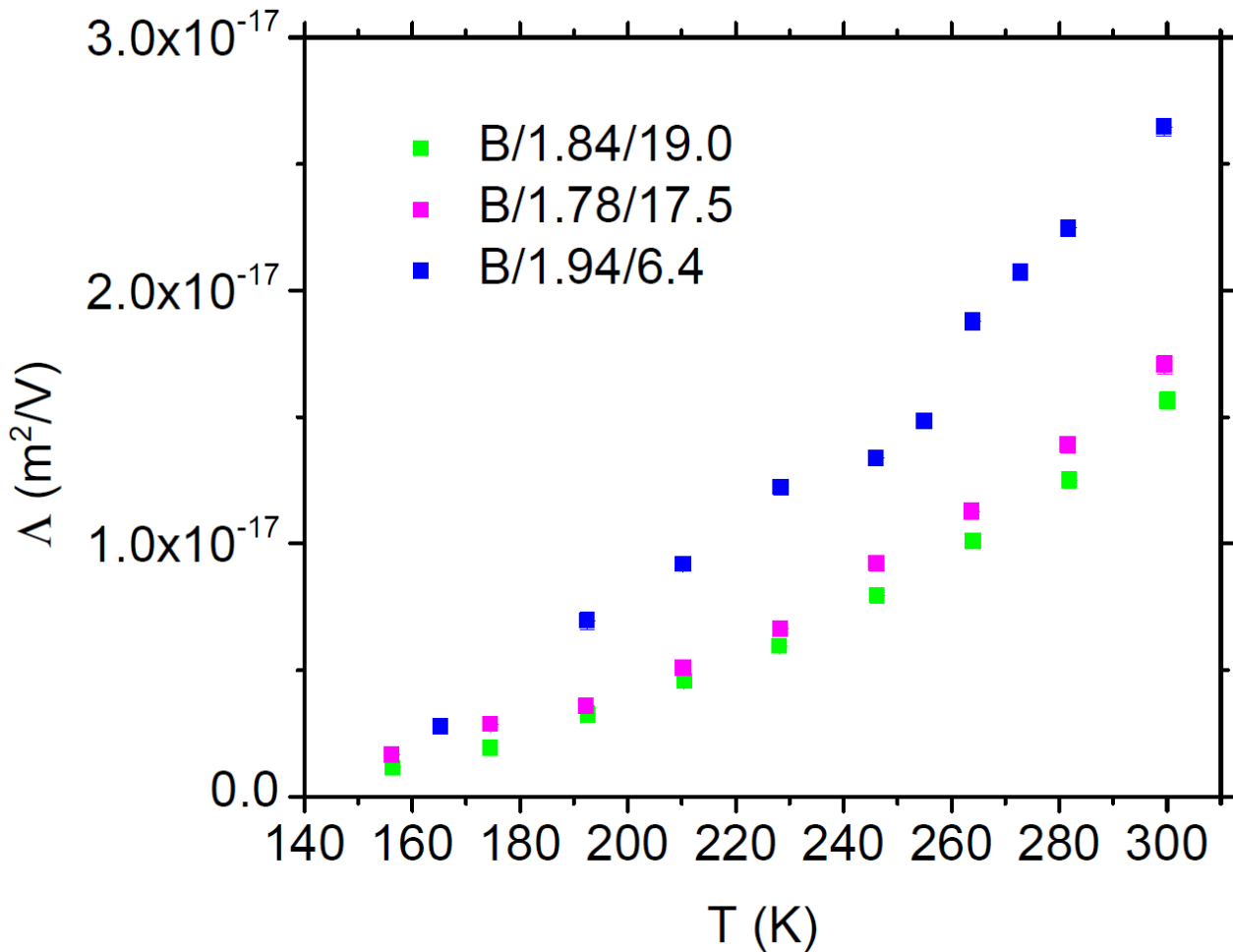


Figure 4.8.2: Simulated drift coefficient  $\Lambda$  for series B.

With the decrease of the temperature the value of the drift coefficients also decrease, which illustrates that the polaron covers on average a smaller spacing at the low values of temperature. Due to the high concentration of iron ions in LN:Fe crystals the antisite concentration is small which keeps the value of the drift coefficient below  $3 \times 10^{-17} \text{ m}^2/\text{V}$ . However,  $\Lambda$  parameter demonstrate the trend of increase with the increase of stoichiometry of the sample due to this fact that a higher trap concentration disturbs the charge displacement in samples with low Li concentration. This samples of a serious illustrate a tend of decrease with the decrease of the temperature and the increase of antisite concentration. Whereas in samples of b serious value of  $\Lambda$  parameter is higher due to the high  $Nb_{Li}$  concentration. In

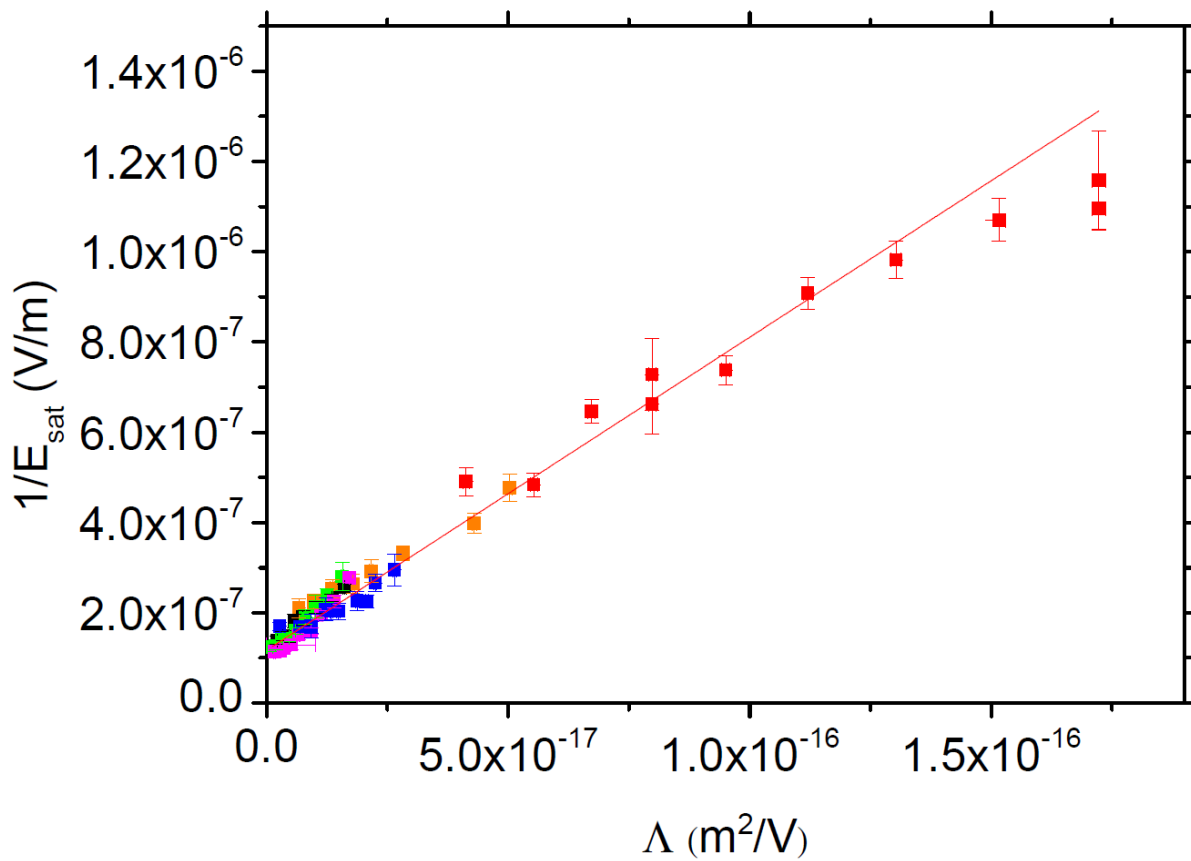


Figure 4.8.3: E

empiric values of  $1/E_{sat}$  as a function of drift coefficients  $\Lambda$  in the accordance with the experimental conditions. The red line is a linear fit of the data.

Figure 4.8.3 values of the reciprocal of the measured saturation space charge field  $1/E_{sat}$  were plotted as a function of the values of drift coefficient simulated in the accordance with the empiric conditions.

### Photogalvanic length

The effective photogalvanic length  $\phi L_{PG}$  was obtained by the multiplication of the drift coefficient  $\Lambda$  and saturation space charge field  $E_{sat}$  illustrating a weak temperature dependence

which is not in agreement with the literature results [86]. This fact is due to the dependence of the mentioned microscopic parameter on the donor center (Fe ions) and the excitation wavelength (534 nm). As the parameter  $L_{PG}$  is an intrinsic property of the crystal, thus, a weak temperature dependence of the product  $\phi L_{PG}$  can be caused only by the photogeneration efficiency  $\phi$ . Consequently, taking into account the independence of  $L_{PG}$  of the temperature,  $L_{PG} = (1.44 \pm 0.05) \text{ \AA}$  it is assumed for both series of samples in the studied temperature range. Due to this estimation the obtained results illustrate a consistency with the Marcus-Holstein hopping model.

The correlation of the reciprocal values of the measured space charge field  $1/E_{sat}$  against  $\Lambda$  parameter is due to the  $1/E_{sat} = \frac{(\Lambda + \Lambda_{dark})}{L_{PG}}$  equation and to the above mentioned fact that  $L_{PG}$  parameter is independent of the temperature and the crystal composition [45]. The specific dark conductivity  $\Lambda_{dark}$  keep the same nonzero value within the experimental accuracy due to the sample and temperature independent of the parasitic conductivity. Some additional jumping mechanism between Fe ions like to the extrinsic contributions as unwanted contact with the metallic sample holder inside the cryostat was also ignored.

From the relation of the  $\Lambda$  and  $1/E_{sat}$  parameters reported in Figure 4.8.3 the parameters  $L_{PG} = (1.44 \pm 0.05) \text{ \AA}$  and  $\Lambda_{dark} = (1.69 \pm 0.07) \times 10^{-17} \text{ m}^2/\text{V}$  consequently the saturation value of space charge field by Eq. 4.4.6 were recovered for all understudy experimental conditions and are given in Figures 4.6.1.3 as solid lines.

### Photogeneration coefficient

Considering the temperature independence of the photogalvanic length  $L_{PG}$ , from the experimental results of  $E_{sat}$  the free carrier generation probability  $\phi$  as a function of the temperature can be obtained as:  $\phi = \frac{j_{PG}}{L_{PG}} = \frac{E_{sat}\Sigma}{L_{PG}}$ . Here it can be mentioned that  $E_{sat}$  is independent of the charge carrier generation probability. The computed results for all samples

are reported in Figures 4.8.4 and 4.8.5. It is visible from the graphs that the value 10-15% of  $\phi$  parameter at room temperature decreases of about 5% at 150 K temperature.

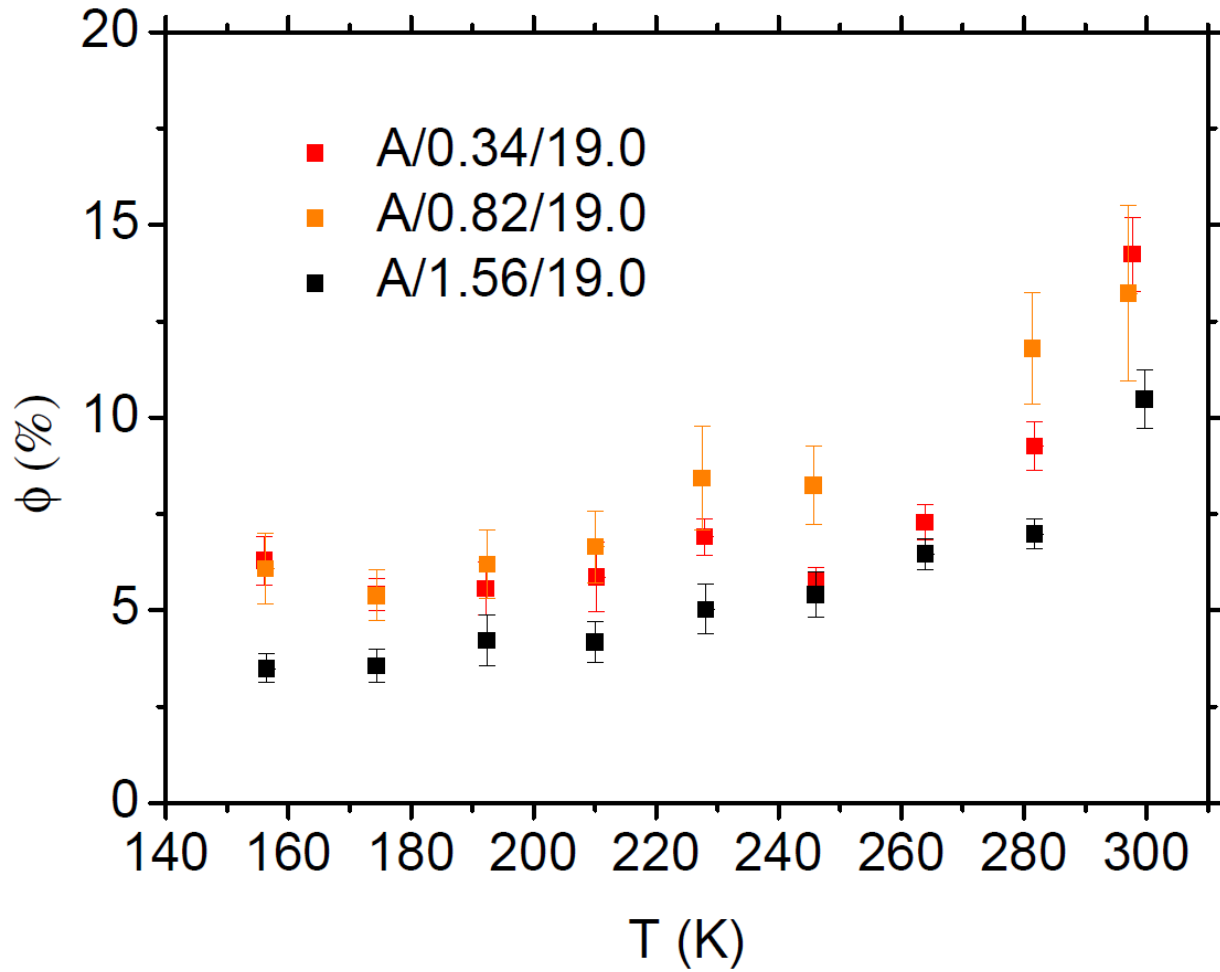


Figure 4.8.4: Photogeneration efficiency  $\phi$  for samples series A.

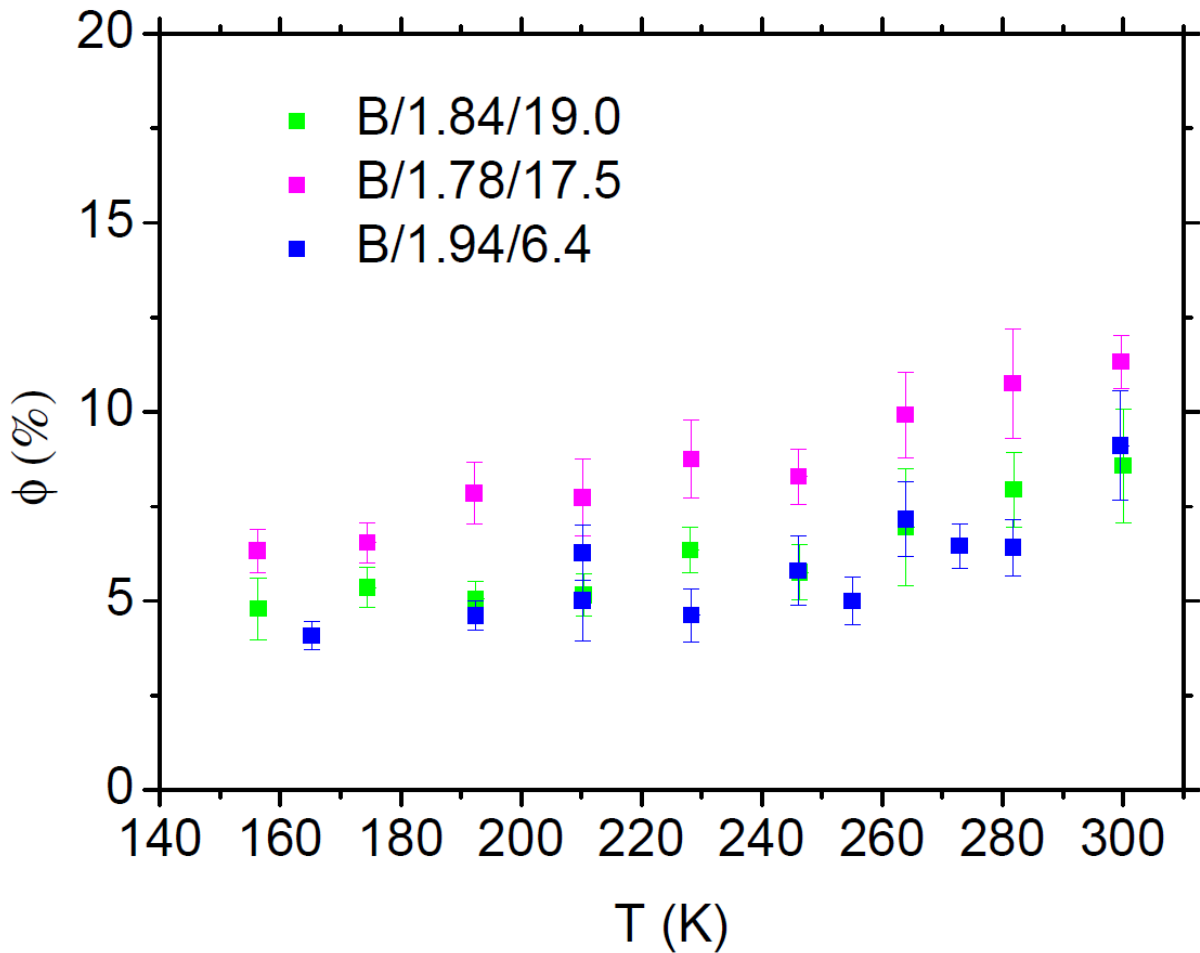


Figure 4.8.5: Photogeneration efficiency  $\phi$  for samples series B.

From the defined results of generation probability  $\phi$ , the specific dark conductivity  $\Lambda_{dark}$  and the simulated drift coefficient  $\Lambda$  the specific conductivity  $\Sigma$  was recovered using Eq. 4.3.2. The results are reported in Figure 4.6.1.4 (lines).

## § 4.9. Discussion

### Drift coefficient

The decrease of the drift coefficient  $\Lambda$  provided by the Monte Carlo simulation with the decrease of the temperature is the result of the reduction of the number of the jumps of the polaron performing since the generation to the captured by deep Fe centers [92]. The dependence of the  $\Lambda$  on the temperature is related to the different values of the activation energy corresponding to the varied types of the hops as the change of the temperature influence variously on the different types of the jump. Especially the hopping frequency of the capture  $Nb_{Nb}(Nb_{Li}) \rightarrow Fe$  dominates compared to other types increasing the trapping probability with the decrease of the temperature.

Two types of the hopping regime are emphasized for the tested samples: Multi-hop, mixed transport regime and trapping regime. Former regime: Due to the high thermal budget the hopping frequency increases or decreases thus, the polaron is able to perform several amount of jump before trapping by the deep center  $Fe^{3+}$ . Drift coefficient  $\Lambda$  depends on the relative number of the different types of jumps, especially for low antisite concentration and/or at high temperature the free polaron hope  $Nb_{Nb} \rightarrow Nb_{Nb}$  predominates [96]. Thus at high temperature and/or in samples with low antisite concentration the resistance to the photorefractivity consequently conductivity increase.

Trapping regime: At enough low temperature the hopping frequency between Fe trap centers dominates for all types hopping increasing the probability of the direct trap of polaron. According to the results of the simulation the newborn polaron can be captured by the trap center being far from it about several tenths of Angstroms. The trapping radius which is the distance of Fe trap center by which polaron can be captured than to jump away increases from 20Å to 40Å with the decrease of room temperature down to 150 K [91]. The trapping volumes start occupy more spaces with the decrease of the temperature of the samples resulting to the capture of polarons within few jumps.

### **Photogalvanic length**

Taking into account the independence of the parameter  $L_{PG}$  of the temperature and the sample the value for it assumed  $L_{PG} = (1.44 \pm 0.05)\text{\AA}$  which is in agreement with the literature result for Fe ions excited by visible light [45]. Above mentioned value may be compared to the absolute spacing of the hop covered by the photo-excited “hot” electrons before condensation into polaron. However, this absolute distance is larger being equal about  $23 \text{\AA}$ . This fact can be explained that the newborn charge is emitted probably isotropically as well as the average movement which keeps the nonzero value is a little fraction of the electron run distance before the self-localization.

### **Photogeneration coefficient**

The assumed value of  $L_{PG}$  allows as to obtain also the photogeneration efficiency  $\phi$  as a function of the temperature and the crystal composition (at higher temperature). The quantity  $\phi$  is equal to about 15% (for LN:Fe1-1 ÷ LN:Fe1-3 samples) and 10% (for LN:Fe2-1 ÷ LN:Fe2-3 samples) at room temperature and it decreases to 5% at 150K temperature. The investigated results illustrate the dependence of the Charge carrier generation probability on the temperature as well as on the wavelength [87]. According to the Marcus-Holstein polaron hopping model the after the starting thermalization stage the newborn (hot) particle is able to hop a spacing of the order  $20 \text{\AA}$  at room temperature from its generation initial site to the trapped site. There are two ways for polaron to continue the life: or run away either to return to the initial site where it starts a hop from. Both types of processes are thermally activated whereas with different energy barrier (See Marcus-Holstein polaron hopping frequency). According to this report the microscopic interpretation of the photogeneration coefficient is the probability of the polaron to hop away thus, not to return to the initial generation site [46]. At low temperature as the capturing of the polaron by the trap centers dominates it can be considered that the trap radius of Fe ions rises up with the decrease of the temperature. The trapping radius has the same value of the thermalization distance of the particle i.e. of the

order 20 Å. The low  $\phi$  corresponds to this fact that the essential amount of polarons are generated and are re-trapped inside the trapping radius by the same donor Fe centers at where they were formed. The temperature dependence of the hopping frequency is related to the increase of the trapping radius with the decrease of the temperature which means that the chance to avoid the capturing decreases more and more. Due to the report in literature the photogeneration coefficient decreases for about four times with the increase of wavelength from the green to the blue color. Taking into account  $\phi < 1$  value during measurements corresponding to our data  $\phi$  parameter must be smaller than 0.25 when  $\lambda = 543$  nm. The dependence of the photogeneration coefficient on the wavelength is related to the increase of the energetic photons which project the charge of emitted photons at a longer spacing from the donor centers [45].

#### ***§ 4.10. Conclusion-Chapter 4***

In this chapter the modeling of the incoherent jump regime of the photon-excited charge transport in iron doped LN has been investigated following to the thermalization of the newborn “hot” electrons using the Marcus-Holstein polaron model when all parameters are fixed taking known parameters from the literature into account. Above mentioned regime is related to the charge localization at a single lattice and its incoherent jumping within defective and/or regular sites. A set of experiments for the investigations of photorefractive, photoconductive and photogalvanic properties were dedicated to this purpose: the LN crystals with different composition doped with TM ions (Fe) were grown by Czochralski technique, prepared and characterized by compositional and structural properties required for the above mentioned investigation. The empiric results obtained using digital holographic technique in the large temperature range from 150 K to room temperature were compared to the results of the theoretical modelling. The experimental results are consistent with the numerical values of specific photoconductivity and saturation space charge field obtained by Monte Carlo simulation when the photogalvanic length  $L_{PG} = (1.44 \pm 0.05)\text{Å}$  and the free carrier

generation probability  $\phi$  for  $Fe^{2+}$  is equal to about 10-15% at room temperature and it decreases to 5% at 150K temperature. Marcus-Holstein polaron hopping model provides the direct estimation of poorly-known two parameters such as: the photogalvanic length  $L_{PG} = (1.44 \pm 0.05)\text{\AA}$  and the free carrier generation probability  $\phi$  for  $Fe^{2+}$  as a function of temperature excited by 543 nm green probe beam. The former quantity  $L_{PG} = (1.44 \pm 0.05)\text{\AA}$  being the average spacing from the donor center at which the photo-induced charge carriers localize into the polaron, demonstrates the independence on the temperature and the crystal composition when the second parameter related to the starting photo-excitation stage illustrates an independence only on the sample composition in the accordance with the tested conditions within experimental accuracy. The dependence of  $\phi$  parameter on the temperature influences directly on the photoconductivity which is interpreted with the help of the probability for newborn polarons to be retrapped by thermally activated jump to the initial donor center.

The discussed polaron model gives the ability to explain how the crystal composition and temperature affect the thermal transport. The major principle is the decrease of the number of jumps and distance of motion by cooling the sample (for a certain trap density). This rule can not be explained by photorefractive standard equations caused by the fact that various values of the activation energy correspond to the different hopping processes thus, the temperature variation affect the relative abundance of the different kinds of jump.

According to the realized analyses at the essential low temperatures a limiting capturing regime must be achieved where the significant number of light induced particles would be captured in a single jump. This regime can be characterized as “photon-assisted jumping” situation in which due to the smallest drift coefficient the saturation space charge field is too higher and provides the excluding of the parallel relaxation channels.

#### *References-Chapter 4*

1. A. Ashkin, G.D. Boyd, J.M. Dziedzic, R.G. Smith, A.A. Ballman, J.J. Levinstein, K. Nassau, "Optically-Induced Refractive Index Inhomogeneities LiNbO<sub>3</sub> and LiTaO<sub>3</sub>", Appl. Phys. Lett. 9, pp. 72-74 (1966).
2. F.S. Chen, J.T. LaMacchia, D.B. Fraser, "Holographic Storage in Lithium Niobate", Appl. Phys. Lett. 13, pp. 223-225 (1968).
3. K. Buse, J. Imbrock, E. Kratzig, K. Peithmann, "Photorefractive Effects in LiNbO<sub>3</sub> and LiTaO<sub>3</sub>", in P. Günter, J.P. Huignard, Photorefractive Materials and Their Applications 2, pp. 83-121 (2007).
4. N.V. Anghert, V.A. Pashkov, N.M. Solovyeva, Zh. Exp. Teor. Fiz. 26, (1972).
5. Y. Furukawa, K. Kitamura, S. Takekawa, K. Niwa, H. Hatano, "Stoichiometric Mg:LiNbO<sub>3</sub> as an effective material for nonlinear optics", Opt. Lett. Vol. 23. No. 24, pp. 1892-1894 (1998).
6. Y. Furukawa, M. Sato, K. Kitamura, Y. Yajima, and M. Minakata. "Optical Damage Resistance and Crystal Quality of LiNbO<sub>3</sub> Single Crystals with Various [Li]/[Nb] ratios", J. Appl. Phys., 72(8), pp. 3250-3254 (1992).
7. G.I. Malovichko, V.G. Grachev, E.P. Kokanyan, O.F. Schirmer, K. Betzler, B. Gather, F. Jermann, S. Klauer, U. Schlarb, M. Wohlecke, "Characterization of Stoichiometric LiNbO<sub>3</sub> Grown from Melts Containing K<sub>2</sub>O", Appl. Phys. A 56, pp.103-108 (1993).
8. F. Jermann, M. Simon, E. Kratzig, "Photorefractive Properties of Congruent and Stoichiometric Lithium Niobate at High Light Intensities", Opt. Soc. Am. B 12, Issue 11, pp. 2066-2070 (1995).
9. E. Kratzig, O.F. Schirmer, in "Photorefractive Materials and Their Applications I", ed. by P. Günter, J.P. Huignard, no. 61 in Topics in Appl. Phys. (Springer, Berlin), pp. 131-166 (1988).
10. H. Kurz, E. Kratzig, W. Keune, H. Engelmann, U. Gonser, B. Dischler and A. Rauber, "Photorefractive Centers in LiNbO<sub>3</sub>, Studied by Optical-, Mössbauer- and EPR-Methods" Appl. Phys., Vol.12, Issue 4, pp. 355-368 (1977).

11. K. Kitamura, Y. Furukawa, H. Hatano, R. Macfarlane, H. Guinther, "Stoichiometric LiNbO<sub>3</sub>: Material Potential for holographic data storage".first published by Taylor & Francis 2002.
12. N.V. Kukhtarev, "Kinetics of Hologram Recording and Erasure in Electrooptic Crystals", Tech. Phys. Lett. 2, pp. 438-440 (1976).
13. E. Krätzig, R. Orlowski, "Light Induced Charge Transport in Doped LiNbO<sub>3</sub> and LiTaO<sub>3</sub>", Ferroelectrics, Vol. 27, pp. 241-244(1980).
14. E. Krätzig, K. Kurz, "Photorefractive and photovoltaic effects in doped LiNbO<sub>3</sub>", Optica Acta 24, Issue 4, pp. 475-482 (1977).
15. G. C. Valley, "Simultaneous Electron/hole Transport in Photorefractive Materials", J. Appl. Phys. 59(10), pp. 3363-3366 (1986).
16. F. Jermann, J. Otten, "Light-induced charge transport in LiNbO<sub>3</sub>:Fe at high light intensities", J. Opt. Soc. Amer. B, Vol. 10, Issue 11, pp. 2085-2092 (1993).
17. D. Eimerl, S. Velsko, L. Davis, F. Wang, "Progress in Nonlinear Optical Materials for High Power Lasers" Prog. Cryst. Growth Charact. Mater. 20(1-2) pp. 59-113 (1990).
18. A. Rauber, in Current Topics in Material sciences (Edited by E. Kaldis), Vol. 1, p. 481. North-Holland, Amsterdam (1978).
19. O.F. Schirmer, O. Thiemann, M. Wohlecke, "Defects in LiNbO<sub>3</sub>—I. Experimental Aspects" J. Phys. Chem. Solids 52, Issue 1, pp. 185-200 (1991).
20. H. Liu, X. Xie, Y. Kong, W. Yan, X. Li, L. Shi, J. Xu, and G. Zhang, "Photorefractive Properties of Near-Stoichiometric Lithium Niobate Crystals Doped with Iron", Opt. Mater. Vol. 28, Issue 3, pp. 212-215 (2006).
21. X. Chen, D. Zhu, B. Li, T. Ling, and Z. Wu, "Fast Photorefractive Response in Strongly Reduced Near-Stoichiometric LiNbO<sub>3</sub> Crystals", Opt. Lett. 26, Issue 13, pp. 998-1000 (2001).

22. F. Xin, G. Zhang, F. Bo, H. Sun, Y. Kong, J. Xu, T. Volk, and N. M. Rubinina, "Ultraviolet Photorefraction at 325 nm in Doped Lithium Niobate Crystals", *J. Appl. Phys.* 107, pp. 033113/1- 033113/7 (2010).
23. Gi-Guo Zhong, Jin Jian, and Zhong-Kang Wu, 11 th International Quantum Electronics Conference, IEEE Cat. No. 80 CH 1561-0, p.631 (1980).
24. D.A. Bryan, R. Gerson, H.E. Tomaschke, "Increased Optical Damage Resistance in Lithium Niobate", *Appl. Phys. Lett.* Vol. 44, Issue 9, pp. 847-849 (1984).
25. L. Palfalvi, J. Hebling, G. Almasi, A. Peter, K. Polgár, K. Lengyel, R. Szipocs, "Nonlinear Refraction and Absorption of Mg Doped Stoichiometric and Congruent  $\text{LiNbO}_3$ ", *J. Appl. Phys.* 95(3), pp. 902-908 (2004).
26. L. Razzari, P. Minzioni, I. Cristiani, V. Degiorgio, and E. P. Kokanyan, "Photorefractivity of Hafnium-doped Congruent Lithium-niobate Crystals", *Appl. Phys. Lett.* 86, pp. 131914/1-131914/3 (2005).
27. Y. Furukawa, A. Yokotani, T. Sasaki, H. Yoshida, K. Yoshida, F. Nitanda, M. Sato, "Investigation of Bulk Laser Damage Threshold of Lithium Niobate Single Crystals by Q-Switched Pulse Laser", *J. Appl. Phys.* 69 (5), pp.3372-3374 (1991).
28. T.R. Volk, N.M. Rubinina, "A New Optical Damage Resistant Impurity in Lithium Niobate Crystals: Indium", *Ferroelectric Letters* 14, pp.37-43 (1992).
29. T.R. Volk, N.M. Rubinina, V.I. Pryalkin, V.V. Krasnikov, V.V. Volkov, "Optical and non-Linear Optical Investigations in  $\text{LiNbO}_3:\text{Mg}$  and  $\text{LiNbO}_3:\text{Zn}$ ", *Ferroelectrics* Vol. 109, Issue 1, pp. 345 (1990).
30. Y. Zhang, Y. Xu, M. Li, Y. Zhao, "Growth and Properties of Zn Doped Lithium Niobate Crystal", *J. Cryst. Growth* Vol. 233, Issue 3, pp. 537-540 (2001).
31. Y. Kong, J. Wen, H. Wang, "New Doped Lithium Niobate Crystal With High Resistance to Photorefraction- $\text{LiNbO}_3:\text{In}$ ", *Appl. Phys. Lett.* Vol. 66, Issue 3, pp. 280-281 (1995).

32. E. P. Kokanyan, L. Razzari, I. Cristiani, V. Degiorgio, and J. B. Gruber, “Reduced Photorefraction in Hafnium Doped Single-domain and Periodically Poled Lithium Niobate Crystals”, *Appl. Phys. Lett.* 84, pp.1880–1882 (2004).
33. A. M. Petrosyan, R. K. Hovsepyan, E. P. Kokanyan, and R. S. Feigelson, “Growth and Evaluation of Lithium Niobate Crystals Containing Nonphotorefractive Dopants,” *Proc. SPIE* 4060, pp. 106–113 (2000).
34. P. Minzioni, I. Cristiani, J. Yu, J. Parravicini, E. P. Kokanyan, and V. Degiorgio, “Linear and Nonlinear Optical Properties of Hafnium-doped Lithium-niobate Crystals”, *Optics Express*, Vol. 15, Issue 21, pp. 14171-14176 (2007).
35. P. Minzioni, I. Cristiani, V. Degiorgio, and E. P. Kokanyan, “Strongly Sublinear Growth of the Photorefractive Effect for Increasing Pump Intensities in Doped Lithium-Niobate Crystals”, *J. Appl. Phys.* 101, pp 116105/1-116105/3 (2007).
36. T.R. Volk, M. Wohlecke, N. Rubinina, N. V. Razumovskii, F. Jermann, C. Fischer, R. Bower, “LiNbO<sub>3</sub> with the Damage-resistant Impurity Indium”, *Appl. Phys. A* Vol. 60, Issue 2, pp. 217-225 (1995).
37. J. K. Yamamoto, T. Yamazaki, K. Yamagishi, “Noncritical Phase Matching and Photorefractive Damage in Sc<sub>2</sub>O<sub>3</sub>:LiNbO<sub>3</sub>”, *Appl. Phys. Lett.* 64, No.24, pp. 3228-3230 (1994).
38. J. K. Yamamoto, K. Kitamura, N. Iyi, Sh. Kimura, Y. Furukawa, M. Sato, “Increased Optical Damage Resistance in Sc<sub>2</sub>O<sub>3</sub>-doped LiNbO<sub>3</sub>”, *App. Phys. Lett.* 61 (18), pp. 2156-2158 1992.
39. H. Wang, J. Wen, J. Li, H. Wang, J. Jing, “Photoinduced Hole Carriers and Enhanced Resistance to Photorefraction in Mg-doped LiNbO<sub>3</sub> Crystals”, *Appl. Phys. Lett.* Vol. 57, No.4, pp. 344-345 (1990).
40. J.C. Deng, J.K. Wen, Z.K. Wu, H.F. Wang, “Decay Dynamics of Laser-induced Gratings in LiNbO<sub>3</sub>:Zn”, *Appl. Phys. Lett.* 64, No. 20, pp. 2622-2624 (1994).
41. T. Volk and M. Wohlecke, “Lithium Niobate: Defects, Photorefraction, and Ferroelectric Switching” Springer, Berlin, p.264 (2008).

42. G. Nava, P. Minzioni, W. Yan, J. Parravicini, D. Grando, E. Musso, I. Cristiani, N. Argiolas, M. Bazzan, M. V. Ciampolillo, A. Zaltron, C. Sada, and V. Degiorgio, “Zirconium-doped Lithium Niobate: Photorefractive and Electro-optical Properties as a Function of Dopant Concentration”, *Opt. Mat. Expr.*, Vol. 1, No. 2, pp. 270-277 (2011).
43. M.E. Lines and A.M. Glass “Principles and Application of Ferroelectrics and Related Materials”, Clarendon Press, Oxford (1997).
44. A. M. Glass, D. von der Linde, and T. J. Negran. High Voltage Bulk Photovoltaic Effect and the Photorefractive Process in  $\text{LiNbO}_3$ ”, *Applied Physics Letters*, 25(4), pp. 233-235 (1974).
45. O. F. Schirmer, M. Imlau, and C. Merschjann. “Bulk Photovoltaic Effect of  $\text{LiNbO}_3$  : Fe and its Small-Polaron-Based Microscopic Interpretation”, *Phys. Rev. B* 83, pp. 165106/1-165106/13 (2011).
46. J. Carnicero, M. Carrascosa, G. García, and F. Agulló-López, “Site Correlation Effects in the Dynamics of Iron Impurities  $\text{Fe}^{2+}/\text{Fe}^{3+}$  and Antisite Defects  $\text{Nb}_{\text{Li}}^{4+}/\text{Nb}_{\text{Li}}^{5+}$  After a Short-Pulse Excitation in  $\text{LiNbO}_3$ ”, *Phys. Rev. B*, 72, pp. 245108/1-245108/7 (2005).
47. I. Nee, M. Muller, K. Buse, and E. Krätzig, “Role of Iron in Lithium-Niobate Crystals for the Dark-storage Time of Holograms”, *J. of Appl. Phys.* 88(7), pp. 4282-4286 (2000).
48. T. Volk, N. Rubinina, and M. Wohlecke, “Optical-damage-resistant Impurities in Lithium Niobate”, *J. Opt. Soc. Am. B*, Vol.11, Issue 9, pp. 1681-1687 (1994).
49. Y. Furukawa, K. Kitamura, S. Takekawa, A. Miyamoto, M. Terao, N. Suda, “Photorefraction in  $\text{LiNbO}_3$  as a Function of  $[\text{Li}]/[\text{Nb}]$  and MgO Concentrations”, *Appl. Phys. Lett.* 77, pp. 2494-2496 (2000).
50. J. C. Burfoot, “Ferroelectrics. An Introduction to the Physical Principles”, Van Nostrand, London - Princeton - New Jersey - Toronto, (1967).
51. R. Sommerfeldt, L. Holtman, E. Krätzig and B. C. Grabmaier, “The Light-induced Charge Transport in  $\text{LiNbO}_3:\text{Mg}$ , Fe crystals”, *Ferroelectrics*, Vol. 92, pp. 219-225 (1989).
52. M. Falk, K. Buse, “Thermo-electric Method for Nearly Complete Oxidization of Highly Iron-doped Lithium Niobate Crystals”, *Appl. Phys. B* Vol. 81, No.6, pp. 853-855 (2005).

53. Z. Zhou, B. Wang, Sh. Lin, Y. Li, K. Wang, "Investigation of Optical Photorefractive Properties of Zr:Fe:LiNbO<sub>3</sub> Crystals" *Optics & Laser Technology* 44 pp. 337–340(2012).
54. R. Orłowski, E. Kratzig, "Holographic Method for the Determination of Photo-induced Electron and Hole Transport in Electro-optic Crystals", *Solid State Commun.* Vol.27, Issue 12, pp. 1351-1354 (1978).
55. F. P. Strohkendi, J. M. C. Jonathan and K. W. Hellwarth, "Hole-electron Competition in Photorefractive Gratings", *Optics Letters*, Vol. 11, No 5, pp. 312-314 (1986).
56. E. Kratzig and H. Kurz, "Spectroscopic Investigation of Photovoltaic Effects in Doped LiNbO<sub>3</sub>", *J. Electrochem. Soc.: Solid-State Science and Technology*, Soc. Vol. 124, No. 1, pp. 131-134 (1977).
57. R. Sommerfeldt, L. Holtmann, E. Kratzig, B. Grabmaier, "Influence of Mg Doping and Composition on the Light-induced Charge Transport in LiNbO<sub>3</sub>", *Phys. Stat. Solidi (a)* Vol. 106, Issue 1, pp. 89-98 (1988).
58. E. Kratzig, "Photorefractive Effects and Photoconductivity in LiNbO<sub>3</sub>:Fe", *Ferroelectrics* 21, pp. 635-636 (1978).
59. H. Qiao, J. Xu, G. Zhang, X. Zhang, Q. Sun, and G. Zhang, "Ultraviolet Photorefractivity Features in Doped Lithium Niobate Crystals" *Phys. Rev. B* 70, pp. 094101/1-094101/14 (2004).
60. F. Rossella, D. Grando, P. Galinetto, V. Degiorgio and E.Kokanyan, "Photoconductive and Electro-Optical Properties of Hf Doped Lithium Niobate Crystals", *Ferroelectrics*, 352, pp. 143–147 (2007).
61. G. Malovichko, V. Grachev, E. Kokanyan, O. Schirmer, "Axial and Low-symmetry Centers of Trivalent Impurities in Lithium Niobate: Chromium in Congruent and Stoichiometric Crystals", *Phys. Rev. B* 59 Issue 14, pp. 9113-9125 (1999).
62. H.X. Feng, J.K. Wen, H.F. Wang, S. Y.Hand, Y.X. Xu, *J. Phys. Chem. Solids* **51**, 397 (1990).
63. X. H. Zhen, Q. Li, L.C. Zhao, Y.H. Xu, "Effect of Li/Nb Ratio on Structure and Photorefractive Properties of Zn:Fe:LiNbO<sub>3</sub> Crystals" *J. Mater. Sci.* Vol. 42, Issue 10, pp. 3670-3674 (2007).

64. J. Garcia-Sole, L. Bausa, D. Jaque, E. Montoya, H. Murrieta, F. Jaque, "Rare Earth and Transition Metal Ion Centers in LiNbO<sub>3</sub>", *Spectrochimica Acta Part A-Molecular Spectroscopy* 54, Issue 11, pp. 1571-1581 (1998).
65. P. J. Jorgensen, R. W. Bartlett, "High Temperature Transport Processes in Lithium Niobate", *J. Phys. Chem. Of Sol.*, Vol. 30, Issue 12, pp. 2639-2648 (1969).
66. G. Bergmann, "The Electrical Conductivity of LiNbO<sub>3</sub>", *Solid State Communications*, Vol. 6, pp. 77-79 (1967).
67. S. Breer, K. Buse, K. Peithmann, H. Vogt, and E. Kratzig, "Stabilized Recording and Thermal Fixing of Holograms in Photorefractive Lithium Niobate Crystals", *Rev. Sci. Instrum.*, Vol. 69, No. 4, pp. 1591-1594 (1998).
68. P. Günter and J.-P. Huignard. *Photorefractive Materials and Their Applications 1*, Vol. 113 of 0342-4111. Springer New York, (2006).
69. J. Frejlich, "Photorefractive Materials: Fundamental Concepts, Holographic Recording and Materials Characterization", Wiley (2006).
70. J.-L. Zhao, P.Zhang, J.-B. Zhou, De-X. Yang, D.-S. Yang, E.-P. Li, "Visualization of Light-induced Refractive Index Changes in Photorefractive Crystals Employing Digital Holography", *Northwestern Polytechnical University, Department of Applied Physics* Vol. 20, No. 10, pp 1748-1751 (2003).
71. L. Vittadello, A. Zaltron, N. Argiolas, M. Bazzan, N. Rossetto, and R. Signorini, "Photorefractive Direct Laser Writing", *J. of Physics D: Appl. Phys.* 49(12), pp. 125103/1-125103-9 (2016).
72. S. Bian, L. Li, and J. Kumar, "Single Laser Beam-induced Surface Deformation on Azobenzene Polymer Films", *Appl. Phys. Lett.*, Vol. 73, No. 13, pp. 1817-1819 (1998)
73. E. A. Bahaa, C. T. Saleh "Fundamentals of Photonics", John Wiley & Sons, Inc., 1991

74. Y. Lingfeng and C. Lilong "Iterative Algorithm with a Constraint Condition for Numerical Reconstruction of a Three-dimensional Object From its Hologram" J. Opt. Soc. of Am., Vol.18, Issue 5, pp. 1033-1045 (2001).
75. R. C. Gonzalez, R. E. Woods "Digital Image Processing", Second Edition, Chapter 4, pp 150-215 (2001).
76. M. Arevallilo Herráez, D. R. Burton, M. J. Lalor, and M. A. Gdeisat, "Fast Two-dimensional Phase-unwrapping Algorithm Based on Sorting by Reliability Following a Noncontinuous path", Appl. Opt., 41(35), pp. 7437-7444 (2002).
77. Ulf Schnars "Direct Phase Determination in Hologram Interferometry with use of Digitally Recorded Holograms", J. Opt. Soc. Am, A, Vol.11, Issue 7, pp. 2011-2015 (1994).
78. E. CuChe, P. Marquet and C. Depeursinge, "Spatial Filtering for Zero-order and Twin-image Elimination in Digital off-axis Holography", Appl. Opt. Vol. 39, No. 23, pp. 4070-4075 (2000).
79. Dennis Ghiglia and Mark Pritt, "Two-dimensional Phase Unwrapping Theory, Algorithms and Applications", John Wiley & Sons, (1998).
80. T. Hall, R. Jaura, L. Connors, and P. Foote, "The Photorefractive Effecta Review", Progress in Quantum Electronics 10(2), pp. 77-46, 1985.
81. G. F. Calvo, F. Agullo-Lopez, M. Carrascosa, MR Belic, and Wieslaw Krolikowski, "Locality vs. Nonlocality of (2+1)-Dimensional Light-induced Space-Charge Field in Photorefractive Crystals", J. EPL (Europhysics Letters), 60(6), pp. 847-853, 2002.
82. C. Herzog, G. Poberaj, and P. Gunter, "Electro-optic Behavior of Lithium Niobate at Cryogenic Temperatures", J. Opt. Comm. 281(4), pp. 793-796 (2008).
83. E. H. Turner, F. R. Nash, and P. M. Bridenbaugh, "Dependence of Linear Electro-optic Effect and Dielectric Constant on Melt Composition in Lithium Niobate", J. of Appl. Phys. 41(13), pp. 5278-5281, 1970.

84. A. Danielyan, N. Kokanyan, S. Kostritskii, E. Kokanyan, M. Aillerie "Composition Dependence of the Electro-optic Properties of Iron-doped Lithium Niobate Crystals Mounted as Bulk Modulator" J. of Am. Cer. Soc., Vol.102, Issue 6, pp. 3535-3546 (2018).
85. P. A. Augstov and K. K. Shvarts, "The Temperature and Light Intensity Dependence of Photorefraction in LiNbO<sub>3</sub>", J. Appl. Phys. 21, pp. 191-194 (1980).
86. K. Peithmann, A. Wiebrock, and K. Buse, "Photorefractive Properties of Highly Doped Lithium Niobate Crystals in the Visible and Near-infrared", J. Appl. Phys. B 68, pp. 777-784 (1999).
87. R. Grousseau, M. Henry, S. Mallick, and S. L. Xu, "Measurement of Bulk Photovoltaic and Photorefractive Characteristics of Iron Doped LiNbO<sub>3</sub>", J. of App. Phys., 54(6), pp. 3012-3016, 1983.
88. T. Holstein, "Studies of Polaron Motion," Annals of Physics 8(3), pp. 343 – 389, 1959.
89. R. A. Marcus. On the Theory of Oxidation-reduction Reactions Involving Electron Transfer. I. The Journal of Chemical Physics, 24(5):966\_978, 1956.
90. D. Emin, "Polarons", Cambridge University Press (2013).
91. I. Mhaouech and L. Guilbert. Temperature Dependence of Small Polaron Population Decays in Iron-doped Lithium Niobate by Monte Carlo simulations. Solid State Sciences, 60< pp. 28-36, 2016.
92. Appi Zylbersztejn, "Thermally Activated Trapping in Fe-doped LiNbO<sub>3</sub>", J. Appl. Phys. Lett., 29(12), pp. 778-780 (1976).
93. M. Imlau, H. Badorreck, and Chr. Merschjann, "Optical Nonlinearities of Small Polarons in Lithium Niobate", J. Appl. Phys. Rev., 2(4), pp. 040606-040606 (2015).
94. O. F. Schirmer, M. Imlau, C. Merschjann, and B. Schoke, "Electron Small Polarons and Bipolarons in LiNbO<sub>3</sub>. J. of Phys.: Condensed Matter, 21, pp. 123201/1-123201/29, 2009.
95. I. G. Austin and N. F. Mott, "Polarons in Crystalline and Non-crystalline Materials", Advances in Physics, 50(7), pp. 757-812 (2001).

96. L. Guilbert, L. Vittadello, M. Bazzan, I. Mhaouech, S. Messerschmidt, and M Imlau, "The Elusive Role of NbLi bound polaron energy in hopping charge transport in Fe : LiNbO<sub>3</sub>", J. of Phys.: Condensed Matter, p. 16 (2018).
97. A. Dhar, A. Mansigh, "Optical Properties of Reduces Lithium Niobate Single Crystals", J. Appl. Phys, Vol. 68(11), pp. 5804-5809 (1990)
98. S. C. Abrahams, J. M. Reddy, and J. L. Bernstein. "Ferroelectric Lithium Niobate. 3. Single Crystal X-ray Diffraction Study at 24 ° C", J. of Phys. Chem. of Solids, 27(6), pp. 997-1012 (1966).
99. B. Faust, H. Müller, and O. F. Schirmer, "Free Small Polarons in Fe:LiNbO<sub>3</sub>", Ferroelectrics, 153(1), pp. 297-302 (1994).
100. R. Metzler and J. Klafter, "The Random Walk's Guide to Anomalous Diffusion: A Fractional Dynamics Approach", J. Phys. Rep., 339(1), pp. 1-77 (2000).

# Conclusion

## Conclusion

1. EO and dielectric coefficients remain quasi constant in congruent crystals LN:Zr with the varied  $ZrO_2$  concentration from 0 mol % to 2.5 mol % excluding a kink at 2 mol % considered as the threshold Zr concentration.
2. In LN:In congruent crystals with the various concentration of  $In_2O_3$  (from 0.12 mol% to 1.7 mol%) EO  $r_{222}$  and dielectric coefficients  $\epsilon_{22}$  possess only a small acoustic contribution attributed to decrease of optical damage related to the smaller deformation parallel to the  $X$  ( $Y$ ) axis induces by the applied electric field.
3. In LN:Fe (0.11 mol%) crystals with varied composition ( $X_c=48.45$  mol %,  $X_c =48.58$  mol %,  $X_c =49.49$  mol %) in low frequency range EO coefficients  $r_{333}$ ,  $r_{133}$ ,  $r_c$  present a monotonous decrease behavior related to the polarisability of Nb ions along Z axis whereas  $r_{222}$  coefficient varies non monotonously with the increase of Li content in the crystal connected to the electro-mechanical contribution.
4. Experimental data of space charge field  $E_{sc}$  obtained for LN:Fe crystals with different Li content in the crystal equal to  $X_c=48.45$  mol %,  $X_c =48.58$  mol %,  $X_c =49.49$  mol %, with iron fixed concentration 0.11 mol % and for LN:Fe congruent crystals with varying Fe amount (0.02 mol %, 0.05 mol %, 0.1 mol %) increase with the decrease of temperature from the room temperature down to 150 K and with the increase of the Li content and iron concentration in the crystal.
5. Experimental values of specific photoconductivity  $\Sigma$  obtained for LN:Fe crystals with different Li content in the crystal equal to  $X_c=48.45$  mol %,  $X_c =48.58$  mol %,  $X_c =49.49$  mol %, with iron concentration 0.11 mol % and for LN:Fe congruent crystals with various Fe concentration (0.02 mol %, 0.05 mol %, 0.1 mol %) demonstrate the decrease of temperature from the room temperature down to 150 K with and with the increase iron concentration in the crystal remaining independent of the Li content in the crystal.

6. Experimental data and numerical values of  $E_{sc}$  and  $\Sigma$  obtained by Monte Carlo simulation based on the Marcus-Holstein hopping model are consistent with each other considering  $L_{PG} = (1.44 \pm 0.05)\text{\AA}$  and  $\Lambda_{dark} = (1.69 \pm 0.07) \times 10^{-17} \frac{\text{m}^2}{\text{V}}$ .
7. For LN:Fe crystals with different composition (Li content in the crystal  $X_c=48.45$  mol %,  $X_c=48.58$  mol %,  $X_c=49.49$  mol %), with iron concentration 0.11 mol % and with congruent composition with various Fe concentration (0.02 mol %, 0.05 mol %, 0.1 mol %) in the illuminated area by using 543 nm wavelength laser beam the photogeneration efficiency of electron small polarons decreases 2-3 times with the decrease of temperature in the range from room temperature down to 150 K due to the increase of the radius of trapping area where donor centers are also considered as trap centers resulting to the decrease of jumping frequency of the free charge carriers.
8. For LN:Fe crystals with different composition  $X_c=48.45$  mol %,  $X_c=48.58$  mol %,  $X_c=49.49$  mol %, with iron concentration 0.11 mol % and with congruent composition with various Fe concentration (0.02 mol %, 0.05 mol %, 0.1 mol %) in the illuminated area by using green laser beam the drift coefficient of electron small polarons decreases with the decrease of temperature in the range from room temperature down to 150 K and with the increase of defects in the crystal due to the increase of the trapping radius of area decreasing the hopping frequency of the free charge carriers.

## Résumé

La thèse est consacrée à l'étude des propriétés photoréfractives, structurales, électro-optiques (EO) et diélectriques dépendantes des propriétés intrinsèques et extrinsèques (introduites par l'incorporation d'ions non-photorefractifs ( $Zr^{4+}$ ,  $In^{3+}$ ) et photorefractifs ( $Fe^{2+/3+}$ ) dans les cristaux de niobate de lithium (LN) congruents et de diverses stoechiométrie entraînant le contrôle voulu des propriétés photoréfractives en tenant compte des caractéristiques des applications des cristaux LN.

Les principaux résultats suivants ont été obtenus ou/et déduits du travail de thèse comme conclusions principales:

1. Dans les cristaux congruents LN:Zr avec la concentration de  $ZrO_2$  variant de 0 à 2,5%mol, les coefficients d'EO et diélectriques restent constants à l'exclusion d'un repliement à 2% mol considéré comme le seuil de concentration en Zr.
2. Dans les cristaux congruents avec la concentration de  $In_2O_3$  dans la plage étudiée, c'est-à-dire de 0,12 %mol à 1,7% mol, le coefficient EO  $r_{222}$  et le coefficient diélectrique  $\epsilon_{222}$  ne possèdent qu'un faible apport acoustique lié au fait que In ion étant trivalent, il peut être incorporé simultanément dans les deux cations de réseau  $In_{Li}^{2+}$  et  $In_{Nb}^{2-}$  et la quantité de  $Nb_{Li}$  est complètement annulée même à une concentration en In <2 %mol.
3. Dans les cristaux LN:Fe (0,11 mol%), de différentes compositions ( $X_c=48,45-49,49$  mol%) les coefficients EO  $r_{333}$ ,  $r_{133}$ ,  $r_c$  basses fréquences présentent une diminution monotone lié à la polarisabilité des ions Nb le long de l'axe Z alors que le coefficient  $r_{222}$  varie de manière non monotone avec l'augmentation de la teneur en Li dans le cristal, comportement attribué à la contribution électro-mécanique.
4. Dans les cristaux LN:Fe (0,11 mol%), de différentes compositions ( $X_c=48,45-49,49$  mol%) et dans les cristaux LN:Fe congruents avec différentes quantités de Fe (0,02%mol, 0,05%mol, 0,1%mol) les données expérimentales de la détermination du champ de charge d'espace  $E_{sc}$  obtenues montrent l'augmentation de  $E_{sc}$  avec la baisse de

température depuis la température ambiante jusqu'à 150 K et avec l'augmentation de la teneur en Li et de la concentration en fer cristal.

5. Dans les cristaux LN:Fe (0,11 mol%), de différentes compositions ( $X_c=48,45-49,49$  mol%) et dans les cristaux LN:Fe congruents avec différentes quantités de Fe (0,02%mol, 0,05%mol, 0,1%mol) les valeurs expérimentales de la photoconductivité spécifique  $\Sigma$  obtenues montrent la diminution de  $\Sigma$  avec la température depuis la température ambiante jusqu'à 150 K avec et avec l'augmentation de la concentration en fer dans le cristal restant indépendante de la teneur en Li du cristal.
6. Les données expérimentales et les valeurs numériques de  $E_{sc}$  et  $\Sigma$  obtenues par la simulation de Monte Carlo reposant sur le modèle de saut de Marcus-Holstein sont cohérentes, puisque  $L_{PG} = (1.44 \pm 0.05)\text{\AA}$  et  $\Lambda_{dark} = (1.69 \pm 0.07) \times 10^{-17} \frac{\text{m}^2}{\text{V}}$ .
7. Dans les cristaux LN:Fe (0,11 mol%), de différentes compositions ( $X_c=48,45-49,49$  mol%) et dans les cristaux LN:Fe congruents avec différentes quantités de Fe (0,02%mol, 0,05%mol, 0,1%mol), dans la zone éclairée en utilisant un faisceau laser de longueur d'onde de 543 nm, l'efficacité de la photogénération des petits polarons électroniques diminue de 2 à 3 fois avec la diminution de la température dans la plage allant de la température ambiante à 150 K en raison de l'augmentation du rayon de la zone de piégeage où les centres donneurs sont également considérés comme des centres de piégeage, ce qui entraîne une diminution de la fréquence de saut des porteurs de charge libres.
8. Dans les cristaux LN:Fe (0,11 mol%), de différentes compositions ( $X_c=48,45-49,49$  mol%) et dans les cristaux LN:Fe congruents avec différentes quantités de Fe (0,02%mol, 0,05%mol, 0,1%mol) dans la zone éclairée en utilisant un faisceau laser vert, le coefficient de dérive des petits polarons électroniques diminue avec la diminution de la température dans la plage allant de la température ambiante à 150 K et avec l'augmentation des défauts dans le cristal due à l'augmentation du rayon de piégeage de la surface diminuant la fréquence de saut des porteurs de charge libres.

## Summary

The dissertation is devoted to the investigation of photorefractive, structural, electro-optical (EO) and dielectric properties depending on the intrinsic and extrinsic defects (introduced by incorporation of non photorefractive ( $Zr^{4+}$ ,  $In^{3+}$ ) and photorefractive ( $Fe^{2+/3+}$ ) ions) in lithium niobate (LN) crystals resulting to the purposeful control the photorefractive effect taking into account the features of the applications of LN crystals.

The main conclusions as obtained are the following:

1. EO and dielectric coefficients remain quazi constant in congruent crystals LN:Zr with the varied  $ZrO_2$  concentration from 0 mol % to 2.5 mol % excluding a kink at 2 mol % considered as the threshold Zr concentration.
2. LN:In congruent crystals with  $In_2O_3$  concentration in the studied range, i.e. from 0.12 mol% to 1.7 mol%, the EO coefficient  $r_{222}$  and the dielectric coefficient  $\epsilon_{22}$  possess only a small acoustic contribution related to the fact that In ion being trivalent, it may be incorporated simultaneously in both lattice cation positions ( $In_{Li}^{2+}$  and  $In_{Nb}^{2-}$ ) and the amount of  $Nb_{Li}$  is completely cancelled even at In concentration  $< 2$  mol%.
3. In LN:Fe (0.11 mol%) crystals with varied composition ( $X_c=48.45-49.49$  mol %) in low frequency range EO coefficients  $r_{333}$ ,  $r_{133}$ ,  $r_c$  present a monotonous decrease behavior related to the polarisability of Nb ions along Z axis whereas  $r_{222}$  coefficient varies non monotonously with the increase of Li content in the crystal connected to the electro-mechanical contribution.
4. Experimental data of space charge field  $E_{sc}$  obtained for LN:Fe crystals with different Li content in the crystal ( $X_c=48.45-49.49$  mol %), with iron fixed concentration 0.11 mol % and for LN:Fe congruent crystals with varying Fe amount (0.02 mol %, 0.05 mol %, 0.1 mol %) illustrate the increase with the decrease of temperature from the room temperature down to 150 K and with the increase of the Li content and iron concentration in the crystal.

5. Experimental values of specific photoconductivity  $\Sigma$  obtained for LN:Fe crystals with different Li content in the crystal ( $X_c=48.45-49.49$  mol %), with iron concentration 0.11 mol % and for LN:Fe congruent crystals with various Fe concentration (0.02 mol %, 0.05 mol %, 0.1 mol %) demonstrate the decrease of temperature from the room temperature down to 150 K with and with the increase iron concentration in the crystal remaining independent of the Li content in the crystal.
6. Experimental data and numerical values of  $E_{sc}$  and  $\Sigma$  obtained by Monte Carlo simulation based on the Marcus-Holstein hopping model are consistent with each other considering  $L_{PG} = (1.44 \pm 0.05)\text{\AA}$  and  $\Lambda_{dark} = (1.69 \pm 0.07) \times 10^{-17} \frac{\text{m}^2}{\text{V}}$ .
7. For LN:Fe crystals with different composition ( $X_c=48.45-49.49$  mol %) doped with 0.11 mol% iron and with congruent composition doped with various Fe concentration (0.02 mol %, 0.05 mol %, 0.1 mol %) in the illuminated area by using 543 nm wavelength laser beam the photogeneration efficiency of electron small polarons decreases 2-3 times with the decrease of temperature in the range from room temperature down to 150 K due to the increase of the radius of trapping area where donor centers are also considered as trap centers resulting to the decrease of jumping frequency of the free charge carriers.
8. For LN:Fe crystals with different composition  $X_c=48.45$  mol %,  $X_c =48.58$  mol %,  $X_c =49.49$  mol %, with iron concentration 0.11 mol % and with congruent composition with various Fe concentration (0.02 mol %, 0.05 mol %, 0.1 mol % in the melt) in the illuminated area by using green laser beam the drift coefficient of electron small polarons decreases with the decrease of temperature in the range from room temperature down to 150 K and with the increase of defects in the crystal due to the increase of the trapping radius of area decreasing the hopping frequency of the free charge carriers.